TRIPLE OXYGEN ISOTOPES IN HIGH-TEMPERATURE HYDROTHERMALLY ALTERED ROCKS: A RECORD OF PALEOCLIMATE AND ANCIENT HYDROSPHERE-ROCK INTERACTIONS

by

DAVID O ZAKHAROV

A DISSERTATION

Presented to the Department of Earth Sciences
and the Graduate School of the University of Oregon
in partial fulfillment of the requirements
for the degree of
Doctor of Philosophy

September 2019

DISSERTATION APPROVAL PAGE

Student: David O. Zakharov

Title: Triple Oxygen Isotopes in High-Temperature Hydrothermally Altered Rocks: A Record of Paleoclimate and Ancient Hydrosphere-Rock Interactions

This dissertation has been accepted and approved in partial fulfillment of the requirements for the Doctor of Philosophy degree in the Department of Earth Sciences by:

Prof. Ilya N. Bindeman	Chairperson/Advisor
Prof. Mark H. Reed	Core Member
Prof. Gregory J. Retallack	Core Member
Prof. Victoria J. DeRose	Institutional Representative

and

Janet Woodruff-Borden	Vice Provost and Dean of the Graduate School

Original approval signatures are on file with the University of Oregon Graduate School.

Degree awarded September 2019

DISSERTATION ABSTRACT

David O. Zakharov

Doctor of Philosophy

Department of Earth Sciences

September 2019

Title: Triple Oxygen Isotope in High-Temperature Hydrothermally Altered Rocks: A Record of Paleoclimate and Ancient Hydrosphere-Rock Interactions

In this dissertation, I use isotopes of H, O and Sr to trace interaction between meteoric waters, seawater and rocks in modern and extinct areas of high-temperature hydrothermal alteration. The ancient hydrothermal systems are used here as a tool to investigating paleoclimate, paleogeography, and the long-term evolution of global isotope budget of hydrosphere. The dissertation begins with exploring triple oxygen isotopes to trace local fluids in modern geothermal systems of Iceland (Krafla, Reykjanes), where seawater and meteoric waters participate in reaction with mid-ocean ridge basalts at high temperatures (> 250 °C). Next, I present results of the triple oxygen and hydrogen isotope study of the 2.43-2.41 Ga altered basalts from the Vetreny belt, Russia to constrain the isotope composition of contemporaneous seawater. I find that the δD, $\delta^{18}O$ and $\Delta^{17}O$ values of the early Paleoproterozoic seawater were similar to that of Cenozoic seawater values. This study is supported by demonstrating the combined strontium and oxygen isotope exchange between Precambrian seawater and basalt with implications for the effects of low marine sulfate levels. Further, I explore the low $\delta^{18}O$ signature of the Belomorian belt, Russia that was likely generated during subglacial rifting and magmatism at low latitudes in the early Paleoproterozoic. Using $\Delta^{17}O$ approach, I reconstruct the $\delta^{18}O$ values of the low latitude precipitation to ca. -40 ± 5 ‰. This value is evident of an active hydrologic cycle facilitated through evaporation of seawater and precipitation at extremely low temperatures (between -45 and -40 °C) during the Paleoproterozoic snowball Earth glaciations. Using high-precision U-Pb zircon dating, I constrain the timing of subglacial magmatism to 2.44-2.41 Ga and 2.29 Ga. The triple oxygen isotope approach is also applied to the low $\delta^{18}O$ 2.42-2.38 Ga Scourie dikes

of the Lewisian complex, Scotland to test for assimilation or/and recycling of very low $\delta^{18}O$ component, similar to the rocks from the Belomorian belt.

This dissertation includes previously published and unpublished co-authored material. This dissertation is accompanied by electronic supplemental file that contains U-Pb geochronology data.

CURRICULUM VITAE

NAME OF AUTHOR: David O. Zakharov

GRADUATE AND UNDERGRADUATE SCHOOLS ATTENDED:

University of Oregon, Eugene, Oregon, USA
Russian State Geological Prospecting University, Moscow, Russia

DEGREES AWARDED:

Doctor of Philosophy, Earth Sciences, 2019, University of Oregon
Diploma of Specialist, Geological Sciences, 2013, Russian State Geological Prospecting University

AREAS OF SPECIAL INTEREST:

Isotope geochemistry
Water-rock interaction
Precambrian geology

PROFESSIONAL EXPERIENCE:

Graduate Teaching Fellow, University of Oregon, 2014-2019

Graduate Teaching Assistant, University of Manitoba, 2013-2014

Lab assistant, University of Illinois, 2013

GRANTS, AWARDS, AND HONORS:

Earth Sciences Research Excellence Award, University of Oregon, 2019

Evolving Earth Foundation Student Grant, 2018

National Geographic Young Explorer Grant, 2017

Graduate Research Grant, Geological Society of America, 2017

Staples Scholarship, University of Oregon, 2016

Outstanding Graduate Teaching Fellow Award, University of Oregon 2016

Good Citizen Award, University of Oregon, 2015

Geological Sciences Award, University of Oregon, 2014

Jay M. McMurray Scholarship, University of Oregon, 2015

Clayton H. Riddell Faculty of Environment, Earth and Recourses Graduate Entrance Scholarship, University of Manitoba, 2013

PUBLICATIONS:

Zakharov D.O., Bindeman I.N., Serebryakov N. S., Prave A.R., Azimov P.Ya., and Babarina I.I. (2019) Low $\delta^{18}O$ rocks in the Belomorian belt, NW Russia, and Scourie dikes, NW Scotland: A record of ancient meteoric water captured by the early Paleoproterozoic global mafic magmatism. *Precambrian Research* (in press).

Zakharov D.O. and Bindeman I.N. (2019) Triple oxygen and hydrogen isotopic study of hydrothermally altered rocks from the 2.43-2.41 Ga Vetreny belt, Russia: An insight into the early Paleoproterozoic seawater. *Geochimica et Cosmochimica Acta*, 248, 185-209.

Bindeman I.N., **Zakharov D.O.**, Palandri J., Greber N.D., Retallack G.J., Hofmann A., Dauphas N., Lackey J.S., and Bekker, A. (2018) Rapid growth of subaerial crust and the onset of a modern hydrologic cycle at the Archean-Proterozoic transition. *Nature*, 557, 545-548.

Avice, G., Marty, B., Burgess, R., Hofmann, A., Philippot, P., Zahnle, K., and **Zakharov, D.** (2018). Evolution of atmospheric xenon and other noble gases inferred from Archean to Paleoproterozoic rocks. *Geochimica et Cosmochimica Acta*, 232, 82-100.

Zakharov D.O., Bindeman I.N., Slabunov A.I., Ovtcharova M., Coble M.A., Serebryakov N. S., and Schaltegger U. (2017) Dating the Paleoproterozoic snowball Earth glaciations using contemporaneous subglacial hydrothermal systems. *Geology*, 45, 5–8.

Bindeman I.N., Bekker, A., and **Zakharov D.O.** (2016) Oxygen isotope perspective on crustal evolution on early Earth: A record of Precambrian shales with emphasis on Paleoproterozoic glaciations and Great Oxygenation Event. *Earth and Planetary Science Letters*, 437, 101-113.

ACKNOWLEDGMENTS

Completion of this dissertation would not be possible without support of my advisor, committee members, collaborators, friends and family. First, I am grateful to Ilya Bindeman for setting me up with my first projects and for demonstrating the mindset needed to explore the novel geochemical approaches. Ilya have provided me with encouragement and guidance during the graduate degree research; he trusted me, that I would take the projects in the right direction. Next, I would really like to say a big thanks to James Palandri. Jim offered a tremendous amount of physical and mental help during the challenging times of high-precision O isotope analyses. I need to thank my committee members, Victoria DeRose, Mark Reed, and Gregory Retallack for their patience and for providing me with the much needed feedback. Mark's mentorship was instrumental for getting me to think about water-rock equilibrium reactions. I need to acknowledge James Watkins, who offered an invaluable support at the end of my PhD and was always available to discuss all things geochemistry. Special thanks to Paul Wallace for serving as a comprehensive exam committee member and for pointing out the ways I should head with my research ideas in order to create testable hypotheses. I am also thankful to all the faculty that taught me graduate-level classes at the University of Oregon, and to all the faculty that taught undergraduate-level classes with me when I was a teaching assistant. A special thanks to Edward Davies for paving my understanding of how to draw differences between things. I need to thank other faculty members at the Department of Earth Sciences (Dana Johsnton, Eugene Humphreys, Alan Rempel, and others) that were supportive of my studies and willing to share their wisdom. This PhD dissertation would not be possible without involvement and influence of the coauthors and collaborators from other institutions. I am grateful to Craig Lundstom (University of Illinois, Urbana-Champaign) and Anton Chakhmouradian (University of Manitoba) that fostered my initial efforts to become a graduate student in North America after leaving my home in Russia.

Having a group of close friends amongst graduate students was critical for successfully completing this dissertation. Especially influential were fruitful discussions with my office mates, lab mates and geochemistry students, namely, Marisa Acosta, Dyaln Colón, Rachel Hampton, Mike Hudak, Madison Myers, Brennan O'Connel, Genevieve Perdue, Angela Seligman, and Larry Syu-Heng Lai. I want to express the gratitude to the Earth Sciences office staff, Marla Trox, Sandy Thoms and Dave Stemple for assisting me in getting through the labyrinth of graduate progress and for providing a really congenial atmosphere within the department. My family, even when remote, always made me feel supported and proud for continuing the tradition of being a geologist that seems to run in our blood.

My dissertation was supported through NSF grant EAR 1447337 awarded to Ilya Bindeman, University of Oregon. I am also grateful for the awards and grants that made my graduate endeavors possible. For that, I would like to thank the Department of Earth Sciences at the University of Oregon, Geological Society of America, National Geographic Society and Evolving Earth Foundation.

In dedication to my family and friends scattered all over the globe.

TABLE OF CONTENTS

Chapter Page

SUPPLEMENTAL FILES

SPREADSHEET: GEOCHRONOLOGY DATA

LIST OF FIGURES

Figure Page

CHAPTER II

CHAPTER III

CHAPTER IV

CHAPTER V

CHAPTER VI

LIST OF TABLES

Table Page

CHAPTER II

CHAPTER III

CHAPTER IV

CHAPTER I

INTRODUCTION

A unique feature of our planet is the ubiquitous presence of liquid water on its surface. In pursuit of equilibrium, the minerals exposed near the Earth's surface react with abundant aqueous fluids at ambient temperatures altering the appearance of the planet's rocky shell. This process has been operating through the geological history, generating and modulating biological nutrient cycles, plate tectonics and long-term climate dynamics. Isotopes of oxygen and hydrogen -- both found in rocks and in water -- are at heart of the research presented here. Their isotope ratios are used here to reconstruct the surface environment and isotope characteristics of the hydrosphere early in the Earth's history.

This dissertation focuses on hydrothermal alteration of shallow upper crust as the driving mechanism for the reaction between surface waters and rocks. The most common type of such water-rock interaction is high temperature (> 250 °C) circulation of seawater at mid-ocean ridges and attendant recrystallization of the upper 2-3 km of oceanic crust. As a result, this process contributes the most voluminous flux into the stable isotope budget of the terrestrial hydrosphere. The recent advent of high-precision triple oxygen isotope analysis allows me to explore the new dimension of water-rock interaction in hydrothermal systems. The systematic variations in fractionation of $^{18}O/^{16}O$ relative to $^{17}O/^{16}O$ recorded by fluids and minerals that underwent isotope exchange are used in this dissertation as a tool to trace the involvement of meteoric waters (e.g. rain and snow) and seawater in modern hydrothermal systems. This dissertation is aimed to use these results to reconstruct the environment during a critical stage of the Earth's history in the early Paleoproterozoic, between 2.5 and 2.2 billion years ago. This periods of geologic history marks an important shift in the environmental conditions including the emergence of free oxygen in the atmosphere, subaerial exposure of continental landmass and large surface temperature fluctuations. The triple oxygen isotope approach helps to tackle some of the current problems in the field of stable isotope geochemistry and Precambrian geology such as long-term trends in oxygen isotope composition of seawater and state of hydrosphere during snowball Earth episodes. The overarching motivation behind this dissertation is to assess the environmental conditions in the early Paleoproterozoic using the unique isotope record that provide constraints which could not be reached otherwise.

In Chapter II, I use modern geothermal areas of Iceland to conduct a thorough test for triple oxygen isotope systematics as a tracers of fluids in the crust. This work uses a well-controlled environment of drilled geothermal areas, so that the $\Delta^{17}O$ approach can be reliably applied to the subsequent studies of ancient hydrothermal systems. Using three particular hydrothermal systems, Geitafell, Krafla and Reykjanes, allows me to trace involvement of both meteoric water and seawater in alteration of mid-ocean ridge basalts. Knowing the initial isotope values of local groundwater sources as well as having the temperature profiles recorded in the drilling wells, I am able to demonstrate the effect of water-rock exchange and boiling on the triple oxygen isotope ratios of fluids and minerals as well as the effect of temperature-dependent fractionation. Finally, this study explores igneous recycling of hydrothermally altered rocks by providing triple oxygen isotope measurements of contaminated magmas.

In Chapter III, the well-preserved pillow structures, hyaloclastites and komatiitic basalts of the 2.43-2.41 Ga Vetreny belt, Baltic Shield are investigated using hydrogen and triple oxygen isotopes. I provide a new estimate of δD, $\delta^{18}O$ and $\Delta^{17}O$ values of the early Paleoproterozoic seawater. This estimate is then used in subsequent chapters as a starting point of evaporation-distillation cycle (i.e. part of the global water cycle) process that controls the oxygen isotope composition of precipitation.

In Chapter IV, a multi-isotope approach is developed to trace the effect of interaction between sulfate-poor seawater and basaltic rocks in the Archean-Proterozoic time before. I use the hydrothermally altered rocks from the 2.43-2.41 Ga Vetreny belt to study Sr-isotope budget of Precambrian seawater and to support the triple oxygen isotope estimates of seawater isotope composition from Chapter III. This chapter is focused on the budget of redox sensitive elements in submarine hydrothermal systems, particularly sulfate, which is controlled by the evolving oxidative capacity of the Earth’s atmosphere. High marine sulfate in the modern ocean is linked to precipitation of anhydrite within altered oceanic crust and near-quantitative removal of Sr from seawater. The Archean and Paleoproterozoic oceans had extremely low sulfate concentrations which must have promoted high fraction of seawater-derived Sr in the isotope budget of submarine hydrothermal fluids.

In Chapter V, I apply the triple oxygen isotope measurements and precise U-Pb dating to constrain the timing and conditions of the snowball Earth glaciations of the early Paleoproterozoic. This study focuses on the new evidence for existence of glacial ice at low latitudes that is based the low $\delta^{18}O$ signature of ancient hydrothermal systems from the Belomorian belt of the Baltic Shield, Russia. Alternative to the traditional research on glacial diamictites, this study allows to reconstruct the $\delta^{18}O$ value of glacial meltwater, mean annual temperatures and to apply precise geochronological dating to determine the timing of glacial episodes. Determining the age of these rocks with high precision is a challenging task due to the imposed metamorphism. To address this, the chapter presents results of secondary ion probe mass spectrometry (SIMS) and chemical abrasion isotope dilution thermal ionization mass spectrometry (CA-ID-TIMS) techniques to produce a precise and accurate age of the early Paleoproterozoic subglacial intrusions.

In Chapter VI, I investigate additional occurrences of low $\delta^{18}O$ rocks that support the evidence for the globally cold climate of the early Paleoproterozoic. This study uses triple oxygen isotope data collected from new localities across the 500 km span of the Belomorian belt. Also, a new triple oxygen isotope dataset is presented for the low $\delta^{18}O$ Scourie dikes, the Lewisian Complex of the NW Scotland. Both provinces contain isotope signatures that reflect high-temperature exchange between rocks and low $\delta^{18}O$ meteoric waters representing a record of active hydrologic cycle during the early Paleoproterozoic. As a tentative connection between the Belomorian belt and the Lewisian complex, I investigate the isotope signature of the protoliths incorporated into the Scourie dikes via igneous process.

Chapter II of this dissertation is co-authored with Ilya N. Bindeman, Ryoji Tanaka, Guðmundur O. Friðleifsson, Mark H. Reed, and Rachel L. Hampton and is under review at *Chemical Geology*. Chapter III is co-authored with Ilya N. Bindeman and was published in *Geochimica et Cosmochimica Acta* in March 2019. Chapter IV is in preparation for publication and is co-authored by Ilya N. Bindeman, Ryoji Tanaka, Craig C. Lundstrom, Mark H. Reed and David A. Butterfield. Chapter V is co-authored with

Ilya N. Bindeman, Alexander I. Slabunov, Maria Ovtcharova, Matthew A. Coble, Nikolai S. Serebryakov, and Urs Schaltegger and was published in *Geology* in July 2017. Chapter VI is co-authored by Ilya N. Bindeman, Nikolai S. Serebryakov, Anthony R. Prave, Pavel Ya. Azimov, and Irina I. Babarina and is in press at *Precambrian Research*.

CHAPTER II

TRIPLE OXYGEN ISOTOPE SYSTEMATICS AS A TRACER OF FLUIDS IN THE CRUST: A STUDY FROM MODERN GEOTHERMAL AREAS OF ICELAND

From Zakharov, D.O., Bindeman, I.N., Tanaka R., Fridleifsson G.O., Reed M. and Hampton R.L. (2019) Triple oxygen isotope systematics as a tracer of fluids in the crust: A study from modern geothermal areas of Iceland. In review at *Chemical Geology.*

1.0 Introduction

Hydrothermal alteration of mid-ocean ridge basalts to greenschist facies mineral assemblages provides the dominant control on the isotopic and elemental budget of seawater and notably modifies the composition of the oceanic crust (Muehlenbachs and Clayton, 1976; Alt and Teagle, 2000). Since, oxygen is the most abundant element both in water and rocks and has a distinct isotopic composition in these reservoirs, the alteration can be monitored and quantified by the $^{18}O/^{16}O$ ratio. The advent of high precision triple oxygen isotope measurements enables us to use hydrothermally altered rocks as tracers of fluids in the past and thereby better understand details of past hydrothermal processes. In this paper, we explore the effects of high-temperature alteration of basaltic crust using simultaneous measurements of $^{17}O/^{16}O$ and $^{18}O/^{16}O$ ratios in continental and near-coastal hydrothermal systems of Iceland. We hope to better distinguish the intertwined effects of temperature and fluid isotopic composition in controlling the isotopic compositions of hydrothermally altered rocks. In this regard, triple oxygen isotope measurements are superior to the conventional $^{18}O/^{16}O$ measurements. The systematic mass-dependent relationship between $^{17}O/^{16}O$ and $^{18}O/^{16}O$ in geothermal fluids and minerals reported here promises to provide a variety of useful applications ranging from ore potential and geothermal exploration to studies of ophiolites, paleoclimate proxies, and tracking recycling of isotopic compositions through main terrestrial reservoirs.

1.1 Hydrogen and oxygen isotope studies of hydrothermal systems

In areas of extensive magmatism hydrothermal systems are charged with fluids from local sources that move through the crust via convective groundwater flow and react with the host rocks at high temperature (Norton, 1984; Hayba and Ingebrigtsen, 1997;

Criss and Taylor, 1986; Manning and Ingebritsen, 1999). Due to high-temperature isotope exchange between fluid and rock, alteration minerals have H- and O-isotope signatures similar to those of the fluids. The ratios of hydrogen and oxygen isotopes, D/H and $^{18}O/^{16}O$, are widely used to investigate fluid sources, temperature of water-rock interaction and processes that occur in hydrothermal systems such as isotopic exchange, boiling, and mixing of various fluid reservoirs (Ohmoto and Rye, 1974; Taylor, 1974; Gregory and Taylor, 1981).

In fossilized hydrothermal system, where fluids are no longer present, measurements of $\delta^{18}O$ values in coexisting mineral pairs, combined with δD measurements of hydrous minerals and fluid inclusion studies, are used for isotopic equilibrium calculations involving mineral-mineral and mineral-water calibrations. Combined H- and O-isotope measurements can fingerprint isotopic composition of initial fluids (e.g. Taylor, 1974, 1977; Ohmoto and Rye, 1974; Truesdell and Hulston, 1980; Dilles et al., 1992; Giggenbach, 1992; Pope et al., 2014), however the δD values of most hydrous minerals rarely reflect equilibrium with the original high-temperature hydrothermal fluids (250-400 °C) due to subsequent retrogressive exchange at lower temperature (< 100 °C), hydration and weathering (Kyser and Kerrich, 1991; Graham, 1981). Thus, the source of fluids in ancient hydrothermal systems cannot necessarily be determined from $\delta^{18}O$ measurements alone without making assumptions about the isotopic composition of fluids or equilibrium temperature. Moreover, the isotopic composition of initial fluids can be significantly overprinted due to high-temperature exchange with rocks, varying temperature of alteration, contribution of steam and brine, and addition of magmatic fluids.

Introducing a new isotopic parameter $^{17}O/^{16}O$, measured simultaneously with $^{18}O/^{16}O$, in a single sample enables a new ability to constrain the isotopic signature of initial fluids. The unique and systematic relationship between triple oxygen isotopic compositions of meteoric waters, seawater and rocks (Luz and Barkan, 2010; Pack and Herwartz, 2014; Sharp et al., 2018) along with recently calibrated equilibrium fractionations (Sharp et al., 2016; Wostrbrock et al., 2018) provide a promising basis to track temperature and O-isotopic signature of fluid at the same time. Similarly to $\delta^{18}O$ – δD systematics, the $\delta^{18}O$ - $\delta^{17}O$ systematics of hydrothermal minerals can identify processes that affect isotopic composition of the fluid phase, such as boiling, mixing of distinct fluids and isotopic exchange with rocks. The advantage of triple oxygen over combined δD and $\delta^{18}O$ measurements is that triple oxygen isotope analyses are obtained concurrently from analyses of same grains.

In this study we investigate the $\delta^{18}O$ - $\delta^{17}O$ relationship in fluids and minerals from active high-temperature (200-400 °C) hydrothermal systems at Reykjanes and Krafla located in southwest and north Iceland, respectively, and at an exposed subvolcanic section in the extinct 6 Ma (Miocene) Geitafell central volcano in southeast Iceland (Fig. 1). These systems serve here as natural laboratories, where distinct fluids with previously determined isotopic compositions are reacting with mantle-derived rocks at known temperatures. Using the previous analyses of local precipitation and groundwater recharge sources (Fig. 2) and measurements of fluid pressure and temperature in the geothermal wells, we are able to test the applications of $\Delta'^{17}O$ values under well-defined conditions. We used drill cuttings of quartz and epidote from known depths at Reykjanes and Krafla where temperature in the boiling systems can be determined at specified depth from the boiling point-water depth curve. Quartz and epidote were targeted because their co-occurrence, especially in veins and vesicles, is indicative of hydrothermal alteration at temperatures above 250 °C (Bird and Speiler, 2004), and they preserve oxygen isotopic composition well below the formation temperature (e.g. Fortier and Giletti, 1989). We also used samples of well fluids from Reykjanes that are dominated by seawater that underwent boiling at depth and isotope exchange with rocks, and from Krafla, where meteoric water boils close to the surface after reaction with rocks at depth.

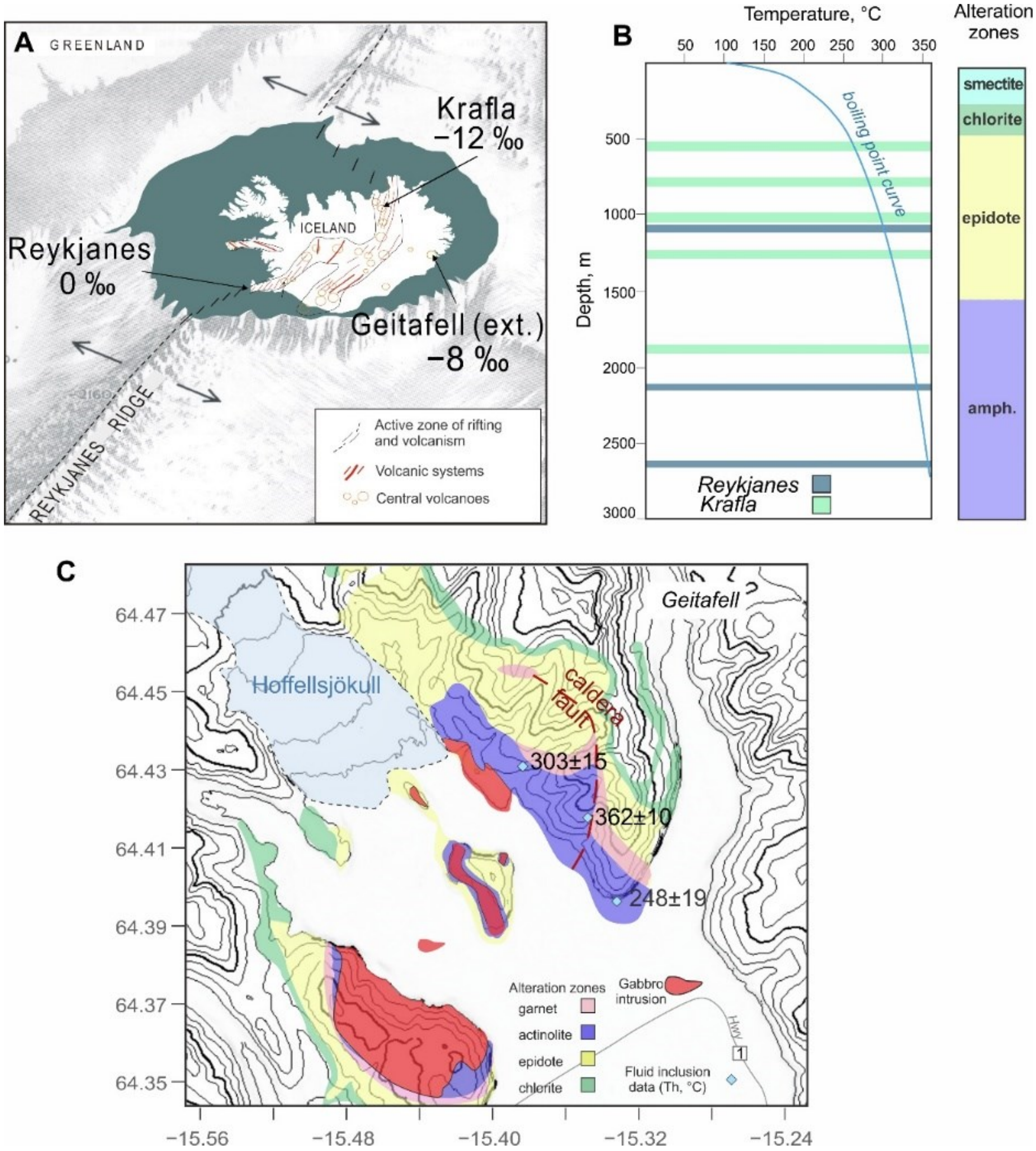

Figure 1. (A) Locations of the geothermal systems of Iceland studied here. The Reykjanes and Krafla systems are currently active, while the 6 Ma Geitafell extinct volcano hosts a fossilized hydrothermal system eroded to the depth of about 2 km (Fridleifsson, 1983). (B) The temperature of alteration for Reykjanes and Krafla systems can be approximated by the boiling point of water at depth. The temperatures are consistent with characteristic alteration mineral zones from top to bottom: smectite, chlorite, epidote and amphibole. The depth of collected samples is shown with horizontal bands. (C) General pattern of alteration at the Geitafell subvolcanic system. The gabbro intrusion is surrounded by a concentric pattern of alteration zones (Fridleifsson, 1983; Thorlacius, 1991) similar to the ones observed in the downward profiles recovered from drill holes in the modern hydrothermal systems. The average homogenization temperature (T_h, °C) of fluid inclusions measured in quartz veins surrounding the intrusion is shown with blue diamonds (after Troyer et al., 2007). These values were used as an approximate estimate of temperature of quartz-water equilibrium for corresponding samples (GER16 and GER34 in Table 1).

Measurements from the 6 Ma Geitafell system are used here to validate our findings in the active hydrothermal systems. We test the ability to reconstruct the triple oxygen isotope values of ancient meteoric water similarly to using combined $\delta^{18}O$ and δD values (see Pope et al., 2014). The zoning of alteration minerals and the pattern of isotope ratios in the host rocks of the Geitafell system display a "bull's eye" pattern that formed in response to temperature gradient and circulation of meteoric water around the cooling intrusion (Taylor and Forester 1979). This study is also a next logical step in validating previous triple oxygen isotope investigations of ancient hydrothermally altered rocks (Herwartz et al., 2015; Zakharov et al., 2017; Zakharov and Bindeman, 2019). Those investigations applied the triple oxygen isotope approach to resolve ancient environment conditions using lithologies that experienced aqueous alteration billions of years ago. Since the triple oxygen isotopic composition of high-temperature minerals is not easily reset, even during regional metamorphism, the current paper provides basis for validating the findings in those previous studies.

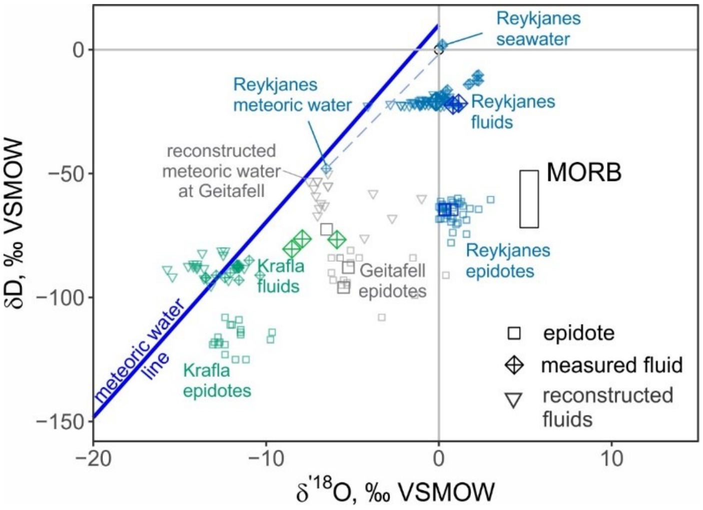

Figure 2. Compiled δD and $\delta^{18}O$ data for well fluids and epidotes at the Reykjanes, Krafla and Geitafell systems. The data gathered from Pope et al. (2011; 2014; small symbols) and multiple measurements from this study (large symbols). The Reykjanes fluids are derived from seawater ($\delta^{18}O$ and δD = 0 ‰) with minor amount of local meteoric water with $\delta^{18}O$ of -6 ‰. Krafla fluids are derived from meteoric water with $\delta^{18}O$ of -13 ‰ and δD of -90 ‰. Geitafell epidote indicate meteoric waters with $\delta^{18}O$ of about -8 ‰. Compositional field of mid-ocean ridge basalt (MORB) represents initial unaltered rock. Figure adapted from Pope et al. (2014).

1.2 $\delta'^{18}O$ and $\Delta'^{17}O$ definitions

Mass-dependent fractionation of triple oxygen isotopes between entities A and B obeys the relationship (Urey, 1947):

$$ln\,^{17}\alpha_{A-B} = \theta \cdot ln^{18}\alpha_{A-B} \quad (1),$$

where $^{17,18}\alpha_{A\text{-}B}$ are the ratios of $^{17}O/^{16}O$ or $^{18}O/^{16}O$ in A to that in B. The value of θ, the triple isotope exponent, is a temperature-dependent variable ranging between 0.5 and 0.5305 for equilibrium and kinetic processes (Matsuhisa et al., 1978; Cao and Liu, 2011). Since the relationship between $^{17}\alpha$ and $^{18}\alpha$ is exponential, we adopt linearized delta notation expressed through natural logarithm and denoted by a prime symbol (′) (Miller, 2002):

$$\delta'\,^{x}O = 1000ln(1 + \frac{\delta\,^{x}O}{1000}) \quad (2),$$

where x is either 17 or 18. The $\delta^{x}O$ value in Eq. 2 is the conventionally defined delta-notation:

$$\delta\,^{x}O = 1000(\frac{{}^{x}O/{}^{16}O_{sample}}{{}^{x}O/{}^{16}O_{VSMOW}} - 1) \quad (3),$$

where VSMOW (Vienna Standard Mean Oceanic Water) represents a standard with isotopic ratios close to that of seawater. Using the linearized notations for triple oxygen isotope fractionation, the θ value can be expressed as a slope in the $\delta'^{17}O - \delta'^{18}O$ coordinates:

$$\theta = \frac{\delta'^{17}O_A - \delta'^{17}O_B}{\delta'^{18}O_A - \delta'^{18}O_B} \quad (4),$$

where A and B are two substances in equilibrium, for example quartz and water, quartz and epidote. When measuring fractionations in triple oxygen isotope system, instead of using the slopes in $\delta'^{18}O - \delta'^{17}O$ coordinates, it is more illustrative to use $\Delta'^{17}O$ notation, often termed ^{17}O-excess. Deviations of $\delta'^{17}O$-$\delta'^{18}O$ fractionations from a reference line are then expressed as $\Delta'^{17}O$:

$$\Delta'^{17}O = \delta'^{17}O - \lambda \cdot \delta'^{18}O \quad (5).$$

Following definitions in previous studies of silicate rocks (Pack and Herwartz, 2014; Bao et al., 2016; Pack et al., 2016), in the Eq. 5 we use the reference line with the slope of

$\lambda_{\text{reference}} = 0.5305$, which is the high temperature limit for the triple oxygen isotope fractionation (see Matsuhisa et al., 1978).

1.3 Isotopic signals in hydrothermal systems

The δD, $\delta^{18}O$ and $\Delta^{17}O$ values of fluids and rocks in hydrothermal systems are distinctive owing to evaporation and condensation that surface waters undergo. Since VSMOW is used as a standard for the definition of δD, $\delta^{18}O$ and $\Delta^{17}O$, all three values are equal to 0 ‰ in modern seawater. In the globally averaged meteoric water, hydrogen and oxygen isotopes are related through the equation also known as the global meteoric water line (Craig, 1961):

$$\delta D = 8 \cdot \delta^{18}O + 10 \qquad (6).$$

Likewise, the $\delta'^{17}O$ value in the global meteoric water line is related to the $\delta'^{18}O$ through the equation (Luz and Barkan, 2010):

$$\delta'^{17}O = 0.528 \cdot \delta'^{18}O + 0.033 \qquad (7).$$

Combined with Eq. (5), triple oxygen isotope meteoric water line in coordinates specific for this reference line (0.5305) can be expressed through $\Delta'^{17}O$:

$$\Delta'^{17}O = -0.0025 \cdot \delta'^{18}O + 0.033 \qquad (8).$$

The local Icelandic evaporation and precipitation likely causes local fractionation effects in meteoric water slightly diverging from the global meteoric water line. However these effects are relatively small compared to the processes that occur within hydrothermal systems, such as isotopic exchange with rocks at high temperature. Thus, we justify using the global meteoric water line (Figure 2) for the approximate isotopic composition of the local precipitation at the localities studied here.

In each of the three localities, water-rock interaction involved distinctly different reservoirs of surface waters – meteoric water and seawater – reacting with basaltic rocks that have relatively uniform H- and O-isotopic composition (Hattori and Muehlenbachs, 1982; Eiler, 2001). The triple oxygen isotopic compositions of these reservoirs differ due to small but systematic mass-dependent variations in fractionation of $^{17}O/^{16}O$ relative to $^{18}O/^{16}O$. Mantle rocks have negative $\Delta'^{17}O$ values ranging between −0.06 and −0.05 ‰ (Herwartz and Pack, 2014; Pack et al., 2016) with δD values of -70 ± 10 ‰ (Kyser and O'Neil, 1984; Dixon et al., 2017). The effect of isotopic exchange between rocks and fluids at high temperature leads to shifts in the $\delta^{18}O$ and $\Delta'^{17}O$ values of the fluids, and to a lesser extent, in their δD values. We show associated isotopic shifts in fluids and its effect on equilibrium quartz and epidote (Fig. 3). In addition, liquid-vapor separation and mixing between seawater and meteoric water affects the stable isotopic composition of the fluids and minerals (Fig. 3).

The Reykjanes, Krafla, and Geitafell systems have well characterized δD and $\delta^{18}O$ compositions of the hydrothermal fluids, local fluid sources and alteration minerals (Fig. 2; Ólafsson and Riley, 1978; Sveinbjornsdottir et al., 1986; Darling and Ármannsson, 1989; Pope et al., 2014; Pope et al., 2016). Reykjanes is a seawater-dominated hydrothermal system where fluids have salinity of local seawater and $\delta^{18}O$ close to those of seawater, with average value of −1.1 ‰ and the δD of about −23 ‰ reflecting a contribution from steam and a small addition of local meteoric water (Ólafsson and Riley, 1978; Pope et al., 2009). At Krafla, the meteoric-derived fluids have $\delta^{18}O$ values close to those of local precipitation, ranging between −13 and −12 ‰, and δD values between −94 and −87 ‰ (Darling and Ármannsson, 1989; Pope et al., 2016). Geitafell has a multi-phase intrusion of gabbro and a several-kilometer radius areole of hydrothermally altered tholeiitic lavas (Fridleifsson, 1983) where Pope et al. (2014) measured δD and $\delta^{18}O$ in epidote and determined that hydrothermal fluids were derived from meteoric water with $\delta^{18}O$ of about −8 ± 1 ‰ and δD of about −60 ± 10 ‰.

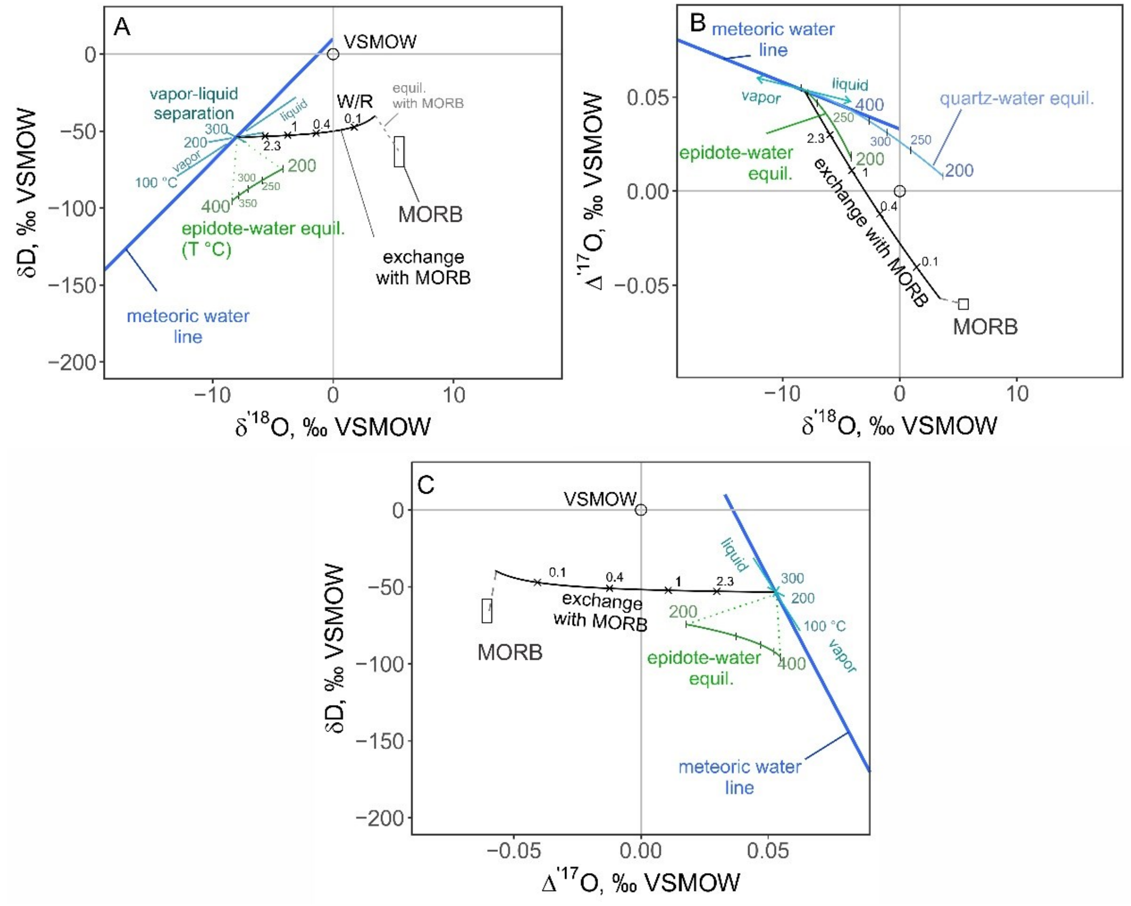

Figure 3. Systematics of water-rock interaction between meteoric water and mid-ocean ridge basalt (MORB) for the three stable isotope parameters plotted in coordinates: conventional δD-δ^{18}O (A), δ′^{18}O – Δ'^{17}O (B) and Δ'^{17}O-δD (C). The processes of isotope exchange (solid black line), boiling (blue straight lines) and equilibrium fractionation of quartz (light blue curves) and epidote (green curves) at 200-400 °C are depicted for interaction between unaltered MORB and pristine meteoric water that has δ′^{18}O of -8 ‰ (on the global meteoric water line, Craig, 1961; Luz and Barkan, 2010). Tick marks on the solid black line and numbers next it indicates water-rock ratios (W/R) of isotope exchange reactions. Quartz-water equilibrium at 200-400 °C is after (Sharp et al., 2016). Epidote-water fractionation has not been calibrated for triple oxygen isotopes but it could be approximated by the value close to the θ values of quartz-water equilibrium at high temperature.

2.0 Methods

2.1 Oxygen isotope measurements

All stable isotope analyses of solids were carried out at the University of Oregon Stable Isotope Lab. For oxygen isotope analyses we used quartz and epidote from all three localities, volcanic glasses from Krafla well IDDP-1 and surface exposures (sample KRF14), and one garnet sample from Geitafell. All samples were examined with a stereo microscope for inclusions of other minerals prior to analysis. Small samples (1.5-2 mg) were placed in a vacuum chamber and pre-treated with BrF_5 overnight to remove the absorbed moisture and reactive compounds. The oxygen was liberated from the samples by heating them with a CO_2 laser in presence of BrF_5. Extracted oxygen was transported in a stainless steel ¼-inch tube vacuum line, and traces of remaining reagent and other fluorine-containing byproducts were removed by cryogenic traps and reaction with Hg-vapor in a mercury diffusion pump. After the purification, oxygen gas was trapped on a 5Å molecular sieve by cooling to liquid nitrogen temperature. Subsequently released, the gas was carried though a GC-column by He-flow at the rate 30mL/minute and room temperature. After about 3 minutes of elution time, oxygen gas was trapped on a 5Å molecular sieve immersed in liquid nitrogen. The gas was further trapped on another, smaller volume 5Å molecular sieve immersed in liquid nitrogen and introduced into a MAT 253 gas-source isotope-ratio mass spectrometer at 50-60 °C. Each measurement consisted of at least 24 cycles of sample-reference gas comparisons with intermittent equilibration of pressure in the bellows of the mass spectrometer. A subset of samples collected from the Geitafell extinct volcano was analyzed for $^{18}O/^{16}O$ ratio only via O_2 - CO_2 conversion for a more rapid analysis as described previously (e.g. Bindeman et al., 2014).

The measurements of well fluids were carried out at the IPM, Okayama University, Japan using fluorination line with a Ni-reactor tube. A few microliters of fluid samples were injected into the reactor and fluorinated using BrF_5 at 250 °C to liberate O_2 gas. The rest of the procedure is similar to analysis of O_2 gas liberated from fluorination of silicates. The complete description of the procedure can be found in Tanaka and Nakamura (2013). The $\delta^{18}O$ and $\delta^{17}O$ values were calibrated by the VSMOW2-SLAP2 scale using the VSMOW2 ($\delta^{18}O_{VSMOW2} \equiv 0 \pm 0.124$ and $\delta^{17}O_{VSMOW2} \equiv 0 \pm 0.070$, N = 5, 2SD) and SLAP2 ($\delta^{18}O_{VSMOW2} = -55.283 \pm 0.226$ and $\delta^{17}O_{VSMOW2} = -29.572 \pm 0.141$, N = 3, 2SD) values measured during this study. The $\delta'^{18}O$ and $\Delta'^{17}O$ values of silicates were adjusted to the VSMOW2-SLAP2-calibrated composition of San Carlos Olivine (SCO) analyzed within each session. As reported previously (Pack et al., 2016), the SCO values are $\delta'^{18}O = 5.140$ ‰ and $\Delta'^{17}O = -0.049$ ‰. Our raw values along with SCO measurements are reported in Table S1 (see Appendix A). The average raw measurements of SCO (n=9) are $\delta' 18O = 5.622 \pm 0.105$ ‰, $\Delta'^{17}O = -0.089 \pm 0.010$ ‰.

We also measured $\delta^{18}O$ values *in situ* in a quartz crystal extracted from the Krafla well KJ36 at depth of 744 m using ion microprobe. First, a polished section of quartz was imaged using a FEI Quanta field emission gun scanning electron microscope equipped with a cathodoluminescence (CL) grayscale detector at the University of Oregon. The $\delta^{18}O$ was analyzed from 10-µm-diameter spots using a secondary ion mass spectrometer (SIMS) CAMECA IMS-1280 at the WiscSIMS lab, University of Wisconsin. A polished grain of UWQ-1 quartz ($\delta^{18}O = 12.33$ ‰) was mounted with the samples and used as a bracketing standard. The precision during the analyses was ± 0.4 ‰ or better (2 standard errors).

2.2 Hydrogen isotope measurements

Hydrogen isotopes were analyzed using a high temperature thermal conversion elemental analyzer (TC/EA) that is connected to the MAT 253 at the University of Oregon, using a continuous flow mode where gases from samples and standards are transported in He carrier gas. Each solid sample and standard were wrapped in a silver foil capsule and dried in a vacuum oven overnight, then transported to the auto sampler where they were purged with He carrier gas. In the TC/EA's furnace lined with a glassy carbon column, samples experienced pyrolysis at 1450 °C, and all of the H_2O in the minerals was pyrolized to H_2 and CO gas. Extracted gas carried by He into a gas chromatograph where H_2 is resolved from CO, which was discarded. The CONFLOIII device was used to lower the sample pressure to atmospheric, suitable for introduction into the MS, which also meters pulses of monitoring gas. Mica standards, USGS57 and USGS58 ($\delta D = -91$ and -28 ‰, respectively) were included in each analytical session to monitor the accuracy of analysis. The δD values of fluid samples were determined using the same TC/EA set up through multiple injections directly into the glassy carbon column.

2.3 Equilibrium fractionation calculations

We used the calibrations by Sharp et al., (2016) and Wostbrock et al., (2018) to derive the $\delta'^{18}O$ values of equilibrium fluids using measurements of quartz:

$$\delta'^{18}O_{quartz} - \delta'^{18}O_{water} = \frac{4.28 \pm 0.07 \times 10^6}{T^2} - \frac{3.5 \pm 0.2 \times 10^3}{T} \qquad (9),$$

and the $\Delta'^{17}O$ of equilibrium fluids:

$$\Delta'^{17}O_{quartz} - \Delta'^{17}O_{water} =$$
$$\left(\frac{4.28 \pm 0.07 \times 10^6}{T^2} - \frac{3.5 \pm 0.2 \times 10^3}{T}\right) \times \left(-\frac{1.85 \pm 0.02}{T}\right) \quad (10),$$

where T is equilibrium temperature in Kelvins. At 250-400 °C, fractionation is such that $\delta'^{18}O_{quartz} - \delta'^{18}O_{water}$ and $\Delta'^{17}O_{quartz}$-$\Delta'^{17}O_{water}$ is about +4-9 ‰ and −0.04 to −0.01 ‰ respectively. At this temperature range, for most other secondary minerals the $^{18}O/^{16}O$ fractionation is smaller, ranging 1 - 2 ‰ difference between minerals and fluids (e.g. Zheng, 1993). Thus, epidote and garnet should have $\delta'^{18}O$ and $\Delta'^{17}O$ values similar to those of equilibrium water (Fig. 3). The approximate $\Delta'^{17}O$ fractionation for epidote-water could be derived from Eq. 10 by substitution of the first term with the incremental calibration of $^{18}O/^{16}O$ ratio given by Zheng, 1993:

$$\Delta'^{17}O_{epidote} - \Delta'^{17}O_{water}$$
$$= \left(\frac{4.05 \times 10^6}{T^2} - \frac{7.81 \times 10^3}{T} + 2.29\right) \times \left(-\frac{1.85 \pm 0.02}{T}\right) \quad (11).$$

The second term in Eq. 11 is borrowed from quartz-water fractionation (Eq. 10) and is likely a valid approximation at high temperature. In general, in the temperature range of 250-400 °C, the $\Delta'^{17}O_{mineral\text{-}water}$ fractionation is very similar across different mineral species because the θ value (see Eq. 1) approaches 0.5305, its high-temperature fractionation limit (Matsuhisa et al., 1978; Bao et al., 2016; Hayles et al., 2018).

To provide an additional estimate of the temperature of alteration in the Geitafell fossilized hydrothermal system, we used the empirical calibration for quartz-epidote equilibrium fractionation given in Matthews (1994):

$$1000ln^{18}\alpha_{quartz-epidote} = \delta'^{18}O_{quartz} - \delta'^{18}O_{epidote}$$
$$= (2 + 0.75 \times Xps)10^6/T^2 \quad (12),$$

where X*ps* is mole proportion of pistacite in epidote, calculated as the proportion of iron in formula coefficient units, $Fe^{3+}/(Al+Fe^{3+})$. We used the X*ps* value of 0.2, which is an average value based on previous measurements for Krafla and Reykjanes epidotes (see Sveinbjornsdottir, 1991).

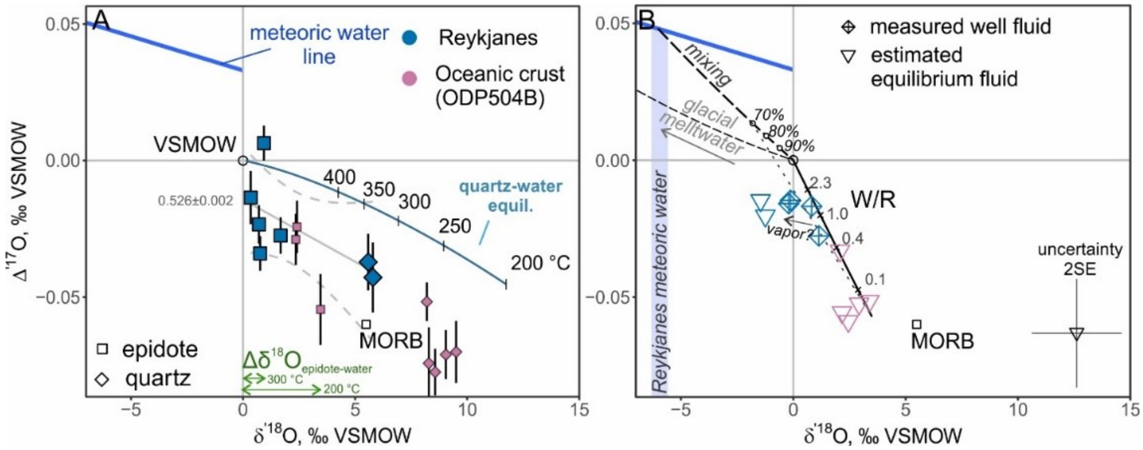

Figure 4. Triple oxygen isotope values of minerals (A) and fluids (B) from Reykjanes. A – Values plotted for quartz and epidote from Reykjanes, and from modern oceanic crust as sampled by the drill hole ODP 504B in east Pacific Ocean (shown for comparison; Zakharov and Bindeman, 2019). The apparent fractionation of triple oxygen isotopes between quartz and epidote at Reykjanes is shown with grey line and 95% confidence intervals (dashed). Quartz-water equilibrium (Sharp et al., 2016) is shown with the blue curve. Epidote-water equilibrium fractionation at 200 and 300 °C is shown with green arrows (Zheng, 1993). B – Values plotted for estimated equilibrium fluids computed from quartz-water fractionation (Eq. 10) and well fluids measured directly. For both Reykjanes and modern oceanic crust, seawater, shown as VSMOW, is the dominant fluid involved in alteration of mid-ocean ridge basalts (MORB). The seawater exchanged with rocks at high temperature becomes higher in δ'^{18}O and lower in Δ'^{17}O as shown with the solid black line. Mixing line with local meteoric water at Reykjanes is shown as a dashed curve with percent fraction of local meteoric water. Contribution of vapor phase is shown with an arrow. Based on quartz-water equilibrium calculations, ancient fluids of Reykjanes are ~1 ‰ lower than modern day fluids, which might reflect contribution from glacial meltwater that has δ'^{18}O value much lower than modern meteoric water.

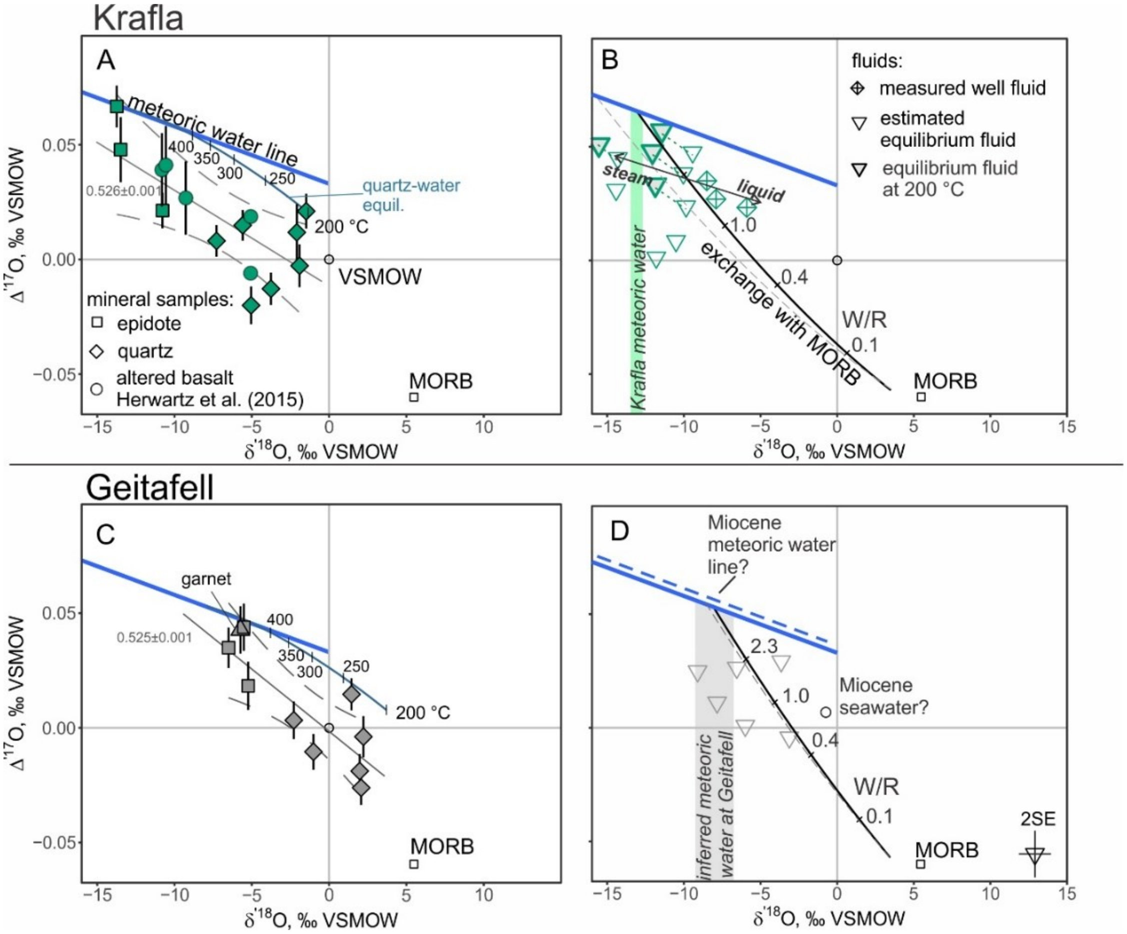

Figure 5. The $\delta'^{18}O$ – $\Delta'^{17}O$ values of minerals (A and C) and fluids (measured and computed; B and D) from Krafla and Geitafell systems. The apparent fractionation of triple oxygen isotopes between quartz and epidote is shown with grey line and 95% confidence intervals (dashed). The vertical bands on the right panels show the $\delta'^{18}O$ values of local fluid sources. The well fluids at Krafla system originated from exchange with rocks and liquid-vapor separation, which is reflected by their high $\delta'^{18}O$ values with $\Delta'^{17}O$ similar to those computed from quartz-water equilibrium. The estimated equilibrium fluids were computed using the boiling point of water at collection depth and the 4 samples of quartz collected at shallow depth (<1000m) at Krafla systems were used to calculate equilibrium fluids at the temperature of local thermocline, ~ 200 °C (grey-filled symbols). The fluids at the 6 Ma Geitafell likely originated from meteoric water with $\delta'^{18}O$ value of -8±1. They represent isotopically exchanged Miocene meteoric water that originated by evaporation of seawater with $\delta'^{18}O$ slightly lower than 0 ‰ due to smaller amount of continental ice compared to modern.

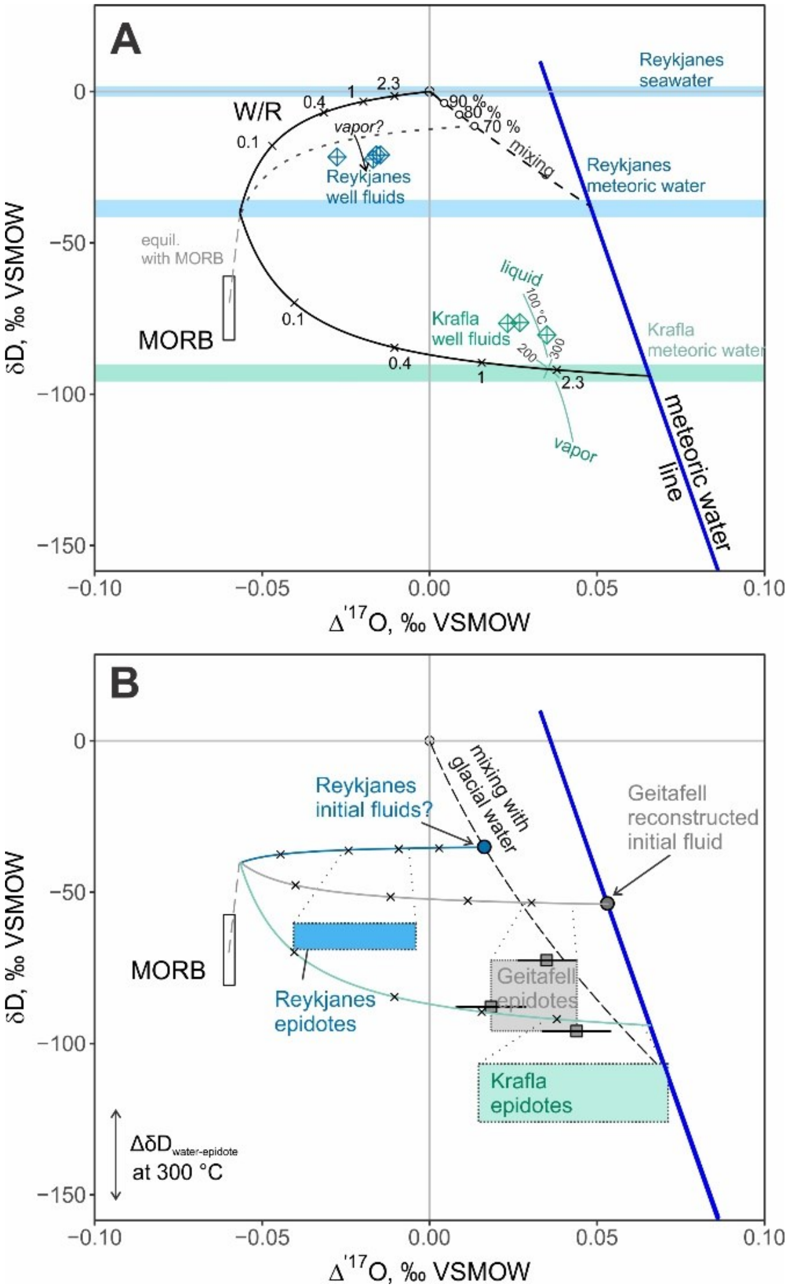

Figure 6. Combined $\Delta'^{17}O$ and δD measurements of well fluids (A) and epidotes (B). A - The Reykjanes well fluids are best explained by small contribution of local meteoric water, subsurface boiling (>100 °C) and isotopic exchange with rocks. Krafla fluids represent residual liquid fraction after steam separation, which explains the heavy δD values compared to the exchange trend. B – The $\Delta'^{17}O$ and δD values of epidotes are shown as boxes (compiled data from here and Pope et al., 2014). At Geitafell these values are consistent with the reconstructed meteoric water ($\delta^{18}O$ of -8 ‰), while epidotes from Reykjanes likely record contribution of low $\delta^{18}O$ and δD Pleistocene waters (see discussion Pope et al., 2009). Krafla epidotes reflect equilibrium fluids close to pristine local meteoric water.

3.0 RESULTS

3.1 Measured $\delta'^{18}O$, $\Delta'^{17}O$ and δD values

The $\delta'^{18}O$, $\Delta'^{17}O$ and δD values of minerals and well fluids from Reykjanes and Krafla and mineral separates from Geitafell are reported in Table 1. Quartz, epidote, measured well fluids and estimated equilibrium fluids are graphically presented in Figures 5 and 6.

Table 1. Hydrogen and triple oxygen isotope measurements of minerals and fluids from Reykjanes, Krafla and Geitafell systems

Drill hole/sample	Depth, m	Material	$\delta'^{18}O$, ‰	SE	$\Delta'^{17}O$, ‰	SE	δD, ‰	SE	H_2O, wt. %
Reykjanes									
RN12	1070	epidote	0.932	0.002	0.006	0.006			
RN12	1070	epidote	1.676	0.004	-0.027	0.007			
RN12	1070	quartz	5.582	0.004	-0.037	0.010			
RN12	1070	quartz	5.793	0.004	-0.043	0.013			
RN17B	2645	epidote	0.760	0.003	-0.034	0.006	-64.5	4	2.0
RN17B	2645	epidote	0.342	0.004	-0.014	0.010			
RN17B	2320	epidote	0.706	0.003	-0.023	0.007			
RN10		well fluids	1.141	0.001	-0.028	0.002	-21.7	1.9	
RN12		well fluids	-0.200	0.001	-0.016	0.002	-20.9	1.6	
RN12		well fluids	-0.125	0.001	-0.015	0.002	-20.9	1.6	
RN25		well fluids	0.818	0.001	-0.017	0.002	-22.4	2.1	
Krafla									
K06	1730	epidote	-13.482	0.006	0.048	0.014			
K06	1868	epidote	-13.732	0.003	0.067	0.009			
K36	744	quartz	-2.091	0.012	0.012	0.012			
K36	744	quartz	-1.482	0.008	0.021	0.008			
K36	744	quartz	-1.910	0.009	-0.003	0.009			
IDDP-1	1220	quartz	-5.048	0.004	-0.020	0.008			
IDDP-1	1220	quartz	-3.759	0.003	-0.013	0.007			
IDDP-1	1220	epidote	-10.777	0.003	0.021	0.008			
K26	1020	quartz	-7.281	0.004	0.008	0.007			
K21	550	quartz	-5.591	0.004	0.015	0.007			
IDDP-01		well fluids	-7.903	0.001	0.027	0.002	-76.4	2.0	
KJ36		well fluids	-8.507	0.001	0.035	0.002	-80.4	2.0	
Klafla pool		powerplant discharge	-5.898	0.001	0.023	0.002	-76.6	2.1	
Geitafell									
GER 5		epidote	-5.234	0.005	0.018	0.011	-87.9	4	2.5
GER 5		quartz	2.073	0.003	-0.026	0.007			
GER1		garnet	-5.737	0.004	0.043	0.010			
GTF 25		epidote	-5.517	0.004	0.044	0.010	-95.9	4	2.3
GTF 25		quartz	2.219	0.004	-0.004	0.009			
GTF28		epidote	-6.500	0.004	0.035	0.009	-72.5	4	1.7
GER16*		quartz	-2.284	0.003	0.003	0.008			
GER16*		quartz	-1.011	0.004	-0.010	0.008			
GER34**		quartz	1.978	0.004	-0.019	0.007			
GER34**		quartz	1.451	0.003	0.015	0.007			

The δD and $\delta'^{18}O$ values of Reykjanes well fluids range within -21±1 ‰ and +0.5±1 ‰, respectively, and are in agreement with the previous studies (see Section 1.3), allowing us to reliably interpret the new $\Delta'^{17}O$ data. The $\Delta'^{17}O$ values of Reykjanes well fluids range between -0.03 and -0.02 ‰, in general agreement with seawater-dominated origin of the fluids. The three measurements of Krafla fluids, that range in $\delta'^{18}O$ between -8 and -6 ‰, are several ‰ higher than the local precipitation ($\delta'^{18}O$ = -13 ‰) since they represent the remaining liquid of the fluids that underwent boiling and steam-liquid separation in the near surface environment (Ármannsson et al., 2014; Pope et al., 2016). One sample has a particularly high $\delta'^{18}O$ value of -5.9 ‰. This sample (Krafla pool; Table 1) represents the power plant discharge at Krafla. Despite being the remaining liquid, the Krafla fluids have distinctly high $\Delta'^{17}O$ values of about +0.02-0.03 ‰, similar to that of meteoric waters (Luz and Barkan, 2010).

Our epidote measurements from all three localities have δD and $\delta'^{18}O$ values consistent with previous reports (Pope et al., 2014), which allows us to validate our triple oxygen isotope approach to trace fluids in fossilized hydrothermal systems. The $\delta'^{18}O$ and $\Delta'^{17}O$ values of Reykjanes epidotes are close to seawater values, varying between 0 and 1 ‰, and -0.04 and +0.01 ‰ respectively (Fig. 4). The Krafla epidotes have low $\delta'^{18}O$ value, between -14 and -11 ‰, and high $\Delta'^{17}O$ values of +0.02 and +0.07 ‰, similar to the values of meteoric water (Luz and Barkan, 2010). Geitafell epidotes have $\delta'^{18}O$ values between -7 and -5 ‰, and $\Delta'^{17}O$ values between +0.01 and +0.05 ‰. The quartz samples are consistent with equilibrium fractionation at the temperature range between 250 and 400 °C being about 5-9 ‰ higher than the well fluids and epidotes. Their $\Delta'^{17}O$ values are about 0.03-0.05 ‰ lower than the respective fluid sources and epidotes. Our measurements constrain apparent fractionation between quartz and epidote in triple oxygen isotope system estimated as shown in the Eq. 4. The mean and standard error of the slope in $\delta'^{17}O$-$\delta'^{18}O$ coordinates is 0.526 ± 0.001 and shown for each locality along with the 95 % confidence intervals (Fig. 4 and 5).

3.2 Computed equilibrium fluids

Using the boiling point-depth to estimate temperature, the $\delta'^{18}O$ values of equilibrium fluids were computed based on quartz measurements and the Eq. 9 and 10 (Sharp et al., 2016; Wostbrock et al., 2018). The resulting $\delta'^{18}O$ and $\Delta'^{17}O$ values are displayed in Figures 4 and 5. At Reykjanes, equilibrium fluids are about -1 ‰, lower than the modern well fluids in $\delta'^{18}O$, with the $\Delta'^{17}O$ values around -0.03 ‰. At Krafla, the equilibrium fluids have $\delta^{18}O$ values between −14 and -10 ‰ (Pope et al., 2016), and range in $\Delta'^{17}O$ between 0 and +0.06 ‰. Equilibrium fluids at Geitafell range in $\delta'^{18}O$ between −9 and −3 ‰, and have $\Delta'^{17}O$ values between 0 and +0.03 ‰. In all three of the systems we studied here, very few measured quartz compositions returned values of pristine seawater or meteoric water.

3.3 Error analysis

The uncertainty of $\delta'^{18}O$ and $\Delta'^{17}O$ values of equilibrium fluids was estimated by propagating the uncertainties in fractionation factors and the analytical errors through the equations 7 and 8. We used the average values of analytical standard errors (SE): 0.005 ‰ for $\delta'^{18}O$ and 0.010 ‰ for $\Delta'^{17}O$. The uncertainty of ±30 °C was used as the largest possible error on the temperature estimate given by the variations in the well log measurements. The resulting propagated uncertainty of equilibrium fluids are 1.151 ‰ for $\delta'^{18}O$ and 0.011 ‰ for $\Delta'^{17}O$ (1SE). It is worth mentioning that the equilibrium fractionation of $\Delta'^{17}O$ values between water and quartz at temperature is not resolvable in the range 350-400 °C due to analytical uncertainty of ~0.01 ‰.

3.4 In situ $\delta^{18}O$ measurements of Krafla quartz

The cathodoluminescence (CL) image and the heterogeneous $\delta^{18}O$ values measured *in situ* in a quartz crystal from Krafla are shown on Fig. 7A. The CL-pattern reveals features indicative of precipitation at different temperature manifested by different brightness (Fig. 7A). The $\delta^{18}O$ values measured *in situ* decrease outwards: the core of the crystal has values between -1 and 0 ‰, while the outermost rims are about -4 ‰ (Fig. 7B). We show the effect of decreasing temperature and evolving fluids on the triple oxygen isotope composition of equilibrium quartz in Figure 7B.

3.5 Distribution of $\delta'^{18}O$ values at the Geitafell system

In addition to the triple oxygen isotope measurements, we present the spatial distribution of $\delta'^{18}O$ values measured in quartz and epidote separates from Geitafell. The values are reported in Table S2 (see Appendix A). The $\delta'^{18}O_{quartz}$ - $\delta'^{18}O_{epidote}$ values range between 5 and 10 ‰, approaching the minimum near the contact of the Geitafell intrusion (Fig. 8). This range of fractionation is consistent with the temperature of alteration between 200 and 450 °C computed from Eq. 12. In addition, we provide one datum based on pyroxene-magnetite pair from the gabbro intrusion. The fractionation between igneous minerals, $\delta'^{18}O_{pyroxene} - \delta'^{18}O_{magnetite} = 2.6$ ‰, corresponds to equilibrium temperature of 890 °C using calibration from (Valley et al., 2003).

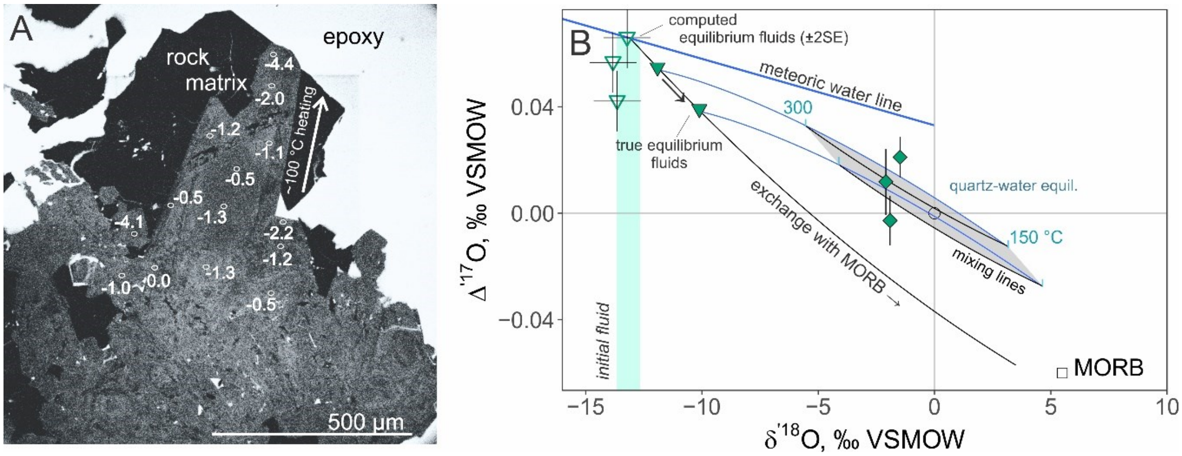

Figure 7. A – Cathodoluminescent image of quartz (grey) from Krafla collected at depth of 744 m and analyzed by SIMS for oxygen isotopes. The $\delta^{18}O$ values (shown in white) vary from 0 ‰ to about -4 ‰ implying a temperature increase from 190 to 270 °C if a constant value of equilibrium fluids ($\delta'^{18}O = -13$ ‰) is assumed. B – The effect of temperature increase and simultaneous isotope exchange between fluids and MORB that causes shifts along the black curve. The two blue concave down curves indicate equilibrium fractionation between quartz and two shifted fluid compositions (filled triangles) with tick marks showing quartz at 300 and 150 °C. The bulk measurement of such quartz crystals returns $\delta^{18}O$ values of around -2 ‰ with $\Delta'^{17}O$ values analytically indistinguishable from the mixed compositions shown as the grey area. Reconstructed equilibrium fluids at 200 °C are shown with open triangles.

4.0 Discussion

Our measurements of minerals and fluids are quite consistent with their respective fluid sources, confirming that $\Delta'^{17}O$ measurements provide useful constraints for tracking water-rock interaction. First of all, our results validate previous studies of ancient hydrothermal systems that have implications for the paleoenvironmental conditions of the Proterozoic (e.g. Herwartz et al., 2015; Zakharov et al., 2017; Zakharov and Bindeman, 2019). Thus, triple oxygen isotope measurements of submarine hydrothermally altered rocks can be applied to reconstructing the isotopic composition of seawater over the course of geologic history, while continental hydrothermally altered rocks can serve as a paleoclimate proxy given strong dependence of $\delta^{18}O$ in meteoric water and mean annual temperature (Dansgaard, 1964). In addition, below we consider how triple oxygen isotope measurements of fluids and minerals can be used to constrain the nature of isotopic shifts owing to boiling, and isotopic exchange, and temperature of mineral alteration based on calibrated thermometers. Following that we consider the macroscopic and microscopic set of observations that capture thermal evolution of hydrothermal systems based on oxygen isotopes that may affect interpretations of mineral data. Lastly, we suggest that the processes of crustal assimilation of hydrothermally altered rocks by mantle-derived magmas can be constrained from the triple oxygen isotope mass balance due to distinction of $\Delta'^{17}O$ values of the end-members.

4.1 $\Delta'^{17}O$ values of well fluids

The distinctly different slopes in the triple oxygen isotope space (see Fig. 3) allow us to interpret the origin of fluids in a new dimension. We measured $\Delta'^{17}O$ in well fluids to capture possible isotopic shifts occurring in modern hydrothermal systems that enable us to establish a basis for understanding fossilized systems. The extent of negative shift in $\Delta'^{17}O$ is similar to the shift previously noted in reconstructed fluids from modern subseafloor rocks that were altered at 300-350 °C (Fig. 4B; Zakharov and Bindeman, 2019). The isotopic exchange with unaltered mantle-derived rocks produces negative shifts in $\Delta'^{17}O$ and positive shifts in $\delta'^{18}O$ values, while the δD values stay unchanged due to limited availability of hydrogen in igneous rocks. In all three systems we measured $\Delta'^{17}O$ shifts that range between -0.01 and -0.03 ‰ and about +0.5 to +2 ‰ shifts in $\delta'^{18}O$. Thus, water-rock interaction produces hydrothermal fluids that evolve along the slope of 0.510-0.516 in $\delta'^{17}O$-$\delta'^{18}O$ space. This is similar to the estimate provided by Sengupta and Pack (2018) for the input of hydrothermal alteration in the hydrosphere. In the seawater-dominated Reykjanes system, the $\delta'^{18}O$ of well fluids are close to those of seawater, i.e. 0 ‰ VSMOW, with $\Delta'^{17}O$ around -0.025 ‰ (Fig. 4). Their $\delta'^{18}O$ values are, however, not quite as high as in seawater-derived fluids (+0.5-2 ‰; Shanks, 2001) and together with the low δD values (-20 ‰), it hints at participation of meteoric water in the measured fluids (Arnórsson, 1978; Pope et al., 2011). Together, the hydrogen and triple oxygen isotopic values of these fluids reflect a combination of isotope exchange with rocks at high temperature and about 10-20 % involvement of local meteoric water (see Fig. 6). Thus, the $\Delta'^{17}O$ values slightly below 0 ‰, are interpreted as the effect of isotopic exchange with rocks at high temperature (Fig. 4). Using the triple oxygen isotope approach, we estimate the effective water-to-rock mass ratios (W/R) between 0.1 and 1, assuming that initial fluids had $\delta'^{18}O$ and $\Delta'^{17}O$ of -1 and +0.01 ‰ respectively (Fig. 4). Finally, some contribution of steam to the well fluids is manifested by $\delta'^{18}O$ and δD values that are shifted negatively from the trajectories of exchange with MORB (Fig. 4 and 6).

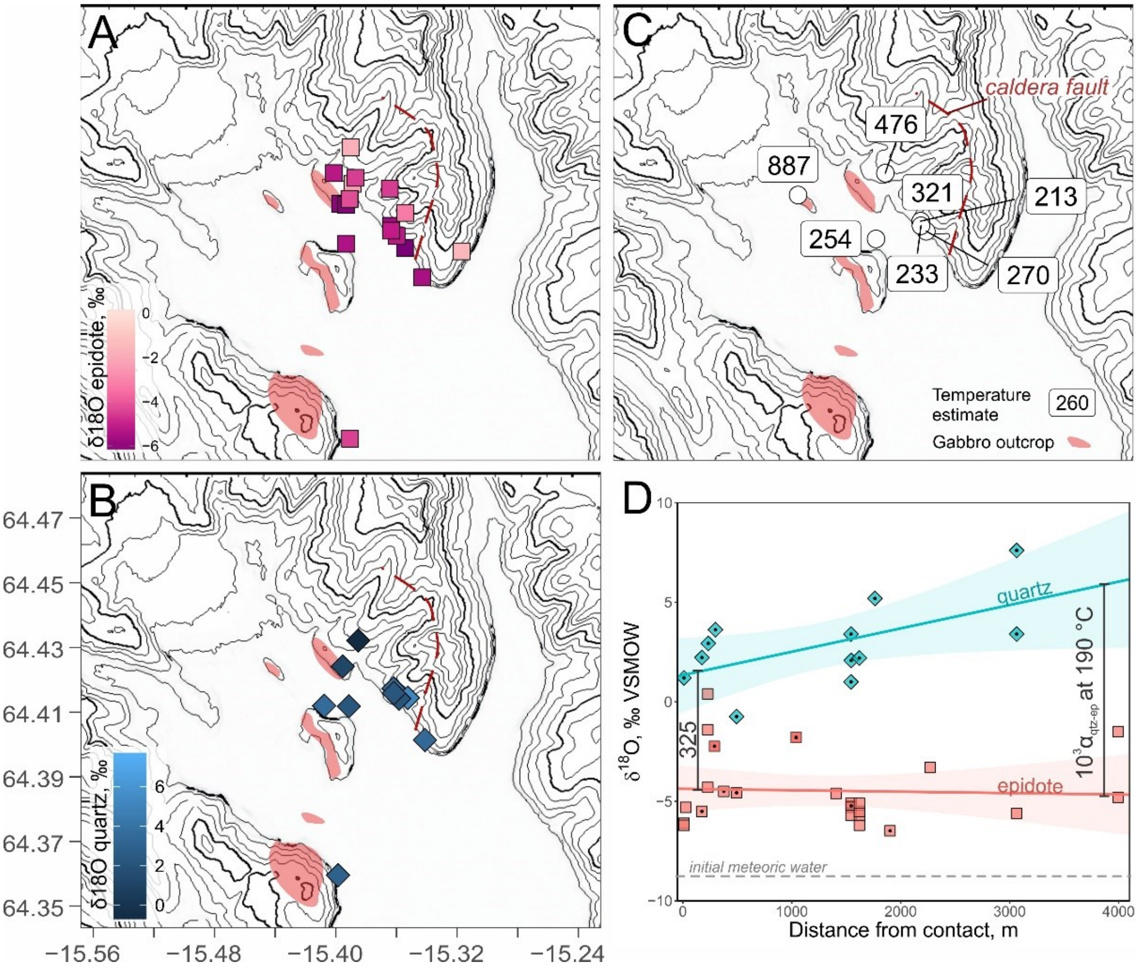

Figure 8. Spatial distribution of $\delta'^{18}O$ values in epidote (A) and quartz (B) from the host rocks of the Geitafell intrusion shown in the map view. The equilibrium temperatures computed from mineral pair measurements extracted from the same sample are shown in (C). The $\delta'^{18}O$ values plotted as a function of distance from the intrusion contact shown in panel (D). Based on the $\delta'^{18}O_{\text{quartz-epidote}}$ fractionation, the temperature around the intrusion is >325 °C near the contact and 190 °C away from it. The data is compiled from Pope et al., 2014 and this study (shown as dotted symbols in D). The isotopic equilibrium is consistent with the mineralogical pattern of alteration (Fridliefsson, 1983) and the fluid inclusion data (Troyer et al., 2007).

Boiling that occurs in shallow hydrothermal systems should follow a slope similar to meteoric water line in the $\delta'^{18}O$ – $\Delta'^{17}O$ space due equilibrium fractionation between vapor and liquid ($\theta_{vapor-liquid} = 0.529$; see Eq. 1). This value was constrained from low temperature experiments (< 50 °C; Barkan and Luz, 2005) and is likely higher, closer to 0.5305, for boiling water at depth. Thus, boiling affects $\delta'^{18}O$ and δD values of fluids in accordance with liquid-vapor equilibrium fractionation (Horita and Weselowski, 1994), causing only small variations in $\Delta'^{17}O$. As an example, the well fluids at Krafla are derived from local meteoric waters ($\delta'^{18}O$ = - 13 ‰) and are enriched in heavy isotopes of oxygen so that their value close to -8 ‰ due to boiling and steam separation that occurs near the surface (Pope et al., 2016). Essentially, these samples were shifted parallel to the meteoric water line from their parental fluids, the $\Delta'^{17}O$ of these fluids were likely shifted only about 0.005 ‰ (Fig. 5). At a temperature close to 100 °C, and the values of oxygen isotope fractionation, $\theta_{liquid-vapor} = 0.529$ (Barkan and Luz, 2005) and $1000\ln^{18/16}\alpha$ close to 5 ‰ (Horita and Weselowski, 1994), the $\delta^{18}O$ of remaining liquid computed as $R_{liquid} = R_{bulk}*(1-f^{\alpha})/1-f$, corresponds to about 70-90 % of original fluid that had $\delta'^{18}O$ of around -10 ‰ due to isotopic exchange with rocks. Similarly to Reykjanes fluids, the $\Delta'^{17}O$ values of projected unseparated fluids are shifted negatively by 0.03 ‰ with respect to the meteoric water line (Fig. 6), which we interpret to result from isotope exchange with rocks, which is supported by previous measurements of unseparated geothermal fluids at Krafla (Ármannsson et al., 2014; Pope et al., 2016). The δD values clarify the effect of boiling and separation of steam from the remaining liquid likely occurred between 100 and 200 °C (see Fig. 6). Consistent with the δD values of measured fluids and their triple oxygen isotope values, the isotopic shifts measured in Krafla well fluids correspond to W/R ratio of about 1-2. We thus conclude, that the $\Delta'^{17}O$ values of Krafla fluid samples are less affected by the isotope exchange than the Reykjanes fluids, however carry a strong signature of boiling. Our measurements show that combined hydrogen and triple oxygen isotope values of well fluids present a powerful way to constrain subsurface processes that occur in a hydrothermal system and could be applicable for geothermal exploration.

4.2 Mineral record of $\Delta'^{17}O$ in fluids at depth

The measured $\Delta'^{17}O$ values of minerals are reflective of fluids that were present at depth in the past, which for the most part are similar to the modern-day geothermal fluids (Sveinbjornsdottir et al., 1986). Supporting this are epidotes that have $\Delta'^{17}O$ and $\delta'^{18}O$ values close to the modern-day sources of fluids owing to small equilibrium fractionation at high temperature ($10^3\ln^{18/16}\alpha_{\text{epidote-water}} \approx$ 0-1 ‰; Zheng, 1993). Epidotes from Krafla and Geitafell, fall nearly on the meteoric water line, while at Reykjanes, epidote compositions are very similar to seawater and to well fluids. Similarly, one sample of garnet from the Geitafell system has triple oxygen isotopic composition close to that of meteoric water. It is expected, that the $\Delta'^{17}O$ of minerals with small fractionation would be close to that of fluids, i.e. within 0.01 ‰ at these temperatures (Hayles et al., 2018). This small range, ±0.01‰, is at the limit of analytical precision (±0.02 ‰, i.e. 2 standard errors), thus precluding meaningful determination of the reason for small variations in the $\Delta'^{17}O$ of epidotes. Nevertheless, epidotes provide first order estimates of $\Delta'^{17}O$ in equilibrium fluids and they reveal reaction with rocks in instances where the fluids were shifted, as were epidotes from modern oceanic crust recovered by Hole ODP 504B (Fig. 4).

The triple oxygen isotope calibrations by Cao and Liu (2011), Sharp et al. (2016) and Wostbrock et al. (2018) provide a promising basis for use of quartz for temperature estimation and as a tracer fluid isotopic composition, especially where measurements from other minerals with small $\Delta'^{17}O_{\text{mineral-water}}$ fractionation are obtained. We however find that few samples of quartz actually plot on the curve of equilibrium fractionation with local fluid sources. Most of the quartz measurements plot below equilibrium fractionation with the composition of unmodified meteoric water or seawater, suggesting that fluids underwent isotopic exchange with rocks (Fig. 4 and 5). In addition to that, at Reykjanes, quartz equilibrium fluids are lower by about 1 ‰ than the directly measured modern-day well fluids. Involvement of ancient meteoric or glacial water with low $\delta^{18}O$ values would explain these values, as suggested by Sveinbjornsdottir et al. (1986) and Pope et al. (2014; Fig. 4). At Krafla, most of the equilibrium fluids have $\delta^{18}O$ values between −15 and −10 ‰ and $\Delta'^{17}O$ between +0.01 and +0.05 ‰, which are close to the modern meteoric water (Fig. 5). The negative shifts in the $\Delta'^{17}O$ of equilibrium fluids compared to meteoric water likely result from isotope exchange with rocks at high temperature. The computed fluids at Krafla have $\Delta'^{17}O$ values that overlap with each other at 95 % confidence level (~2 standard errors), however the $\delta'^{18}O$ values of -15 ‰ are puzzling. We interpret this could be a combined effect of isotopic exchange between rocks and fluids in addition to high input of separated steam rising up from the depth, which would have $\delta'^{18}O$ values lower than the modern-day fluids (Fig. 6). In addition, the applied mineral-water calibration might yield inaccurate equilibrium fluids due to non-isothermal growth of analyzed quartz crystals as revealed by SIMS and discussed below.

The measurements from the Geitafell system indicate that the $\delta'^{18}O$ values of equilibrium fluids range between −9 and −3 ‰, resembling previous estimates (Pope et al., 2014). The reconstructed $\Delta'^{17}O$ values of the fluids (-0.01 to +0.04 ‰) are consistently lower than those of inferred meteoric water with $\delta'^{18}O$ of -8 ± 1 ‰ as indicated by measurements of epidotes. The much lower $\Delta'^{17}O$ values are likely due to exchange with rocks during prolonged water-rock interaction that might be recorded by quartz but not epidote. Quartz can grow over a wider range of temperatures than epidote and commonly forms late-stage veins at low temperature, as low as 150 °C. Below we discuss the evidence for variable temperature regime during quartz crystal growth and implications for triple oxygen isotopic measurements of bulk crystals.

4.3 The records of evolving hydrothermal systems

The $\delta^{18}O$ measurements by SIMS presented here show that quartz crystals at Krafla may have grown as temperature changed. The range of values (Fig. 7A) from core to rim, ~ 0 ‰ to ~ -4.4 ‰, could result from temperature increase from about 190 to 270 °C, assuming constant value of equilibrium fluids (Eq. 9). This particular quartz crystal was extracted from a relatively shallow depth of 744 meters, where borehole temperature measurements indicate a thermocline in which temperatures are consistently lower than the boiling point of water. The thermocline interval is inferred to match a lithological unit with low permeability that prevents heat transfer and thus conducts heat slower than the surroundings (Sveinbjornsdottir et al., 1986). The decrease of $\delta^{18}O$ in the quartz grain would be consistent with a temperature increase as heat propagated through the rock from the underlying intrusion at ~2 km depth (Elders et al., 2011). As for triple oxygen isotope measurements, the bulk crystal contains a mixture of equilibrium compositions, with $\Delta'^{17}O$ values intermediate between maximum and minimum fractionation defined by the

Eq. 10 at the temperature range 190-270 °C. Due to concave up shape of the mixing curve, such quartz crystal would have $\Delta'^{17}O$ value lower than that of quartz growing from fluid isothermally (Fig. 7B). In this quartz crystal, mixing between low- and high-temperature end-members within same sample contributes to inaccurate determination of $\Delta'^{17}O$ in equilibrium fluids. This can be further exacerbated by evolving fluids as the exchange between pristine water and unaltered rock progresses (Fig. 7B).

The spatial distribution of $\delta^{18}O$ values in the rocks surrounding the Geitafell intrusion display a pattern also consistent with non-isothermal equilibrium fractionation around plutons (Fig. 8) that were emplaced in the shallow crust causing circulation of meteoric waters around them (Taylor, 1974; Forester and Taylor, 1979; Wotzlaw et al., 2012). The $\delta^{18}O$ values of epidote vary much less than those of quartz, partly due to its smaller fractionation factor and partly, due to high temperature of formation (>250 °C; Bird and Spieler, 2004). The $\delta^{18}O$ of quartz increases with distance from the contact and forms multiple generations of precipitation at different temperatures and equilibrium fluids (Liotta et al., 2018). The $\Delta'^{17}O$ measurements of quartz from the host rocks used here to reconstruct the $\delta'^{18}O$ value of evolving fluids could be further employed to provide a record of heat and mass transfer followed the emplacement of the intrusion.

4.4 Implications for magmatic assimilation and origin of low $\delta^{18}O$ rhyolites

Shallow hydrothermal alteration of volcanic rocks produces low- $\delta^{18}O$ rocks that can be deeply buried then assimilated by partial melting to yield low- $\delta^{18}O$ magmas. Similarly to radiogenic isotopes, major elements, and trace elements, triple oxygen isotopic composition of contaminated magmas can trace the input of hydrothermally altered rock. In Krafla, erupted rhyolites, such as glasses quenched by drilling of hole IDDP-1 and high silica rocks exposed on the surface carry a low-$\delta^{18}O$ signature from assimilated hydrothermally altered crust (Elders et al., 2011). We construct (Figure 9) the trajectory of assimilation of shallow hydrothermally altered rocks in triple oxygen isotope space based on our measurements of epidote and quartz, rhyolitic glasses and the previous measurements of altered basalts by Herwartz et al. (2015) recalibrated to more accurate standards (Pack et al., 2016). These measurements provide the basic information needed to estimate the effect of crustal assimilation on the triple oxygen isotopic composition of contaminated magmas. Since magmatic differentiation occurs at high temperature, the $\Delta'^{17}O$ values of primitive and evolved magmas do not vary significantly at the level of analytical precision in the range of values $\Delta'^{17}O$ = -0.06±0.01 ‰ (Tanaka and Nakamura, 2013; Pack and Herwartz, 2014; Pack et al., 2016; Sharp et al., 2018). Thus, incorporation of an isotopically distinctly component, such as hydrothermally altered rocks ($\Delta'^{17}O$ = +0.03 ± 0.01 ‰), could be resolved within the analytical precision. From triple oxygen isotope composition, we estimate that the low-$\delta^{18}O$ rhyolitic magmas from Krafla, including those quenched and extracted by drill hole IDDP-1, were derived from assimilation of 10-30 % hydrothermally altered crust and 70-90 % uncontaminated magmas (Fig. 9). These estimates assume that uncontaminated magmas had a $\delta'^{18}O$ value between 5.5 and 6.5 ‰ and assimilated hydrothermally altered rocks had $\delta'^{18}O$ of around -8 ‰. These estimates agree well with previous calculations based on combined oxygen and hydrogen isotopic composition of the quenched glasses yielding about 20 % material assimilated (Elders et al., 2011). This approach for estimating the amount of assimilant through isotopic mass balance might help to resolve the nature of recycled material in other geological situations where the contaminant has very high $\delta^{18}O$ and low $\Delta'^{17}O$ values, such as low temperature sedimentary rocks (e.g. shales with $\Delta'^{17}O$ = -0.10 ± 0.01 ‰; Bindeman et al., 2018).

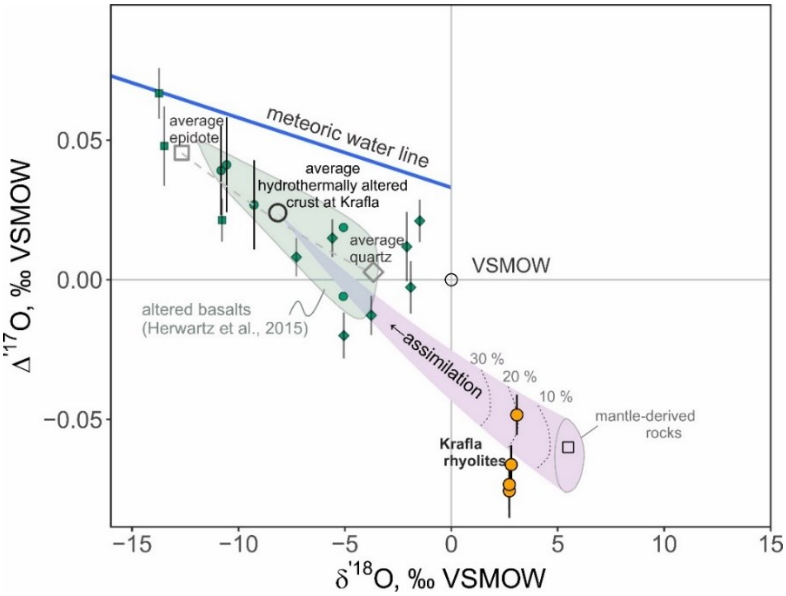

Figure 9. Triple oxygen isotopic systematics of assimilation of low $\delta^{18}O$ hydrothermally altered crust at Krafla by mantle-derived magmas. The contribution of low $\delta'^{18}O$ and high $\Delta'^{17}O$ hydrothermally altered crust from Krafla is resolved due to its distinct isotopic signature compared to the isotopic composition of uncontaminated magmas. Measurements of volcanic glasses quenched by the drilling hole IDDP-1 and surface rhyolites are consistent with assimilation of 20 % of hydrothermally altered crust by mantle-derived melts. The composition of hydrothermally altered crust is represented by average composition of bulk hydrothermally altered basalts measured previously (data from Herwartz et al., 2015 recalibrated to SCO composition from Pack et al., 2016) that can be also reproduced by mixing between average values of epidote and quartz.

5.0 Conclusions

We have presented high-precision measurements of $\Delta'^{17}O$ in hydrothermal minerals and fluids from Krafla and Reykjanes modern geothermal areas and from the fossilized hydrothermal system at Geitafell. The measurements provide a record of isotope exchange between rocks and variable fluid sources, such as seawater and meteoric waters of different isotopic composition. We found that:

1. Similar to combined δD and $\delta^{18}O$ measurements of hydrous minerals, the triple oxygen isotope measurements can uniquely fingerprint initial fluids, constrain temperature of alteration and effective water-rock ratios. Our results support previous triple oxygen isotope studies of Proterozoic rocks that exchanged with extremely low-$\delta^{18}O$ meteoric waters (Herwartz et al., 2015; Zakharov et al., 2017) and seawater (Zakharov and Bindeman, 2019).

2. Triple oxygen isotope measurements of geothermal fluids collected at the surface present a novel way to resolve the effects of isotopic exchange with rocks at high temperature and boiling, which complements the conventional δD-δ^{18}O measurements. The negative Δ'^{17}O shifts in fluids are due to high-temperature exchange between rocks and local fluid sources, whereas shifts in δ'^{18}O without a significant change in Δ'^{17}O are due to boiling and vapor-liquid separation.

3. Especially insightful are measurements of high-temperature minerals with small oxygen isotope fractionation, such as epidotes and garnet, that provide a close estimate of Δ'^{17}O in the equilibrium fluids. In our case, epidote has isotope compositions almost identical to the well fluids in Reykjanes and Krafla. Geitafell epidotes record isotopic composition of Miocene meteoric water with δ'^{18}O of -8 ‰.

4. Measurements of quartz are supposed to provide a more accurate record of equilibrium fluids and temperature using calibrated equilibrium fractionation. The estimated fluids range within ±1.5 ‰ and ± 0.02 ‰ in δ'^{18}O and Δ'^{17}O of the well fluids at respective localities. However, the *in situ* δ^{18}O measurements provide evidence that the equilibrium calculations might suffer inaccuracy from presence of multiple generations of equilibrium compositions within single crystals. Estimated slope of quartz-epidote triple oxygen isotope fractionation in the studied hydrothermal systems has the mean value of 0.526 ± 0.001 (± 1 standard error).

5. Triple oxygen isotope composition of contaminated magmas might be used to inform about the amount of assimilated material. The Δ'^{17}O values of low δ^{18}O rhyolites from Krafla are consistent with assimilation of 10-30% of high-temperature hydrothermally altered crust.

6.0 Bridge

Chapter II highlights the effectiveness of Δ^{17}O measurements based on the study of modern geothermal areas of Iceland. The Δ^{17}O values measured in fluids and minerals add a new dimension to resolving the effect of water-rock exchange and shallow boiling. These results provide basis for all subsequent chapters that address the environment of ancient hydrothermal systems. Our measurements of δD, Δ^{17}O, and δ^{18}O in well fluids show that the reactions proceeded at water-rock ratios of 0.1 to 2, and they reveal the addition of meteoric water in the Reykjanes system, and near-surface boiling and steam-liquid separation at Krafla. Epidote isotope composition in all three localities closely resemble the isotope composition of local fluid sources (either inferred from δD values or measured directly). The Chapter II shows that the $\Delta^{17}O$ values can provide key control on the extent of water-rock exchange that was not accessible through conventional analyses of δD and $\delta^{18}O$. The distinction between basalt-seawater and basalt-meteoric-water reactions in hydrothermal systems are clearly resolved and thus, can be studied in ancient environments. In Chapter III, I present the results of mineralogical, fluid inclusion, hydrogen, and triple oxygen isotope analyses of submarine hydrothermal altered rocks from the early Paleoproterozoic (2.43-2.41 Ga) Vetreny belt. I also present triple oxygen isotopic composition of quartz and epidote that formed in a high-temperature hydrothermally altered, relatively young (6-7 Ma), oceanic crust sampled by the Ocean Drilling Program Hole 504B in the eastern Pacific Ocean. The study is aimed to derive the $\delta^{18}O$, $\Delta^{17}O$ and δD values of the 2.43-2.41 Ga seawater. These constraints provide insights into the role of submarine hydrothermal alteration in the stable isotopic budget of seawater throughout Earth's history.

CHAPTER III

TRIPLE OXYGEN AND HYDROGEN ISOTOPIC STUDY OF HYDROTHERMALLY ALTERED ROCKS FROM THE 2.43-2.41 GA VETRENY BELT, RUSSIA: AN INSIGHT INTO THE EARLY PALEOPROTEROZOIC SEAWATER

From Zakharov, D.O. and Bindeman, I.N. (2019) Triple oxygen and hydrogen isotopic study of hydrothermally altered rocks from the 2.43-2.41 Ga Vetreny belt, Russia: An insight into the early Paleoproterozoic seawater. *Geochimica et Cosmochimica Acta*, 248, 185-209.

1.0 Introduction

The secular variations in the stable isotopic composition of seawater provides constraints on interactions between major reservoirs of oxygen and hydrogen, ultimately relating plate tectonics, continental weathering, and temperature of the oceans. Consequently, the $\delta^{18}O$ and δD values of the ancient seawater, especially in the Precambrian, has been an alluring subject for geochemical investigations (Perry, 1967; Knauth and Lowe, 1978; Gregory and Taylor, 1981; Holland, 1984; Shields and Veizer; 2002; Knauth and Lowe, 2003; Robert and Chaussidon, 2006; Furnes et al., 2007; Marin-Carbonne et al., 2012). Detailed studies of rocks recovered from the modern seafloor (Muehlenbachs and Clayton, 1976; Stakes and O'Neil, 1982; Alt et al., 1986; Alt et al., 1995; Alt and Bach, 2006) made a significant contribution by showing that low- and high-temperature interaction between oceanic crust and seawater plays a ubiquitous role in the stable isotope budget of hydrosphere over the course of geologic time. Compared to fresh unaltered basalt with $\delta^{18}O = 5.5 – 5.8$ ‰ VSMOW (Hoefs, 2015), the upper 600 m of modern seafloor basement composed of pillow basalts attains high $\delta^{18}O$ values, between 6 and 10 ‰ due to low-temperature (<100 °C) alteration and submarine weathering. The next 5-6 km of oceanic crust below that are low in $\delta^{18}O$, between 1 and 5 ‰ due to high-temperature hydrothermal alteration generated at mid-ocean ridges (Muehlenbachs and Clayton, 1976; Alt et al., 1996). The interaction between ancient seawater and seafloor rocks is recorded in fragments of preserved oceanic crust, providing an opportunity to assess quantitatively the temporal changes in the isotopic budget of Earth's hydrosphere. Studies of exposed Mesozoic oceanic crust including the

Samail, Troodos, Josephine ophiolites (Heaton and Sheppard, 1977; Gregory and Taylor, 1981; Schiffman and Smith, 1988) showed that the $\delta^{18}O$ of seawater was unlikely to be significantly different from the modern-day value. Older ophiolites are rare and are often altered by metamorphism, hampering the ability to make accurate determinations of the $\delta^{18}O$ value of seawater. Several such studies, however, suggested that the $\delta^{18}O$ value of Paleozoic, Proterozoic and even Archean seawater must have also been within ± 2 ‰ of the modern-day value (e.g. Holmden and Muehlebachs, 1993; Fonneland-Jorgensen et al., 2005; Furnes et al., 2007).

On the other hand, Precambrian and early Phanerozoic marine sediments yield $\delta^{18}O$ values as much as 10 to 20 ‰ lower than modern analogues (Veizer et al., 1999; Shields and Veizer; 2002; Knauth and Lowe, 2003). To explain this, many authors called for very low $\delta^{18}O$ values of the Precambrian seawater, between −15 and −10 ‰, or much higher temperatures (up to 80-90 °C) of oceans at constant $\delta^{18}O$ of seawater, or a combination of the both (Robert and Chaussidon, 2006; Jaffrés et al., 2007; Veizer and Prokoph, 2015). The discrepancy between the sedimentary and ophiolite records has been the subject of debate for a few decades now (see Jaffrés et al., 2007 and references therein). While the argument of poor preservation of the original $\delta^{18}O$ signal in sedimentary rocks is often invoked, there are possible explanations for low $\delta^{18}O$ values of the Precambrian seawater involving long term secular changes of the ^{18}O fluxes in the hydrosphere due to ongoing subduction and changing ocean depth (e.g. Kasting et al., 2006; Wallmann, 2001). Since the low $\delta^{18}O$ values of ancient marine sediments are common in Proterozoic and Archean formations, and the record provided by Precambrian ophiolites is sparse, it is worth pursuing more accurate and precise determinations of the seawater $\delta^{18}O$ value from well preserved rocks using modern analytical methods.

The coupled behavior of hydrogen and oxygen isotopic composition of seawater through geologic time could help to resolve the controversy (e.g. Hren et al., 2009) but the δD value of seawater in the distant past is difficult to explore due to poor preservation of the original δD values in common hydrous minerals (Kyser and Kerrich, 1991). Additionally, the potential decoupling of the δD and $\delta^{18}O$ values in the Archean seawater (e.g. due to hydrogen loss; Zahnle et al., 2013) has not yet been explored extensively in the rock record (one study by Pope et al., 2012).

The advent of high-precision $\delta^{17}O$ measurements could provide much needed additional constraints on the $\delta^{18}O$ of ancient hydrosphere based on mass-dependent fractionation of oxygen isotopes. Improved understanding and the growing number of high-precision studies on mass-dependent equilibrium fractionation of triple oxygen isotopes in terrestrial reservoirs (Matsuhisa et al., 1978; Pack and Herwartz, 2014; Pack et al., 2016; Sharp et al., 2016; Bindeman et al., 2018; Sengupta and Pack, 2018) are now sufficient to derive the $\Delta^{17}O$ of ancient seawater from measurements of minerals that originated in a submarine environment. Combined analysis of δD and $\Delta^{17}O$ values in submarine hydrothermally altered rocks should help resolve the effect of variable water-rock ratios and might provide a missing record for future modeling efforts of coupled hydrosphere-lithosphere interactions.

In this paper we investigate the products of hydrothermal alteration of well-preserved komatiitic basalts from the 2.43-2.41 Ga Vetreny belt of Karelia craton, Baltic Shield located in the NW part of European Russia (Fig. 1) using hydrogen and triple oxygen isotopes aided by mineralogical and fluid inclusion studies. Hydrothermally altered rocks offer snapshots of high-temperature interaction with seawater recorded shortly after eruption, during the period of cooling of magmas (10^4-10^5 years), and are often far less subjected to post-depositional alteration compared to the sedimentary record. Oxygen isotopes bonded in large crystals (>1 mm) of silicate minerals were likely closed to diffusion and could be altered only at much higher temperatures, exceeding 300 °C (Dodson, 1973). The Vetreny belt rocks likely erupted in a submarine environment providing a rare insight into the 2.43-2.41 Ga seawater, which existed in an anoxic environment, shortly after or during the earliest Paleoproterozoic snowball Earth glaciation and the Great Oxidation Event (Bekker et al., 2004; Lyons et al., 2014; Gumsley et al., 2017). This formation is well-suited to study ancient water-rock interactions due to the presence of abundant hydrothermal features preserved in the pillow section, and hyaloclastites that are almost untouched by regional metamorphism (see Fig. 2). Excellent preservation of rocks from the Vetreny belt motivated us to draw a comparison to the high-temperature hydrothermally altered rocks from the relatively young (6-7 Ma) oceanic crust recovered by the Ocean Drilling Project (ODP) Hole 504B located in the eastern Pacific seafloor. The drill core provides samples of basalts, sheeted dikes, and plutonic rocks from the sub-seafloor section of oceanic crust that were altered at 300-400 °C by seawater-derived fluids. Coarse-grained aggregates of epidote, quartz, calcite, and other secondary minerals that commonly form veins allow for separation, and analysis of single mineral grains, and subsequent equilibrium isotopic calculations to derive δD, $\delta^{18}O$, $\Delta^{17}O$, and the temperature of equilibrium fluid that closely reflects seawater. This work adds to several existing $\delta^{18}O$ studies of Archean and Paleoproterozoic submarine hydrothermally altered basalts (Holmden and Muehlenbachs, 1993; Gutzmer et al., 2003; Furnes et al., 2007) and provides first estimates of $\Delta^{17}O$ and δD values of the 2.43-2.41 Ga seawater. We are also motivated by our previous studies of the ultra-low $\delta^{18}O$ rocks (as low as −27 ‰) from the neighboring metamorphic Belomorian belt, where 2.44-2.41 Ga mafic intrusions interacted with glacial meltwaters during the earliest episode of snowball Earth glaciation (Bindeman et al., 2014; Zakharov et al., 2017). While the Belomorian belt recorded oxygen isotopic composition of low $\delta^{18}O$ glacial meltwaters near equator (Salminen et al., 2014; Bindeman and Lee, 2018), the almost coeval and geographically proximal Vetreny belt provides a complementary insight into the stable isotopic composition of ancient seawater.

Figure 1. Generalized geological map and stratigraphic column of the Vetreny belt showing the sedimentary fill, komatiitic basalts, and coeval intrusions. The inset shows its location within the Baltic Shield and other 2.44-2.41 Ga supracrustal belts (grey-green). The localities are shown with open squares: Myandukha, Shapochka, Golec and nearby Ruiga intrusion. Separated by a tectonic fault, the Belomorian belt preserves the snowball-Earth-age ultralow-$\delta^{18}O$ rocks coeval with formation of the Vetreny belt (Bindeman et al., 2014; Zakharov et al., 2017). The schematic stratigraphic column includes published age determinations bracketing the age of komatiitic basalts between 2.43 and 2.41 Ga. The relationship between sedimentary rocks of the Vilenga and Kalgachikha formations are not identified reliably and shown as presented in Kulikov et al., (2010).

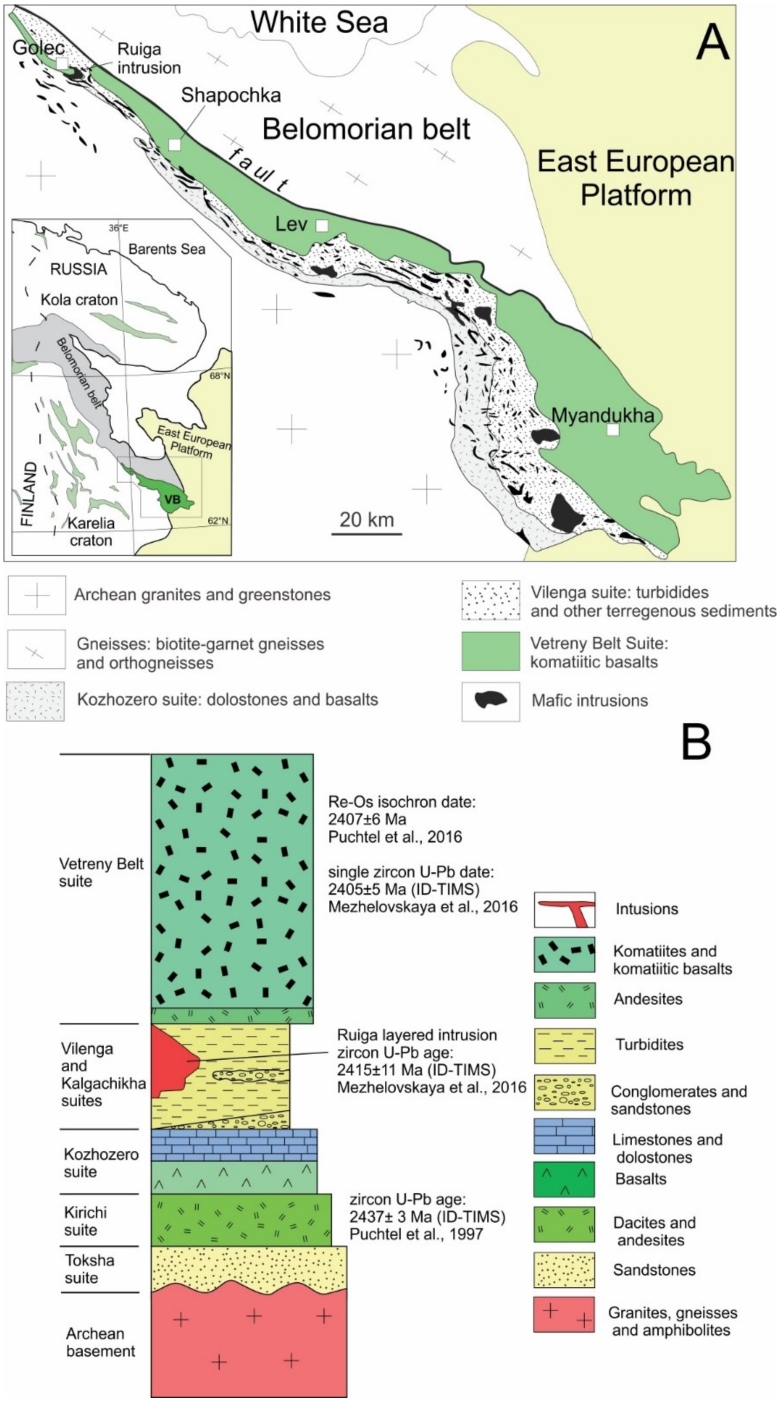

2.0 Geological setting and age

The Vetreny belt is a northwest trending basin over 250 km in length, with width varying from 15 to 85 km from north to south. It developed during early Paleoproterozoic rifting of the Karelia craton of the Baltic Shield and is filled with a volcano-sedimentary succession (Fig. 1; Puchtel et al., 1997; Kulikov et al., 2010). Up to 4 km of dominantly sedimentary rocks and subordinate amounts of volcanic rocks fill the lower section of the Vetreny belt (Fig. 1). The sedimentary fill is composed of sandstones, conglomerates, dolostones, including stromatolites, and turbidites, similar to other early Paleoproterozoic basins of the Baltic Shield, some of which contain glacial deposits related to the Huronian global glaciations marking the transgression of sea onto the land (Strand and Laajoki, 1993; Ojakangas et al., 2001; Melezhik et al., 2013). Even though the Vetreny belt is not a well-studied basin with no conclusive results about the depositional environment, the environment of other contemporaneous basins of the Karelia craton have been interpreted as shallow marine or glacial-marine at 2.4-2.3 Ga (Ojakangas et al., 2001), suggesting that the Vetreny belt also represents accumulation in a submarine environment.

The komatiitic basalts were deposited on top of the sedimentary-volcanic succession, and their cumulative thickness reaches 4 km (Kulikov et al., 2010; Mezhelovskaya et al., 2016). Coeval intrusive bodies of mafic and ultramafic rocks penetrate the underlying formations, representing the subvolcanic complex of the Vetreny belt (Kulikov et al., 2008). Upper sections of these flows contain pillow basalts and hyaloclastites that rest on top of more massive komatiitic basalts, that display porphyritic, variolitic, and spinifex textures. The rocks are remarkably well-preserved for their age, containing original delicate igneous textures, structures resulted from subaqueous emplacement (Fig. 2), and they even preserve amorphous volcanic glass identified by transmitted electron spectroscopy (Sharkov et al., 2003), and potentially traces of microbial life in the upper pillow basalts (Astafieva et al., 2009). Hydrothermal alteration hosted in komatiitic basalts of the Vetreny belt was likely facilitated by the heat from a large volume of cooling lavas and subvolcanic mafic intrusions. Occurrence of pillow structures and "spilitic" assemblages of secondary minerals similar to those observed in modern-day submarine basalts also suggests hydrothermal alteration in presence of seawater. Moreover, the submarine nature of alteration at the Vetreny belt is supported by the presence of saline fluid inclusions hosted in quartz veins.

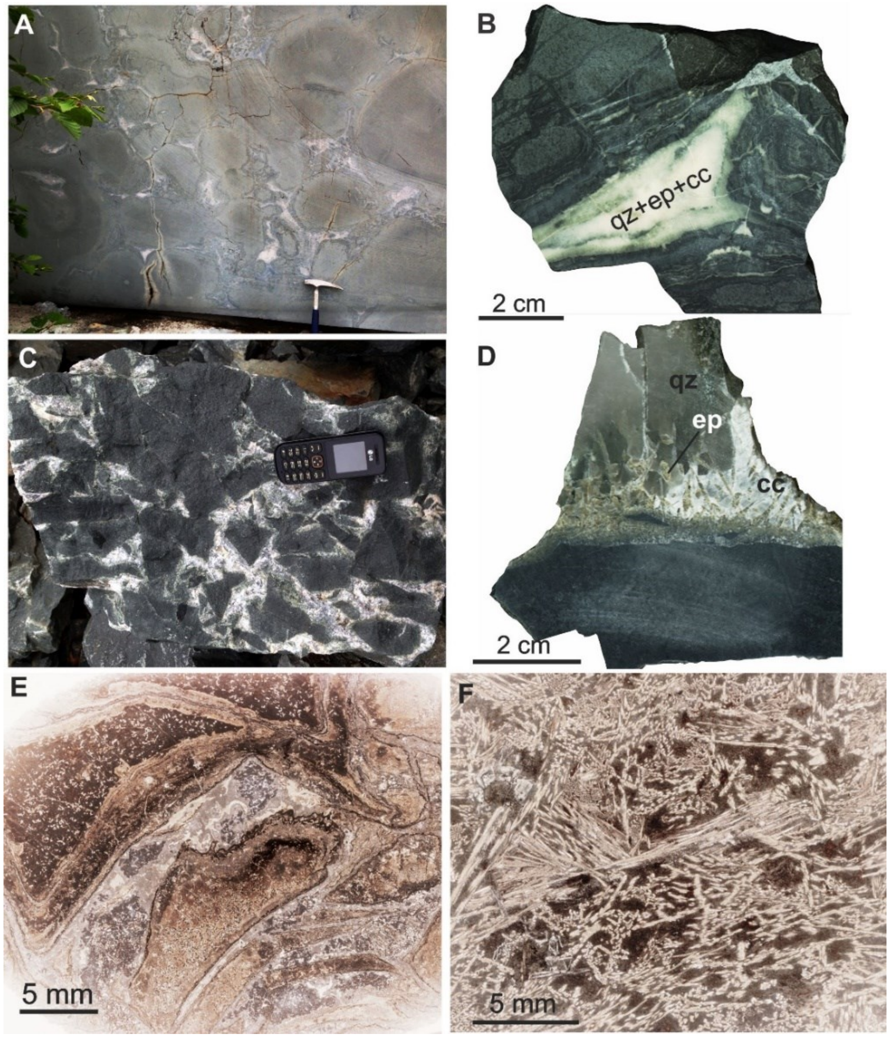

Figure 2. Hydrothermal alteration of komatiitic basalts in the Vetreny belt. A – Pillow basalts as exposed in a quarry wall cut with a large circular saw. Pillows distinctly exhibit alteration of the rinds (green) and less altered cores (brown). The interpillow fills are composed of quartz, epidote, chlorite, actinolite, calcite, and diopside; B – polished hand specimen of interpillow fill showing hyaloclastitic texture at the pillow rind. The interior of interpillow fills are composed of quartz, calcite, epidote, amphibole, diopside, and garnet (sample VB16 in Fig. 3B). C – Hydrothermal breccia with angular fragments of komatiitic basalt (black) surrounded by alteration aggregates of chlorite and amphibole (green) and cemented by white quartz (sample VB13). D – Quartz vein cutting through komatiitc basalt. Quartz (qz), calcite (cc) and epidote (ep) were extracted from the sample and analyzed for $\delta^{18}O$, $\delta^{13}C$ and δD (sample VB8A in Table 1). Homogenization of fluid inclusions in the quartz yields temperature of 358 ± 31 °C. E - Thin section of hydrothermally altered hyaloclastite. Fragments of komatiitic basalt (brown) are surrounded by chilled margins (black sharp) that are concentrically altered inward (light brown) and cemented by quartz-amphibole-chlorite aggregate with muscovite (sample Mya1 in Fig. 3C); D – komatiitic basalt with spinifex texture formed by splintery crystals of clinopyroxene enveloped by amphibole and brown groundmass altered to chlorite, albite, epidote, and quartz (sample GO25 in Fig. 3A).

The age of the komatiitc basalts is bracketed by multiple determinations. Andesites of the Kirichi suite that underlie the komatiitic basalts (Fig. 1) were dated to 2437 ± 3 Ma using high-precision ID-TIMS zircon geochronology (MSWD = 0.8; Puchtel et al., 1997). We interpret this age as the lower limit for the formation of the komatiitic basalts of the Vetreny belt, while the upper limit is interpreted to be 2407 ± 6 Ma as constrained by Re-Os isochron method (MSWD = 6.5) for whole-rock samples, olivine, and chromite separates (Puchtel et al., 2016). A single zircon extracted from a differentiated komatiitic basalt flow yielded an identical age of 2405 ± 6 Ma (ID-TIMS; Mezhelovskya et al., 2016). The subvolcanic mafic layered intrusion Ruiga located at the Golec locality (Fig. 1) was dated to 2390 ± 50 Ma using Sm-Nd isochron method (MSWD = 1.6; Kulikov et al., 2008) and to 2415 ± 15 Ma using three discordant zircons (MSWD = 0.7; Mezhelovskaya et al., 2016). Herein we accept that the komatiitic basalts and associated hydrothermally altered rocks formed within the interval between 2.43 and 2.41 Ga.

2.1 Influence of 1.9 Ga regional metamorphism

Most parts of the Karelia craton experienced metamorphic overprint during the Svecofennian period of metamorphism (1.90-1.85 Ga) with metamorphic grade being the highest in the northern part of the craton (Bushmin and Glebovitsky, 2015). The Vetreny belt located in the extreme south-east part of the Karelia craton (Fig. 1) is one of the least metamorphosed early Paleoproterozoic structures of the Baltic Shield. The komatiitic basalts, with original delicate igneous textures and minerals, and coexisting features of hydrothermal alteration (see Fig. 2) were previously categorized as rocks of prehnite-pumpellyite facies (Bushmin and Glebovitsky, 2015), similar to how modern-day submarine hydrothermally altered rocks are described to be metamorphosed in zeolite, prehnite-pumpellyite to greenschist facies. The preservation of entire sections of unaltered differentiated lava flows with fresh volcanic glass and original igneous minerals (see the description in Puchtel et al, 1996) suggest that the alteration of the hyaloclastites and pillow structures occurred by hydrothermal fluids *in situ* during the eruption in subaqueous medium, and not during the regional metamorphism. While some rocks have an unmetamorphosed appearance (Puchtel et al., 1996), some sections in the western margin of the belt were subjected to greenschist facies metamorphism (Bushmin and Glebovitsky, 2015; Puchtel et al., 1997). Such rocks display signs of deformation, schistosity and foliation, and were intentionally avoided in this study.

3.0 Sample description

For this study we collected samples spanning over 100 km along the length of the belt from localities Golec, Myandukha, Shapochka and subvolcanic Ruiga intrusion (see Fig. 1). The Myandukha locality is an area with several natural outcrops exposed during glacial retreats and in multiple quarries in the vicinity of the town of Severoonezhsk, Russia, and is the southern-most locality studied here. The Golec locality is a hill with steep slopes that expose the volcanic flows and subvolcanic intrusion Ruiga in the northern-most area of the belt (Kulikov et al., 2008). The Myandukha and Golec localities are studied here most extensively because they were either not affected or least affected by superimposed greenschist facies metamorphism at 1.90-1.85 Ga (Puchtel et al., 1996; Puchtel et al., 1997). The rocks studied here show no signs of schistosity or recrystallization indicating an absence of deformations associated with regional metamorphism.

The most prominent hydrothermal alteration is expressed in pillow structures and hyaloclastites. Pillows ranging in size from several tens of centimeters to over a meter in diameter are ubiquitously present in multiple quarries near the Myandukha locality (Fig. 2A). The pillow rinds are notably colored green compared to brown-grey centers of the pillows, and the voids formed by junction between pillows and brecciated fragments are filled with fine-grained aggregates of quartz, epidote, calcite, amphibole, and chlorite (Fig. 2B, 2C). Herein such aggregates are referred as interpillow fills. Locally, komatiitic basalts are intensely dissected by quartz veins, brecciated, and cemented by quartz. In such cases quartz and associated epidote and calcite occur as coarse crystals (several cm in size), which were separated for oxygen, carbon, and hydrogen isotopic analyses (Fig. 2D). Hyaloclastitic varieties of komatiitic basalts exhibit jointing of small fragments (up to 10 cm) of rock that are altered from rim to center varying the color from dark green to dark brown and surrounded by chilled margins (Fig 2E). Hydrothermally altered massive basalts exhibit relict porphyritic, variolitic and spinifex textures, where most of original igneous minerals are replaced by epidotes, amphibole, albite, and chlorite (Fig. 2F). The samples of altered gabbros collected from the Ruiga intrusion contain amphibole, serpentine, chrolite, talc and relicts of plagioclase, olivine, and pyroxene. The massive basalts, hyaloclastites, fine-grained interpillow fills and altered gabbros were analyzed for $\delta^{18}O$ and δD as whole rock samples due to difficulty of extracting single grains of minerals.

The 6-7 Ma submarine hydrothermally altered rocks from the eastern Pacific seafloor were extracted by the Hole 504B (ODP legs 83 and 70). Most samples are from leg 83 (prefix 83-; see Tables 1 and 2), from depths 995 – 1000 m below the sub-seafloor basement (without sedimentary cover). This interval represents the upper section of sheeted dikes complex, where basaltic rocks are altered to low $\delta^{18}O$ values at temperatures above 250 °C (Alt et al., 1996). One sample was extracted from shallower levels (leg 70, depth of 378 m; prefix 70-) representing a mid-ocean ridge basalt (MORB) that underwent modest submarine weathering. The mineralogical, chemical, and isotopic composition throughout Hole 504B, including the Legs 70 and 83 can be found in Alt et al. (1996).

4.0 Methods

Powdered samples of fine-grained massive altered komatiitic basalts were analyzed using X-ray diffraction (XRD) with several matching samples analyzed by X-ray fluorescence (XRF). The XRD patterns were collected by Rigaku Rapid II system (Mo-Kα radiation) at the University of Wisconsin, and major element composition was determined using an XRF Axios analyzer at Pomona College, California. Percentages of mineral phases in the samples were computed by JADE 9.0 software using the Rietveld refinement method. Thin sections were examined under a petrographic microscope, and analyzed using the Cameca SX100 electron microprobe at the University of Oregon. The fine-grained samples were scanned to create elemental maps using grid analysis with following operating conditions: 40° takeoff angle, beam current 30 nA, 15kV operating voltage, beam diameter 10 μm and 0.1 sec count time for each element per pixel. Spot analyses of selected minerals were performed under same conditions except count time was 60 seconds per element. Microthermometry measurements of fluid inclusions in quartz were conducted using Fluid Inc. USGS-type heating-cooling stage. Reproducibility of each measurement is within ±2°C.

The Δ^{17}O and δ^{18}O analyses were carried out at the University of Oregon Stable Isotope Lab using a gas-source MAT253 mass spectrometer equipped with a laser fluorination line. For oxygen isotope analyses we used whole rock samples (1.2 – 2 mg) of massive, altered, komatiitic basalts, fine-grained interpillow fills and separated crystals of quartz, calcite, and epidote. Mineral separates were examined under a binocular for inclusions of other minerals prior to analysis. Analytical procedures for conventional δ^{18}O analyses followed as reported in Bindeman et al. (2014). Triple oxygen isotope analyses carried out using the same procedure reported in Zakharov et al. (2017) including the gas chromatographic column for purification of generated O_2. For hydrogen isotope analyses we used a continuous flow system TC/EA-MAT253 at the University of Oregon, following standardization and normalization procedures described in Martin et al. (2017). The δ^{18}O, δD, Δ'^{17}O are reported relative to the VSMOW (Vienna Standard Mean Oceanic Water). The average precision of conventional δ^{18}O analysis is ±0.1 ‰. The average precision of δD analysis by TC/EA is ± 1 to 4 ‰; the precision of H_2O determination is estimated to be ±0.05 wt. %. The precision of triple oxygen isotope analysis is ±0.01 ‰ or better for δ'^{18}O and ±0.010-0.015 ‰ for Δ'^{17}O. Carbonates were analyzed for δ^{18}O and δ^{13}C by reaction with phosphoric acid using GasBench in continuous flow mode with He-gas as carrier. The precision is ±0.2 ‰ for δ^{18}O and ±0.1 ‰ for δ^{13}C values of carbonates. All analytical precisions are reported as 2 standard errors. The δ^{34}S analysis was carried out at the University of Nevada, Reno, Stable Isotope Lab followed the procedure reported in Grassineau et al. (2001) with precision of ± 0.2 ‰ reported relative to VCDT (Vienna Canyon Diablo Troilite).

Accuracy of the triple oxygen isotope analyses was monitored by analyzing San Carlos olivine (SCO) for which high-precision measurements are published (Pack and Herwartz, 2014; Pack et al., 2016). The SCO yielded $\delta'^{18}O = 5.445 \pm 0.088$ ‰ and $\Delta'^{17}O = -0.081 \pm 0.008$ ‰ (mean ± standard error, n=9; Table A.1), which agrees with results published in previous studies (Pack and Herwartz, 2014). However, the more recent analysis of SCO measured against oxygen extracted directly by fluorination of VSMOW and SLAP conducted in two labs (see Pack et al., 2016) yields systematic offset of the

$\Delta'^{17}O$ value of SCO by about 0.030 ‰ from our value (Pack and Herwartz, 2014). Since we did not perform fluorination of VSMOW to calibrate our reference gas we adjusted our measurements within each analytical session to compensate for the offset given for the composition of SCO (Pack et al., 2016; see Table S1 in Appendix B).

The linearized delta-notation $\delta'^{18}O$ and $\delta'^{17}O$ is used here to address the non-linearity of the relationship between conventionally expressed $\delta^{18}O$ and $\delta^{17}O$. Following Miller (2002), linearized notation is expressed as:

$$\delta'^{\,x}O = 1000ln(1 + \frac{\delta^{\,x}O}{1000}) \qquad (1),$$

where x is either 17 or 18. The value of $\Delta'^{17}O$ is used here to describe ^{17}O-excess from a reference line with a slope of 0.5305 (Matsuhisa et al., 1978; Pack and Herwartz, 2014):

$$\Delta'^{17}O = \delta'^{17}O - \lambda \cdot \delta'^{18}O \qquad (2).$$

Additionally, we measured $\delta^{18}O$ values *in situ* in two quartz samples (VB8A and ODP504B 83-90R, 71-72) using ion microprobe. First, polished sections of quartz were imaged using a FEI Quanta field emission gun scanning electron microscope equipped with a cathodoluminescence grayscale detector at the University of Oregon. The $\delta^{18}O$ was analyzed from 10-µm-diameter spots using a secondary ion mass spectrometer (SIMS) CAMECA IMS-1280 at the WiscSIMS Lab, University of Wisconsin. A polished grain of UWQ-1 quartz ($\delta^{18}O$ = 12.33 ‰) was mounted with the samples and used as a bracketing standard. The precision during the analyses was ± 0.4 ‰ or better (2 standard errors).

5.0 Results

5.1 Mineralogical compositions

As determined by XRD (Table S2 in Appendix B), the major minerals in altered komatiitic basalts are amphibole (50 - 70 wt. %), chlorite (10 - 30 wt. %), epidote (5 - 10 wt. %) and albite (5 - 10 wt. %). Muscovite, phlogopite, titanite, prehnite, quartz and calcite commonly occur in minor amounts. The XRF major elemental data (Table S2) show that altered komatiitic basalts have high MgO and iron oxide (reported as $Fe_2O_3^{total}$), 8-16 and 14-17 wt. % respectively, with SiO_2 content of 45-47 wt. % similar to composition reported previously (Puchtel et al., 1997). Electron microprobe data shows that phenocrysts of olivine and pyroxene preserve their shapes and are pseudomorphically altered to Ca-amphiboles (Fig. 3). The spinifex-textured komatiitic basalts contain original undeformed pyroxenes, augite, and pigeonite, enveloped in actinolite-epidote rims (Fig. 3A). The groundmass of altered komatiitic basalts is altered to fine-grained aggregates of albite, chlorite, epidote, mica, quartz, and calcite. The interpillow fills exhibit zoning; the areas adjacent to the pillow are rich in epidote, quartz, and Ca-amphibole, while the center of interpillow fills contain abundant medium-grained calcite, epidote, diopside, irregularly zoned amphibole, and rare grossular (Fig. 3B). Fine-grained veins that dissect and cement hyaloclastite fragments of altered komatiitic basalts are composed of fine-grained aggregates of albite, chlorite, muscovite, prehnite, and Ca-amphibole (Fig. 3C).

Table 1. Equilibrium temperatures, $\delta^{18}O$ and δD of equilibrium fluids based on conventional oxygen and hydrogen isotope analyses. All isotopic values are reported in ‰ VSMOW

Sample	$\delta^{18}O_{qz}$	$\delta^{18}O_{ep}$	δD_{ep}	$\delta^{18}O_{cc}$	$\delta^{13}C_{cc}$	Computed temperature, °C		Computed fluid		
						qz-ep[1]	qz-cc[2]	$\delta^{18}O_{fluid}$[3]	δD_{fluid}[4]	δD_{fluid}[5]
Myandukha locality, Vetreny belt										
VB8A	8.56	3.08	-51	7.37	0.07	349	375	3.01	-13	-31
VB8B	7.83	2.97	*-32*			387		3.20	9	-12
VB14C	5.67	-0.34	*-20*	4.08	-5.36	321	286	-0.68	16	0
VB24	9.27	2.99	*-8*			308		2.51	26	12
1321	11.36			7.32	-4.01		79	-	-	
Golec locality, Vetreny belt										
GO4	5.06	-0.06	*-23*			370		0.04	16	-3
GO22	5.13	-0.97	-56			316		-1.36	-21	-36
Golec	4.93	-0.25	-119			365		-0.20	-80	-99
hole ODP 504B, eastern Pacific Ocean										
83-90R, 148-149	8.42	3.47	*-8*			380		3.62	32	12
83-90R, 71-72	8.75	2.38	*-21*			303		1.82	13	-1

Abbreviations: qz – quartz, ep –epidote, cc – calcite

δD values in epidotes with ≤ 2 wt. % are highlighted in italic

1- fractionation factor used from Matthews (1994)

2- fractionation factor from Matthews et al. (1983)

3- fractionation between water and quartz is computed as recommended in (Sharp et al., 2016)

4- hydrogen fractionation factor from (Chacko et al., 1999)

5- hydrogen fractionation factor $1000\ln\alpha_{epidote\text{-}seawater} \approx -20$ ‰ from (Graham and Sheppard, 1980)

The compositions of epidotes, amphiboles, chlorites, and pyroxenes found in massive altered komatiitic basalts and veins and interpillow fills are shown on Fig. 4. Spot analyses of these minerals are reported in Tables S3 through S6 in Appendix B. For comparison we show the compositions of the minerals from modern hydrothermally altered oceanic crust demonstrating a significant overlap with the compositions of chlorites, amphiboles and secondary diopside from the Vetreny belt (Fig. 4). The notable difference between Fe^{3+} content in some epidotes from the Vetreny belt and epidotes recovered from modern oceanic crust is difficult to interpret with certainty because of the very complicated relationship between epidote composition and thermodynamic parameters. However, the measured epidote compositions are not unusual for epidotes from hydrothermal systems in general (Bird and Spieler, 2004).

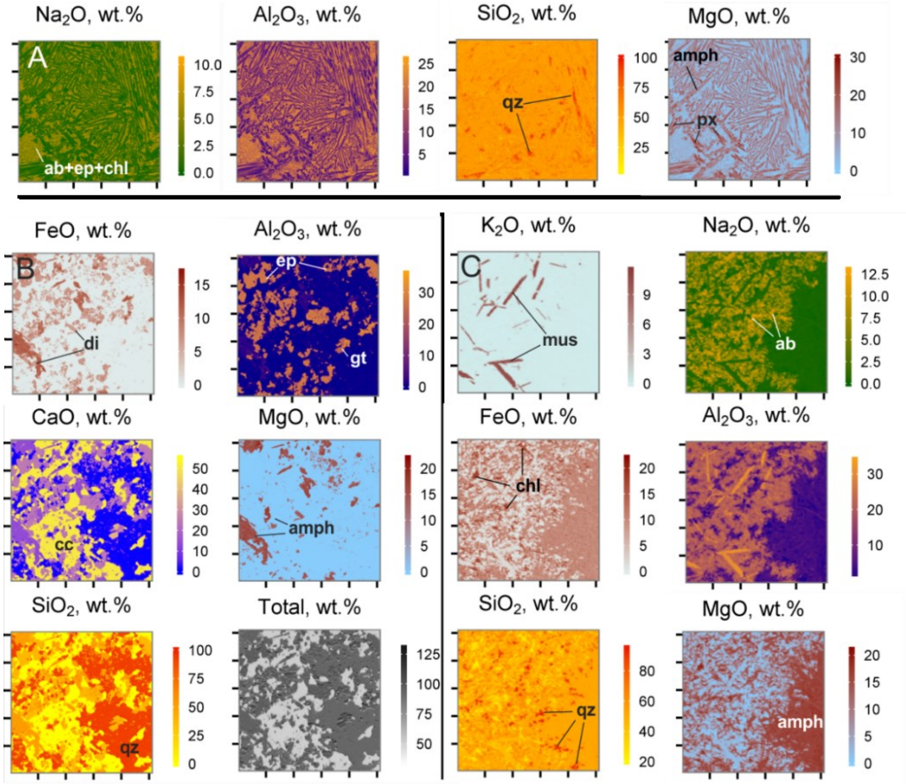

Figure 3. Elemental distribution maps created for fine-grained hydrothermally altered rocks using EMPA. A – komatiitic basalt (sample GO25) showing original igneous texture with preserved skeletal relicts of pyroxene enveloped by amphibole. Side length of the image is 500 μm; B – internal part of interpillow fill (sample VB16) composed of amphibole, diopside, epidote and garnet cemented by anhedral quartz and calcite; C – fine-grained rind of altered hyaloclastitic fragment. The rock is altered to albite, muscovite, chlorite, amphibole, and quartz. Side of each square is about 300 μm in panels B and C. Mineral abbreviations: (ab) albite, (amph) amphibole, (chl) chlorite, (cc) calcite, (di) diopside, (ep) epidote, (gt) garnet, (px) primary pyroxene, and (qz) quartz.

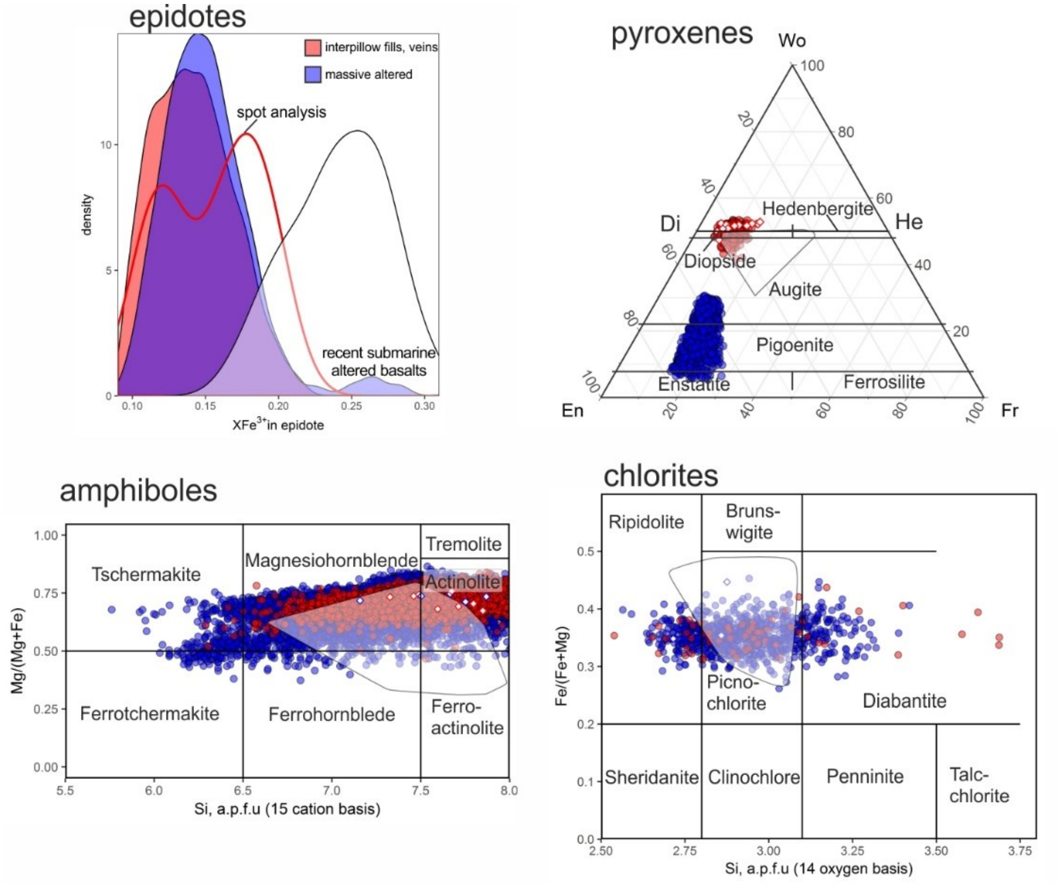

Figure 4. Chemical composition of solid-solution minerals from the hydrothermally altered komatiitic basalts. Blue circles represent minerals in massive altered komatiitic basalts, red circles – in interpillow fills and veins. Filled circles represent data extracted from the elemental maps (Fig. 3) and open diamonds show compositions as determined by EMPA spot analysis (see Methods). Composition of epidotes expressed as the xFe^{3+} denoting the $Fe^{3+}/(Al+Fe^{3+})$ ratio in formula units computed based on 13 anions. The average value $xFe^{3+} = 0.16$ was used for computing quartz-epidote fractionation factor (Matthews, 1994). Composition of pyroxenes expressed in end-members: Di – diopside, He – hedenbergite, En- enstatite, Fr – ferrosilite, Wo – wollastonite. Pyroxenes in massive komatiitic basalts are primary augites and pigeonites, whereas secondary pyroxenes occurring in interpillow fills are diopsides. Occurrence of both primary and secondary pyroxenes is common in high-T hydrothermally altered mafic rocks from modern seafloor (Laverne et al., 1995). Amphiboles and chlorites are plotted on a classification diagrams of Hey (1954) and Leake et al. (1997), respectively. Transparent white areas in each diagram represents the chemical composition of secondary minerals from recent submarine altered rocks (Vanko et al., 1995; Laverne et al., 1995).

5.2 Microthermometry of fluid inclusions

We conducted a microthermometry study of fluid inclusions using two samples of clear vein quartz collected from Myandukha (VB8A) and Golec (GO22) localities (Fig. 1). The results of measurements are presented on Fig. 5. Most fluid inclusions are ~10 μm in size, fluid-dominated with a vapor bubble occupying 10-20 vol. %. We were focused on inclusions with negative crystal shapes, without signs of stretching or alignment along cracks. Such inclusions likely experienced the least amount of modification after the formation of quartz. The fluid-dominated inclusions commonly contain a cubic-shaped daughter mineral, most likely halite. Other unidentified daughter minerals are clear and opaque, of cubic and rectangular form, but occur much more rarely than halite crystals. The fluid-dominated inclusions containing halite homogenize to fluid only, through a series of transitions: fluid + bubble + crystal -> fluid + bubble (average temperature 320 °C) -> fluid (at ~400°C). Vapor-dominated inclusions are also found within the same samples. They contain 70-90 % vapor and homogenize to vapor. The average homogenization temperatures for both types of inclusions in the samples from Golec (sample GO22) and Myandukha (VB8A) localities are 304 ± 25 and 358 ± 31 °C respectively, with the average value of 331 ± 22 °C for both samples (mean ± 2 standard errors). The total range of observed temperatures is 228 – 537 °C, however, some of the high-temperature measurements result from difficulty in seeing complete homogenization in vapor-dominated inclusions though vapor + liquid -> vapor.

The presence of multiple daughter minerals in fluid-dominated inclusions indicates high salinity of the fluid. Presence of halite crystals constrains the salinity between the saturation level of 26.3 wt. % equivalent NaCl, and ~40 wt. % eq. NaCl as determined by dissolution of halite crystals at around 320°C. Presence of other daughter minerals indicates that the salinity is defined not only by NaCl but by other dissolved salts, consistent with the melting temperatures below the NaCl-H_2O eutectic point (−21.2 °C). Measuring salinity in vapor-dominated inclusions is difficult due to limitations of the optics and those measurements are not presented here. However, in several fluid inclusions the bubble "jerks" when heated to about 0 °C suggesting melting of last ice crystal at that temperature, which would indicate low salinity of the inclusions. In summary, we observe both brine and vapor as trapped inclusions in these samples indicating that the hydrothermal fluid was undergoing phase separation. This is a common process in modern submarine hydrothermal systems at subcritical and supercritical critical temperatures (critical point of seawater is 407°C, 298 bars; Bischoff et al., 1986) as observed directly in near-vent fluids (Foustoukos and Seyfried, 2007 and references therein) or in fluid inclusions hosted in hydrothermal minerals from oceanic crust and ophiolites (Nehlig, 1991).

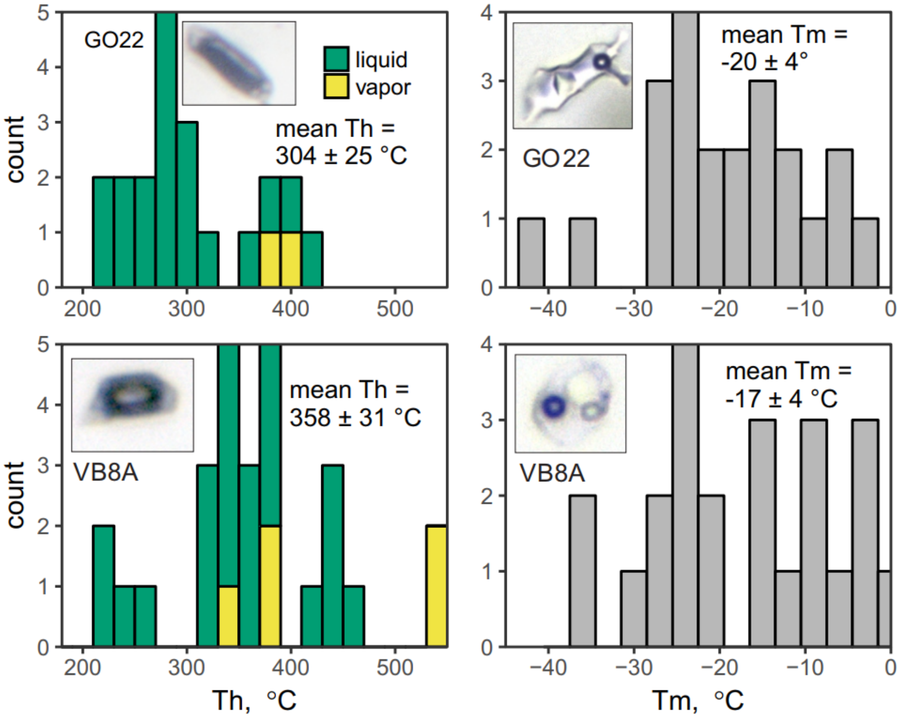

Figure 5. Histograms showing the results of fluid inclusion microthermometry. Homogenization (Th, °C) and melting temperatures (Tm, °C) were measured in samples GO22 and VB8A collected at Golec and Myandukha localities, respectively. Examples of vapor-dominated inclusions and fluid-dominated inclusions with daughter minerals are shown for each sample on the left and right sides of the respective panel image. Temperatures of homogenization are in good agreement with the temperatures derived from quartz-epidote oxygen isotope equilibrium (see Table 1). Very low melting temperatures and abundance of halite and other daughter minerals reflect extremely high salinity of the fluid that likely originated from phase separation of seawater.

5.3 Conventional $\delta^{18}O$, δD and $\delta^{13}C$ analysis

In total, we analyzed 54 samples for different isotope ratios collected from localities Myandukha, Shapochka, Golec and intrusion Ruiga (Fig. 1), including separates of quartz, epidote, calcite, and whole rock samples of altered komatiitic basalts, gabbros, veins and interpillow fills. The results of oxygen and hydrogen isotopic analysis are plotted on Fig. 6 and presented in the Table S7. The $\delta^{18}O$ in whole rock samples of altered komatiitic basalts containing abundant amphiboles, chlorites and epidotes ranges between 1.03 and 3.54 ‰ and the δD ranges between −210 and −69 ‰, containing 2-5 wt. % H_2O. The $\delta^{18}O$ values of altered gabbros from the Ruiga intrusion vary between 1.63 ‰ and 3.68 ‰, with δD values between −187 and −161 ‰ and H_2O contents of 2.0-2.5 wt. %. Interpillow fills and fine-grained veins analyzed as whole rocks have $\delta^{18}O$ varying between 1.81 and 8.67 ‰ and δD varying between −192 and −96 ‰. The veins and interpillow fills are much heavier compared to altered komatiitic basalts due to presence of quartz. The measurements of pure quartz and epidote separates yield average values $\delta^{18}O_{quartz} = 6.46 \pm 1.38$ ‰ and $\delta^{18}O_{epidote} = 1.30 \pm 1.84$ ‰ (mean ± se). Pure clear quartz from quartz veins ranges in $\delta^{18}O$ from 4.40 to 9.27 ‰ with samples from the Golec locality having slightly lower $\delta^{18}O$ values ranging from 4.40 to 6.17 ‰, while quartz from the Myandukha locality ranges in $\delta^{18}O$ from 5.66 to 9.27 ‰ (Fig. 6A). The $\delta^{18}O$ of epidotes from quartz veins and interpillow fills range between −0.97 and 3.08 ‰, while the δD in most epidotes range between −56 ‰ and −8 ‰. One epidote from the Golec locality yielded a low δD value of −119 ‰, which we attribute to poor preservation of original isotopic signature (see Discussion below). Epidotes from the Golec locality range in $\delta^{18}O$ from −0.97 to −0.06 ‰ and two δD measurements yield values −56 and −23 ‰. Epidotes from the Myandukha locality range in $\delta^{18}O$ and δD between −0.35 and 3.11 ‰ and −51 and −8 ‰ respectively. Analyzed epidotes have 1.7-2.1 wt. % H_2O, which is in broad agreement with their stoichiometry. Water contents of analyzed samples plotted against other isotopic parameters, and δD plotted against $\Delta'^{17}O$ values are shown on Figure 7. We used H_2O content to discern pure epidote separates with stoichiometric amounts of water (1.7-2.0 wt. %) that were used to compute δD of the equilibrium fluids (Fig. 6B). We show fields of $\delta^{18}O$ and δD values of epidotes from ophiolites and modern seafloor rocks that exhibit significant overlap with the Vetreny belt data (Fig. 6C).

The four samples of calcite intergrown with quartz and epidote from veins and interpillow fills yielded $\delta^{18}O$ between 4.1 and 7.4 ‰ VSMOW and $\delta^{13}C$ values between of −5.36 and 0.07 ‰ VPDB. The $\delta^{13}C$ values of calcite are consistent with carbon being sourced from the mantle and partly from re-mineralized organic matter (Hoefs, 2015).

One pyrite separate extracted from an interpillow fill (sample VB24) was analyzed for sulfur isotopes yielding $\delta^{34}S = 0.2$ ‰VCDT, which indicates that sulfur could have been derived from the mantle or marine reservoir. Multiple isotope analysis of sulfur isotopes should help distinguishing one from another (Seal, 2006).

Figure 6 (next page). Oxygen and hydrogen isotopic values of hydrothermally altered rocks from the Vetreny belt and computed isotopic compositions of hydrothermal fluids. A – Histograms showing the distribution of $\delta^{18}O$ values in common type of samples. The lowest $\delta^{18}O$ values are interpreted to represent equilibrium with the least modified early Paleoproterozoic seawater with the $\delta^{18}O$ value of −1.7 ‰. B – $\delta^{18}O$ and δD values plotted for hydrous samples. The water content in epidotes is shown; epidotes with ≤ 2.0 wt.% H_2O are considered most reliable (see Discussion). Computed fluids are shown with triangles based on equilibrium calculations. The shaded and open triangles are computed based on hydrogen fractionation factors from Graham and Sheppard (1980) and Chacko et al. (1999) respectively. The average equilibrium fluid (blue triangle) is very close to modern seafloor hydrothermal fluids ($\delta^{18}O = +1$ ‰ and $\delta D = 0$ ‰). C – Oxygen and hydrogen isotopic composition of hydrothermally altered rocks from the modern seafloor (Kawahata et al., 1987; Kempton et al., 1991) and epidotes from modern seafloor and ophiolites (Heaton and Sheppard, 1977; Stakes and O'Neil, 1982; Harper et al., 1988). The two epidotes from Hole 504B analyzed here are shown with open squares. Secondary minerals in equilibrium with seawater at 300 °C are shown with green crosses for amphibole (tremolite), chlorite and epidote, and with dashed lines for quartz and albite (Zheng, 1993; Matthews, 1993; Chaco et al., 1999). Horizontal scatter of the Vetreny belt rocks is comparable to scatter of $\delta^{18}O$ values in hydrothermally altered rocks from the modern seafloor and can be explained by variable proportions of minerals in equilibrium with seawater. Very large vertical scatter (down to $\delta D = -210$ ‰; panel B) is best explained by secondary hydration of hydrous minerals such as chlorite by local precipitation (blue thick line) while large epidote crystals preserved their original isotopic integrity and were used to compute the isotopic composition of equilibrium fluids. Fractionation effect of secondary H_2O exchange between surface water and chlorite as well as other phyllosilicates is shown with the grey line (Wenner and Taylor, 1974).

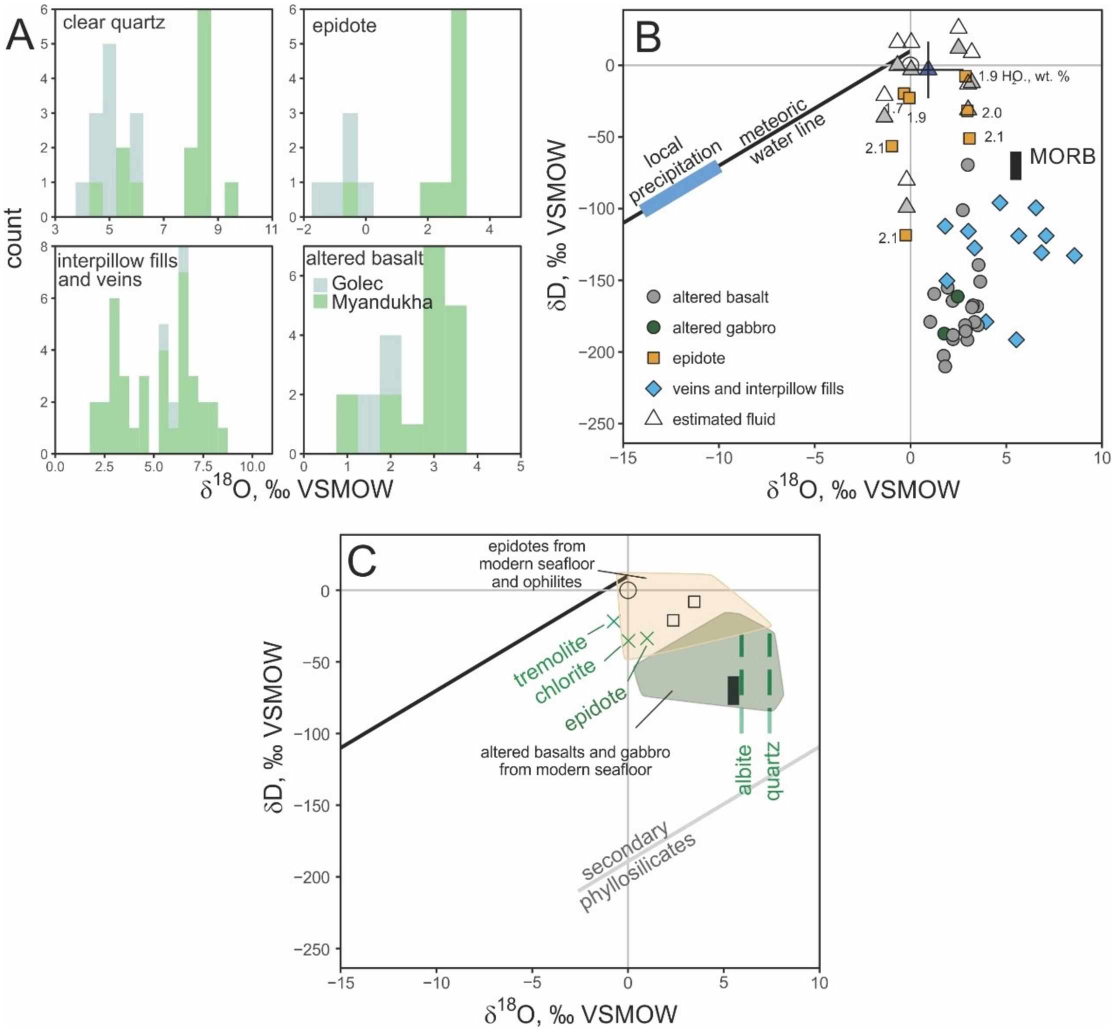

We used oxygen isotopic equilibrium fractionation to determine the temperature of hydrothermal alteration and $\delta^{18}O$, and δD of the equilibrium fluid. Assuming isotopic equilibrium between measured minerals A and B, the difference $\delta^{18}O_A - \delta^{18}O_B \approx 1000\ln\alpha_{A\text{-}B}$ is temperature-dependent. To derive equilibrium temperatures we applied the oxygen isotope calibration from Matthews (1994) for quartz-epidote and from Matthews et al. (1983) for quartz-calcite. We used the average composition of epidote with $Fe^{3+}/(Fe^{3+}+Al) = 0.16$ (formula units; see Fig. 4A) for quartz-epidote fractionation, which is dependent on pistasite $Ca_3Fe_2{}^{3+}Si_3O_{12}(OH)$ content in epidote (Matthews et al., 1994). Based on 8 individual quartz-epidote measurements from samples collected at Myandukha and Golec localities, the computed equilibrium temperature is between 308 and 387° C (see Table 1). The two samples from the ODP Hole yield computed equilibrium temperatures of 303 and 380 °C. Quartz-calcite fractionation in samples (VB8A and VB14C) yielded temperatures of 375 and 286 °C comparable to quartz-epidote equilibrium temperatures from the same samples. In one sample (#1321; Table 1), quartz-calcite fractionation yields temperature of 79 °C, which we consider unrealistically low and possibly related to alteration and the small (< 0.5 mm) grain size of calcite in the sample compared to samples VB8A and VB14C. Using a different quartz-calcite calibration (Sharp and Kirschner, 1994), the same samples yields elevated temperatures ranging between 582 °C and 266 °C. We prefer to rely on quartz-epidote fractionation since it yields consistent results for multiple samples and both quartz and epidote are more resistant to alteration (via dissolution, recrystallization) compared to calcite. Moreover, quartz-epidote calibration (Matthews, 1994) yields systematic results consistent with temperatures and $\delta^{18}O$ of fluids measured in modern hydrothermal systems (see Pope et al., 2014). The close match of homogenization temperatures measured in fluid inclusions and temperatures computed from quartz-epidote equilibrium is a good indicator of preservation of isotopic equilibrium between minerals and fluids.

Figure 7 (next page). Effects of secondary hydration on the δD, $\delta^{18}O$, and $\Delta'^{17}O$ values of hydrothermally altered rocks from the Vetreny belt. A – δD values and water content in analyzed samples. Secondary hydration is manifested by large scatter of δD and negative correlation between δD and H_2O wt.%. The reconstructed δD value of pure chlorite that exchanged δD with meteoric water at low temperature is shown. Epidote separates however were much less affected by secondary hydration except epidotes with > 2.0 wt. % water. The dashed blue line defines an approximate trend of secondary hydration of epidotes. B – The $\delta^{18}O$ plotted against H_2O wt. % shows no significant trend in samples with water content above 1 wt. %. The average $\delta^{18}O$ value of altered komatiitic basalts is shown with the blue dashed line. The $\delta^{18}O$ values of the rocks are controlled by proportion of major minerals in the sample. C - The $\Delta'^{17}O$ plotted against the δD of altered komatiitic basalts and epidotes. Despite the drastic change in δD due to secondary H_2O exchange, altered komatiitic basalts still retain their original $\Delta'^{17}O$ value. Epidotes that are much less susceptible to alteration of hydrogen isotopes and plot near the composition of modern seawater.

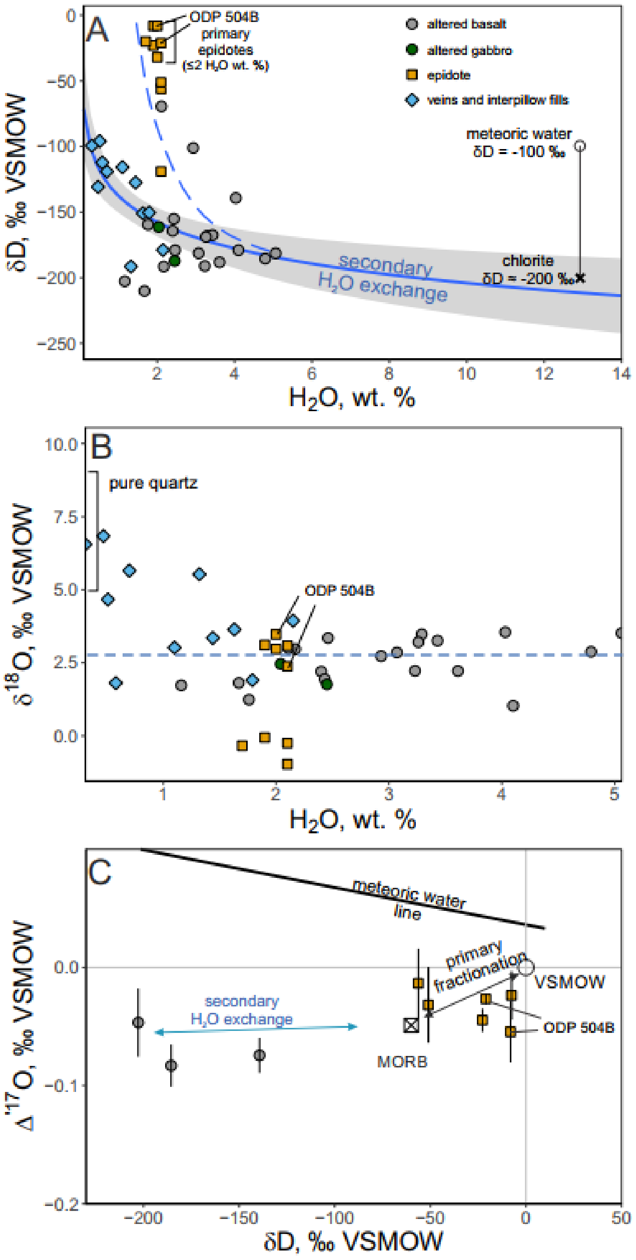

Next, we used quartz-water and epidote-water calibrations (Zheng, 1993; Sharp et al., 2016; Graham and Sheppard, 1980; Chacko et al., 1999) to compute the δ^{18}O and δD of the equilibrium fluid based on the temperatures returned from $\delta^{18}O_{quartz} - \delta^{18}O_{epidote}$ measured in coexisting mineral pairs, assuming isotope equilibrium. The individually computed equilibrium temperatures for each sample, and δ^{18}O and δD values of equilibrium fluids are presented in Table 1 and are plotted in Fig. 6B. The computed equilibrium $\delta^{18}O_{fluid}$ values vary between −1.4 and +3.2 ‰. The computed δD_{fluid} range between –80 ‰ and +27 ‰ based on the calibration from Chacko at el. (1999) and between –99 and +12 ‰ when the calibration from Graham and Sheppard (1980) is applied. The δD fractionation between epidote and seawater at 330-350 °C is about −20 ‰ (Graham and Sheppard, 1980), and might suit this study better since it accounts for the salinity of equilibrium fluid. The same procedure was applied to the 2 samples from Hole 504B (Table 1), with the computed equilibrium temperatures, $\delta^{18}O_{fluid}$ and δD_{fluid} being very similar to those computed for the Vetreny belt. The uncertainties for equilibrium temperatures and $\delta^{18}O_{fluid}$ are ± 15 °C and ± 0.7 ‰, respectively as defined by analytical uncertainties, uncertainties in quartz-water fractionation (Sharp et al., 2016) and the Fe^{3+} content range (0.16±0.05; Fig. 4) in the epidote. The estimated uncertainty of δD_{fluid} is ± 11 ‰ defined by the uncertainty in fractionation factor (Chacko et al., 1999), equilibrium temperature estimates and our δD measurements. All error propagations were performed using Monte Carlo simulations.

5.4 Triple oxygen isotope compositions

The $\delta'^{18}O$ and $\Delta'^{17}O$ values of 18 samples of quartz, epidote and altered whole rocks of the Vetreny belt as well as samples from the ODP Hole 504B are reported in Table 2. We also report one sample of MORB from Hole 504B, Leg 70 that experienced a modest extent of submarine weathering or low-temperature alteration with values $\delta'^{18}O = 6.323$ ‰ and $\Delta'^{17}O = -0.063$ ‰ which is very similar to previously published compositions of fresh and weathered MORBs (Pack and Herwartz, 2014; Sengupta and Pack, 2018).

We used linear regression analysis of coexisting $\delta'^{18}O_{epidote}$ and $\delta'^{18}O_{quartz}$ to derive the average value of $1000\ln\alpha_{quartz\text{-}epidote}$ and to calculate $\delta'^{18}O$ and $\Delta'^{17}O$ of equilibrium fluids. We estimated the average equilibrium temperature for all studied samples and their duplicates as 333 ± 30 °C (mean ± 3 standard errors) based on the mean value of $1000\ln\alpha_{quartz\text{-}epidote}$ (Fig. 8). This was done to address the small variations in the $1000\ln\alpha_{quartz\text{-}epidote}$ given by multiple measurements (see Table 2) and to produce a more accurate estimate of equilibrium temperatures that vary within a narrow range (Table 1). The measured $\delta'^{18}O$ and $\Delta'^{17}O$ values are displayed in Fig. 9A along with the computed equilibrium fluids at 333 °C (Fig. 9B) based on previously published quartz-water triple oxygen isotope fractionation (Sharp et al., 2016; Wostbrock et al., 2018). The computed

$\delta'^{18}O_{fluid}$ and $\Delta'^{17}O_{fluid}$ values range between −0.82 and 4.07 ‰ and −0.110 and −0.034 ‰ respectively (Fig. 9B). The average uncertainties of $\delta'^{18}O_{fluid}$ and $\Delta'^{17}O_{fluid}$ were estimated at ± 1.1 and 0.011 ‰, respectively by propagating the following uncertainties through the calibration equation (Wostbrock et al., 2018): analytical uncertainty, uncertainty of the temperature estimate (±30 °C) and uncertainty given in the fractionation factors.

Table 2. High-precision triple oxygen isotopic analysis of hydrothermally altered rocks and minerals from the Vetreny belt and ODP Hole 504B. all values are reported in ‰ VSMOW.

Sample	material	$\delta^{17}O$	SE	$\delta^{18}O$	SE	$\delta'^{17}O$,	$\delta'^{18}O$	$\Delta'^{17}O$	SE
ODP Hole 504B									
70-48R 20-22	altered basalt	3.297	0.010	6.343	0.003	3.292	6.323	-0.063	0.010
83-80R, 106-108	quartz	4.986	0.011	9.553	0.002	4.974	9.507	-0.070	0.011
83-80R, 106-108	quartz	4.740	0.009	9.089	0.004	4.729	9.048	-0.071	0.009
83-90R, 71-72	altered basalt	1.529	0.011	3.079	0.004	1.528	3.074	-0.102	0.011
83-90R, 148-149	epidote	1.782	0.013	3.465	0.003	1.781	3.459	-0.055	0.013
83-90R, 148-149	quartz	4.478	0.008	8.606	0.004	4.468	8.569	-0.077	0.009
83-90R, 148-149	quartz	4.307	0.007	8.232	0.004	4.297	8.198	-0.052	0.007
83-90R, 71-72	epidote	1.253	0.009	2.409	0.004	1.252	2.406	-0.024	0.010
83-90R, 71-72	epidote	1.219	0.009	2.353	0.003	1.218	2.351	-0.029	0.009
83-90R, 71-72	quartz	4.728	0.008	9.171	0.003	4.717	9.129	-0.126	0.009
83-90R, 71-72	quartz	4.331	0.013	8.320	0.004	4.321	8.285	-0.074	0.013
Vetreny belt									
GO-22	epidote	-0.916	0.014	-1.701	0.005	-0.917	-1.703	-0.013	0.015
GO-22	quartz	2.490	0.011	4.795	0.004	2.487	4.783	-0.050	0.011
GO-25	altered basalt	0.700	0.014	1.408	0.004	0.700	1.407	-0.047	0.014
GO4	epidote	-0.215	0.005	-0.321	0.003	-0.215	-0.321	-0.045	0.005
GO4	quartz	2.509	0.008	4.851	0.002	2.506	4.839	-0.061	0.008
VB-14C	quartz	2.387	0.010	4.629	0.003	2.384	4.619	-0.066	0.010
VB-24	epidote	1.340	0.010	2.572	0.005	1.339	2.569	-0.024	0.010
VB-24	quartz	4.333	0.011	8.326	0.005	4.324	8.291	-0.075	0.011
VB-25	altered basalt	1.596	0.007	3.150	0.003	1.594	3.145	-0.074	0.007
VB8A	epidote	1.534	0.011	2.989	0.004	1.532	2.985	-0.051	0.011
VB8A	epidote	1.539	0.010	2.986	0.004	1.537	2.982	-0.044	0.010
VB8A	epidote	1.139	0.012	2.148	0.008	1.138	2.146	0.000	0.012
VB8A	quartz	4.496	0.009	8.696	0.005	4.486	8.659	-0.107	0.009
VB8A	quartz	4.493	0.008	8.591	0.003	4.483	8.555	-0.056	0.008
VB8A	quartz	4.328	0.012	8.319	0.007	4.318	8.285	-0.077	0.013
VB9	altered basalt	1.445	0.009	2.884	0.003	1.444	2.879	-0.083	0.009

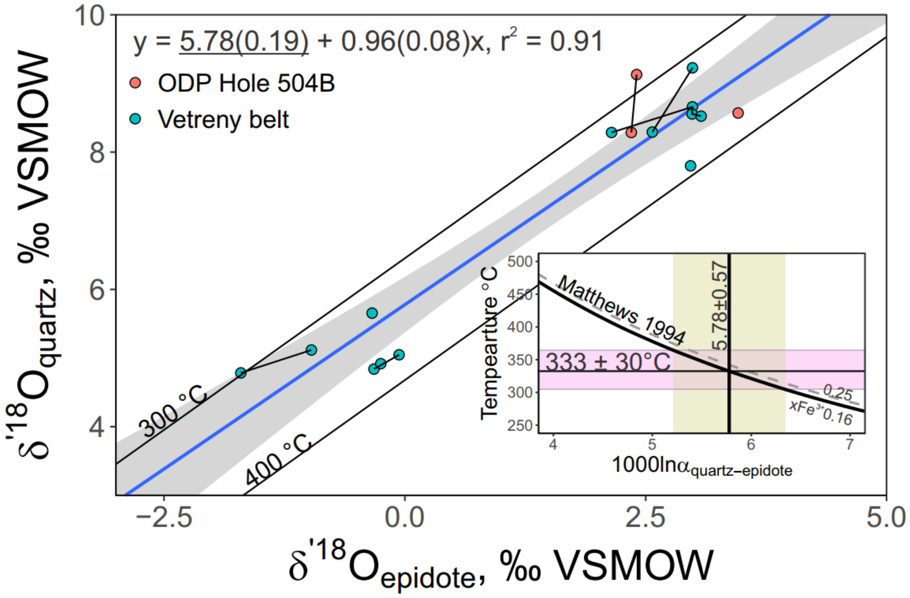

Figure 8. The $\delta'^{18}O$ values of coexisting quartz-epidote pairs are plotted to estimate the average equilibrium fractionation expressed through the regression line $\delta'^{18}O_{quartz} = 1000\ln\alpha_{quartz\text{-}epidote} + \delta'^{18}O_{epidote}$. The quartz-epidote equilibria at 300 and 400 °C are shown with black parallel lines (Matthews, 1994). The regression line defines the average value of $1000\ln\alpha_{quartz\text{-}epidote} = 5.78 \pm 0.19$ (1 standard error). The data points connected with solid black lines represent measured duplicates. The inset shows that the estimated value of $1000\ln\alpha_{quartz\text{-}epidote}$ corresponds to the equilibrium temperature of 333 °C using calibration from Matthews (1994). The propagated uncertainty is ± 30 °C (3 standard errors). The average xFe^{3+} content of epidotes from the Vetreny belt and Hole 504B varies between 0.16 and 0.25 playing a minor role compared to the uncertainty of ± 30 °C.

5.5 CL images and $\delta^{18}O$ values measured by SIMS

In cathodoluminescence (CL) images, the sample of vein quartz from the Vetreny belt (VB8A) is dark and homogenous in $\delta^{18}O$. The SIMS measurements collected from spots distributed over 100 µm apart yield average value $\delta^{18}O = 8.2 \pm 0.1$ ‰ (n = 20). The quartz crystal from Hole 504B (83-90R, 71-72) exhibits zoning in CL images with the evidence for dissolution, re-precipitation, and healing of cracks (see Fig. 9D). Majority of the crystal is bright in CL images, while healed cracks are dark. The overall range of $\delta^{18}O$ values measured by SIMS in this sample is between 6.6 and 15.9 ‰. The CL-bright parts have $\delta^{18}O$ values of 8.0 ± 0.8 ‰ (n = 32). The CL-dark healed cracks are about 8 ‰ heavier than that, with the average $\delta^{18}O$ value of 15.4 ± 0.5 ‰ (n = 7).

Figure 9 (next page). A - Triple oxygen isotopic composition of altered basaltic rocks, epidotes, and quartz from the Vetreny belt and recent oceanic crust sampled by the ODP Hole 504B. The main reservoirs of oxygen such as seawater (VSMOW) and MORB (Pack and Herwartz, 2014) are shown. Meteoric water line constructed after Luz and Barkan (2010). Seawater-derived fluids should plot between VSMOW and the mantle. There is no significant difference between most samples from the 2.43-2.41 Ga Vetreny belt and modern oceanic crust implying that they formed in equilibrium with seawater-derived fluids that had $\Delta'^{17}O \approx 0$ ‰. Due to small fractionation, epidotes must be especially reflective of the $\Delta'^{17}O$ values of equilibrium fluids. Quartz-VSMOW fractionation curve (solid black line; Sharp et al., 2016) shows that $\Delta'^{17}O$ values of quartz are too low to be in equilibrium with pristine seawater or shifted seawater except the two samples that connect to the grey line between VSMOW and MORB. The error bars represent 2 standard errors. B – Estimated $\delta'^{18}O$ and $\Delta'^{17}O$ of equilibrium fluids from the Vetreny belt and Hole 504B based on quartz-water fractionation at 333 ± 30 °C. Based on the lowest $\delta'^{18}O$ values of epidotes and computed equilibrium fluids (blue cloud), we suggest that pristine 2.43-2.41 Ga seawater had $\delta'^{18}O$ of −1.7 ‰ and $\Delta'^{17}O$ of −0.001 ‰ (blue diamond) which is similar to the values of seawater in the ice-free world. Measurements of modern seawater (Luz and Barkan, 2010) are shown with the open diamond and error bars (2σ). Black solid lines and tick marks represent hydrothermal fluids at different water-rock ratios as shown in the right corner. C – The low $\Delta'^{17}O$ values measured in quartz samples can be partially explained by crystal growth at different temperatures without compete re-equilibration with the fluid. A mixture of low-T (25-150 °C) and high-T quartz (400 °C) forms an array of compositions that is concave up in these coordinates. A composition with 10 % of low-T quartz is shown. The ranges of $\delta^{18}O$ values measured by SIMS are shown with pink vertical bands. The $\delta^{18}O$ values measured in the healed cracks (CL-dark) from the Hole 504B quartz crystal are consistent with the low temperature of formation (~150 °C) in equilibrium with seawater-derived fluids. D – The CL-image of the 1 mm-long quartz crystal from the Hole 504B (sample 83-90R 71-72; see Table 2) which shows that dissolution, re-precipitation, and healing of cracks occurred at different temperatures as manifested by different. The $\delta^{18}O$ values measured by SIMS in CL-bright and CL-dark (healed cracks) parts of the crystal are shown.

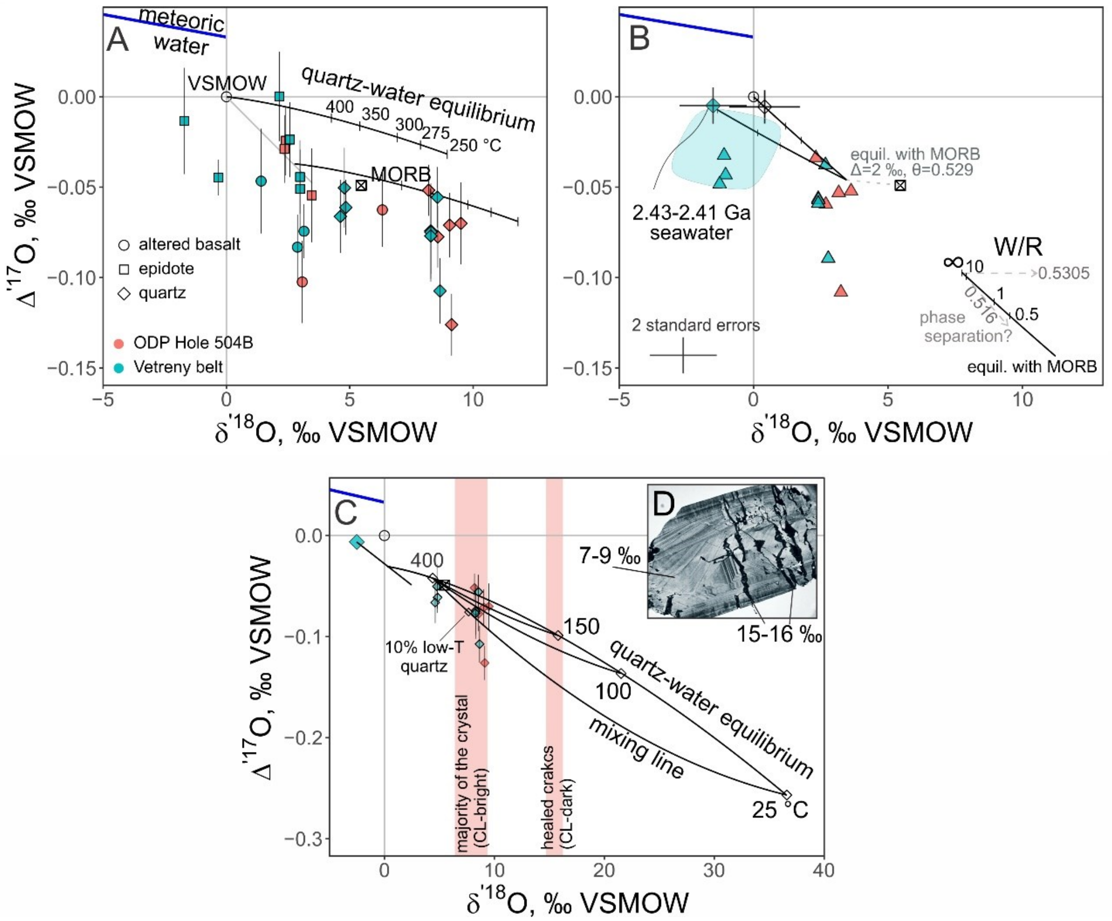

6.0 Discussion

6.1 δ¹⁸O values of hydrothermal fluids

Good agreement between homogenization temperatures and quartz-epidote equilibrium temperature estimates (Fig. 4; Table 1), as well as the internal agreement of quartz-epidote estimates (Fig. 9), suggest these temperatures can be reliably used to calculate equilibrium fluids. Most of the computed equilibrium fluids from the Vetreny belt have δ^{18}O of 1 ± 2 ‰, which is not significantly different from the δ^{18}O value modern-day seawater-derived hydrothermal vent fluids (Shanks, 2001) that are slightly shifted due to the isotopic exchange during high temperature interaction with rocks (+0.5 to +2 ‰, Shanks, 2001). Thus, the lower δ^{18}O values in the range of equilibrium fluids are the closest to seawater due to minimal effect of interaction with rocks. We suggest that the Vetreny belt rocks were altered at water-rock ratios similar or higher than modern-day submarine basalts, and thus, experienced the same or smaller amount of isotopic shift. Most of the analyzed rocks from the Vetreny belt were collected within pillow structures and hyaloclastites that contained large volume of voids, and that became filled in with quartz, epidote, amphibole, and other minerals bearing evidence for direct contact with fluids (Fig. 2B). The high hydrologic permeability of pillow basalts and hyaloclastites with void spaces and fractures (10^{-13}-10^{-11} m^2 measured in the Hole 504B; Alt et al., 1996) promotes flow of seawater along them resulting in alteration at water-rock ratios with minimized isotopic shift (DePaolo, 2006). In Figure 10 we show the effect of isotopic shift for hydrogen and triple oxygen isotope systems at variable water-rock ratios as calculated using the static mass-balance approach (Taylor, 1977). Using these calculations, we estimate that in modern hydrothermal systems the fluids experienced water-rock ratios between about 0.5 and 5. At the water-rock ratio of 5, the $\delta^{18}O$ of fluid is shifted only 0.3 ‰, which would be very close to the starting composition of seawater. The lowest computed $\delta^{18}O$ value at the Vetreny belt is −1.4 ± 0.7 ‰, thus we can estimate the $\delta^{18}O$ value of 2.43-2.41 Ga seawater to be around −1.7 ± 1 ‰, similar to seawater of the ice-free world (Shackleton and Kenneth, 1975).

In agreement with the computed equilibrium fluids, the range of $\delta^{18}O$ values and mineral assemblages of altered komatiitic basalts and gabbros from the 2.43-2.41 Ga Vetreny belt are strikingly similar to the low $\delta^{18}O$ submarine basaltic rocks that were hydrothermally altered at temperature above 250°C (Fig. 6B). We attribute abundant low $\delta^{18}O$ values in the komatiitic basalts to pervasively high temperatures (300-400 °C) of alteration in the intracontinental rift. A steep geothermal gradient due to storage and eruption of hot (1400°C) high-magnesium melts (~150 °C hotter than modern MORBs) within the slow spreading continental rift would facilitate the high temperature of hydrothermal alteration. Presence of numerous subvolcanic mafic intrusions within the belt (see Fig. 1) support this suggestion.

6.2 The $\Delta^{17}O$ values of hydrothermally altered rocks

Mass–dependent fractionation of triple oxygen isotopes between minerals and water is controlled by the temperature of equilibrium and the identity of minerals which determines respective fractionation factors α:

$$\ln({}^{17/16}\alpha_{mineral-water}) = \theta \cdot \ln({}^{18/16}\alpha_{mineral-water}) \qquad (3),$$

where ${}^{17/16}\alpha$ and ${}^{18/16}\alpha$ are ratios of ${}^{17}O/{}^{16}O$ or ${}^{18}O/{}^{16}O$ in a mineral to that in water. The value of θ defines the slope of equilibrium fractionation in the $\delta'^{18}O$ – $\delta'^{17}O$ space, varying in nature from ~0.5 to 0.5305, increasing with temperature and depending on kinetic/equilibrium type of fractionation process (see Bao et al., 2016 for review). The equilibrium fractionation is such that minerals are higher in $\delta^{18}O$ and lower in $\Delta'^{17}O$ compared to water (e.g. Zheng, 1993; Sharp et al., 2016). At infinitely high temperatures the α values approach 1, and the θ approaches 0.5305 (Matsuhisa et al., 1978). As a first order observation, epidotes from Hole 504B and the Vetreny belt, which formed within a similar range of temperatures, overlap in their $\Delta'^{17}O$ values, suggesting the similarity of $\Delta'^{17}O$ of modern-day and the early Paleoproterozoic seawater-derived fluids (Fig. 9A). In this study we emphasize that especially useful comparison can be drawn using epidotes, because the $\alpha_{\text{epidote-water}}$ factor is very close to 1 at 300-390 °C ($1000\ln^{18/16}\alpha \approx 0$ ‰; Zheng, 1993). At these temperatures, the difference between $\Delta'^{17}O$ values of fluids and minerals approach zero (Hayles et al., 2018). Thus, the oxygen isotope values of epidotes can serve as a direct proxy for that of the fluid. This is reflected in general agreement between $\delta'^{18}O$ values of computed fluids and measured epidotes (see Fig. 10). Epidotes both from Hole 504B and the Vetreny belt plot between modern seawater and the mantle (Fig. 9), which suggests that they likely formed in equilibrium with seawater-derived fluids with initial $\Delta'^{17}O$ value close to 0 ‰. Hydrothermal modification of seawater produces positive shift in $\delta^{18}O$ and negative shift in $\Delta'^{17}O$ values compared to pristine seawater. Two epidotes from the Vetreny belt plot in the region with $\delta^{18}O$ slightly lower than VSMOW (Fig. 9A) could be reflective of smaller degree of modification of original seawater with $\delta'^{18}O = -1.7$ ‰ and $\Delta'^{17}O$ of about -0.001 ‰. The altered komatiitic basalts that are composed amphibole, chlorite, quartz, epidote, and other minerals, have $\Delta'^{17}O$ lower than that of epidotes perhaps due to larger fractionation between the constituent minerals (especially quartz) and water compared to pure epidote.

Triple oxygen isotope fractionation between water and quartz is much larger compared to epidotes and it has been recently calibrated: $^{18/16}\alpha_{\text{quartz-water}} = 1.006\text{-}1.007$ and $\theta = 0.526\text{-}0.527$ at 300-390 °C (see Eq. 1; Cao and Liu, 2011; Sharp et al., 2016; Wostbrock et al., 2018). Thus, quartz in equilibrium with pristine seawater must have $\Delta'^{17}O$ between -0.030 and -0.020 ‰ relative to the reference line with slope 0.5305. However, the majority of $\Delta'^{17}O$ values of analyzed quartz from the Vetreny belt and Hole 504B are too low to be in equilibrium with seawater at any temperature (Fig. 9A). Two samples of quartz can be explained by equilibrium with shifted seawater at low water-rock ratios (Fig. 9B). We suggest two possibilities that can explain this observation: i) the isotopic shift in equilibrium fluids was caused by phase separation in addition to water-rock interaction; ii) analyzed samples represents a mixture of high- and low-temperature quartz; iii) the triple oxygen isotope fractionation that was originally calibrated using low temperature equilibrium, between 4 and 100 °C (Sharp et al., 2016; Wostbrock et al., 2018), could not be accurately applied to higher temperatures.

Figure 10 (next page). The expected isotopic shift in $\delta'^{18}O$ (A), $\Delta'^{17}O$ (B) and δD (C) in hydrothermal fluids in a closed system plotted at variable mass water-rock ratios with initial composition of fluids as shown with curves: modern seawater, 2.43-2.41 Ga seawater and meteoric water with $\delta^{18}O = -15$ ‰. The grey shaded region around the solid black line represents glacial-interglacial variation for each isotopic parameter. The composition of the 2.43-2.41 Ga seawater is approximated by the ice-free world seawater (Shackleton and Kennet, 1975; Lécuyer et al., 1998; Sengupta and Pack, 2018). The isotopic shift in the fluid is computed for each isotope using mass balance approach from Taylor (1977): $(x_{water}c_{water} + (1-x_{water})c_{rock})\delta_{fluid} = x_{water}c_{water}\delta_{water} + (1-x_{water})c_{rock}(\delta_{rock} - 1000\ln\alpha_{rock\text{-}water})$, where x_{water} is the mass fraction of initial water, c is concentration of either hydrogen or oxygen, δ is the isotopic composition of shifted fluid, initial water and rock (MORB). The water/rock ratio (W/R) is expressed through $x_{water}/(1-x_{water})$. The fluid in equilibrium with MORB is computed based on the values $1000\ln^{D/H}\alpha_{\text{rock-water}}$, $1000\ln^{18/16}\alpha_{\text{rock-water}}$ and $\theta_{\text{rock-water}}$ of −30 ‰, +2 ‰ and 0.529, respectively. The $\delta^{18}O$ and δD values in modern hydrothermal fluids are shown with pink dashed lines (Shanks et al., 2001), indicating that water-rock ratios at submarine hydrothermal systems vary between 0.5 and 5 (green shaded area at the bottom plot). Based on high permeability of the studied rocks, we suggest that the Vetreny belt might represent hydrothermal system that operated at comparable or higher water-rock ratios. The lowest $\delta'^{18}O$ values of equilibrium fluids and epidotes likely represent seawater values with minimal isotopic shift close to the ice-free world $\delta^{18}O$ value of around −1.5 ‰ (Shackleton and Kennet, 1975). The $\Delta'^{17}O$ values of equilibrium fluids computed from quartz-water calibration (Sharp et al., 2016) are too low to be explained by shifted fluids as discussed in Discussion 6.2. Due to small fractionation, the $\Delta'^{17}O$ of epidotes may be used as a direct proxy for the $\Delta'^{17}O$ in equilibrium fluids. The highest $\Delta'^{17}O$ value of epidote should be the closest to pristine seawater, thus, indicating that the 2.43-2.41 Ga seawater had $\Delta'^{17}O$ very close to that of modern seawater. Similarly, the highest δD values of computed equilibrium fluids are very similar to the δD values of modern seawater.

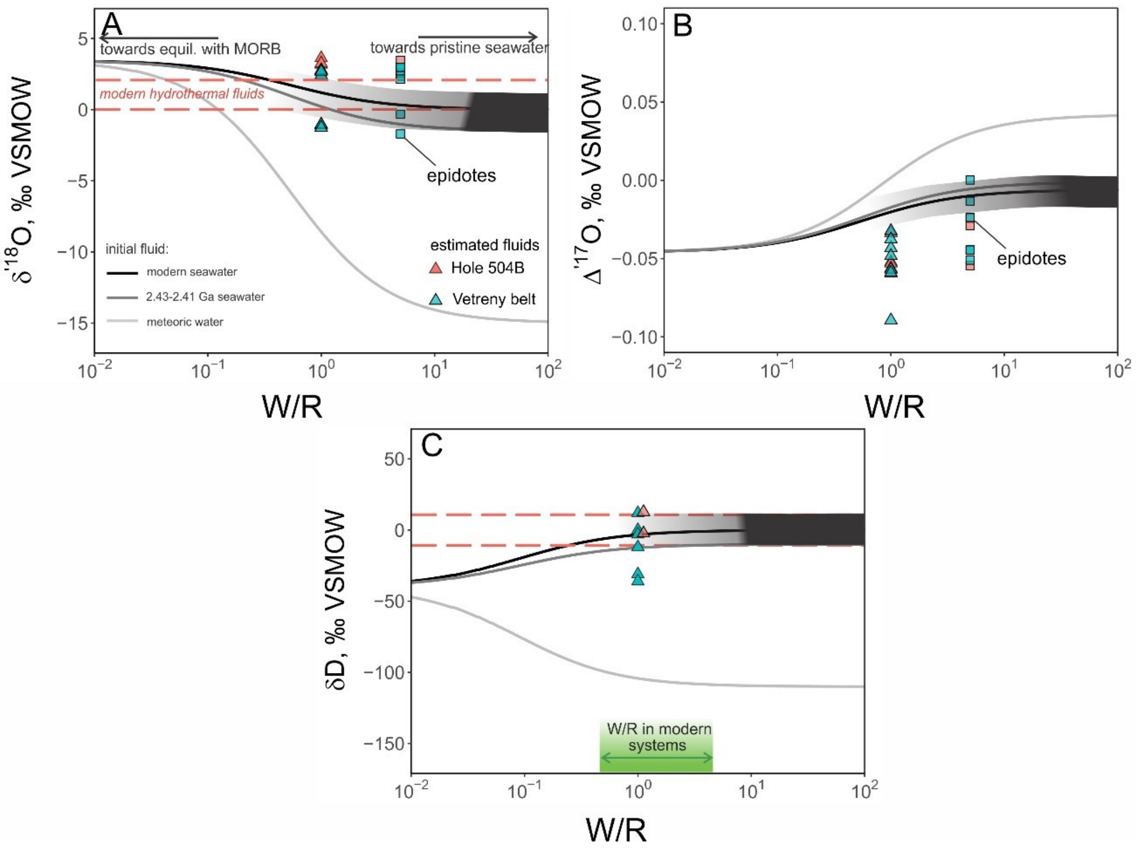

Even though high-temperature boiling and phase separation have not been studied for triple oxygen isotopes, we suggest that together with water-rock interaction these process might have contributed to the negative $\Delta'^{17}O$ shift in hydrothermal fluids due to the slope of vapor-brine fractionation is smaller than the reference line 0.5305 (see Fig. 9B). We propose this to be a possible mechanism because we observe that fluid inclusions trapped in quartz consist of brine and vapor (Fig. 5) recording phase separation of the hydrothermal fluid. The maximum expected equilibrium fractionation of $\delta^{18}O$ between fluid and vapor phase is ~2 ‰ (Shmulovich et al., 1999). The expected $\Delta'^{17}O$ shift could be as low as −0.03 ‰, if separation of brine from vapor induces fractionation with very shallow slope (~0.516) in the $\delta'^{17}O$ -$\delta'^{18}O$ space (see Fig. 9B).

Alternatively, systematically low $\Delta'^{17}O$ values could be attained by quartz that grew at different temperatures without complete re-equilibration with the fluid. Unlike epidote (Bird and Spieler, 2004), quartz is stable over a wide range of temperature and can grow from high- and low-temperature (below 100 °C; e.g., Wostbrock et al., 2018) hydrothermal fluids attaining very low $\Delta'^{17}O$ values, reaching −0.25 ‰ in equilibrium with seawater at 25 °C (Fig. 9C). Mixing high-temperature and low-temperature quartz creates an array that is concave up in $\delta'^{18}O$ – $\Delta'^{17}O$ space, thus yielding $\Delta'^{17}O$ values lower than equilibrium curves (Fig. 9C). This process can be exemplified by the cathodoluminescence (CL) image of one of the quartz samples from the Hole 504B, showing a complex history of growth involving dissolution and re-precipitation (Fig. 9D). Since CL-brightness is controlled by Ti concentration in quartz with the partitioning being strongly dependent on temperature (Wark and Watson, 2006), dissolution and re-precipitation likely occurred at different temperatures as manifested by the CL-bright crystal with CL-dark healed cracks and outermost zones (Fig. 9D). Assuming that the quartz grew from the same shifted seawater, a combination of quartz that formed at 350-400 °C with about 10 - 40 % of low-temperature quartz (25 - 150 °C) would account for most of the low $\Delta'^{17}O$ values. Quartz with minimal amount of low-temperature overgrowth would then have the lowest $\delta^{18}O$ and highest $\Delta'^{17}O$ values yielding the most accurate equilibrium temperatures and fluids. Similar results could be obtained with respect to the low $\Delta'^{17}O$ values by changing the composition of equilibrium fluids or/and including multiple sets of high-temperature and low-temperature overgrowths.

In order to gain a better insight, we conducted a preliminary *in situ* analysis by secondary-ion mass spectrometry (SIMS) of quartz from the Hole 504B and Vetreny belt which showed that most crystals have $\delta^{18}O$ = 7-9 ‰, agreeing well with our laser fluorination measurements. The CL-dark healed cracks in the quartz crystal from Hole 504B (Fig. 9D) have $\delta^{18}O$ of 15-16 ‰ indicating lower equilibrium temperature (~150 °C) supporting our suggestion that at least some of the low $\Delta'^{17}O$ values in quartz can be a result of mixing between high- and low-temperature quartz.

Most importantly, the similarity between the values of ancient and recent submarine hydrothermally altered rocks, especially in epidotes, is a convincing evidence that the 2.43-2.31 Ga seawater had $\Delta'^{17}O$ close to that of modern seawater. The highest $\Delta'^{17}O$ and the lowest $\delta'^{18}O$ values of epidotes are likely the most reflective of alteration by seawater at high-water ratios (Fig. 10). We suggest that direct measurements of $\Delta'^{17}O$ values in hydrothermal fluids could be useful, providing insights in the subsurface processes at hydrothermal systems, and validating the application of quartz-water calibration.

6.3 Recognizing primary δD values

Hydrogen isotopes in hydrous minerals are much more susceptible to post-depositional alteration than oxygen isotopes (see Kyser and Kerrich, 1991). Thus, not surprisingly, the δD values in bulk altered komatiitic basalts and gabbros display large scatter (between −210 and −50 ‰) compared to the restricted range of $\delta^{18}O$ values. Meanwhile, most of the coarse crystals of epidotes have much smaller range of δD values (between −56 and −8 ‰; Fig. 6B). We attribute this scatter and occurrence of very low δD values in bulk samples to secondary exchange of hydrogen in chlorites and other water-rich phyllosilicates at low temperature which causes large negative shifts in δD (Kyser and Kerrich, 1991; Wenner and Taylor, 1974). Chlorite contains up to 13 wt. % H_2O and thus, contributes to the δD value of a whole rock in much larger proportion compared to other less hydrous minerals. This is especially noticeable by the negative correlation between δD and H_2O in whole rock samples (Fig. 7). The small grain size (<10 μm) and large surface area of chlorite in bulk samples (see Fig. 3) dramatically enhances secondary hydrogen isotope exchange at low temperatures, which could have occurred at any point between 2.43-2.41 Ga and now (Fig. 7).

We attempted to reconstruct the δD of pure chlorite assuming it is responsible for the low δD values in our samples. These rocks contain at least 8 wt. % chlorite (see Fig. 3 and XRD data; Table S2) accounting for ~1 wt. % H_2O in the whole rock. Since there is about −100 ‰ fractionation at low temperature (< 100 °C) between water and phyllosilicates like serpentine, kaolinite, and chlorite (Taylor and Wenner, 1974; Kyser and Kerrich, 1991), we hypothesize that hydrating water had to have δD value between −80 and −110 ‰ to produce values between −180 and −210 ‰ in the whole rock (Fig. 7). This is in good agreement with most of the low δD values ranging between 1 and 4 wt. % water and chlorite content between 10 and 25 wt. %. While modern day local meteoric water with the range of values between –70 and –100 ‰ (Bowen, 2010) can explain most of the low δD values, we should mention the possibility of hydrogen isotope exchange between chlorite and meteoric water at any point after the original hydrothermal alteration including the cold climate of subsequent Paleoproterozoic snowball Earth episodes.

In this work we are able to rely on large crystals of epidotes with 1.7-2.0 wt. % water and consider them as primary recorders of hydrogen isotopic composition of seawater. Any alteration or addition of chlorite can be recognized by elevated H_2O content. For example, one epidote yields δD of – 119 ‰ and contains a slightly elevated amount of water (2.1 wt. %) which is the upper limit of the accepted range (Fig. 7B), and thus is considered to be an outlier that was either altered or contains inclusions of chlorite. Epidotes with ≤2.0 wt. % water are constrained even a narrow range of δD values, between −32 and −8 ‰ (see Fig. 7A). Alteration of the hydrogen isotope signal in hydrothermally altered rocks minimally affects the $\delta^{18}O$ and $\Delta'^{17}O$ values, which makes triple oxygen isotope analysis a powerful tool for back tracking the $\delta^{18}O$ of original water involved in hydrothermal alteration (Fig. 7C).

6.4 The δD values of hydrothermally altered rocks and fluids

Reported values of δD in epidotes from modern ocean floor (e.g. Stakes and O'Neil, 1982), ophiolites (Heaton and Sheppard, 1977; Harper et al., 1988; Fonneland-Jorgensen et al., 2005), as well as epidotes from Hole 504B measured here (Table 1) have very similar ranges of values, between −40 and +5 ‰. These overlap with the range of δD measured in well-preserved epidotes from the Vetreny belt, between −51 and −8 ‰ (Fig. 6C). The computed δD values of hydrothermal fluids range between −36 and +26 ‰ which is not distinguishable from the modern seawater with δD = 0 ± 20 ‰, and overlaps with computed δD values for the Hole 504B samples (see Table 1). The choice of fractionation factor (Graham and Sheppard, 1980; Chacko et al., 1999) creates a discrepancy of about ~10-20 ‰ (see Fig. 6); we favor the fractionation factor of Graham and Sheppard (1980) because it accounts for the salinity of equilibrium fluids. The range of computed δD values is then between −36 and +12 ‰. The four epidotes with water content ≤ 2 wt. % have the highest δD values (see Fig. 6), constraining the equilibrium fluids to the range of δD values between −12 and +12 ‰ (Table 1). These values should be very close to that of pristine seawater as hydrogen is contained in minute amounts in igneous rocks. As indicated by the high salinity of fluid inclusions, phase separation of seawater-derived hydrothermal fluid took place during the eruption of the komatiitic basalts, potentially fractionating hydrogen isotopes. However, fractionation of hydrogen isotopes between vapor and brine at high-temperatures (above 200 °C) is only a few ‰

(Horita and Wesolowski, 1994; Shmulovich et al., 1999; Shanks, 2001). The range of computed δD values limits significant contribution of meteoric water involved in the alteration of Vetreny belt rocks, because meteoric water has distinctly low δD (as well as $\delta^{18}O$) values (see Fig. 6B). We thus conclude that the δD value of the early Paleoproterozoic seawater was very close to that that of modern seawater within the range 0 ± 20 ‰.

6.5 The $\delta^{18}O$, $\Delta^{17}O$ and δD of seawater through time

Our multi-isotope study indicates that $\delta^{18}O$, $\Delta'^{17}O$ and δD values of the early Paleoproterozoic seawater were close to zero. The results are corroborated by previous $\delta^{18}O$ studies (Fig. 11) of bulk rock samples from the ~3.8 Ga Isua belt, Greenland (Furnes et al., 2007) and the 2 Ga Purtuniq ophiolite, Canada (Holmden and Muehlenbachs, 1994). The more detailed oxygen isotope investigation involving mineral pairs and fluid inclusion analyses of the 2.43 Ga submarine Ongeluk volcanics from South Africa (Gutzmer et al., 2001; Gutzmer et al. 2003) also indicate that seawater had the $\delta^{18}O$ value of 0 ± 2 ‰.

From mass-balance considerations, the oxygen isotopic composition of seawater on the time scales of tens of million years is controlled by inputs from hydrothermal alteration at mid-ocean ridges and continental weathering, and to a lesser extent by submarine weathering (Holland, 1984; Muehlenbachs, 1998). Faster than modern spreading rates would not significantly affect the $\delta^{18}O$ of seawater, while slower rates would lead to negative $\delta^{18}O$ and positive $\Delta'^{17}O$ values (Holland, 1984; Sengupta and Pack, 2018). Similarly, an increase in input of ^{18}O from continental weathering throughout geologic time, for example, due to growth of continental crust, its rapid emergence at the Archean-Proterozoic boundary (Taylor and McLennan, 1985; Bindeman et al., 2016; Bindeman et al., 2018), would cause negative shifts in the $\delta^{18}O$ and positive shifts $\Delta'^{17}O$ of seawater (Muehlenbachs, 1998; Sengupta and Pack, 2018). Our results suggest that the constancy of $\delta^{18}O$ and $\Delta'^{17}O$ of seawater implies that the Paleoproterozoic plate tectonics, particularly spreading at mid-ocean ridges and continental weathering, operated in a similar way as it does today.

Figure 11 (next page). A – The secular trend of $\delta^{18}O$ values in seawater as recorded by equilibrium fluids computed from submarine hydrothermally altered rocks (diamonds and vertical bars) and carbonates (grey circles). The $\delta^{18}O$ values of equilibrium fluids are from ophiolites: Troodos (Heaton and Sheppard, 1977), Semail (Gregory and Taylor, 1981), Josephine (Alexander et al., 1993), Erquy succession (Lécuyer et al., 1996), Solund-Stavfjord (Fonneland-Jorgensen et al., 2005), Betts Cove (Turchyn et al., 2013) and Bou Azzer (Hodel et al., 2018). The more recent seawater is recorded by dredged and drilled submarine hydrothermally altered rocks from modern seafloor (Alt et al., 1986; Alt et al., 1995; Stakes and O'Neil, 1982 and this study). The green bars indicate rough estimates of $\delta^{18}O$ of seawater based on patterns of distribution of $\delta^{18}O$ values in sections of ancient oceanic crust: 2.0 Ga Pirtuniq ophiolite (Holmden and Muehlenbachs, 1993) and 3.8 Ga Isua belt (Furnes et al., 2007). The Vetreny belt (purple diamonds), almost contemporaneous with the Ongeluk volcanics (Gutzmer et al., 2001), represents one of the oldest records of preserved isotopic equilibrium with seawater. The lowest $\delta^{18}O$ values of equilibrium fluids suggest that the value of seawater stayed between -1 and 0 ‰ for the most of the Earth's history, while the carbonate record shows the secular increase in the $\delta^{18}O$ value of seawater over the course of geologic time (Prokoph et al., 2008). B – The secular trend of δD of seawater as recorded by epidotes, chlorites and antigorites formed in submarine hydrothermally altered rocks. The evolution of seawater δD values is after Pope et al., (2012) with curves for epidote, chlorite and antigorite going parallel to that with the offset based on the δD values in the recent submarine rocks. The Vetreny belt epidotes have the δD values very close to modern submarine epidotes, likely reflecting the δD value of ~0 ‰ in the 2.43-2.41 Ga. Since antigorites and chlorites are susceptible to secondary hydrogen isotope exchange at low temperatures (Kyser and Kerrich, 1991), epidotes represent the best available record of δD evolution of seawater. The compilation of antigorites is adopted from Pope et al. (2012) and references therein. Phanerozoic submarine chlorites and epidotes are from the same references as for the $\delta^{18}O$ values. C – Generalized evolution of atmospheric oxygen in equivalent of present atmospheric level (PAL), relative change in hydrogen escape rates and $\delta^{18}O$ values of shales with supercontinent assemblies and episodes of global glaciations imposed (after Zanhle et al., 2013; Lyons et al., 2014; Bindeman et al., 2016).

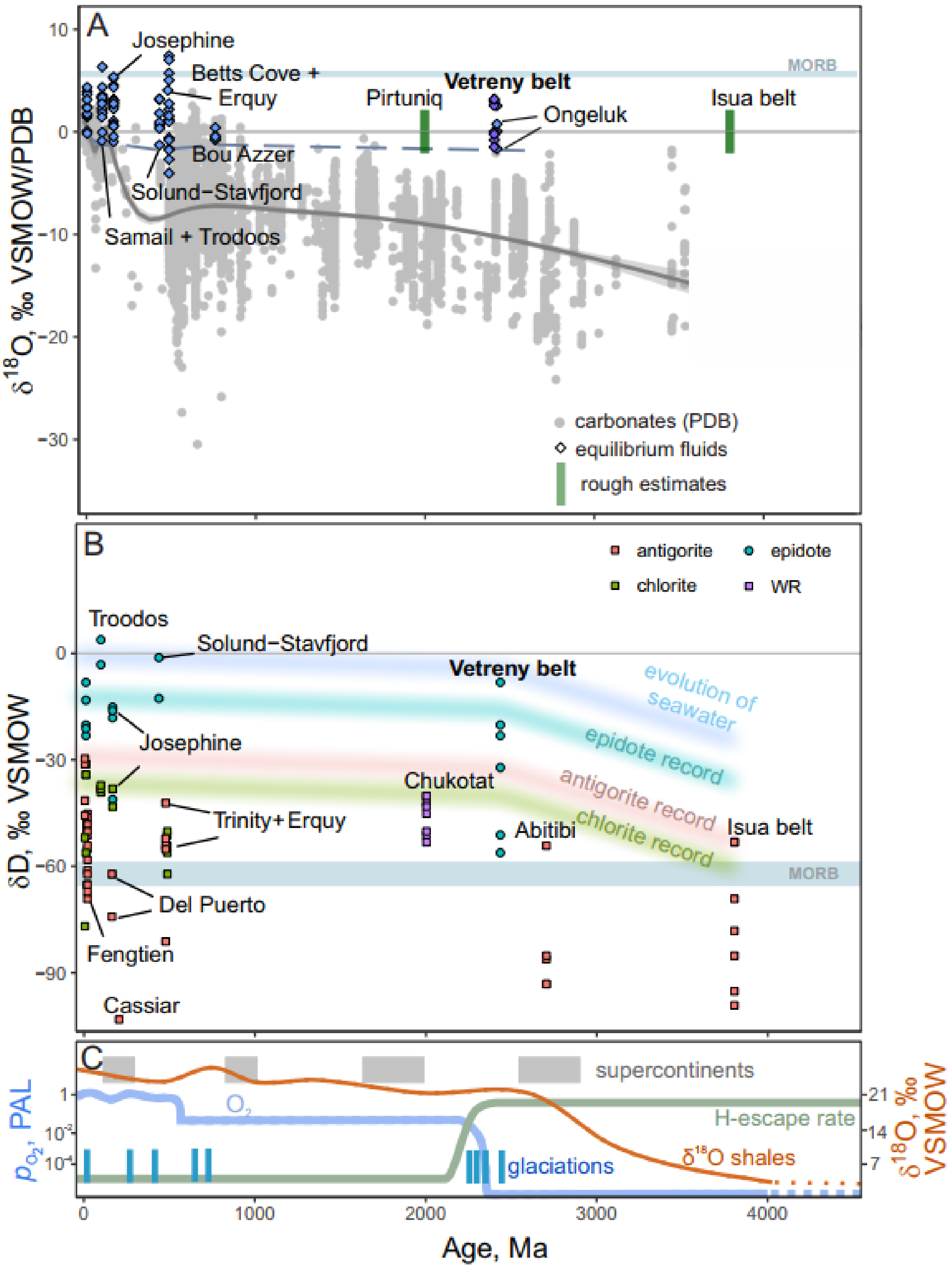
A
Josephine
Betts Cove +
Erquy
Vetreny belt
Pirtuniq
Ongeluk
Isua belt
MORB
Bou Azzer
Solund−Stavfjord
Samail + Trodoos
carbonates (PDB)
equilibrium fluids
rough estimates
δ18O, ‰ VSMOW/PDB
10
0
−10
−20
−30
B
antigorite
epidote
chlorite
WR
Troodos
Solund−Stavfjord
Vetreny belt
evolution of seawater
epidote record
antigorite record
chlorite record
Josephine
Chukotat
Trinity+Erquy
Abitibi
Isua belt
MORB
Del Puerto
Fengtien
Cassiar
δD, ‰ VSMOW
0
−30
−60
−90
C
supercontinents
O2
H-escape rate
glaciations
δ18O shales
pO2, PAL
1
10−2
10−4
δ18O, ‰ VSMOW
21
14
7
0
1000
2000
3000
4000
Age, Ma

These long-term trends may carry short-term (0.01-0.1 Ma) Milankovich-scale variations. The $\delta^{18}O$ value of 0 ± 1 ‰ of seawater is recorded by Pleistocene marine carbonates reflecting variations in the ocean temperature, and amount of water locked in continental glacial ice (Imbrie et al., 1984; Schrag et al., 1996). The supposedly large amount of continental glacial ice stored on Earth's surface during snowball Earth episodes would lead to 2-3 ‰ higher in $\delta^{18}O$ oceans; this effect would be counter-balanced by the opposite isotopic effect of sea-ice formation, together not contributing to a significant shift in the $\delta^{18}O$ of seawater (see discussion in Bindeman and Lee, 2018). Our estimated $\delta^{18}O$ and $\Delta'^{17}O$ values of 2.43-2.41 Ga seawater are close to the estimated seawater composition during warm climate of the ice-free Cenozoic (Shackleton and Kennett, 1975; Sengupta and Pack, 2018). The evidence from the Vetreny belt validates the assumptions made previously that low $\delta^{18}O$ meteoric water (as low as -35 ‰) was formed by evaporation of seawater with $\delta^{18}O \approx 0$ ‰. The record of such low $\delta^{18}O$ meteoric water is provided by the coeval ultralow $\delta^{18}O$ Belomorian belt rocks (Bindeman et al., 2014; Herwartz et al., 2016; Zakharov et al., 2017; Bindeman and Lee, 2018).

Our measurements of well-preserved epidotes from the 2.43-2.41 Ga Vetreny belt provide the oldest robust evidence for $\delta D \approx 0$ ‰ in seawater (see Fig. 11B). Previous estimates of the hydrogen isotope composition of Precambrian seawater were based on samples containing easily exchangeable water. Such studies used bulk rock δD values in the 2.0 Ga chlorite-bearing basalts constraining the δD value of seawater at 0 ‰ (Lécuyer et al., 1996), and serpentines from the 3.8 Ga Isua belt suggesting that the early Archean seawater was about 25 ‰ lighter in δD (Pope et al., 2012). As discussed in Section 6.4, water-rich phyllosilicates such as chlorite and serpentine are poor recorders of original equilibrium fluids due to susceptibility to secondary isotope exchange with ambient water at low temperature. Our results suggest that the long-term evolution of the hydrogen isotopic composition of seawater is controlled primarily by hydrothermal alteration at mid-ocean ridges, subduction, and water outgassing at subduction zones. The variability in the rates of these processes might contribute about ± 20 ‰ to the δD of seawater (Lécuyer et al., 1998). Significant decrease of ocean volume and accompanied increase in the seawater δD due to net mantle regassing (Kurokawa et al., 2018) must have occurred by 2.43-2.41 Ga as indicated by our results. Additionally, in the Archean and early

Paleoproterozoic oxygen-poor atmosphere, the hydrosphere was likely subjected to intense hydrogen escape, which is one of the proposed mechanisms that caused atmospheric oxygenation of our planet (Zahnle et al., 2013). Through water photolysis, ^{1}H escape from the planet is greater than deuterium, causing the δD value of seawater become progressively higher with time (Lécuyer et al., 1998; Pope et al., 2012). Our results are most consistent with seawater having δD values of ~0 ± 20‰ at 2.43-2.41 Ga, which suggests that most of the hydrogen loss occurred and the Earth's by the time the Vetreny belt formed (Lécuyer et al., 1998; Zahnle et al., 2013;). The isotopic composition of paleo-atmospheric Xe trapped in the quartz veins studied here is also consistent with most of hydrogen escape occurring prior to 2.43 Ga (Avice et al., 2018).

The sedimentary record, however, suggests different conclusions: ancient carbonates and cherts show a strong steady increase in δ^{18}O corresponding to about 13 ‰ from 3.5 to 0 Ga (Fig. 11A). This observation implies a significantly lower δ^{18}O value for seawater in the Precambrian ocean than the δ^{18}O recorded by ancient hydrothermally altered rocks (see Jaffrés et al., 2007 for details). From a mass-balance perspective, these shifts are possible by adjusting sinks and sources of ^{18}O in the ocean. Several models have been proposed to address possible long-term shifts in the sinks and sources of ^{18}O over the geological time scale relating them to the cycling of water through subduction zones, mantle degassing, increasing ocean depth and development of pelagic sediments at mid-ocean ridges (Wallmann, 2001; Wallmann, 2004; Kasting et al., 2006; Korenaga et al. 2017). In such case, the high temperature hydrothermal systems are decoupled from the δ^{18}O of seawater and could not be used to constrain the composition of ancient seawater. However, this would be inconsistent with results from elsewhere, for example, from low-δ^{18}O hydrothermal systems charged with meteoric water (e.g. Taylor, 1977; Pope et al., 2014). The secular trend of δ^{18}O in seawater could also be explained by much higher temperature of the Precambrian ocean (80-90 °C; e.g. Robert and Chaussidon, 2006) which is often portrayed as implausible for sustaining life. The main argument contradicting the sedimentary record has been the susceptibility of carbonates and cherts to recrystallization during diagenesis in open system, which would alter the δ^{18}O (and δD; Hren et al., 2009) to lower values. Today the argument is strengthened by a growing body of clumped isotope studies that can resolve the effect of diagenetic recrystallization.

Well preserved carbonates suggest that the temperature of ocean did not experience significant variations and the $\delta^{18}O$ of seawater stayed within ± 2‰ at least in the early Phanerozoic (Eiler, 2011; Cummins et al., 2014) potentially bridging the gap between the sedimentary record and hydrothermally altered rocks.

7.0 Conclusions

1. From the stratigraphic context and geochemical data presented here, the 2.43-2.41 Ga Vetreny belt rocks likely recorded interaction with contemporaneous seawater. Based on average homogenization temperatures of saline fluid inclusions and oxygen isotope thermometry, komatiitic basalts were hydrothermally altered at temperatures ranging from 300 to 390 °C.

2. Our data are the most consistent with the $\delta^{18}O$ value of the 2.43-2.41 Ga seawater being close to the $\delta^{18}O$ of seawater in the pre-Pleistocene ice-free world. This result is supported by similar studies of Paleoproterozoic and Archean submarine hydrothermally altered rocks.

3. The $\Delta'^{17}O$ values measured in quartz and epidotes from the Miocene (6-7 Ma) hydrothermally altered oceanic crust as sampled by ODP Hole 504B are very similar to those measured from the Vetreny belt indicating that the seawater had $\Delta'^{17}O$ value similar to modern. Due to small fractionation at 300-390 °C, epidotes are a good direct proxy for the $\Delta'^{17}O$ of equilibrium fluids. Quartz has $\Delta'^{17}O$ values lower than expected from equilibrium fractionation (Sharp et al., 2016; Hayles et al., 2018). This could be explained by presence of low-temperature overgrowths and healed cracks in quartz which produces mixed compositions with low $\Delta'^{17}O$ values (see Fig. 9C).

4. The δD values of large and unaltered epidotes presented here provide one of the earliest evidences of seawater with δD of 0 ± 20 ‰, similar to the modern-day value of seawater. This indicates that if a significant increase in the δD of seawater occurred due to hydrogen escape and net mantle regassing (Kurokawa et al., 2018), it must have happened by 2.43-2.41 Ga.

5. Our study verifies the previously made assumptions about the plausibility of obtaining ultralow $\delta^{18}O$ meteoric waters through hydrological cycle involving evaporation of the early Paleoproterozoic seawater with near-zero $\delta^{18}O$, δD and $\Delta'^{17}O$

values (Bindeman et al., 2014; Herwartz et al., 2016; Zakharov et al., 2017; Bindeman and Lee, 2018).

8.0 Bridge

Chapter III investigates products of submarine hydrothermal alteration of the 2.43-2.41 Ga komatiitic basalts from the Vetreny belt, Russia using triple oxygen and hydrogen isotopes. The excellent preservation of the alteration textures, and the consistency between the microthermometry data and oxygen isotope thermometry estimates present a strong evidence for preservation of original isotope integrity by these rocks. Based on equilibrium isotope fractionation between quartz, epidote and water, the values of the early Paleoproterozoic seawater values are constrained to $\delta^{18}O = -1.7 \pm 1.1$ ‰, $\Delta^{17}O = -0.001 \pm 0.011$ ‰, and $\delta D = 0 \pm 20$ ‰. These are similar to the values of seawater during the Cenozoic, emphasizing that the balance between circulation of water at mid-ocean ridges and weathering controls the isotope composition of seawater over the long (over 10 Ma) timescales. These results are important for all subsequent chapters of this dissertation as they provide basis for studying the early Paleoproterozoic meteoric water cycle that originates from evaporation of seawater. In Chapter IV, I present the results of combined triple oxygen and strontium isotope investigation of the Vetreny belt rocks. The purpose of the study presented in Chapter IV is twofold to assess my previous estimate of the oxygen isotope composition of the 2.43-2.41 Ga seawater and to explore the effect of low marine sulfate on the Sr-isotope budget of Precambrian submarine fluids.

CHAPTER IV

THE EFFECT OF LOW SULFATE IN THE PRECAMBRIAN OCEANS ON SEAWATER-BASALT REACTION TRACED BY TRIPLE OXYGEN AND STRONTIUM ISOTOPES

This chapter is in preparation for publication with Ilya N. Bindeman, Ryoji Tanaka, Craig C. Lundstrom, Mark H. Reed and David A. Butterfield. Ryoji Tanaka and Craig Lundstrom assisted in generating isotopic data for this chapter and provided input in the interpretations of this study. Ilya N. Bindeman provided useful edits on the initial draft of this chapter. Mark H. Reed provided input on the interpretations of the results and helped with setting up the aqueous-mineral equilibrium calculations. David A. Butterfield contributed samples of the near-vent fluids and their geochemical data necessary for this study.

1.0 Introduction

Over geologic time scales exceeding 10 Ma, the composition of the Earth's atmosphere and seawater change in response to evolving biota, changing landscapes, and global volcanic activity. In previous chapters, my investigations focused on the high temperature isotope exchange between hydrothermal fluids and sea floor rocks and the implications for seawater O- and H- isotope composition over geologic time. However, one of the most prominent changes that affected the seawater composition is the rise of free oxygen, which had consequences for many biogeochemical element cycles in all of the Earth's systems. Its effect is subtle for seawater-basalt interaction at high temperature, a process that ubiquitously occurs at the mid-ocean ridges in the modern oceans and is responsible for alteration of 2-3 km of modern oceanic crust (Alt et al., 1996; Alt and Teagle, 2000). Oxygen or hydrogen isotopes alone cannot be used directly to detect oxidation state of dissolved chemical species, however combined with other isotope systems, a comprehensive approach could be developed for understanding the intertwined effects of basalt-seawater reaction and varying concentrations of redox sensitive species. As a step towards exploring this link, we present the results of triple oxygen and strontium isotope investigation of a reaction between basalt and sulfate-poor seawater that took place in the early Paleoproterozoic. The purposes of this study are to assess the previous estimate of seawater oxygen isotope value at 2.43-2.41 Ga (Zakharov and Bindeman, 2019) and to explore the effect of low seawater sulfate concentration on the composition of Precambrian submarine fluids and altered oceanic crust.

Chemical composition of seawater is controlled by the inputs from continental weathering, hydrothermal circulation of seawater and precipitation of oversaturated minerals from the seawater column. The rise of atmospheric pO_2 levels over geological time promoted an increase in oxidized marine species, particularly sulfate, which is intimately tied to the increasing oxidative capacity of continental weathering and thus, weathering of terrestrial sulfides (Holland, 1984; Farquhar and Wing, 2003; Kah et al., 2004; Halverson and Hurteng, 2007). Amongst redox-sensitive species, sulfur is abundantly present in oxidized form due to its high solubility and, thus, sulfate concentration could be used as an overall reflection of oxidation state of seawater solutes (Canfield, 1998). As the result of Earth's atmosphere oxygenation, modern day seawater contains 28 mM/kg sulfate, ~8 % of total dissolved load (Berner and Berner, 1996). The sulfate in modern seawater precipitates in anhydrite at temperatures above 130 °C, disturbing seawater-derived Ca, S and Sr in the upper section of seafloor. During the Precambrian, seawater sulfate concentrations were 3-4 orders magnitude lower than in modern, as estimated from evaporate deposits (Kah et al., 2004; Habicht et al., 2002; Canfield and Farquhar, 2009). Even though it is obvious that low sulfate seawater would result in anhydrite-free Precambrian submarine systems (e.g., Kump and Seyfried, 2005), the evidence of it has not been studied using actual submarine altered rocks. It is important to demonstrate the role of low sulfate in Precambrian hydrothermally altered rocks, since anhydrite oversaturation plays a pivotal role in elemental and isotopic budget of seawater, thus, it should be an important parameter in the budget of these elements in the altered oceanic crust and possibly in subduction zones. It is not completely understood how much anhydrite undergoes retrograde solubility at seafloor ambient temperatures away from mid-ocean ridges. However it is clear that anhydrite oversaturation exerts a significant effect on the seawater-basalt exchange budgets of Sr isotopes recorded by oceanic crust (Teagle et al., 1998; Bach et al., 2003; Antonelli et al., 2017) and in the sulfur budget of arc magmas (Tomkins and Evans, 2015).

In this study we focus on anhydrite as a sink for seawater-derived Sr in hydrothermal fluids. Being a common trace element in anhydrite, Sr is almost completely removed from seawater in the incipient stages of hydrothermal circulation at mid-ocean ridges. Consequently, the $^{87}Sr/^{86}Sr$ ratios measured in modern oceanic crust are dominated by values of unaltered mid-ocean ridge basalt with deviations towards seawater value in sections of high permeability (Alt et al., 1996; Fisher, 1998; Alt and Teagle, 2000; Harris et al., 2015). Thus, using Sr isotopes in ancient submarine rocks can give insights into the redox evolution of submarine fluids over the geologic time scales.

The reaction of oceanic crust with seawater has occurred since plate tectonics began to operate in a way similar to modern mid-ocean ridge spreading, i.e. at least since Archean (Laurent et al., 2014; Tang et al., 2016; Greber et al., 2017). Even though Archean and Paleoproterozoic greenstone belts and intracontinental rifts are not, strictly speaking, fragments of oceanic crust (Bickle et al., 1994), they contain evidence for interaction between ancient seawater and mafic volcanics. In this study, we use the hydrothermally altered section of komatiitic basalts of the Vetreny Belt, Russia that originated during voluminous subaqueous eruption of high-Mg lavas (several km thick) in a rift of the Karelia craton at around 2.43 – 2.41 Ga (see Chapter III). Unlike the marine sedimentary record, high-temperature alteration minerals that form within oceanic crust are poor indicators of seawater composition because hydrothermal concentrations are rock-buffered with exception of Na and Cl. Nevertheless, we can apply multiple isotope ratios, $\delta^{18}O$, $\Delta^{17}O$ and $^{87}Sr/^{86}Sr$, to restore the isotopic signature of seawater within the alteration silicate minerals of ancient submarine basalts. The $\delta^{18}O$ and $\Delta^{17}O$ measurements reported in this chapter and in Chapter III are used to trace the evolution of fluids in hydrothermal systems due to reaction between seawater and basalt, while the $^{87}Sr/^{86}Sr$ ratios measured in silicates are used to constrain the seawater-derived Sr input into the ancient oceanic crust. Even though, there is a great uncertainty in the $^{87}Sr/^{86}Sr$ ratio of Precambrian seawater (Shields and Veizer, 2002) owing to poor preservation of original isotope integrity by marine carbonates, this study has a potential to improve our understanding of isotope signals in the sedimentary record and the chemical balance seawater solutes before initiation of oxidative continental weathering.

Our approach takes into consideration the effect of isotope exchange between basalt and seawater using triple oxygen isotopes in epidotes, supported by previous measurements of D/H ratios (Zakharov and Bindeman, 2019), which helps to disentangle the effect of temperature and variable water-rock ratio, and to constrain seawater isotopic values. We specifically target epidote for a record of isotope composition because the mineral records hydrothermal circulation of fluids at high temperature (> 250°C) and forms veins that fill formerly empty spaces, thus reflecting high fluid to rock ratios. Epidote crystals are resistant to secondary alteration, contain little Rb, and have high Sr concentration, requiring minimal correction for initial $^{87}Sr/^{86}Sr$ ratios. In addition, small fractionation of oxygen isotopes between water and epidote provides a close estimate of the oxygen isotope ratio in the fluids. The rocks of the Vetreny Belt are well suited for this study because of their excellent preservation and evident alteration at large water/rock ratios owing to high permeability. We use modeling approach to predict isotopic shifts experienced by hydrothermal fluids in modern and ancient submarine systems by applying a dual porosity model (DePaolo, 2006). This model allows us to apply different physical parameters in the hydrothermal system for specified elements. To substantiate our investigations of the rock record, we apply mineral-aqueous equilibrium calculations to simulate seawater-basalt reactions using starting seawater compositions with abundant and low sulfate concentrations (i.e. modern *vs* Paleoproterozoic seawater). The calculations provide us an educated guess of what mineral assemblages are useful for isotopic measurements. We show in the study that equilibrium assemblage of epidote and quartz in absence of feldspar represent a limited range of the water-rock ratios supporting the connection between measured $^{87}Sr/^{86}Sr$ values and that of seawater.

2.0 Model set up

2.1 Dual porosity model at steady state

Fluids that enter the hydrothermal system initially have the isotopic composition of pristine seawater. Along the flow path they acquire isotopic ratios and chemical composition corresponding to aqueous fluids in equilibrium with basaltic rocks at the temperature at 250 to 400 °C. Among other chemical and isotopic changes, this process has a strong effect on the isotope ratios of oxygen, hydrogen, and strontium in hydrothermal fluids, since both elements are present in seawater and rocks with distinct

$\delta^{18}O$, $\Delta^{17}O$ and $^{87}Sr/^{86}Sr$ values. The equilibrium fractionation of oxygen isotopes at 250-350 °C between water and secondary assemblages with bulk basaltic composition defines the values of $\delta^{18}O$ and $\Delta^{17}O$ of fully exchanged fluids. The value +2.5 ‰ for $\delta^{18}O$ and -0.06 ‰ for $\Delta^{17}O$ are accepted here as the oxygen isotope ratios of fully exchanged water in equilibrium with mid-ocean ridge basalts (MORBs). Unlike oxygen isotopes, $^{87}Sr/^{86}Sr$ ratio does not fractionate between minerals and fluids; it evolves from high seawater-value (modern $^{87}Sr/^{86}Sr_{SW} = 0.7085$) towards lower ratios as more mantle-derived Sr ($^{87}Sr/^{86}Sr_{MORB} = 0.702$) is released through dissolution of basaltic plagioclase. As a result of this process, average submarine hydrothermal fluids are isotopically shifted and have $\delta^{18}O$ values between +0.5 and +2.0 ‰, whereas $^{87}Sr/^{86}Sr$ ratio is low, typically around 0.704-0.703 (e.g. Bach and Humphreys, 1999).

Previous one-dimensional fluid-rock interaction models (e.g. Lassey and Blattner, 1998; Bowman et al., 1994; Baumgartner and Valley, 2001) describe dependency of isotope shifts on the physical properties of reactive transport within porous flow. They provide useful insights into modes of isotopic shift (diffusion/advection dominated) in porous rocks and a fractured medium. In this paper, we undertake steady-state modeling of water-rock reaction in a dual porosity system (DePaolo, 2006) since we use measurements from filled fractures and veins, where both advective and diffusive transport occurs in different parts of the systems. The model is used to simulate simultaneous shifts of strontium, oxygen and hydrogen isotope values in hydrothermal fluids. In essence, this modeling approach allows us to implement physical constraints on isotope exchange and to assess the concentration of Sr in fluids relative to concentration of O and H, which results in different profiles of isotopic shifts. The principal equation must include diffusion, advection and reaction terms that contribute (dissolution) or consume (precipitation) chemical species:

$$\rho_f \frac{\partial \phi C_f}{\partial t} = \rho_f D \frac{\partial}{\partial x}\left(\frac{\partial \phi C_f}{\partial x}\right) - v \rho_f \frac{\partial \phi C_f}{\partial x} + \sum_i R_{di}\, C_{si} - \sum_j R_{pj}\, K_j C_f \qquad (1),$$

where C is concentration of element in the fluid and solid (subscript f and s respectively), ρ and ϕ denote density and porosity, D is ionic diffusivity, v is fluid velocity, K is distribution coefficient for solid/fluid. The terms R describe rates of dissolution (subscript d) and rates of precipitation (subscript p) of species i and j.

The equation can be re-written for a fractured medium, where fluid transport occurs via advection along fractures and diffusion in the low-porosity matrix. It can be assumed that dissolution and precipitation (i.e. recrystallization) occur at the same rate causing no net change in porosity. Combining dissolution and precipitation into one term yields recrystallization rate (denoted *R*) expressed in $g \cdot g^{-1} \cdot yr^{-1}$, i.e. grams of alteration material forming per grams of original rock in a year. As explained by DePaolo (2006), the steady-state assumption of the dual porosity model is a good starting point for demonstrating possible trajectories of combined isotope shifts and it is an easy calculation to implement. The application of such assumptions is also justified by the relative longevity of hydrothermal systems, on the order of 10^4 yr and an inability to make safe assumptions about how the isotopic ratio of fluids changed with time, when only the final product (hydrothermally altered rocks) can be analyzed. In the steady-state formulation of the model, the fluid isotopic ratios change with distance (*x* in meters). The rate of change of isotopic ratio in fracture fluid (r_f) with the distance is described as:

$$\frac{\mathrm{d}r_f(x)}{\mathrm{d}x} = \frac{8D\phi_m}{\phi_f v_f b d}\left[r_s - \alpha r_f(x)\right] \sum_{n_{odd}} \left(1 + n^2\pi^2 \frac{L^2}{b^2}\right)^{-1} \qquad (2),$$

where *D* is ionic diffusivity of a species (e.g. self-diffusion of H_2O, Sr^{2+}), ϕ is porosity in the matrix, v_f velocity of the fracture fluid, ϕ_f porosity of the fracture (always equals 1), *b* is fracture spacing and *d* is fracture width. The variable *L* defines the reactive length which derives from the relationship $(D\rho_{fluid}\phi C_{fluid}/R\rho_{rock}(1-\phi)C_{rock})^{1/2}$, where letters ρ, ϕ, C denote density, rock porosity and concertation of an element of interest. It represents the distance along which the pore fluid remains sensitive to the fluid in the fractures. It also means that a large *L* value results in a small isotopic shift along the direction of fracture fluid flow. Since different elements have different values of *L*, the rate of change with distance is expected to be different for different elements in hydrothermal systems. For example, the reactive length of hydrogen during reactive transport is much longer (~4 times larger than for oxygen) than for any other element due to of its abundance in water and near absence in rocks. Thus, the δD values of fluids do not experience significant change over a large range of distances compared to other elements.

2.2 Monte-Carlo simulation of the dual porosity model

The results of steady-state dual porosity model are highly dependent on the physical conditions represented by variables *R*, v_f, *d*, *D* and *b*. The variables such as length of fluid flow, reaction rates and fluid velocities are difficult to measure directly and perhaps should not be constrained by single values. The effect of variable fracture spacing (*b*) and recrystallization rates are discussed in the DePaolo (2006), Turchyn et al. (2013) and Brown et al. (2013). According to those studies, the average fracture spacing derived from the model varies within several meters (1-5 m), while the recrystallization rates vary on the order of 0.0001 yr^{-1} as constrained by monitoring of short-lived isotopes in active hydrohtermal systems (Kadko and Moore, 1988; Kadko et al., 2007). It is important to note, that the two variables R (recrystallization rate) and v_f (fluid flow rate) produce opposite effect on the result of isotope exchange between fluid and solid, yet both can vary in the large ranges. The ground water flow convects around intrusive bodies at rates anywhere between several meters a year to ~100 m/yr (Norton, 1978; Wood and Hewett, 1982; Hayba and Ingebritsen, 1997). Thus it is important to consider the possible outcomes produced by ranges of these values rather than picking one or several arbitrary ones. Here we perform Monte-Carlo simulation of the isotopic shift using ranges of values listed in Table 1. Critically, the values R range between 0.0001-0.0005 yr^{-1} and v_f between 10 and 100 m yr^{-1}. The isotopic shifts were simulated by calculating the $r(x)$ value 2000 times from Eq. 2 randomly picking variables within the specified ranges.

Table 1. Range of values used in the Monte Carlo simulation of dual porosity model

Variable	Minimum	Maximum	Units	Sources
b, fracture spacing	2	5	m	DePaolo, 2006
R, dissolution-precipitation rate	0.0005	0.0001	g g^{-1} $year^{-1}$	DePaolo, 2006; Kadko et al., 2007
v_f, fluid velocity	10	100	m yr^{-1}	Hayba and Ingebritsen, 1997
ϕ, matrix porosity	0.01	0.02	none	Becker, 1985

2.3 Aqueous-mineral equilibrium calculations

To understand the mineralogical and isotopic modification of altered oceanic crust of the Precambrian submarine systems, it is a sensible exercise to perform mineral-aqueous equilibrium simulation of a reaction between basalt and seawater with low sulfate content. The calculations are intended to replicate the equilibrium mineral assemblages and aqueous species of modern hydrothermal systems, and to apply them to the ancient submarine hydrothermal systems by using starting seawater with low sulfate. The Archean – early Paleoproterozoic submarine systems are simulated with the same set of conditions and steps as described below allowing for convenient comparison. The starting seawater compositions are listed in Table 2 and are taken from (Berner and Berner, 1996) and modified for the ancient seawater by lowering sulfate content by three orders of magnitude (Habicht et al., 2002) and increasing Mg and Ca content using the Phanerozoic maximum estimates that apply when sulfate content was also the lowest (Horita et al., 2002; Berner, 2004). Using the Phanerozoic estimates for the concentration of these elements is validated because seawater solute concentrations in the early Precambrian are not reconstructed as reliably as for the Phanerozoic owing to the absence of suitable record, however using these values allows us to make a realistic comparison of the effect of variable sulfate. In addition, investigations of Precambrian chemical sediments (Holland, 1984) suggest that, relative to modern seawater, the concentrations of major elements such as Mg, Na, K, Ca, Sr and Cl, but not sulfate, are expected to lie within the same orders of magnitude. It is worth noting that dissolved Si content of Precambrian seawater was likely higher than the modern day value due to biological silica uptake by radiolarians that modulates silica concentrations since early Cambrian time. Further research should address the possible effects of high silica content on the composition of high-temperature alteration mineral assemblages in the oceanic crust.

Table 2. Molar content of initial seawater used in the mineral-aqueous equilibrium calculations. Dashes indicate that the concentrations in ancient seawater are taken to match that of modern seawater.

Ion	Concentration in modern seawater (mM/kg)	in early Paleoproterozoic seawater
Cl^-	551	698*
SO_4^{2-}	28	$28\cdot10^{-5}$
HCO_3^-	2.3	-
HS^-	$3.0 \cdot10^{-6}$	-
H_4SiO_4	0.12	-
Al^{3+}	$3.0\cdot10^{-3}$	-
Ca^{2+}	10	40
Mg^{2+}	56	71
Fe^{2+}	$5.4\cdot10^{-3}$	-
K^+	10	-
Na^+	469	-
Sr^{2+}	0.15	-

* - chlorinity of seawater was adjusted for maintaining neutral charge balance

We perform seawater-basalt reaction with modern levels of sulfate as a point of reference using program CHIM-XPT (Reed et al., 2010) to simulate a set of titration experiments in which small amount of basalt is incrementally added to 1020 g (1L) of seawater and the solution is then allowed to achieve equilibrium concentrations of aqueous species and minerals. To model a realistic order of events, the simulations include following steps: 1) reaction of small amount of basalt (5 g) at 150 °C and 400 bar and removal of solid phases at the end; 2) reaction with another 5g of basalt at 350 °C and 500 bar and removal of solid phases at the end; 3) incremental titration of basalt until aqueous concentrations become dominated by equilibrium with basalt. At this stage, albite and microcline molar quantities exceed other minerals. This set up is intended to reproduce hydrothermal system in which seawater first heats up to ~150 °C with precipitation and removal of anhydrite and other oversaturated phases as they occupy empty spaces, vesicles and pores, yet with minimal participation of basaltic material. This regime is similar to the upper oceanic crust and off-axis alteration (Fisher, 1998; Alt et al., 1996). Next, fluid moves through hot wall rock, precipitating minerals at higher temperature and pressure (350 °C and 500 bar), leaving the minerals behind in permeable upper crust. After that fluid reacts with basalts at low water-rock ratio (W/R). The water-rock ratio in these calculations is used as a measure of titration progress; it is calculated from dividing the amount of initial seawater (1020 g) by the mass of titrated basalt. So that, for example, step 1 described above represents reaction between seawater and basalt at W/R between infinity (0 g basalt added) and 204 (5 g basalt titrated).

To keep track of Sr concentration, we specified a distribution coefficient between anhydrite and fluid (D_{Sr}) of 0.35 (Ichikuni and Musha, 1978). That is a minimum estimate from laboratory precipitation experiments; in natural systems anhydrite shows a wide range of D_{Sr} values and many have a significant Sr enrichment that corresponds to $Sr_{fluid}/Sr_{anhydite}$ close to 1 (Mills et al., 1998). Thus, $^{87}Sr/^{86}Sr$ ratio of hydrothermal fluids can be calculated from the molar concentration of equilibrium anhydrite and titrated amount of basalt assuming that it contains 300 ppm Sr (3.42 mmoles/g) and initial seawater has 13 ppm Sr (0.15 mmoles/g; see Table 2) :

$$^{86}Sr/^{87}Sr_{fluid} = ([Sr]_{SW}\,^{86}Sr/^{87}Sr_{SW} +$$
$$[Sr]_{basalt}\,^{86}Sr/^{87}Sr_{basalt} - [Sr]_{anhydrite}\,^{86}Sr/^{87}Sr_{anhydrite})/[Sr]_{total} \qquad (4).$$

This simple mass balance equation is used to show how ^{87}Sr/^{86}Sr ratio of hydrothermal fluids changes at incipient stages of hydrothermal alteration, i.e. at the point when seawater reaches point oversaturation with anhydrite.

From the mass balance approach in the closed system, the δ^{18}O value of fluids can be calculated as:

$$n_{system}\delta^{18}O_{system} = n_{SW}\delta^{18}O_{SW} + n_{basalt}\delta^{18}O_{basalt} =$$
$$\sum n_{products}\,(\delta^{18}O_{products}\ 1000ln\alpha_{products-H_2O}) + n_{H_2O}\delta^{18}O_{H_2O} \qquad (5),$$

where subscript “SW” describes moles and δ^{18}O of water contained in the starting solution; subscript “rock” denotes moles and isotope composition of titrated basalt; “products” denote minerals forming in equilibrium with H_2O with their respective fractionation factors $1000ln\alpha_{products\text{-}H2O}$.

3.0 Analytical methods

The triple oxygen isotope values of submarine hydrothermal fluids were analyzed by fluorination with BrF_5 and cryogenic purification of O_2 gas with subsequent gas chromatography (GC) separation from potential contaminants. The gas was measured in dual-inlet mode by gas source isotope ratio mass spectrometer (GS-IRMS) MAT 253 at the Institute for Planetary Materials, Okayama University. The complete description of the procedure can be found in Tanaka and Nakamura (2013). The δ^{18}O and δ^{17}O values of fluids were calibrated by the VSMOW2-SLAP2 scale using the VSMOW2 ($\delta^{17}O_{VSMOW2} \equiv 0 \pm 0.090$ and $\delta^{18}O_{VSMOW2} \equiv 0 \pm 0.167$, 2SD, N = 6) and SLAP2 ($\delta^{17}O_{VSMOW2} = -29.668$ and $\delta^{18}O_{VSMOW2} = -55.498$, N = 1) values measured during this study.

The strontium isotope values were measured using the Nu Plasma HR multicollector inductively-coupled-plasma mass-spectrometer (MC-ICPMS) hosted at the University of Illinois, Urbana-Champaign. The standard SRM 987 yielded ^{87}Sr/^{86}Sr ratio of 0.71039 ± 0.0001 (mean ± 1 standard deviation). The sample values were adjusted by 0.00014, the difference between measured standard values and its nominal value.

4.0 Results

4.1 *Modeled isotope shifts*

The output is saved at x = 200 m representing the effect of isotope exchange after the fluid flow over such distance. The outcome of this calculation with modern seawater values of δ^{18}O, Δ^{17}O and ^{87}Sr/^{86}Sr are shown in Figure 1. The effect of variable R and v_f is shown in Figure 2. The effect is such that ^{87}Sr/^{86}Sr ratio of hydrothermal fluids is slightly more radiogenic than that of fresh MORB and δ^{18}O values are shifted between +0.5 and +2.5 ‰. This is consistent with measured values in modern submarine vent fluids, solid samples from oceanic crust and ophiolites (Alt et al., 1996; Alt and Teagle, 2000; Shanks, 2001). These calculations also serve to demonstrate reproducibility of the results for mid-ocean ridge systems shown in DePaolo (2006). Additionally, we show the output of the model for hydrogen isotopes and triple oxygen isotope system (Fig. 3).

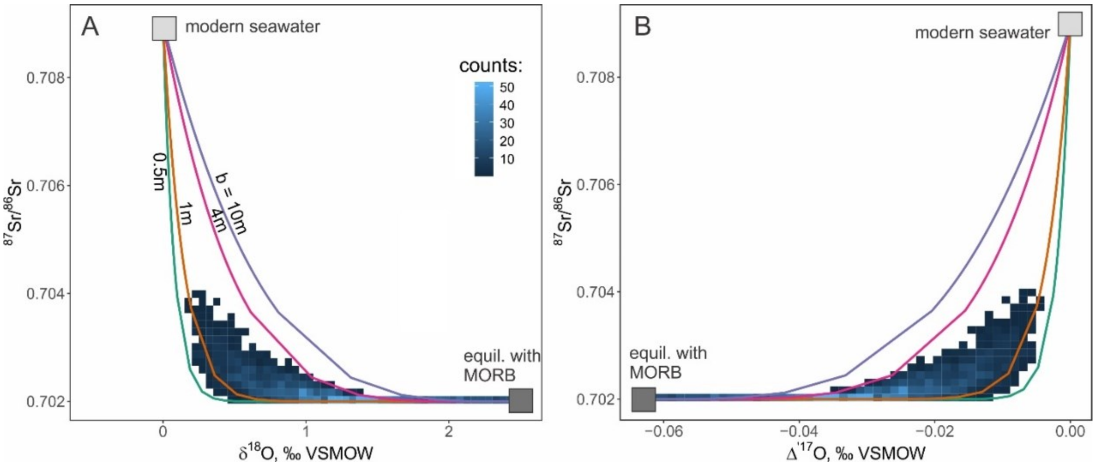

Figure 1. The output of dual-porosity model adopted from DePaolo (2006) with added Monte-Carlo simulations exemplifying probabilistic approach to reconstructing fluid isotopic shifts during interaction between modern seawater and mid-ocean ridge basalt (MORB). (A) – The isotopic shifts are shown for ^{87}Sr/^{86}Sr and δ^{18}O values and simulated range of values shown with the blue field. The lightest blue regions correspond to the most frequent outcome of the Monte-Carlo simulation with parameters shown in Table 1. These fields are in agreement with the ranges of values measured in modern submarine vent fluids. (B) – The same output shown for the three-isotope oxygen system (Δ'^{17}O defined as $10^3\ln[1+10^{-3}\delta^{17}O] - 0.5305\cdot10^3\ln[1+10^{-3}\delta^{18}O]$) and ^{87}Sr/^{86}Sr ratio. The parameters of the model are identical as in the panel A. The δ^{18}O and Δ'^{17}O of fluids in equilibrium with MORB ($\delta^{18}O = 5.5$ ‰, $\Delta'^{17}O = -0.07$ ‰) calculation from high-temperature fractionation of triple oxygen isotopes between secondary minerals and water ($10^3\ln^{18}\alpha_{\text{rock-water}} = 1.003$ and $10^3\ln^{17}\alpha_{\text{rock-water}} = 0.529\cdot10^3\ln^{18}\alpha_{\text{rock-water}}$).

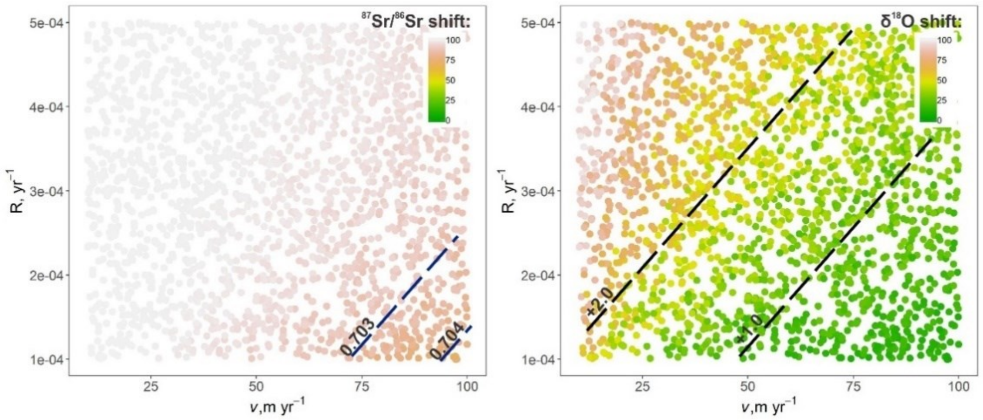

Figure 2. The output of the dual-porosity model with the parameter ranges from the Table 1. The variables R (recrystallization rate, yr^{-1}) and fluid velocity (m/yr) are amongst the most variable and uncertain parameters of a given hydrothermal systems. The ranges of values shown on the plots were constrained from physical and modeling approaches. The simulated isotopic shifts with these parameters results in isotopic values comparable with the modern near vent fluids: $^{87}Sr/^{86}Sr_{fluid}$ = 0.702-0.704 and $\delta^{18}O_{fluid}$ = +0.5 − +1.5 ‰.

These outputs are less sensitive to fracture spacing, reactive rates or fluid velocity in the dual porosity formulation. However, they are informative of the extent of isotopic shifts when such is unknown for $^{87}Sr/^{86}Sr$, and/or when the initial $^{87}Sr/^{86}Sr$ ratio of seawater is unknown. The most frequent output of the model results in about +1 ‰ shift in $\delta^{18}O$ of fluids accompanied by a significant shift in Sr-isotopes producing values ~0.001 above that of the MORB (0.702; Fig. 1A). The accompanied shift in $\Delta^{17}O$ value is -0.03 ‰ (Fig. 3B). The evolving seawater sulfate content in this model would be reflected in the trajectories of Sr isotope shifts proportional to value of *L*. While O- and H-isotopes would not change its *L* values over the time of geologic history, different concentration of Sr entering the hydrothermal system would be noticeable by the shape of combined isotope shift trajectory. The predicted shifts in the Paleoproterozoic seawater are shown in Figure 4 with output of Monte-Carlo simulation displayed with color-coded data points, corresponding to the ratio of concentration of Sr in initial fluid and unaltered rock, expressed as Sr_{rock}/Sr_{sw}.

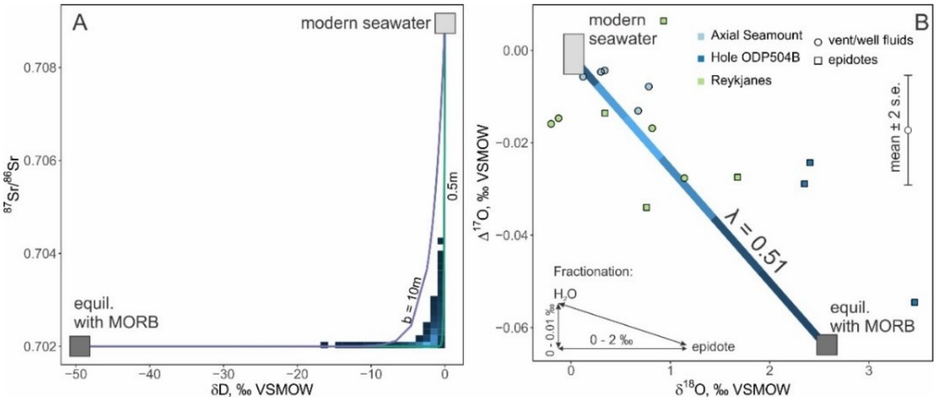

Figure 3. The result of the dual-porosity model plotted for (A) hydrogen isotopes and (B) triple oxygen isotopes. The triple oxygen isotope measurements of modern vent- and well-fluids, and epidotes from near-costal and submarine systems are also shown. These isotopic shifts are not sensitive with respect to the physical parameters of hydrothermal systems such as recrystallization rates, velocity, or fracture spacing. However, these isotopic values can be measured to estimate the extent of isotopic shift for other isotopic systems for which either initial concentration of an element or its isotopic values are not known (e.g. concentration of Sr and $^{87}Sr/^{86}Sr$ in 2.4 Ga seawater). Approximate fractionation between water and epidote in a triple oxygen isotope system at the bottom of panel (B).

4.2 Calculated mineral and aqueous species

The total moles of dissolved component species during the reactions are shown in Figure 5. The result of O- and Sr-isotope mass balance calculations (Eq. 1) are shown in Figure 5B. The equilibrium Ca- and Fe/Mg-bearing minerals are shown in Figures 6 and 7. Equilibrium micas, feldspar minerals and quartz are shown in Figure 8.

Figure 4 (next page). The predicted isotopic evolution of hydrothermal fluids in Archean-Paleoproterozoic hydrothermal systems. The open squares show estimated values of hydrothermal fluids based on the measurements of epidotes from the Vetreny Belt. The horizontal bars are uncertainties in the fluid value estimates. The simulated runs of the Montel-Carlo model are shown with filled circles color-coded by the ratio of Sr in basalt relative to Sr in seawater. The $\delta^{18}O$ value of initial seawater is taken to match that of ice-free ocean and the $^{87}Sr/^{86}Sr$ of seawater is approximated by the lowest ratios measured in the late Archean/early Paleoproterozoic carbonates (0.7045; Shields and Veizer, 2002). The contemporaneous depleted mantle is taken to have $^{87}Sr/^{86}Sr$ ratio of 0.701. The $^{87}Sr/^{86}Sr$ values measured in epidotes from the Vetreny Belt contain evidence for high input of seawater isotope value, assuming the measured values are close to the initial isotope ratio. Coupled with triple oxygen isotope values, the $^{87}Sr/^{86}Sr$ ratio shifts record high seawater-derived Sr entering the system or/and high value *b* (fracture spacing). Unlike $\delta^{18}O$ values, the $\Delta^{17}O$ values of epidotes do not differ significantly from that of equilibrium fluids due to high temperature mass-dependent fractionation.

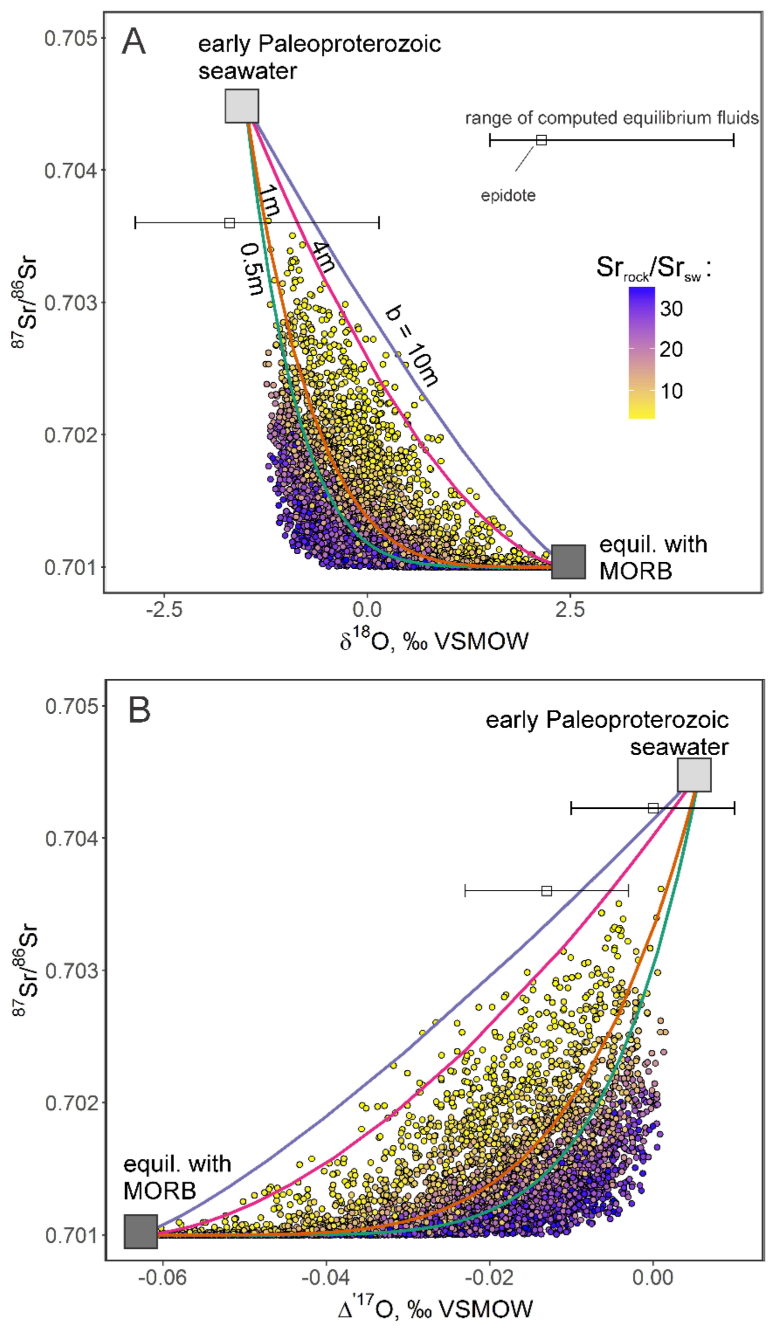

As expected, these calculations show that abundance/absence of abundant anhydrite is the most noticeable difference between high- and low-sulfate seawater-basalt reactions (i.e. modern and Paleoproterozoic altered oceanic crust assemblages). Molar abundances of other mineral and dissolved species in the performed aqueous-mineral equilibrium calculations are similar across the two cases. In the high-sulfate run, when anhydrite forms at high temperature (350 °C) and is removed from the fluid, the remaining hydrothermal fluid is 50 % shifted from its original seawater $^{87}Sr/^{86}Sr$ value towards the basaltic value. One other notable feature though is the relative abundance of low-temperature (150 °C) hematite that forms in both calculations at high W/R (between 10^3 and 10^5). In the sulfate-rich seawater-basalt reaction, about 10^{-4} moles of hematite is present in equilibrium assemblage pyrite + talc + hematite + chlorite ± chrysotile ± magnesite (Fig. 7). Only about half of that amount of hematite is present in equilibrium with same minerals in the sulfate-poor calculation, with more abundant Fe^{2+} present as a dissolved species. Occurrence of pyrite in both calculations is a minor feature at W/R below 1. The solid sulfide forms in response to the total sulfur and iron increase as more and more basalt is titrated.

Figure 5 (next page). Result of seawater-basalt equilibrium reaction calculations at variable water-rock ratio (W/R) with (A) low and (B) high levels of sulfate (Archean and modern seawater sulfate levels, $3 \cdot 10^{-5}$ and $3 \cdot 10^{-2}$ moles/kg). Total molality of aqueous component species are shown with the exception of sodium and chlorine. Activity of H^+ ion is shown as aH+ to reflect the changes of pH in the solution, i.e. $-\log_{10}a(H^+)$. The temperature and pressure of the reaction was switched from 150 °C, 400 bar to 350 °C, 500 bar at the titration step corresponding to W/R of ~ 200. Panel (C) shows the resulted isotopic shifts of Sr in hydrothermal fluids (red curves) expressed as ($^{87}Sr/^{86}Sr_{seawater}$ – $^{87}Sr/^{86}Sr_{fluid}$)/($^{87}Sr/^{86}Sr_{seawater}$ – $^{87}Sr/^{86}Sr_{basalt}$). The hydrothermal fluids with high seawater sulfate experience rapid shifts compared to low sulfate calculations due to formation and fractionation of anhydrite in the calculated reactions. The blue curve shows the evolution of $\delta^{18}O$ fluid value with decreasing W/R.

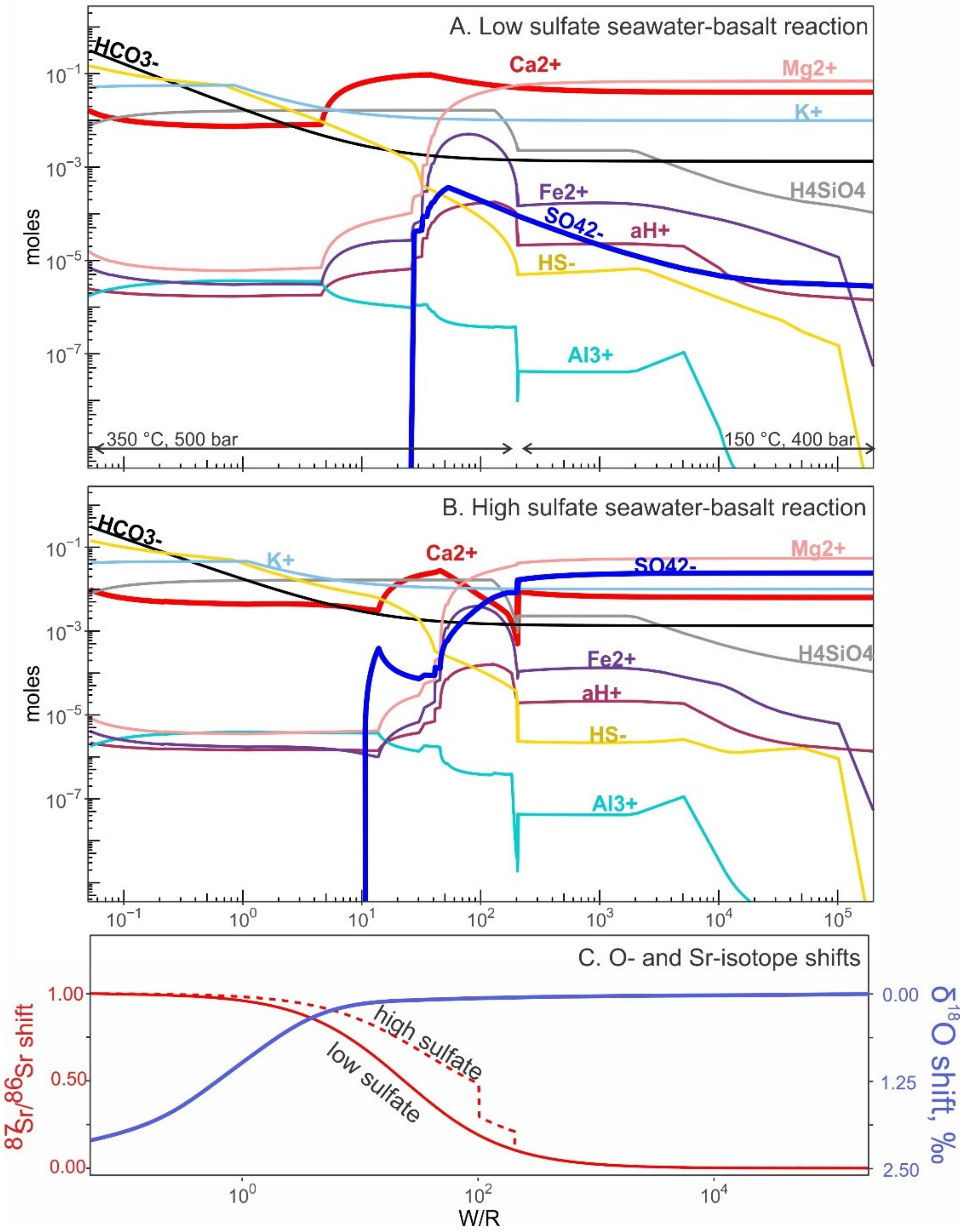
A. Low sulfate seawater-basalt reaction
HCO3-
Ca2+
Mg2+
K+
H4SiO4
Fe2+
SO42-
aH+
HS-
Al3+
moles
350 °C, 500 bar
150 °C, 400 bar
B. High sulfate seawater-basalt reaction
HCO3-
K+
Ca2+
SO42-
Mg2+
H4SiO4
Fe2+
aH+
HS-
Al3+
moles
10^{-1}
10^{-3}
10^{-5}
10^{-7}
10^{-1}
10^{0}
10^{1}
10^{2}
10^{3}
10^{4}
10^{5}
C. O- and Sr-isotope shifts
$^{87}Sr/^{86}Sr$ shift
1.00
0.50
0.00
high sulfate
low sulfate
$\delta^{18}O$ shift, ‰
0.00
1.25
2.50
10^{0}
10^{2}
10^{4}
W/R

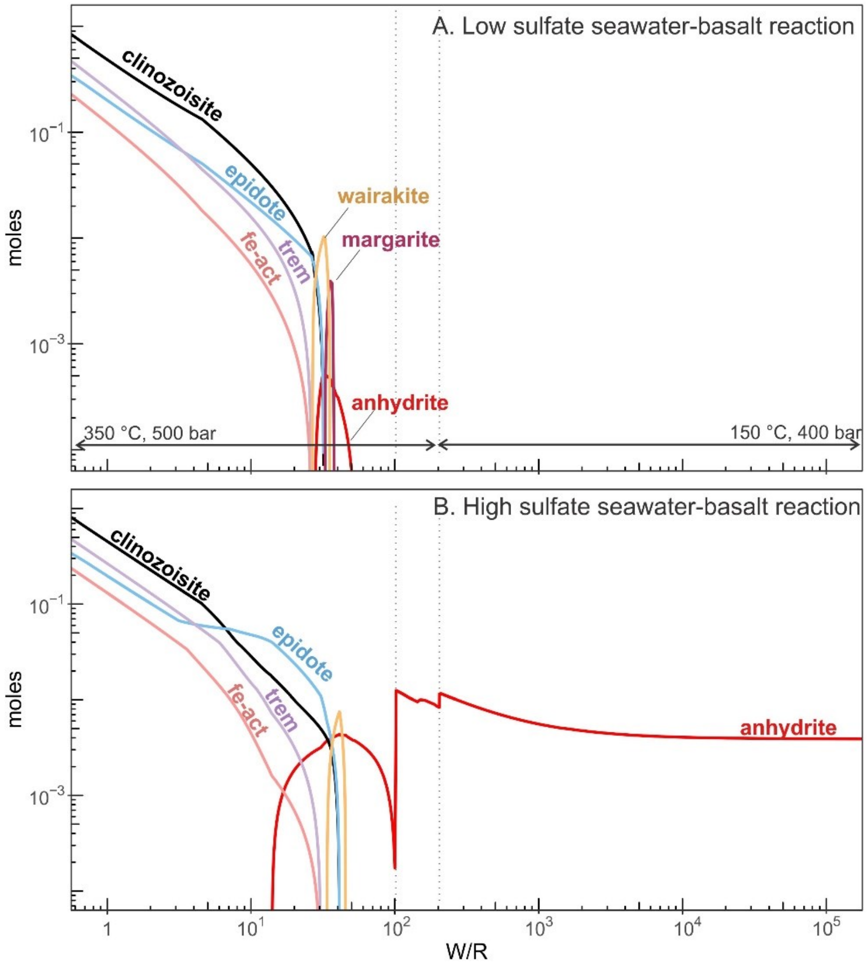

Figure 6. The molar abundances of Ca-bearing minerals from the calculation shown in Fig. 1. Removal of minerals from the solution (fractionation) was done at the titration steps corresponding to W/R of about 200 and 100 (dotted vertical lines). (A) - The low sulfate seawater-basalt reaction simulates Archean hydrothermal systems, in which anhydrite is virtually absent at high W/R ratios with minor amounts forming around W/R of 10. (B) - High levels of sulfate in the modern seawater and precipitation of anhydrite from seawater are simulated by titration small amount of basalt (5 grams) and removing anhydrite from the calculation, which results in large fraction of seawater-derived Ca (and Sr) and SO_4^{2-} to be removed from the system.

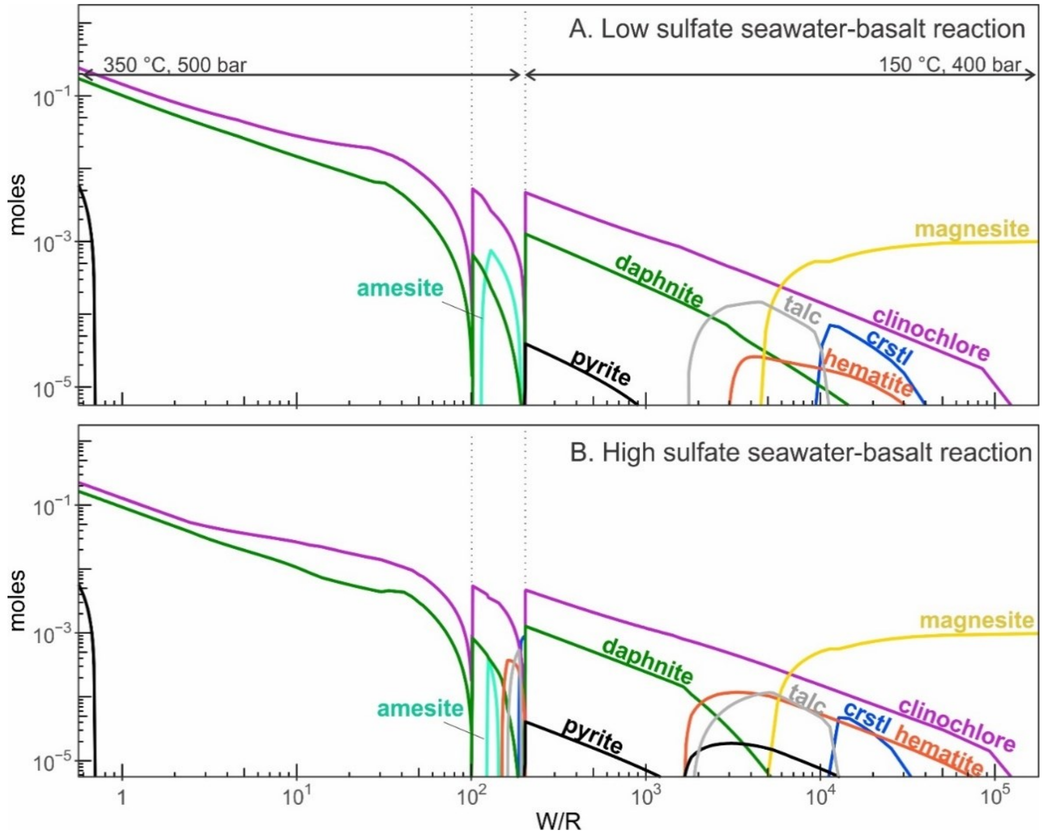

Figure 7. Molar abundance of Fe/Mg-bearing minerals from the calculation shown in Fig. 1. Separation of minerals from the solution (fractionation) was done at the titration steps corresponding to W/R of about 200 and 100 (dotted vertical lines). The outputs of the calculation do not vary significantly at high W/R between low- and high-sulfate modes. Although in the low sulfate seawater-basalt reaction (A) the amount of hematite forming at 150 °C is significantly (10 times) lower compared to the modern high sulfate-seawater basalt reaction (B). In the reaction (A), the low sulfate content promotes preferred aqueous speciation of Fe^{2+}, while abundant sulfate in (B) is reduced to HS^- accompanied by oxidation of iron and precipitation of hematite.

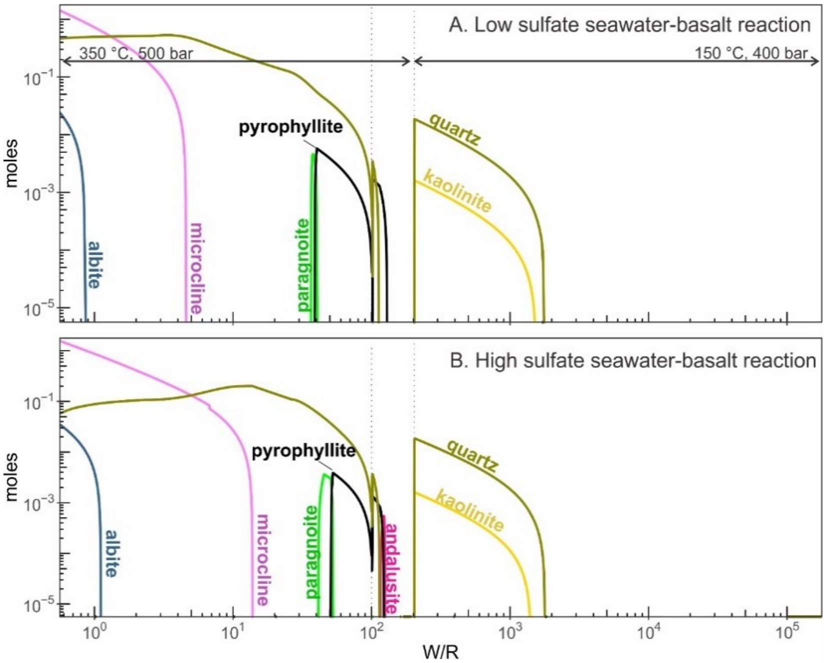

Figure 8. Molar abundance of equilibrium alumosilicate minerals and quartz in the calculations shown in Figs 5-7. Separation of minerals from the solution (fractionation) was done at the titration steps corresponding to W/R of about 200 and 100 (dotted vertical lines). The outputs of the calculation do not vary significantly at high W/R between low- and high-sulfate modes. This general similarity shows that our calculations were carried out in a self-consistent manner.

4.3 Δ^{17}O and ^{87}Sr/^{86}Sr values

We report Δ^{17}O measurements along with Na and Mg concentrations in modern fluids from the Axial Seamount hydrothermal vents of the Juan de Fuca Ridge (Table 3). In the rest of the paper, we discuss the values for only those samples that have Mg concentrations below 20 mM. Those fluids reflect extensive interaction with basaltic rocks at high temperature and oxygen isotope shifts due to seawater-basalt equilibrium reactions that buffer low aqueous Mg. Other samples with higher Mg concentrations were either less modified by interaction with basalt or underwent phase separation. Thus, their oxygen isotope values are more difficult to interpret. The δ^{18}O and Δ^{17}O values of modern seawater-derived fluids and epidotes from previous chapters are plotted together in Figure 3.

Table 3. Triple oxygen isotope values and Mg and Na concentrations of vent fluids from the Axial Seamount system. Oxygen isotope values reported relative to VSMOW (Vienna Standard Mean Oceanic Water)

Sample	$\delta^{18}O$ ‰	± 1s.e.	$\Delta'^{17}O$ ‰*	± 1s.e.	Mg, mM/kg	Na, mM/kg
J965P3	0.301	0.003	-0.005	0.006	3.90	359.2
J2-965P7	0.340	0.002	-0.004	0.006	6.28	360.6
J966P4	0.122	0.003	-0.006	0.005	10.09	539.6
J967P2	0.784	0.003	-0.008	0.006	2.37	291.0
J967P9	0.677	0.003	-0.013	0.005	6.88	293.1

* - $\Delta'^{17}O$ is calculated from the expression $10^3\ln(1+\delta^{17}O\cdot10^{-3}) - 0.5305\cdot10^3\ln(1+\delta^{18}O\cdot10^{-3})$

We also present $^{87}Sr/^{86}Sr$ ratios measured in whole rocks samples and mineral separates from the 2.43-2.41 Ga Vetreny Belt (Table 4). Epidote values are plotted together with predicted outcomes of the dual porosity model in the $^{87}Sr/^{86}Sr$ – $\delta^{18}O$ - $\Delta^{17}O$ space in Figure 4. The $\delta^{18}O$ and $\Delta^{17}O$ values of epidotes from modern systems and Vetreny Belt are adopted from Chapters II and III of present dissertation.

Table 4. Strontium isotope data for Vetreny Belt rocks

Sample	Description	Rb/Sr	$^{87}Sr/^{86}Sr$
VB16	altered pillow	0.004	0.704281
VB16 (repeat)	altered pillow	0.004	0.704227
VB25	massive altered basalt	0.029	0.706429
VB8A	epidote	$4\cdot10^{-5}$	0.704226
My1	altered hyaloclastite	0.019	0.706034
GO22	epidote	0.001	0.703602
VB9	epidote-rich rind	0.032	0.707388
02-08-04	carbonate	0.016	0.706250
02-08-03	carbonate	0.005	0.705099

5.0 Discussion

5.1 The combined isotope shifts recorded by epidote

First, we need to discuss the data that provide evidence for minimal triple oxygen isotope fractionation between water and epidote, namely $\Delta^{17}O_{water} - \Delta^{17}O_{epidote}$. This value must be very close to 0 ‰ at 300-450 °C (Hayles et al., 2018), at least within analytical uncertainty (± 0.01 ‰) and $\Delta^{17}O$ values of epidotes can be used as a close proxy for triple oxygen isotope shifts in the hydrothermal fluids (Fig. 3B). This allows us to constrain combined isotopic shifts during water-rock interaction using ancient rock record without needing to rely on temperature-dependent fractionation of $\delta^{18}O$ values (Zheng 1993). This approach has its own weaknesses owing to relatively low precision of $\Delta^{17}O$ measurements (± 0.010 ‰ 1 SE) and calibration issues with the reference materials and gases used in these measurements (Pack et al., 2016; Yeung et al., 2018), but it relies on a strong assumption that temperature-related triple oxygen isotope mass-dependent fractionation at the temperatures of epidote stability (> 250 °C) is not sensitive to 50-100 °C variations.

Our measurements of epidotes and fluids that we report here (Fig. 3B) generally define the slope of triple oxygen isotope exchange between seawater and MORB. The more evolved fluids and epidotes from Reykjanes system are in good agreement with each other. They roughly define the triple oxygen isotope shifts along the line with the slope $\lambda = 0.51$. The maximum $\delta^{18}O$ values for modern vent fluids approach +2.5 (Shanks, 2001). None of our values are that evolved, however the triple oxygen isotope measurements can be used to constrain the $\Delta^{17}O$ values in end-member fluids to the range between -0.06 and -0.04 ‰ (see Fig. 3B). These values are close to the $\Delta^{17}O$ values measured in epidote in modern oceanic crust (Zakharov and Bindeman, 2019). Based on these measurements we consider that $\delta^{18}O$ – $\Delta^{17}O$ values of ancient epidotes are well suited for reconstructing oxygen isotopic shifts experienced by hydrothermal fluids.

Now, we need to justify the use of $^{87}Sr/^{86}Sr$ values in ancient epidotes as a proxy of hydrothermal fluids. We review the existing data on the $^{87}Sr/^{86}Sr$ ratios measured in the epidotes and other high-temperature alteration minerals recovered from the modern altered oceanic crust to make an argument that their values are reflective of the $^{87}Sr/^{86}Sr$ ratios in hydrothermal fluids. The values available for the drill sites ODP Hole 504B and 1256D show that the $^{87}Sr/^{86}Sr$ values of epidotes (Alt et al., 1996; Harris et al., 2015) range within 0.7034-0.7039 and 0.7051-0.7053 respectively, while fluids from modern submarine fluids range within a more narrow interval between 0.7030 and 0.7045 (Bach and Humphreys, 1999). In the Reykjanes system most epidotes have values ranging between 0.7036 and 0.7054 (Marks et al., 2015), while the geothermal fluids range between 0.7041 and 0.7042 (Elderfield and Greaves, 1981; Millot et al., 2009). These reported values of epidotes on average lie within and above the range of $^{87}Sr/^{86}Sr$ ratios reported for directly measured vent-fluids. In general, these isotopic shifts recorded by epidotes reflect up to 50 % contribution of seawater-derived Sr in the composition of epidotes, similar to the isotopic shifts we calculated by simple closed-system reaction calculations with removal of anhydrite (Fig. 5). For this study, where large differences in the behavior of Sr in the hydrothermal fluids are considered, we propose that epidotes provide a sufficient insight into the fluids that circulate within the oceanic crust at high temperature (> 300 °C).

5.2 Testing the effect of low sulfate with the Vetreny Belt epidote

Strontium isotopes combined with triple oxygen isotope and hydrogen isotope measurements from the previous study (Zakharov and Bindeman, 2019) are used to reconstruct the trajectory of Sr isotope shifts in fractured medium using the dual-porosity model. First of all, the combined triple oxygen and strontium isotope shifts recorded by epidotes (Fig. 4) present evidence for high input of seawater-derived Sr. The elevated $^{87}Sr/^{86}Sr$ ratio (0.7036-0.7042) and $\Delta^{17}O$ that is close to 0 ‰ (-0.02 – 0 ‰) confirm previous estimates of seawater oxygen isotope composition at 2.43-2.41 Ga relying on the high input of seawater-derived elements in the hydrothermally altered rocks of the Vetreny Belt (see Chapter III). Using the lowest Sr-isotope ratio of the early Paleoproterozoic carbonates (Shields and Veizer, 2002) of 0.7045, the Vetreny Belt epidote indicates that 70-80 % of Sr in hydrothermal fluids was derived from seawater. In comparison, the modern day seawater has ~10 ppm strontium, and by removal of anhydrite, hydrothermal fluids and epidotes have a very limited amount of seawater-derived Sr--less than 40 %. To explain the trajectory of combined isotope shifts, the Sr content in the hydrothermal fluids of the Vetreny Belt must have been ~10 times more than that of modern fluids, close to 100 ppm (Fig. 4B). Similar effect could be achieved by smaller concentrations of Sr but higher fracture spacing (10 m or above), however the sampled section of Vetreny Belt is intensely brecciated, with ~0.5-2m in diameter pillow basalts separated by several-cm thick quartz-filled voids, and overall comparable to permeable layers of upper pillow basalt and sheeted section of modern seafloor. It is also consistent with the results of static mineral-aqueous equilibrium calculations, in which epidote forms at water-rock ratios of 100 and below. To facilitate high seawater-derived Sr of these epidotes, the initial concentration of seawater-derived Sr must be high. Another factor that needs to be considered is the possible effect of phase separation. The increase in salinity by about 140 % as recorded by halite saturation at 300 °C in fluid inclusions (Zakharov and Bindeman, 2019), would be consistent with the initial Sr concentration of ~70 ppm. This figure is not unrealistic; for example, it is comparable to the estimate from Ordovician epidotes (Turchyn et al., 2013; Antonelli et al., 2017) that formed from interaction between basalt and low sulfate seawater with a high fraction of seawater-derived Sr.

Our estimate of Sr concentration in hydrothermal fluids (70-100 ppm) is consistent with absence of abundant anhydrite in the altered oceanic crust. The very small amount of anhydrite (10^{-5} moles) forming in equilibrium with hydrothermal fluids likely induced higher input of seawater-derived Sr into altered oceanic crust of the Archean-Proterozoic time. In a similar study regarding more recent seawater history, Antonelli et al. (2017) demonstrated that changing sulfate to calcium concentration ratios in seawater over the Phanerozoic timeline played a critical role in the Sr isotope budget of hydrothermal fluids. Their findings suggest that the input of seawater-derived Sr in hydrothermal fluids is dependent on the anhydrite oversaturation. The high $^{87}Sr/^{86}Sr$ values measured in epidote from Phanerozoic ophiolite sequences (McCulloch et al., 1981; Alexander et al., 1993; Bickle and Teagle, 1992; Turchyn et al., 2013) also suggest that there is a link between seawater composition and isotope budget of hydrothermal fluids. Importantly, Cretaceous and Ordovician epidotes extracted from relicts of oceanic crust have high $^{87}Sr/^{86}Sr$ ratios, coinciding with periods of geologic history when oceans were low in sulfate (≤10 mM/kg; Berner, 2004; Antonelli et al., 2017). In Vetreny Belt, an early Paleoproterozoic seawater-basalt system, the low-sulfate effect should be even more extreme than in the Phanerozoic ophiolites. In ancient systems that operated during the first 2/3 of the geologic history, when the oxidative capacity of the atmosphere was weak and marine sulfate was low (Canfield, 1998; Lyons et al., 2014), the $^{87}Sr/^{86}Sr$ ratio of hydrothermal fluids would be merely controlled by the extent of interaction with basalt and the amount of Sr dissolved in pristine seawater. Thus, the seawater budget of Sr over the most of geological time scale might have been fundamentally different compared to that of the Phanerozoic.

5.3 The effect of low sulfate on Sr isotope budget of altered oceanic crust

The preservation of a high $^{87}Sr/^{86}Sr$ ratio in epidotes of Vetreny Belt allows us to speculate about the Sr isotope budget of seawater during Precambrian time before the onset of oxidative weathering at around 0.6 Ga (Kah et al., 2004; Lyons et al., 2014). Weathering of terrestrial sulfides might have modulated the $^{87}Sr/^{86}Sr$ shifts in hydrothermal fluids over geological time through concentrations of dissolved sulfate in seawater and anhydrite oversaturation in hydrothermal systems. As submarine fluids became oversaturated with anhydrite over the geological time, the proportion of mantle-derived Sr flux into seawater has likely also increased. This effect is somewhat counter-balanced by the retrograde solubility of anhydrite as discussed in the Introduction, which releases the seawater-derived Sr back into the ambient ocean. The anhydrite fate likely depends on the history of individual fragments of oceanic crust, on the spreading rates and the heat flow within the crust once it is far from the axis. Modern young oceanic crust profiles that are ~6 Ma (ODP Hole 504B) and 15 Ma (ODP Hole 1256D) still contain anhydrite in the upper section where the temperatures are around and below 150 °C. Moreover, anhydrite is also abundant in the high-temperature recharge zones off-axis where anhydrite saturates. Anhydrite is even found, although rarely, in ophiolites suggesting long-term storage in oceanic crust (Alt et al., 2003). Thus, it is likely that anhydrite *is* a sink for marine Sr and by extension, there is a positive feedback between sulfate concentration in seawater and proportion of mantle-derived Sr in the seawater budget. As a consequence, low sulfate concentrations in Precambrian hydrothermal fluids must have promoted a high fraction of seawater-derived Sr to be recycled back into the oceans. This might help explain the main feature of $^{87}Sr/^{86}Sr$ curve before ~600 Ma – its steady increase without significant lows – unlike in the Phanerozoic. Even though, there is a great uncertainty in the $^{87}Sr/^{86}Sr$ ratio of Precambrian seawater, traced by the lowest Sr-isotope ratios of marine carbonates, pre-Phanerozoic ratios seem to be steadily growing (Shield and Veizer, 2002). Continent growth modulated by super-continent assemblies and break-ups, and intense continental weathering with low mantle input of Sr are generally consistent with the growth rates of the $^{87}Sr/^{86}Sr$ in the Precambrian seawater (e.g. Halverson et al., 2007). The rising $^{87}Sr/^{86}Sr$ values thus not only reflect high intensity of continental weathering in a high-CO_2 atmosphere but also low marine sulfate concentration. If our measurements of the Vetreny Belt epidote provide representative evidence for hydrothermal circulation of seawater in submarine systems, then further studies of Precambrian seawater Sr isotope evolution should account for the effect of low seawater sulfate.

A suite of samples from the 2.43-2.41 Ga Vetreny Belt was chosen for testing the effect of low marine sulfate on the Sr isotope budget of altered oceanic crust, and it could be used for further testing the effect of other reduced species present in the Paleoproterozoic seawater. As shown in the mineral-aqueous equilibrium calculations, another interesting aspect of low seawater sulfate is high concentration of hematite produced at high water-rock ratios at temperature of 150 °C (see Fig. 7). This seems to be a key feature intrinsic to ancient altered basalts as monitored by their Fe^{2+}/Fe_{tot} ratios in the compilation of analyses by Stolper and Keller (2018) and also contributes to the interpretation of Banded Iron Formations as a product of hydrothermal precipitation (e.g. Dauphas et al., 2004). Future research avenues might benefit from calibrating the relationship between sulfate concentration in seawater and concentrations of redox sensitive transition metals (e.g. Fe, Mn, Cr) in solid-solution silicate minerals in submarine altered basalt. For example, the extent of water-rock interaction and low oxidation state of sulfur and iron present in hydrothermal fluids are likely to be reflected in Fe^{2+}/Mg ratios measured in Ca-amphiboles and chlorites as well as Fe^{3+}/Al ratios in epidotes (Fig. 7).

6.0 Conclusion

In summary, we demonstrated the effect of low sulfate concentrations in the Precambrian oceans on water-rock interaction in submarine hydrothermal systems using observations and modeling. The main conclusions of this study are:

1) The apparent triple oxygen isotope fractionation between epidote and modern marine hydrothermal fluids is minimal. That allows to use $\Delta^{17}O$ values of epidote as a direct proxy for the seawater-basalt reaction progress.
2) Our previous estimates of stable isotope composition of seawater (see Chapter III) are now supported by high $^{87}Sr/^{86}Sr$ ratios of the Vetreny Belt epidote. Their Sr isotope composition of reconstructed fluids along with their $\Delta^{17}O$ values are indicative of moderate modification of seawater values due to reaction with rocks at high temperature. The reconstructed oxygen isotope value in seawater is close to the

modern day value with ice-caps melted and $^{87}Sr/^{86}Sr$ ratios in epidotes match the lowest values measured in contemporaneous carbonates.

3) These measurements constrain the $\Delta^{17}O$ and $^{87}Sr/^{86}Sr$ values of the 2.43-2.41 Ga seawater around -0.005 ‰ and 0.7045, respectively.
4) The combined isotope shifts of oxygen and strontium are related to the concentrations of marine sulfate in initial seawater. Oversaturation of seawater with anhydrite at temperatures above 130 °C removes most of seawater-derived Sr from hydrothermal systems playing a key role for $^{87}Sr/^{86}Sr$ budget of hydrothermal fluids. We find that Vetreny Belt epidotes reflect very high fraction of seawater-derived Sr, corresponding to about 100 ppm of original Sr in the fluids, which indicates an absence of anhydrite in the early Paleoproterozoic submarine systems.
5) The Sr isotope budget of seawater in the Precambrian oceans might have been fundamentally different from that in the Phanerozoic. Low marine sulfate promoted a higher fraction of seawater-derived Sr that was able to reach high-temperature sections of submarine hydrothermal systems. Related to the oxidative capacity of continental weathering, emergence of high sulfate levels after about 0.6 Ga facilitates abundant anhydrite precipitation and consequently, a higher flux of mantle derived Sr into the seawater budget. Prior to this, hydrothermal systems were essentially anhydrite-free and seawater-derived Sr was more common in submarine fluids.

7.0 Bridge

Chapter IV shows that combined isotope shifts of multiple elements can be informative of the chemical compound of initial fluids. The chapter explores the redox evolution of the Earth’s systems using the effect of low sulfate content in the Precambrian oceans on the strontium isotope budget of hydrothermal fluids. The results presented here suggest that epidotes from the Vetreny belt contain high fraction of seawater-derived Sr, supporting my previous findings in Chapter III. Now when the isotope composition of the seawater is sufficiently constrained, next chapters (V and VI) explore the evaporation-distillation cycle in the continental part of contemporaneous hydrosphere. Since hydrological cycle originates with evaporation of seawater and subsequent condensation-precipitation of water over the continents, my work on the Vetreny Belt provides a much-needed foundation to understand isotopic signatures of precipitation recorded in continental hydrothermal systems. Next chapters provide oxygen isotope record of meteoric waters that existed during the early Paleoproterozoic globally cold climate (a.k.a. the early Paleoproterozoic snowball Earth episodes). Since the $\delta^{18}O$ of contemporaneous seawater is close to 0 ‰, the values of reconstructed meteoric waters can be tied together in a coherent paleoclimate and paleogeograpic context.

CHAPTER V

DATING THE PALEOPROTEROZOIC SNOWBALL EARTH GLACIATIONS USING CONTEMPORANEOUS SUBGLACIAL HYDROTHERMAL SYSTEMS

From Zakharov, D.O., Bindeman, I.N., Slabunov, A.I., Ovtcharona M., Coble, M.A., Serebryakov, N.S., and Schaltegger, U. (2017) Dating the Paleoproterozoic snowball Earth glaciations using contemporaneous subglacial hydrothermal systems. Geology, 45, 667-670.

1.0 Introduction

The occurrence of several glacial diamictites in Paleoproterozoic stratigraphic sections around the world indicate that three or four episodes of global glaciations occurred between 2.45 and 2.22 Ga (Hoffman, 2013 and references therein). The ages of individual glaciations are currently constrained by the relative position of glacial diamictites with respect to dated tuffs, lavas, and intrusions, and disappearance of mass-independent fractionation of sulfur isotopes resulting in several cross-continental correlation schemes (Kirschvink et al., 2000; Hoffman, 2013; Rasmussen et al., 2013). Firmer time constraints are needed to correlate glaciations across continents and to understand the cause-effect connection between global cooling and to the Great Oxidation Event (GOE) bracketed between 2426 Ma and 2308 Ma (Bekker et al., 2004; Gumsley et al., 2017). In contrast to using relative ages, in this study we attempt to obtain absolute ages of the glaciations using high-precision U-Pb geochronology of intrusions that induced subglacial hydrothermal alteration. We used conventional and triple oxygen isotope systematics of low-$\delta^{18}O$ hydrothermally altered rocks associated with these intrusions from the Baltic shield to reconstruct $\delta^{18}O$ of original meteoric water and to show presence of glacial ice on the continent during the early Paleoproterozoic. As the Baltic shield was located at low latitudes (latitudes 20°–30º; Bindeman et al., 2010; Salminen et al., 2014) when the low-$\delta^{18}O$ hydrothermally altered rocks formed, reconstructed low $\delta^{18}O$ (as low as −40 ‰) of original meteoric water suggest low latitude, snowball Earth glaciations which is in line with deposition of glacial diamictites at low latitudes (Evans et al., 1997). Thus, by applying precise U-Pb geochronology to intrusions with the low-$\delta^{18}O$ signatures from the Baltic Shield we can directly date the presence of glacial ice at low latitudes in the early Paleoproterozoic.

2.0 Geological setting

The Sumian large igneous provinces include numerous mafic intrusions that formed on the Baltic Shield as the result of global mantle plume activity in the early Paleoproterozoic (Sumian) time (Amelin et al., 1995; Kulikov et al., 2010). The Belomorian belt, located in Karelia, Russia, between the Karelian and Kola cratons (Fig. 1), was a zone of extensive rifting from 2.44 to 2.39 Ga. The rift zone formed during plume activity and hosts numerous high-Mg mafic intrusions varying in size from dikes to large layered intrusions (Lobach-Zhuchenko et al., 1998; Bibikova et al., 2004; Slabunov et al., 2011). A younger, less-voluminous episode of magmatism produced high-Fe gabbro intrusions at around 2.3–2.1 Ga in the same region (Salminen et al., 2014; Stepanova et al., 2015). Extreme oxygen isotope depletions are found in the Belomorian belt and are commonly associated with these mafic intrusions (Fig. 1). The distribution of low-$\delta^{18}O$ values has been mapped out as halos (bull's-eyes) around the intrusions (Bindeman et al., 2014). This indicates that short-lived (10^3–10^4 yr) high-temperature meteoric hydrothermal systems were driven by the heat of cooling intrusions. The lowest $\delta^{18}O$ measured in terrestrial silicates and very low δD (as low as −27‰ and −233‰ respectively; Bindeman et al., 2014) uniquely fingerprint high-temperature interaction between the rocks and glacial melt waters. We report new low $\delta^{18}O$ values from the southernmost locality within the Belomorian belt, the Kiy Island, Karelia, which extends the occurrence of low-$\delta^{18}O$ rocks to a 500-km-long zone that traces the elongation of the Paleoproterozoic rift that was supposedly operating under continental ice sheets. The Belomorian Belt underwent regional metamorphism at 1.9 Ga, which did not alter the original low $\delta^{18}O$ signature of hydrothermally altered rocks.

3.0 Triple oxygen isotope geochemistry

Here we use low-$\delta^{18}O$ rocks from the Belomorian belt to derive the $\delta^{18}O$ of Paleoproterozoic meteoric water by employing $\Delta^{17}O$-$\delta^{18}O$ systematics of the hydrothermally altered rocks (Herwartz et al., 2015). The relationship between $\delta^{18}O$ and $\delta^{17}O$ in mantle, crustal rocks and meteoric water is exponential with the power varying between 0.528–0.529 (Luz and Barkan, 2010; Pack and Herwartz, 2014). The offset from a function with slope of 0.5305 that approximates high-temperature equilibrium can be expressed in form of $\Delta^{17}O = \delta^{17}O - 0.5305 \times \delta^{18}O$ using conventional notation of $\delta^{18}O$ and $\delta^{17}O$ (Pack and Herwartz, 2014). Earth's mantle has $\Delta^{17}O$ of approximately −0.1‰ (Pack and Herwartz, 2014) and $\delta^{18}O$ of 5.5‰ relative to VSMOW (Vienna Standard Mean Ocean Water). Meteoric water has a range of $\Delta^{17}O$ and $\delta^{18}O$ that is defined by the extent of distillation (Luz and Barkan, 2010; Fig. 2). Hydrothermally altered rocks represent input from two reservoirs: unaltered silicate rock and meteoric water. A regression line drawn through an array of analyses of hydrothermally altered rocks represents a mixing line between unaltered rock and original meteoric water (Fig. 2). Since metamorphism is largely an isochemical process, triple oxygen isotopic abundances in the hydrothermally altered rocks are preserved. Using the Khitoostrov locality (Karelia), Herwartz et al. (2015) showed that using the $\delta^{18}O$-$\Delta^{17}O$ relationship enables back-tracking through the effect of metamorphism to deduce the $\delta^{18}O$ of original meteoric water.

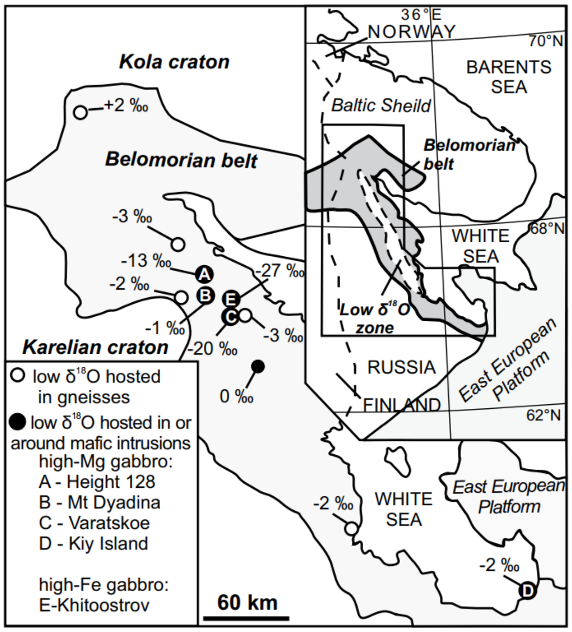

Figure 1. Location of hydrothermally altered low-$\delta^{18}O$ rocks on the Baltic Shield. Each locality is shown with a circle and a number, ‰ indicating the lowest $\delta^{18}O$ value found at the locality (see Bindeman and Serebryakov (2011) and Bindeman et al. (2014) for details). Mafic intrusions used here for dating episodes of snowball Earth are shown with letters (see legend). Variable $\delta^{18}O$ of rocks is interpreted to represent alteration by glacial melt waters at variable water to rock ratios.

Here we analyzed hydrothermally altered rocks from low-$\delta^{18}O$ localities Khitoostrov, Height 128, Varatskoe, Mount Dyadina, and Kiy Island for triple oxygen isotopes (Fig. 2). Last four localities are associated with the 2.44–2.39 Ga intrusions of high-Mg gabbros. The $\delta^{18}O$-$\Delta^{17}O$ relationship in hydrothermally altered rocks indicate that the high-Mg gabbros interacted with meteoric water with $\delta^{18}O$ of −39‰ ± 7‰ (Fig. 2A). Dated here to 2.29 Ga, the high-Fe gabbro gabbro intrusion from Khitoostrov interacted with meteoric water with $\delta^{18}O$ of −40‰ ± 3‰ (Fig. 2B) which is in agreement with previous measurements done by Herwartz et al. (2015). High-Mg gabbro intrusions interacted with meteoric water with $\delta^{18}O$ of −39‰ ± 7‰ (Fig. 2B). In modern world, such low $\delta^{18}O$ water values only occur in continental glacial ice from Antarctica and Greenland (Dansgaard, 1964).

4.0 Geochronology

The ages of low-$\delta^{18}O$, high-Mg mafic intrusions that we analyzed for triple oxygen isotope were determined previously using in situ U-Pb zircon geochronology: the intrusion from Varatskoe locality is dated at 2410 ± 10 Ma (Bibikova et al., 2004); the intrusion of Kiy Island is dated to 2441 ± 51 Ma (Slabunov et al., 2006) and one concordant zircon is dated at ca. 2.40 Ga from gabbro of Mt. Dyadina (Fig. 1; Bindeman et al., 2014). The low-$\delta^{18}O$ intrusion from the Height 128 locality has a geochemical affiliation of high-Mg gabbro (Lobach-Zhuchenko et al., 1998), has the same regional stratigraphic position as the other high-Mg gabbros, and thus is likely of the same age group.

The younger high-Fe gabbro intrusions from the Baltic Shield were dated in Stepanova et al. (2015) to 2.31 Ga. We present new ages for the high-Fe gabbro intrusion from Khitoostrov using a combination of U-Pb zircon methods. Baddeleyite in these intrusions is rarely preserved and we were not able to find it in the Khitoostrov intrusion. First, extracted zircons were thoroughly analyzed (>100 points) using sensitive high-resolution ion microprobe, reverse geometry (SHRIMP-RG) to target primary igneous zircons (see Appendix C). These data show scatter in Pb-Pb ages between igneous and metamorphic ages, ~2.3 and 1.9 Ga respectively (Fig. 3A). The best fit regression age for igneous zircons yields 2257 ± 7 Ma, which we interpret as the age of emplacement. We attribute the scatter to be associated with a complicated history of Pb loss that occurred between the time of emplacement and regional 1.9 Ga metamorphism. Guided by SHRIMP-RG spot analyses, we targeted zircons that yielded concordant ages within 2σ uncertainty for high precision analysis by chemical abrasion–isotope dilution–thermal ionization mass spectrometer (CA-ID-TIMS; see Appendix C). Essentially, we used SHRIMP-RG as a tool for searching igneous zircon to obtain the high precision CA-ID-TIMS dates. Older inherited grains, and younger metamorphic zircons or grains that may have experienced significant Pb-loss were avoided. Zircons were thermally annealed and chemically abraded to eliminate domains within the crystal that were structurally damaged and susceptible to lead-loss. Among multiple analysis, the ages of two concordant zircons were determined with high precision (Fig. 3B). One of the zircons has the Pb-Pb age of 2291 ± 8 Ma and is interpreted to reflect the age of emplacement of intrusion. Another concordant zircon has the Pb-Pb age of 1873 ± 2 Ma which is thought to represent the age of metamorphism typical for the Belomorian belt (Bibikova et al., 2004). These ages are in agreement with the range of ages measured by SHRIMP-RG analysis. The measured values acquired by SHIRMP-RG and CA-ID-TIMS are reported in the supplemental electronic file.

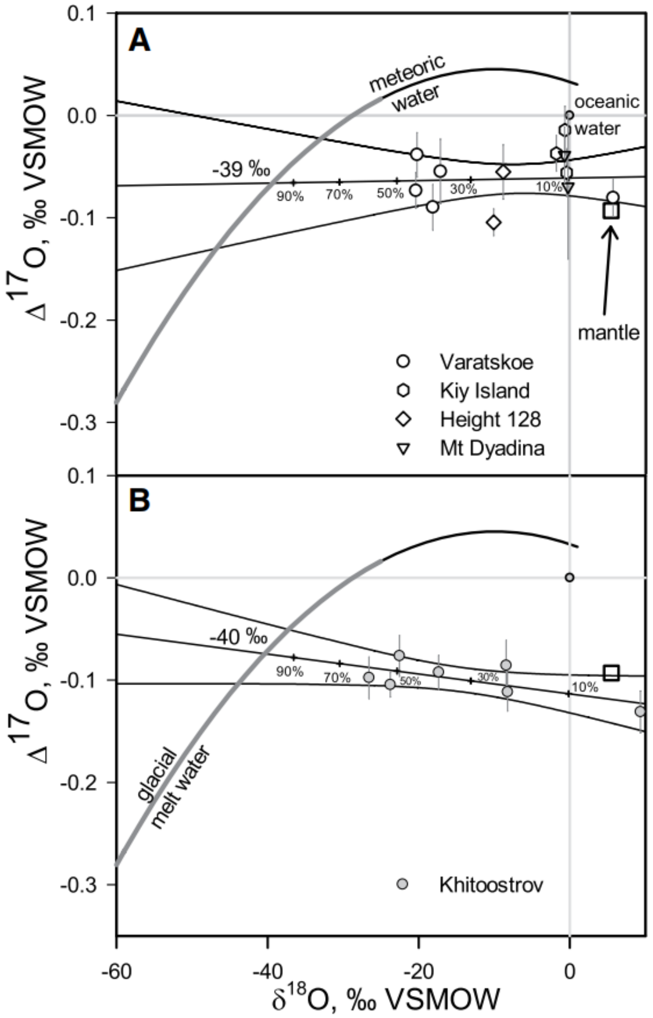

Figure 2. Triple oxygen isotope plot for low-$\delta^{18}O$ rocks from the Baltic shield. The curved line shows oxygen isotope composition of meteoric water. Thick gray portion of the curve shows glacial melt waters. Regression line constructed through hydrothermally altered rocks intercepts the meteoric water curve at the $\delta^{18}O$ of original meteoric water. The range of $\delta^{18}O$ of hydrothermally altered rocks is due to variable water to rock ratio. The water-to-rock ratio is expressed with the percentage of water that reacted with the rock. The 90%-envelopes on the regression lines are shown. The $\delta^{18}O$ of Paleoproterozoic oceanic water is assumed to have $\delta^{18}O$ of modern-day ocean (Muehlenbachs, 1998). A: Ca. 2.43–2.41 Ga high-Mg gabbros interacted with meteoric water with $\delta^{18}O$ of −39‰ ± 7‰ (for location of samples, see Fig. 1). Two out of three samples from Kiy Island, Karelia, Russia, yield elevated $\Delta^{17}O$ that can be explained by involvement of oceanic water in the formation hydrothermally altered rocks. B: Dated here to 2291 ± 9 Ma, Khitoostrov intrusion shows well-defined trend between mantle and meteoric water with $\delta^{18}O$ of –40‰ ± 3‰. The data are reported in Appendix C (Table S1).

5.0 Discussion

The studied intrusions provide instantaneous snapshots of the Paleoproterozoic climate through short-lived shallow meteoric hydrothermal systems. Our new and compiled U-Pb ages, coupled with $\delta^{18}O$-oxygen isotope data, are interpreted as dates when glacial ice was present at low latitudes. Two episodes of global glaciations are recognized by oxygen isotope signature in 2.43–2.41 Ga high-Mg gabbros and in the 2291 ± 8 Ma high-Fe gabbro Khitoostrov intrusion. The reconstructed meteoric waters in both cases have $\delta^{18}O$ of around −40‰ which corresponds to glacial ice. In modern-day climate such low $\delta^{18}O$ meteoric water forms in regions with mean annual temperature (MAT) of approximately −40 °C (Dansgaard, 1964).

The low-latitude geographic position of the Baltic Shield is determined at 2.45 Ga (Mertanen et al., 2006) and at 2.06 Ga (Pesonen et al., 2003). The Baltic shield drifted from near-equatorial to subtropical position between these ages. Recent work determined a low-latitude position (-20.4ºN) for the Baltic Shield at 2.3 Ga using a mafic dike from Karelia (Salminen et al., 2014). This confirms the global extent of two Paleoptoterozoic glaciations recorded in low-$\delta^{18}O$ rocks from the Baltic Shield.

How do these ages correlate with the sedimentary record of the glaciations? Dated horizons of Paleoproterozoic diamictites of similar age are found in north-eastern part of the Baltic Shield (the Kola Peninsula, Russia). The deposition age of glacial diamictites of the Polisarka Formation on the Kola Peninsula is constrained to ca. 2434 Ma based on the U-Pb age of overlying tuff (Brasier et al., 2013). Based on stratigraphic correlations and evidence from detrital zircons (Gärtner et al., 2014), other glacial diamictites (Seidorechka and Veverskrukk Formations) from the Baltic Shield were deposited around the same time. Deposited at low latitudes (Evans et al., 1997) Makganyene diamictites from the Griqualand West basin of Kaapvaal craton, South Africa are bracketed between the Ongeluk volcanics dated at 2426 ± 3 Ma (Gumsley et al., 2017) and 2431 ± 31 Ma Griquatown Iron formation (Trendall et al., 1990) and are perhaps correlated with glacial diamictites from the Baltic Shield. These units likely correlate with the oldest glacial units from the Huronian Supergroup of the Superior craton, Canada (Bekker, 2014). We suggest that 2.43–2.41 Ga low-$\delta^{18}O$ high-Mg gabbros formed during the first episode of snowball Earth glaciation, when the oldest Paleoproterozoic glacial diamictites were deposited across continents ca. 2.45–2.42 Ga (Bekker, 2014).

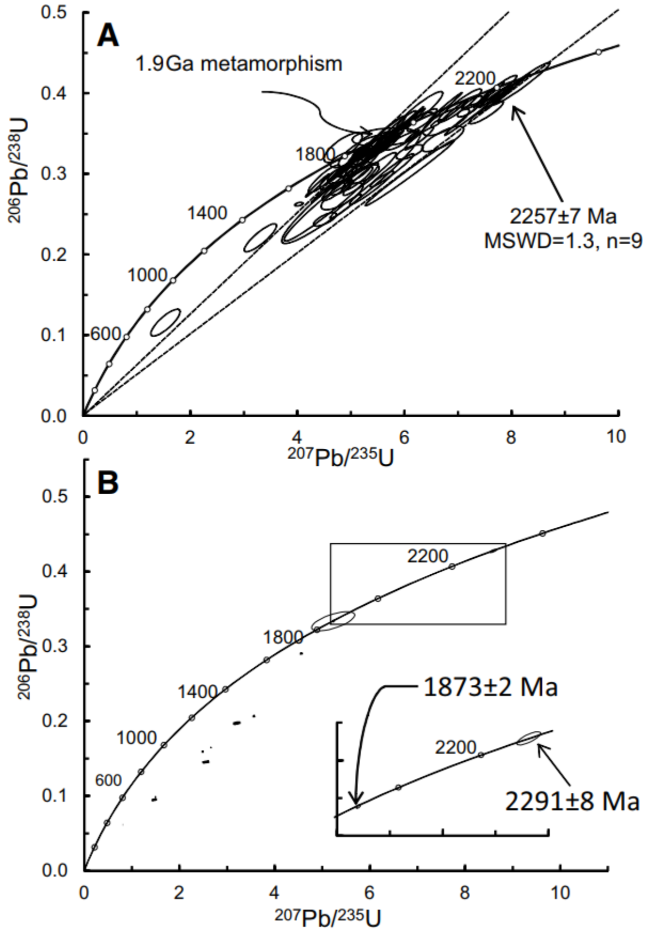

Figure 3. Concordia diagrams for U-Pb zircon dating of the Khitoostrov intrusion, Russia. A: Analyses acquired using sensitive high-resolution ion microprobe, reverse geometry (SHRIMP-RG). The best-fit regressions age yields 2257 ± 7 Ma and is interpreted to be the age of emplacement. Ellipse errors are 1σ. B: Data acquired using isotope dilution–thermal ionization mass spectrometer (ID-TIMS). Most of analyzed grains demonstrate the effect of recent Pb-loss, however two grains (see inset) yield concordant ages. The size of ellipses in the inset is exaggerated for demonstrational purposes. Ellipse errors are 2σ. The U-Pb initial ratios are reported in the Supplemental File included with this dissertation.

There are no geochronologically well-constrained glacial diamictites younger than 2.41 Ga found on the Baltic Shield, making regional correlation with the 2291 Ma Khitoostrov intrusion difficult. Assuming close geographic proximity of the Baltic Shield and Superior craton in the Paleoproterozoic (Bleeker and Ernst, 2006; Bindeman et al., 2010), deposition of glacial diamictites of the Huronian basin, Canada might correlate with the formation of the 2291 ± 8 Ma low-δ^{18}O Khitoostrov intrusion. The third glacial diamictites of the Gowganda Formation, Huronian Supergroup, are constrained by the U-Pb age of overlaid tuff beds at ca. 2310 Ma (Rasmussen et al., 2013). The age of Khitoostrov intrusion overlaps within analytical uncertainty with the age of the tuff beds suggesting that the intrusion formed during the third Paleoproterozoic glacial event. The low δ^{18}O signature of Khitoostrov intrusion is so far the only existing evidence for this glacial event on the Baltic Shield. Dating subglacial intrusions from other continents that were located at low latitudes between 2.45 and 2.22 Ga using the new method we proposed here can aid cross-continental correlations of the early Paleoproterozoic glacial episodes.

6.0 Bridge

Chapter V combines triple oxygen isotope systematics and high-precision U-Pb zircon ages to date two episodes of snowball Earth glaciations. The evidence is presented for the subglacial hydrothermal alteration being induced by intrusions of high-Mg and high-Fe gabbros during the early Paleoproterozoic rifting of the Baltic Shield, which at the time was located at low latitudes. The triple oxygen isotope approach is used here to show that the δ^{18}O values of glacial meltwaters were approximately −40 ‰. The high-Mg gabbro intrusions formed during the earliest episode of snowball Earth glaciations, between 2.43 and 2.41 Ga. The high-Fe gabbro from the Khitoostrov locality hosts the lowest δ^{18}O value of -27.3 ‰ measured in Karelia and is dated here using high-precision U-Pb zircon geochronology at 2291 ± 8 Ma. This age is interpreted to reflect the interaction between the intrusion and glacial meltwaters perhaps during the third Paleoproterozoic glaciation, which occurred after the Great Oxidation Event between 2.43-2.31 Ga. In the final chapter, Chapter VI, I extend the triple oxygen isotope investigations to other occurrences of low δ^{18}O rocks in Karelia, and to the low δ^{18}O Scourie dikes located in NW Scotland. Given the potential proximity (spatial and temporal) between the Scourie dikes and the high-Mg intrusions of Karelia, their low δ^{18}O signature might be related through the globally cold climate and the global mafic magmatism of the early Paleoproterozoic. Chapter VI explores triple oxygen and hydrogen isotope systematics (δD, δ^{18}O and Δ^{17}O) of these rocks to evaluate the isotopic composition of meteoric water, which provides a record of active hydrologic cycle during the early Paleoproterozoic

CHAPTER VI

LOW $\delta^{18}O$ ROCKS IN THE BELOMORIAN BELT, NW RUSSIA, AND SCOURIE DIKES, NW SCOTLAND: A RECORD OF ANCIENT METEORIC WATER CAPTURED BY THE EARLY PALEOPROTEROZOIC GLOBAL MAFIC MAGMATISM

From Zakharov, D.O., Bindeman, I.N., Serebryakov, N.S., Prave, A.R., Azimov, P.Ya., and Babarina, I.I. (2019) Low $\delta^{18}O$ rocks in the Belomorian belt, NW Russia, and Scourie dikes, NW Scotland: A record of ancient meteoric water captured by the early Paleoproterozoic global mafic magmatism. In press at *Precambrian Research*.

1.0 Introduction

1.1 Low $\delta^{18}O$ rocks of the early Paleoproterozoic

Between 2.45 and 2.40 Ga, extensive magmatism of the globally distributed Large Igneous Provinces (LIPs) temporally overlapped with the onset of series of snowball Earth glaciations (Evans et al., 1997; Heaman, 1997; Bleeker, 2003; Bleeker and Ernst, 2006; Ernst and Bleeker, 2010; Hoffman, 2013; Gumsley et al., 2017). Since the timing of these events is so close, it is reasonable to consider that the abundant continental magmatism and rifting was accompanied by water-rock interaction induced by hydrothermal circulation of meteoric water. Such interaction is recognized in geological record by low $\delta^{18}O$ values, as, for example, in altered basalts and products of crustal melting in the modern rift system of Iceland (Hattori and Muehlenbachs, 1982). In fact, the 2.44-2.41 Ga rocks from the Belomorian belt of the Karelia craton have been shown to contain the very low $\delta^{18}O$ values, between -27 and +3 ‰, explained by the same style of interaction between glacial meltwaters and rocks induced by numerous intrusions forming in a rifting environment (Bindeman et al., 2010; Bindeman and Serebryakov, 2011; Bindeman et al., 2014; Herwartz et al., 2015; Zakharov et al., 2017). Along with the Paleoproterozoic glacial deposits, these low $\delta^{18}O$ rocks present geochemical evidence for the presence of glacial ice that accumulated in the subaerial portions of ancient continents. They document presence of active hydrologic cycle in the early Paleoproterozoic, in which the isotopic signature of meteoric water originates from evaporation of seawater, and subsequent condensation and precipitation over the land. As in modern world, the precipitation latitude/$\delta^{18}O$ gradients reflects the intimate dependency between the mean annual temperature, vapor-liquid water fractionation and the extent of Rayleigh distillation (Dansgaard, 1964; Bindeman and Lee, 2018). Thus, the isotopic values of the early Paleoproterozoic meteoric waters not only provide the evidence for extensive continents exposed above the sea level, but they also reflect very low mean annual temperatures during the early Paleoproterozoic. Combined with paleogeographic reconstructions, low $\delta^{18}O$ rocks present a unique way to gain insight into the hydrosphere and paleoclimate of the deep past. Given that they are suitable for precise U-Pb dating, they also provide a temporal constraint for the timing of inferred conditions (e.g. Zakharov et al., 2017).

In this study we explore the low $\delta^{18}O$ rocks of the early Paleoproterozoic by providing new measurements from the Belomorian belt and from the low $\delta^{18}O$ Scourie dikes. We focus on documenting recently discovered occurrences of low $\delta^{18}O$ rocks from the Belomorian belt (Fig. 1). This study expands upon those of Bindeman et al. (2010; 2014), Bindeman and Serebryakov (2011) and Zakharov et al. (2017) by providing new H- and triple O-isotope data to further test the hypothesis that these rocks record interactions between low $\delta^{18}O$ glacially derived waters and mafic magmatism during the Paleoproterozoic snowball Earth climate state. These rocks exemplify the water-rock interaction that occurred at low latitudes (c. 30 °S; Mertanen et al., 1999; Salminen et al., 2014) induced by extensive rifting and magmatism in the early Paleoproterozoic snowball Earth climate.

We also provide new H- and O-isotope datasets for the Scourie dikes of the Lewisian complex of NW Scotland (Fig. 2). This study expands upon the work of Cartwright and Valley (1991; 1992) and Davies et al., (2015). Unlike the Belomorian belt rocks, the Scourie dikes likely formed as initially low $\delta^{18}O$ mafic magmas with the values as low as -2 ‰ (Cartwright and Valley, 1991; Davies et al., 2015). To explain their unique O-isotope signature, Scourie dike magma must have interacted with very low $\delta^{18}O$ rocks, comparable to those from the Belomorian belt. This is potentially one of the earliest documented evidence for generation of low $\delta^{18}O$ mafic magmas reflecting interaction between the low $\delta^{18}O$ continental rocks and mantle-derived melts in the Earth's history. Using the triple O-isotope approach we test for incorporation of the

Belomorian-belt-like rocks into the melts that produced Scourie dikes. In addition, the Archean-Paleoproterozoic successions of the Baltic Shield and Lewisian complex share several common features beyond having rocks with low $\delta^{18}O$ values: both provinces have similar 2.7 Ga Archean rocks, mafic intrusions have similar geochemical characteristics and both provinces underwent amphibolite-facies metamorphism between 1.9 and 1.7 Ga (Bridgewater et al., 1995; Whitehouse et al., 1997; Hughes et al., 2014; Stepanova et al., 2017). Their potential geographical proximity in the early Paleoproterozoic (Bleeker, 2003) and globally cold climate with prevalence of low $\delta^{18}O$ precipitation (Bindeman and Lee, 2018) provides a motivation to use O isotopes as a new tool for cratonic correlations (see, Park, 1995; Bleeker, 2003; Nilsson et al., 2010; Davies and Heaman, 2014).

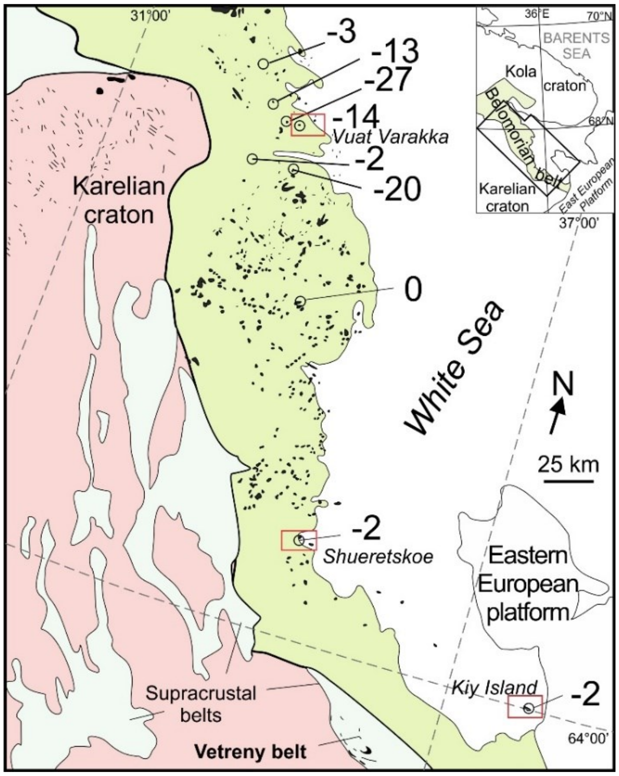

Figure 1. Generalized geological map of the Belomorian belt and adjacent Karelian craton with Proterozoic supracrustal belts (green) and intrusions (black; modified after Slabunov, 2006). The occurrences of low $\delta^{18}O$ rocks are shown with circles. Numbers indicate the lowest $\delta^{18}O$ value measured in garnets at each locality reported in ‰ VSMOW (modified after Bindeman et al., 2014). The samples studied here were collected from the low $\delta^{18}O$ localities outlined with rectangles. Just south of the Belomorian belt, the 2.43 - 2.41 Ga Vetreny belt contains submarine hydrothermally altered rocks providing a record of nearly contemporaneous seawater (Zakharov and Bindeman, 2019).

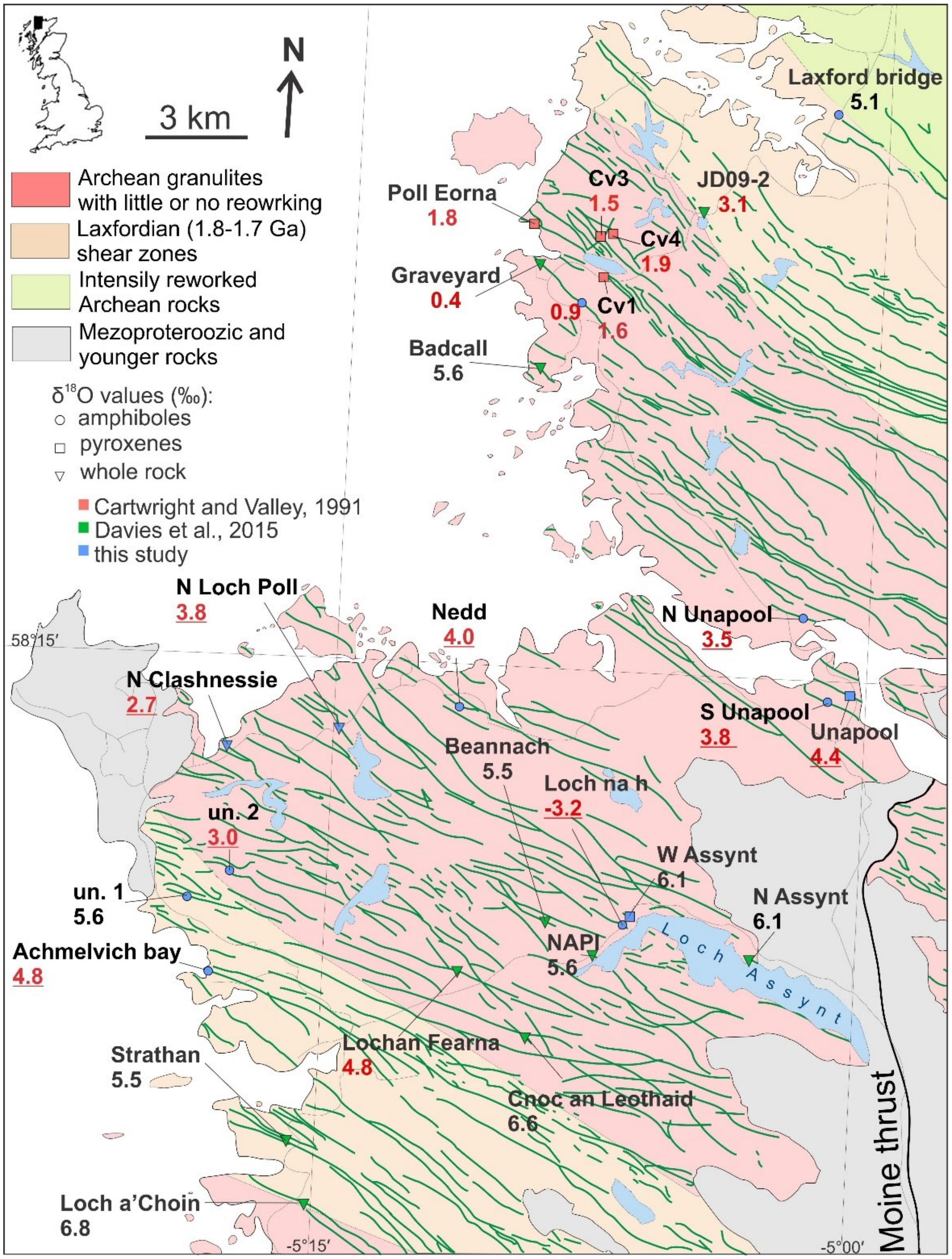

Figure 2. Geological map of the Assynt terrain, Lewisian complex, NW Scotland with numerous Scourie dikes shown in green (modified after Davies et al., 2015). The δ^{18}O values are shown with numbers and were measured in amphiboles, pyroxenes and whole rock samples as indicated by different symbols. The low δ^{18}O values (below the mantle value of 5.6 ‰) are shown in red and newly discovered low δ^{18}O values are underlined. The dikes reported in Cartwright and Valley (1991) are labeled as numbered in the paper with prefix "Cv" except Poll Eorna and Graveyard dikes. Two unnamed dikes sampled in this study are labeled "un.". The dike W Assynt could be a continuation of the N Assynt dike (Davies and Heaman, 2014).

1.2 Definition and use of $\Delta^{17}O$

This study utilizes $\Delta^{17}O$ values to derive $\delta^{18}O$ values of meteoric waters from the rock record. To express triple oxygen isotope composition of a sample, the $\Delta^{17}O$ notation is adopted here and defined as $\delta^{17}O - 0.5305 \cdot \delta^{18}O$, where $\delta^{17}O$ and $\delta^{18}O$ values are conventionally expressed as $1000 \cdot (^{18 \text{ or } 17}O/^{16}O)_{sample}/(^{18 \text{ or } 17}O/^{16}O)_{standard} - 1000$. Recent developments in high precision measurements of $^{17}O/^{16}O$ and $^{18}O/^{16}O$ have resolved systematic variations in $\Delta^{17}O$ in terrestrial materials presenting a novel way to trace water-rock interaction (Herwartz et al., 2015; Sharp et al., 2018; Zakharov and Bindeman, 2019). Meteoric waters originate by evaporation of seawater and have negative $\delta^{18}O$ values relative to the standard Vienna Standard Mean Oceanic Water (VSMOW). The values of meteoric waters become more negative with progress of condensation and precipitation spanning in $\delta^{18}O$ between -60 and 0 ‰, while mantle-derived and continental rocks have distinctly high, positive $\delta^{18}O$ values between +5 and +10 ‰. Governed by small but resolvable differences in mass-dependent fractionations of $^{18}O/^{16}O$ relative to $^{17}O/^{16}O$ between coexisting phases (e.g., water vapor and liquid, or olivine and melt), meteoric waters and rocks form fractionation arrays with different slopes (e.g., 0.528 vs 0.530; Miller, 2002; Luz and Barkan, 2010; Pack and Herwartz, 2014; Pack and Herwartz, 2014; Pack et al., 2016). The $\Delta^{17}O$ values then represent an offset between values measured in a sample and reference line with the slope of 0.5305 in $\delta^{18}O$ - $\delta^{17}O$ space.

This difference in $\delta^{18}O$ - $\Delta^{17}O$ values of meteoric waters and continental crust creates distinctive fields in the triple oxygen isotope space (Fig. 3), with continental hydrothermally altered rocks plotting in between the two. Because of exponential relationship between fractionation factors $^{17}\alpha$ and $^{18}\alpha$, the $\delta^{18}O$ - $\Delta^{17}O$ relationship is nonlinear resulting in the curvature of meteoric water line that spans over several tens of permil. In Figure 3 we also consider possible mechanisms for generation of low $\delta^{18}O$ rocks. Hydrothermally altered rocks acquire low $\delta^{18}O$ signature via high-temperature (> 250 °C) equilibrium fractionation between secondary minerals and meteoric water. At this temperature, fractionation is small, around ~2-3 ‰, resulting in $\delta^{18}O$ and $\Delta^{17}O$ values of hydrothermally altered rocks being very close to that of hydrothermal fluids. At a given temperature and fixed δ^{18}O, Δ^{17}O values of unaltered meteoric water entering a hydrothermal system, the O-isotopic composition of rocks are dependent on the extent of isotopic exchange with fluids, commonly expressed as water/rock ratios (Taylor, 1977). In these coordinates, an array of water/rock (W/R) ratios is a straight line (Fig. 3). Thus, a set of measurements spanning several ‰ due to variable W/R ratios allows to reconstruct the δ^{18}O of meteoric water by finding an intersection of the linear regression and meteoric water line. Further, we consider assimilation of hydrothermally altered rocks by mantle-derived melts, which represents simple mixing between low δ^{18}O component and normal, mid-ocean ridge basalt (MORB) values (Fig. 3). Due very small isotope fractionation at solidus temperatures, the δ^{18}O and Δ^{17}O values of contaminated magmas forms a linear trend, connecting the assimilated material and primary magma (MORB in Fig. 3). Using these considerations and geologic data, we attempt to constrain the δ^{18}O values of meteoric waters in equilibrium with low δ^{18}O hydrothermally altered rocks that were either preserved as is or assimilated by mantle-derived melts. We work under the assumption that the δ^{18}O value of the early Paleoproterozoic seawater was not significantly different from modern-day values (Zakharov and Bindeman, 2019 and references therein). That allows us to explore the relationship between climate, paleogeographic reconstructions and isotope signature of local precipitation. We work under the assumption that the δ^{18}O value of the early Paleoproterozoic seawater was not significantly different from the range of Cenozoic values (Zakharov and Bindeman, 2019 and references therein). That allows us to explore the relationship between climate, paleogeographic reconstruction and isotope signatures of local precipitation.

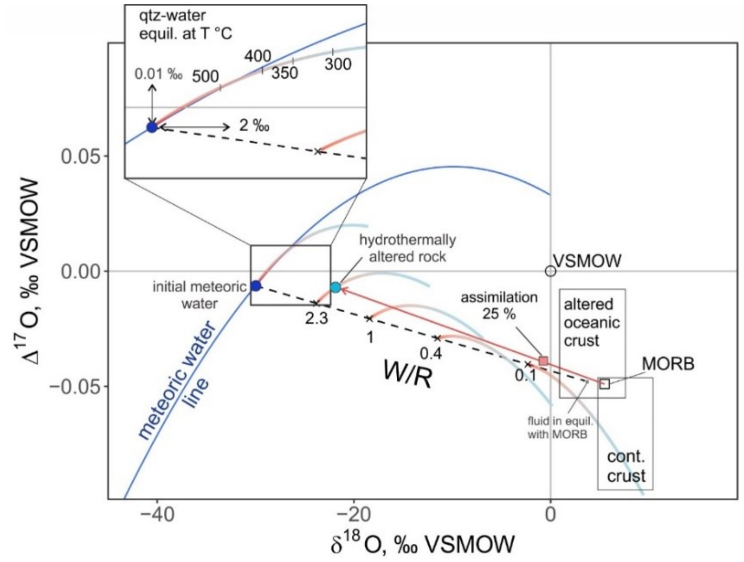

Figure 3. The triple O-isotope approach used here to trace meteoric water-rock interaction (modified after Herwartz et al., 2015). At a given temperature of water-rock interaction, the $\delta^{18}O$ and $\Delta^{17}O$ composition of minerals are dependent on the water-rock ratio (W/R) as shown for interaction between mid-ocean ridge basalt (MORB) and meteoric water with $\delta^{18}O$ of -30 ‰. Equilibrium quartz-water fractionation at 200-900 °C (Sharp et al., 2016) is shown with red-blue curves for W/R rations ranging between 0.1 and infinity, where the red segment corresponds to the temperature >400 °C representing approximate equilibrium fractionation between fluids and common secondary minerals in hydrothermal systems ($\Delta\delta^{18}O_{\text{rock-water}} \approx$ 2-3 ‰ for a mixture of amphiboles, chlorite, epidote and albite; Zheng, 1993). The high-temperature segment of fractionation curve is shown in the inset with arrows indicating the range of values attained by high-temperature hydrothermally altered rocks in equilibrium with pristine meteoric water. Igneous assimilation of low $\delta^{18}O$ rocks that were originally altered at W/R ratio of 2.3 is shown with a red arrow. The resultant magma represents a mixture of 25 % hydrothermally altered rock and 75 % MORB magma. Compositional fields of altered oceanic crust and continental crust are shown after (Bindeman et al., 2018; Sharp et al., 2018).

2.0 Geological setting

2.1 The Belomorian belt, Baltic Shield, NW Russia

The Belomorian belt is an assembly of ~2.7 Ga metasedimentary and metavolcanic rocks intruded by 2.44-2.41 Ga high-Mg gabbro-norites and, in some cases, by Fe-rich gabbros that are 2.3-2.1 Ga in age (Lobach-Zhuchenko et al., 1998; Balagansky et al., 2001; Bibikova et al., 2004; Stepanova and Stepanov, 2010; Stepanova et al., 2017; Zakharov et al., 2017). Collectively, they are interpreted as a fragmented LIP associated with rifting of the Baltic Shield (i.e. Kola and Karelia cratons; Melezhik and Hanski, 2013; Kulikov et al., 2010) and the entire belt was metamorphosed at 1.89 Ga in amphibolite facies (Skiöld et al., 2001; Bibikova et al., 2004). The low $\delta^{18}O$ values ranging from −27 to +3 ‰ are hosted in amphibolites, gneisses and high-Al rocks adjacent to the intrusions (Fig. 1; Bindeman and Serebryakov, 2011; Bindeman et al., 2014). The high-Al rocks contain abundant kyanite, staruolite, garnet, gedrite, corundum, and margarite and their protoliths are thought to be hydrothermally altered rocks (see Bindeman et al., 2014).

Here we focus on 3 new occurrences of low $\delta^{18}O$ rocks. *Vuat Varakka* locality is on the northern shore of the Upper Pulongskoe lake (Verkhneye Pulongskoe ozero, *Russian*), ~5 kilometers away from the Khitoostrov locality described by Bindeman and Serebryakov (2011) with the lowest $\delta^{18}O$ value ever measured in silicate rocks (Fig. 4A). The O-isotope depletion follows a layer of amphibolite and high-Al rocks containing abundant garnet, kyanite, corundum and staurolite in the proximity of the 2.44-2.41 Ga high-Mg gabbro-norite intrusion (Fig. 4B). The core of intrusion is weakly metamorphosed with original igneous pyroxene, plagioclase and olivine crystals preserved. The surrounding amphibolites likely represent metamorphosed and dislocated parts of the same intrusion. *Shueretskoe*, at the southern end of the Belomorian belt, 190 km south from Vuat Varakka, consists of high-Al garnet- and gedrite-bearing biotite gneiss (some are as much as 70 vol. % of garnet) and garnet amphibolite (Fig. 5). These rocks can be traced for 15 km (Glebovitsky and Bushmin, 1983) and in many places are intruded by undated gabbros (Antropov and Kratz, 1960) that likely correspond to the 2.44-2.41 Ga high-Mg gabbro-norites. The third locality is *Kiy Island,* a layered mafic intrusion and is the southern-most occurrence of low $\delta^{18}O$ rocks in the Belomorian belt before sedimentary cover of the East European platform overlay the Baltic shield south of it. The low $\delta^{18}O$ values are hosted in garnet amphibolites and epidosites (Fig. 6). The hosting intrusion consists of differentiated mafic rocks with mostly preserved original igneous minerals and textures, and was dated to 2441±51 Ma using U-Pb geochronology in zircons (Slabunov et al., 2006).

2.2 The Scourie dikes, Lewisian complex, NW Scotland

The Archean Lewisian complex in northwest Scotland (Fig. 2) consists dominantly of felsic orthogneiss with minor metasedimentary units (Park et al., 1995) and records a geological history similar to that of the Belomorian belt. The original rocks of the complex were metamorphosed to granulite facies at ~2.7 Ga, cut by the 2.42-2.38 Ga mafic Scourie dikes (another set of dikes are 1.9-2.0 Ga in age but these are minor; Tarney and Weaver, 1987a; Heaman and Tarney, 1989; Davies and Heaman, 2014; Hughes et al., 2014), and then experienced amphibolite facies conditions during the c. 1.7 Ga Laxfordian event (e.g. Park et al., 1995; Wheeler et al., 2010). The majority of Scourie dikes are quartz tholeiites with minor subsets of them being bronzite picrites, olivine gabbros and norites (Tarney and Weaver, 1987b). They vary in width from a few tens of centimeters to many tens of meters; many of the larger dikes containing coarse interiors with interlocking and ophitic aggregates of plagioclase, pyroxene and iron oxides altered variably to secondary minerals. Their mineralogy, petrography and geochemistry were described with great detail by O'Hara (1961), Tarney (1963), Weaver and Tarney (1981), Tarney and Weaver (1987b), Hughes et al. (2014) and others. Our samples come from the Graveyard, Poll Eorna, Loch na h dikes and other dikes (Fig. 2) in the Assynt terrain of the Lewisian complex, where rocks were least affected by the Laxfordian event and in which low $\delta^{18}O$ values were reported previously (Cartwright and Valley, 1991; Davies et al., 2015). Some of the dikes are locally sheared and turned to amphibolites and thus the exact effect of metamorphism on Scourie dikes in the Assynt terrain has not been resolved completely (Beach 1973; Cartwright and Valley, 1992).

Figure 4 (next page). A – Geological map of the lake Upper Pulongskoe area with the Vuat Varakka locality outlined by solid black rectangular area. The lowest $\delta^{18}O$ value is measured at Khitoostrov locality dated to 2291±8 Ma as labeled (Zakharov et al., 2017). Shown as color coded circles, the $\delta^{18}O$ values are compiled from previous studies (Bindeman et al., 2014) and this study including 200 new values measured dominantly in garnets. Legend: 1 – Kotozero gneiss; 2 – Chupa gneiss; 3 – Khetolambino gneiss; 4 – high-Mg mafic intrusions; 5 – high-Fe gabbro intrusions; 6 - Archean granites; 7 – lowest measured $\delta^{18}O$ value measured at a cluster of measurements; 8 - metamorphic orientation; 9- major faults. B – Detailed map of the Vuat Varakka locality with $\delta^{18}O$ values measured in garnets shown with color coded circles. The lowest $\delta^{18}O$ values (labeled with red numbers) are hosted in amphibolites, gneisses and lenses of high-Al rocks surrounding the 2.44-2.41 Ga high-Mg mafic intrusion shown in black. The two $\delta^{18}O$ values measured in pyroxenes from the gabbro intrusion are shown in white. Legend: 1- high-Al rocks (corundum-bearing); 2 – leucocratic biotite gneiss; 3 – kyanite-garnet-biotite gneiss; 4 – garnet amphibolite; 5 – undifferentiated biotite gneisses and amphibolites.

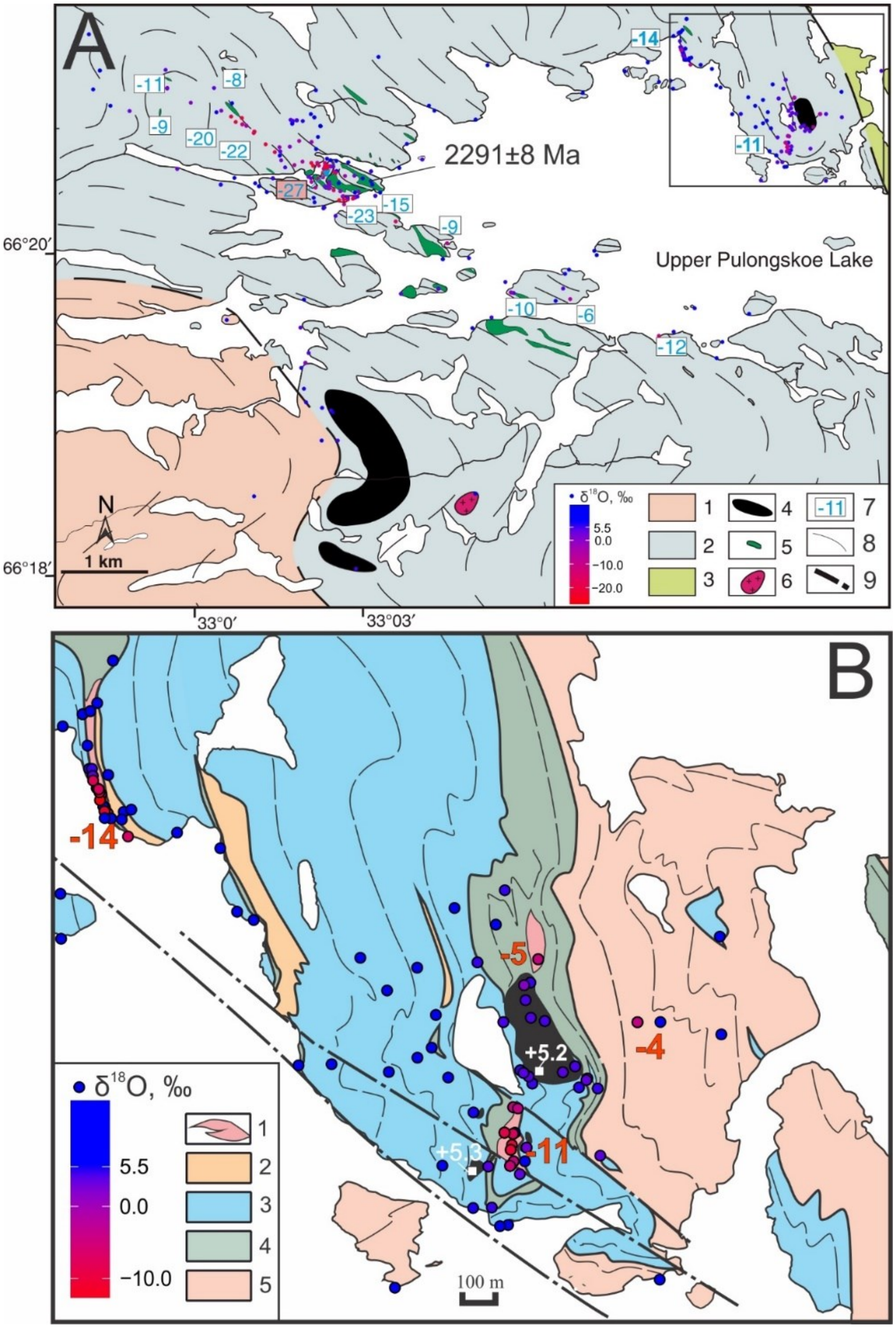
A
-14
-11
-8
-9
-20
-22
-27
-23
-15
-9
2291±8 Ma
-11
66°20′
Upper Pulongskoe Lake
-10
-6
-12
N
1 km
66°18′
33°0′
33°03′
δ18O, ‰
5.5
0.0
−10.0
−20.0
1
2
3
4
5
6
-11
7
8
9
B
-14
-5
+5.2
-4
+5.3
-11
δ18O, ‰
5.5
0.0
−10.0
1
2
3
4
5
100 m

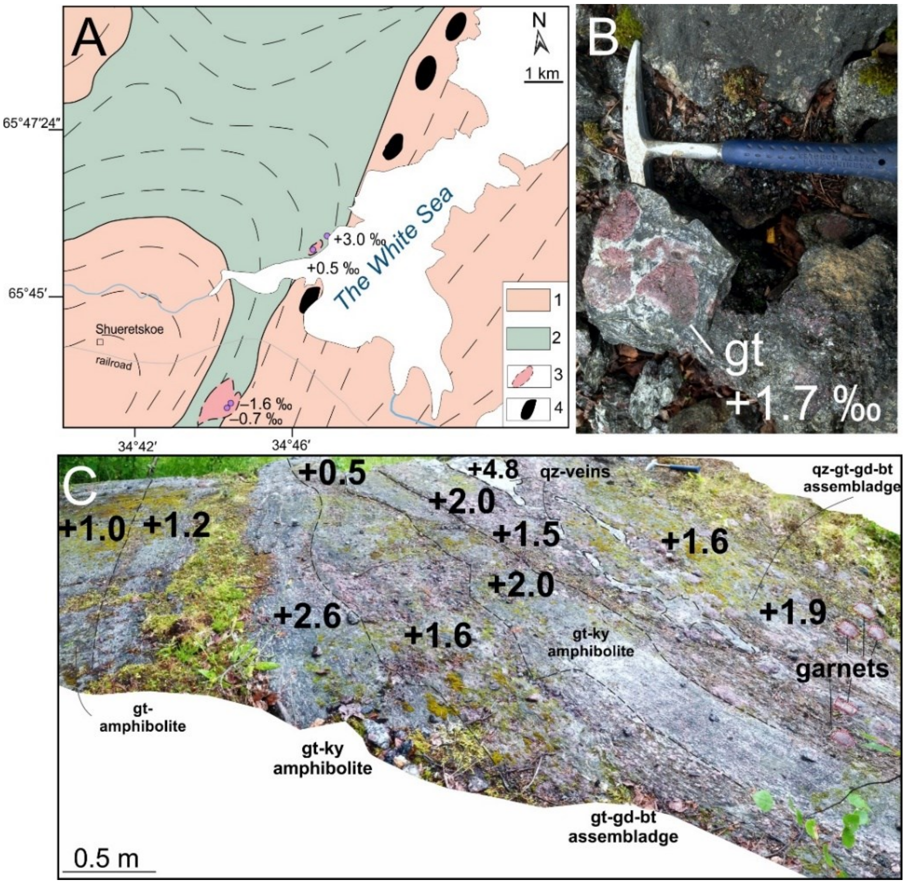

Figure 5. A – Generalized geological map of the Shueretskoe location with the lowest $\delta^{18}O$ values measured in garnets shown with circles and numbers in ‰. Legend: 1 – biotite and garnet-biotite gneiss; 2 – amphibolites; 3 – outcrops of high-Al rocks with kyanite, gedrite and garnet; 4 –mafic intrusions. B – A representative sample of low $\delta^{18}O$ garnet (red) hosted in gedrite (dark green) matrix. C - Panoramic photo view of the outcrop exposed in an old quarry on the White Sea shore (Elovyi Navolok, *Russian*). Large 10-20 cm across crystals of garnet (pink) hosted in garnet-kyanite amphibolite and massive gedrite-biotite rock. The $\delta^{18}O$ values measured in garnets across the outcrop are shown with numbers in ‰. Minerals abbreviations: bt – biotite, gd- gedrite, gt - garnet and ky - kyanite.

3.0 Methods

3.1 Sampling and analytical procedures

A total of 270 samples were collected from the Belomorian belt and 60 from the Lewisian complex, and analyzed for $\delta^{18}O$, $\Delta^{17}O$ and δD. The sampling scheme was designed to identify the aerial extent of O-isotope depletion, the variability of $\delta^{18}O$ values along the strike length of units and from the interior to margins of the intrusive bodies. Further, $\Delta^{17}O$ and δD analyses were used to determine the involvement of meteoric water in the protoliths and its original $\delta^{18}O$ value (see Section 1.2). The $\delta^{18}O$ and $\Delta^{17}O$ measurements were done by laser fluorination with a MAT 253 mass spectrometer following conventional procedure with conversion to CO_2 (see Bindeman et al., 2014) and high-precision triple O-isotope analyses as described in Zakharov et al. (2017). Accuracy of conventional $\delta^{18}O$ analysis involving the CO_2-conversion was monitored by routine measurements of University of Oregon garnet (UOG; $\delta^{18}O = 6.52$ ‰ VSMOW). The measured UOG standards were within 0.3 ‰ of the nominal value. The unknowns were adjusted for the day-to-day variability of the UOG $\delta^{18}O$ values. Accuracy of the triple O-isotope analyses was monitored by including San Carlos olivine (SCO; $\delta'^{17}O = 2.677$ ‰, $\delta'^{18}O = 5.140$ ‰ and $\Delta'^{17}O = -0.049$ ‰ VSMOW-SLAP2; Pack et al., 2016) within each analytical session. After Miller (2002), the linearized delta-notation $\delta'^{17/18}O = 10^3\ln(1 + 10^{-3}\cdot\delta^{17/18}O)$ was used for correcting the values using the measurements of SCO within same analytical session. The average values of our SCO during all analytical sessions were $\delta'^{17}O = 2.828 \pm 0.057$ ‰, $\delta'^{18}O = 5.494 \pm 0.103$ ‰ and $\Delta'^{17}O = -0.086 \pm 0.004$ ‰ (mean ± standard error, n=7). The H isotopes were analyzed in amphiboles, biotites, zoisites and epidotes using a high-temperature conversion elemental analyzer (TC/EA) as described in Martin et al. (2017). The $\delta^{34}S$ analyses of three pyrite samples from the Scourie dikes were carried out at the University of Nevada, Reno, USA, using the same procedure as Grassineau et al. (2001). The uncertainty (±1 standard error) of $\delta^{18}O$ values determined by CO_2 conversion method is 0.1 ‰ or better. For high-precision analysis, the uncertainty of $\delta^{18}O$ and $\Delta^{17}O$ is ±0.010 ‰ and ±0.015 ‰, or better, respectively. The precision of δD analysis is ±4 ‰. Hydrogen and O-isotope values are reported relative to the VSMOW (Vienna Standard Mean Oceanic Water). The $\delta^{34}S$ values were measured at a precision of ±0.2 ‰ and are reported relative to VCDT (Vienna Canyon Diablo Troilite).

4.0 Results

4.1 $\delta^{18}O$ values of the Belomorian belt rocks

We here report the new $\delta^{18}O$ values (see Table S1 in Appendix D) for the three Belomorian belt localities (Figs. 4-6). The $\delta^{18}O$ values were measured in garnets because the mineral is resistant to isotopic re-equilibration during metamorphic retrogression due to slow diffusion of oxygen isotopes, and thus they provide the closest analogue to the

$\delta^{18}O$ values of protoliths (Kohn and Valley, 1998). Garnet is also resistant to weathering and represents the bulk $\delta^{18}O$ value of the sample, within 1-2 ‰, due to high temperature equilibrium between coexisting minerals established during the 1.89 Ga high-grade metamorphism. Several samples of amphibole, corundum, epidote, kyanite, pyroxene, quartz, zoisite and whole rocks were also measured from different localities and reported in Table S1 (Appendix D). We found that measurements of amphibole, corundum, garnet, kyanite and zoisite extracted from same samples return $\delta^{18}O$ fractionation (i.e. $\delta^{18}O_{garnet} - \delta^{18}O_{amphibole} \approx 1000\ln\alpha_{garnet-amphibole}$) between 0 and 1 ‰ in all but one sample; S-18A returned 4.6 ‰ fractionation between amphibole and garnet (coexisting mineral are assembled in Table S2). Fractionation of $\delta^{18}O$ between coexisting quartz and garnets ranges from 1.8 to 3.4 ‰. These fractionations are consistent with high temperature equilibrium (~650 °C; Zheng, 1993) and the metamorphic grade of studied rocks. The $\delta^{18}O$ values measured in garnets at Vuat Varakka scatter between −14 to +8 ‰. Proximal to intrusions, high-Al rocks have garnets with $\delta^{18}O$ values between −14 and +4 ‰ and the adjacent amphibolites also have garnets with low $\delta^{18}O$ compositions, the lowest measured value at −4 ‰ (Fig. 4A). The high-Mg gabbro-norite intrusions sampled in the interior have $\delta^{18}O$ of +5.3 ‰ measured in pyroxenes (Fig. 4B). At Shueretskoe, the $\delta^{18}O$ values measured in garnets vary between −2 and +5 ‰ in amphibolites and high-Al rocks hosting large crystals of garnet and gedrite (Fig. 5). At Kiy Island, the ultramafic layers of the intrusion display original igneous textures and minerals and have $\delta^{18}O$ values from +4.6 to +5.1 ‰ measured in orthopyroxene and amphibole (Fig. 6A). High-Al rocks that contain amphibole, corundum, epidote, garnet, kyanite, and zoisite have δ18O values between -2.1 and +5.7 ‰ (Fig. 6B, C). The lowest δ18O values were measured in garnets hosted in a massive epidosite at the contact between the intrusion and the host rocks (Fig. 6D).

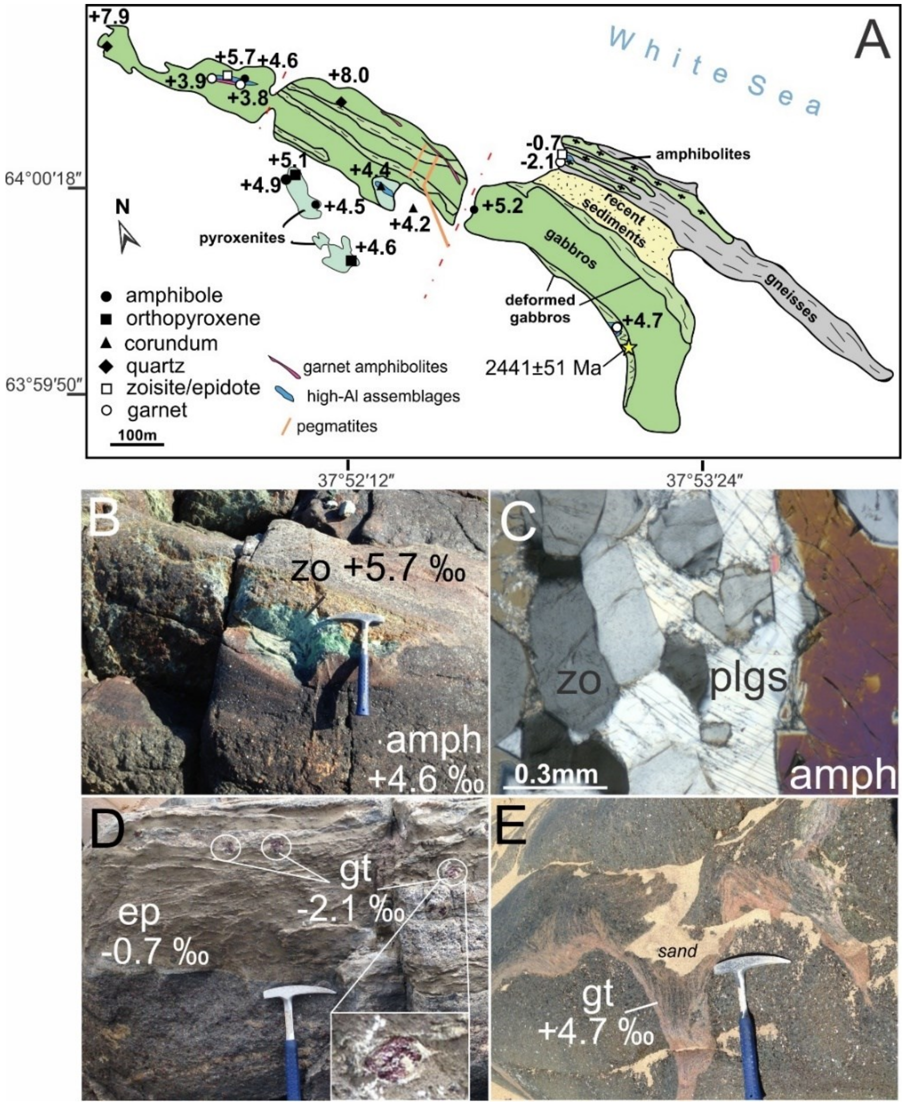

Figure 6. A – Geological map of the Kiy Island locality (modified after Kulikov and Kulikova, 1990). Most of the island is composed of a large layered mafic intrusion (green) dated to 2441 ± 51 Ma using in-situ U-Pb dating (the sample location is shown; Slabunov et al., 2006). Multiple occurrences of high-Al rocks composed of amphibole, zoisite, garnet, corundum, and epidote are exposed within the intrusion and have δ^{18}O values ranging between −2.1 and +5.7 ‰. The lowest δ^{18}O values were measured in garnets from epidosite at the contact of the intrusion with hosting amphibolite; B –high-Al rock containing green zoisite (zo) and black amphibole (amph) with their δ^{18}O values shown; C – a microphotograph of the massive zoisite-rich rock shown in B in transmitted cross-polarized light featuring idiomorphic crystals of zoisite (zo), surrounded by plagioclase (plgs) and amphibole (amph); D – the low δ^{18}O epidosite (ep) with crystals of garnet (gt) hosted at the contact between the gabbros and amphibolites. The inset shows a magnified image of a garnet crystal ~5 cm across; E – An outcrop of deformed gabbro with foliated garnet-rich layer. Photograph taken near the sample collected for U-Pb geochronology.

4.2 δ^{18}O values of the Scourie dikes

The δ^{18}O values of Scourie dikes from the Assynt terrain are show in Fig. 2, and reported in Table S3; these include new values for dikes analyzed previously (Cartwright and Valley, 1991; Davies et al., 2015) and nine new low δ^{18}O occurrences. The δ18O values of coexisting minerals from the lowest δ18O dike Loch na h are assembled in Table S4. In Table S5 we also report new δ^{18}O values for the Archean rocks of the Lewisian complex, including felsic, mafic granulites, metasedimantery units from Stoer area as well as three samples from the South Harris Igneous complex including a sample of hosting metasedimentary gneiss (Cliff et al., 1983). Most Scourie dikes were measured using amphibole and pyroxene separates collected from the freshest portions of the coarse-grained interiors of the dikes. These minerals are abundant in the dikes and are more resistant to secondary exchange and retrogression than other common minerals such as plagioclase and magnetite (Farver and Giletti, 1985; Kohn and Valley, 1998). Cartwright and Valley (1991) showed previously that whole-rock δ^{18}O values from the Scourie dikes matched closely (<1 ‰ difference) those from amphiboles and pyroxenes. We also analyzed several whole rock samples of the dikes' fine-grained chilled margins.

Our work has identified several permil variations within dikes sampled along their strike and large differences between the interiors and chilled margins (Fig. 7). To show variability in each dike and equilibrium fractionations, we compiled previously and newly reported δ^{18}O values for mineral separates and whole rock values for the Graveyard, Poll Eorna, Loch na h and other dikes in Figs. 7 and 8. We report several new occurrences of low-δ^{18}O Scourie dikes with values that span between −3 and +6 ‰. The lowest values are measured in amphiboles and magnetites of the Loch na h dike on the west shore of the lake Loch Assynt (see Fig. 8). Sampled in multiple locations along strike (Fig. 7B), the Loch na h dike returned range of values from −3.68 to −2.22 ‰ (n = 8) measured in amphibole, −4.78 to −3.27 ‰ (n = 3) in magnetite, and −0.36 to +3.23 ‰ (n= 5) in plagioclase. Given compositions of c. 47 % amphibole, c. 47% plagioclase and c. 6% magnetite, and assuming that the lowest δ^{18}O values represent original magmatic values (Cartwright and Valley, 1991; Davies et al., 2015), the coarse-grained interior of the dike has calculated whole rock δ^{18}O value of about −2.5 ‰. Plagioclase-amphibole (plagioclase composition ~An_{40}; Davies et al., 2015) pairs exhibit fractionations between

2.0 and 6.2 ‰, yielding computed isotope equilibrium temperatures between 200 and 560 °C using the diopside-plagioclase fractionation factor (Chiba et al., 1989) as a close approximation for amphibole-plagioclase fractionation (see Table S4). Amphibole-magnetite pairs yield fractionations between 1.0 and 2.6 ‰, corresponding to equilibrium temperatures of above 900°C (Chiba et al., 1989). The whole rock sample of chilled margin returned $\delta^{18}O$ value of 5.04 ‰, significantly higher than the $\delta^{18}O$ values calculated for the interior of the dike, while the hosting Lewisian gneiss has $\delta^{18}O$ value of 7.51 ‰.

Figure 7 (next page). The $\delta^{18}O$ values analyzed in amphiboles, pyroxenes and whole rock samples in dikes Poll Eorna, Graveyard and Loch na h based on previous studies and this work. The $\delta^{18}O$ value measured in chilled margins are shown in italic. The $\delta^{18}O$ values measured in zircons (zr_{min}) and respective whole rock samples are from Davies et al., (2015). A - The Poll Eorna and Graveyard dikes in the area of Scourie with variable $\delta^{18}O$ values measured along the strike. Large variations were observed in the shear zones and are accompanied by increase in $\delta^{18}O$ of Poll Eorna dike by 4 -5 ‰ as reported previously (Cartwright and Valley, 1991). Smaller variations (1-3 ‰) were measured in amphiboles from coarse-grained interior even without sign of shearing. B – Location and $\delta^{18}O$ values of analyzed amphiboles from the Loch na h dike. The total range of values measured in amphiboles (n = 8) spans between −3.7 and −2.2 ‰, much lower than previously reported for the Scourie dikes. C – A cross polarized light microphotograph of the coarse-grained interior of the Loch na h dike showing abundant amphibole almost completely replacing clinopyroxene; plagiolclase is altered to sericite in the cores and magnetite is partially covered with a rim of biotite. A thin quartz-calcite vein dissects the section indicating fluid-induced alteration. D – A cross polarized light image of the fine-grained chilled margin of the Loch na h dike showing abundance of secondary actinolite, sericite and chlorite almost completely replacing primary pyroxenes and plagioclase. Clay minerals record low-temperature alteration of the chilled margin which is consistent with the $\delta^{18}O$ value of 5.04 ‰, much heavier than the low $\delta^{18}O$ interior of the dike. The inset shows a magnified portion of the image (~2 times larger).

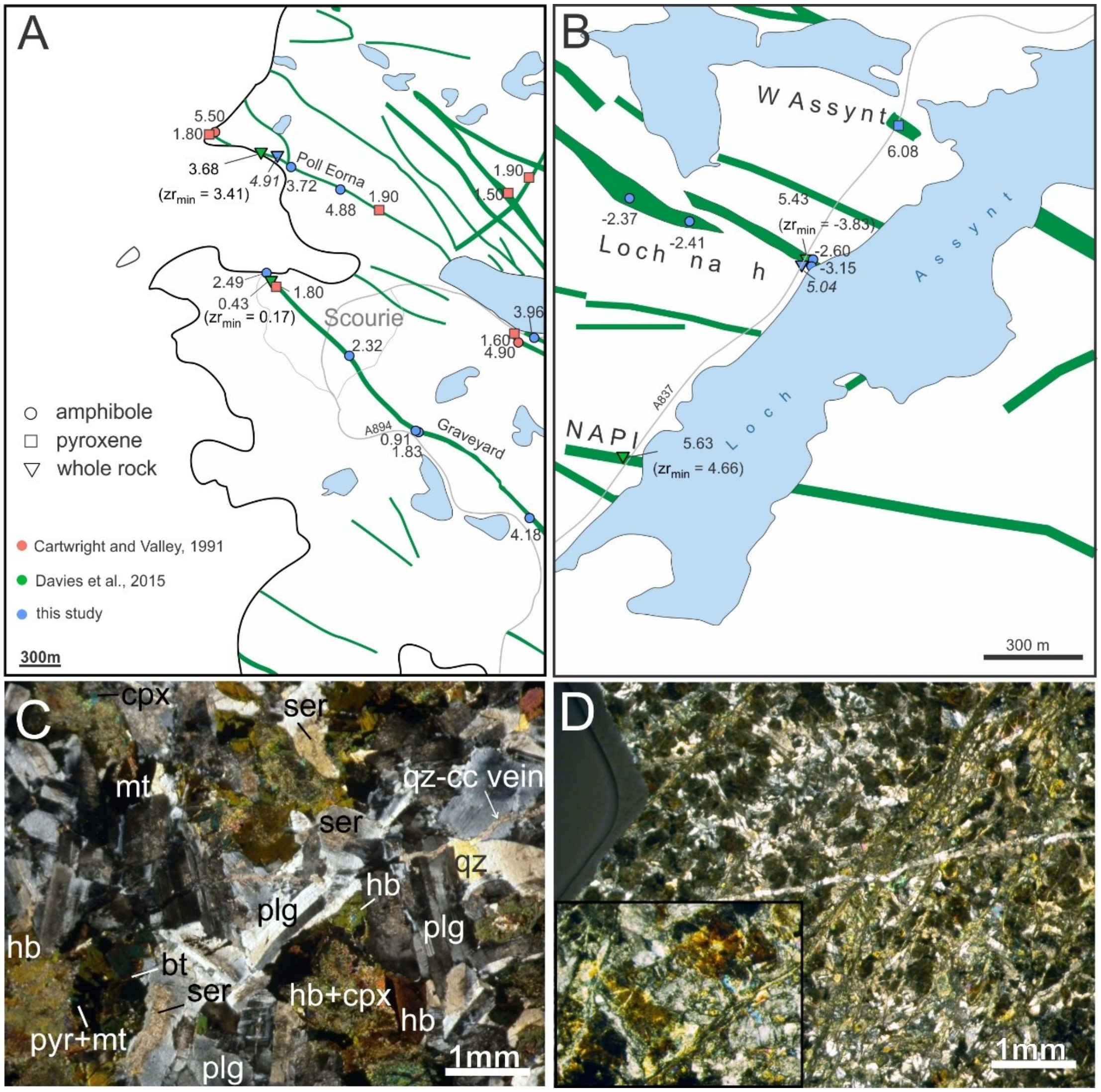

4.3 Petrography of the Loch na h dike

To better understand the $\delta^{18}O$ values from the Loch na h dike, we made thin sections from the coarse-grained interior and fine-grained chilled margin. The interior displays original igneous textures with preserved igneous minerals and abundant secondary minerals replacing them (Fig. 7C). Pyroxenes are extensively altered to an aggregate of amphiboles; magnetites are altered to biotite and calcic-rich plagioclase to sericite. The dike contains abundant fine quartz-calcite veinlets (Fig. 7C). Pyrite is found in the dike forming disseminated anhedral grains in spatial association with magnetite. The fine-grained chilled margins are thoroughly altered to an aggregate of sericite, chlorite and actinolite with some relicts of original igneous phases (Fig. 7D). We observed several generations of fine chlorite-actinolite veins and quartz-calcite veins cross-cutting each other indicating pervasive sub-solidus alteration by aqueous fluids.

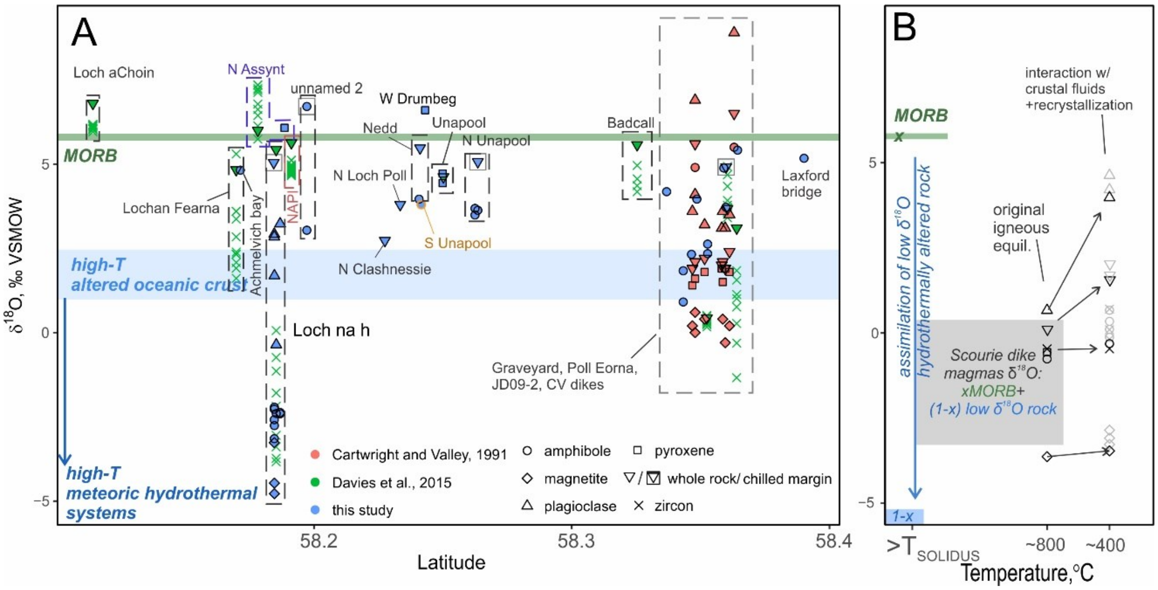

Figure 8. A - Oxygen isotope values for mineral separates and whole rock samples compiled from the study and from previously published results plotted against their latitude position (see Fig. 2). The δ^{18}O values of MORB and high-temperature altered oceanic crust are shown with horizontal bands. Shallow meteoric hydrothermally altered rocks have a wide range of values, mostly below 0 ‰, which indicates that at least a fraction of Scourie dikes originated due to interaction with such rocks. B - A possible origin of low δ^{18}O signature of Scourie dikes: the initial MORB-like melts were contaminated by low δ^{18}O hydrothermally altered rocks. Initial high-temperature magmatic O-isotope equilibrium at ~800 °C was attained by crystallized igneous minerals. The effect of post-emplacement alteration via recrystallization and interaction with crustal fluids at 400 °C is shown. Note that due to variable susceptibility of minerals to isotope exchange with fluids, the associated δ^{18}O shift in different minerals is also variable (shown with arrows). Hypothesized range of values caused by recrystallization is shown with grey symbols.

4.4 Δ^{17}O values

The results of high-precision triple O-isotope analyses of the Belomorian belt rocks and Scourie dikes are listed in Tables S6 and S7, and are displayed in Figure 9. The values adapted from previous investigation of the Belomorian rocks (Herwartz et al., 2015; Zakharov et al., 2017) were recalibrated to San Carlos olivine (SCO) standard with Δ^{17}O = −0.053 ‰ (Pack et al., 2016). The compositions of reference materials used here are reported in Table S8. Ranging from −14 to −8 ‰ in δ^{18}O, the Vuat Varakka garnets have $\Delta^{17}O$ values between −0.10 and −0.05 ‰, similar to other low and ultra-low $\delta^{18}O$ localities Khitoostrov, Varatskoe, Height 128 (see Zakharov et al., 2017; Fig. 9A). Grouped together with these localities, the linear regression line yields an intersection with meteoric water at $\delta^{18}O$ of −38 ± 3 ‰ (Fig. 9).

Figure 9 (next page). Triple O-isotope composition of the low-$\delta^{18}O$ rocks from the Belomorian belt (A) and Scourie dikes (B) with linear regression and 95 % confidence intervals shown. Meteoric water line is shown with the blue curve (Luz and Barkan, 2010). Values of modern glacial ice ($\delta^{18}O$ below −20 ‰) are depicted by the cyan-blue segment. A - The samples from Vuat Varakka are consistent with involvement of meteoric water with $\delta^{18}O$ value of −38 ‰, plotting together with in other low- and ultralow $\delta^{18}O$ localities in the Belomorian belt. Samples from Shueretskoe and Kiy Island indicate that meteoric water with $\delta^{18}O$ of −9 ‰ is recorded in some hydrothermal systems. Small grey squares represent samples from previous studies (light grey – Herwartz et al., 2015; dark grey – Zakharov et al., 2017). See Figure S1 (Appendix D) for the list of localities from the previous studies. Compositions of hydrothermally altered rocks in equilibrium with pristine meteoric water are shown with curves next to the meteoric water line. They represent end-member compositions altered at infinite W/R ratios (ratios 0.1-2.3 are shown with crosses and numbers). One sample with $\Delta^{17}O$ value close to -0.2 ‰ was likely altered at low temperature (<200 °C) or undergone weathering. B - The $\delta^{18}O$ and $\Delta^{17}O$ values of the Scourie dikes are shown along with possible compositions of hydrothermally altered rocks that can produce the signature of analyzed samples through assimilation (dark shaded regions). For dike localities shown here see Figure S1. High W/R ratio end-members are shown with curved segments parallel to the meteoric water line. A subset of samples (Loch na h dike) with values <0 ‰ plotting in the dark-yellow shaded region outlined by dashed lines require involvement of extremely low $\delta^{18}O$ hydrothermally altered rocks, similar to the samples from Belomorian belt. Two possible trajectories of magmatic assimilation of such rocks by mantle-derived magmas are shown with the red dash-dotted lines. The numbers in percent denote the mixing fraction of incorporated material. About 30 % of assimilated material with isotopic signature of Belomorian belt samples ($\delta^{18}O$ = -20 ‰, $\Delta^{17}O$ = -0.05 ‰) is required to reproduce the lowest $\delta^{18}O$ samples from Loch na h dike. It can be achieved by addition of smaller amount (~ 20 %) of hydrothermally altered end-member at high W/R with $\delta^{18}O$ = −35 ‰. The encircled blue area represents submarine hydrothermally altered basalts which were previously suggested as the source for Scourie dike magmas (values from Sengupta and Pack, 2018; Zakharov and Bindeman, 2019). The assimilation paths for the dikes with modest O-isotope depletion ($\delta^{18}O$ = 0 – 2 ‰) are difficult to constrain due to limited range and scatter of values.

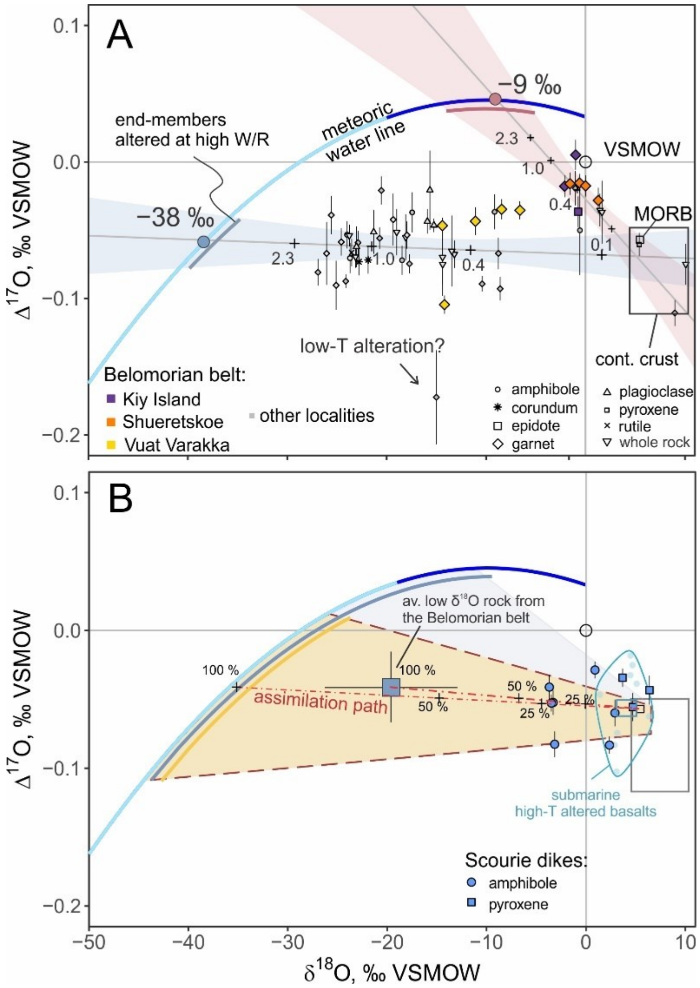

The Shueretskoe and Kiy Island garnets have distinctly different values compared to those from Vuat Varakka: $\Delta^{17}O$ values vary between −0.05 and 0 ‰ and yield an intersection at −9 ± 5 ‰ for the $\delta^{18}O$ of the meteoric water (Fig. 9A). The Scourie dikes were measured using pyroxenes and amphiboles that range in $\Delta^{17}O$ from −0.10 to −0.02 ‰. The $\delta^{18}O$ and $\Delta^{17}O$ values in amphiboles of Loch na h dike plot between the mantle and meteoric waters, indicating incorporation of a component similar to the low $\delta^{18}O$ rocks from the Belomorian belt (Fig. 9).

4.5 δD values

The δD values as well as H_2O wt. % are reported in Table S9. The δD values are plotted against $\delta^{18}O$ values in Figure 10. Most δD analyses were done on amphiboles; a few on epidote, zoisite, staurolite and whole rock samples (see Table S9). The δD values for the Belomorian belt are between −185 and −24 ‰ and those for the Scourie dike amphiboles are between −92 and −65 ‰. The hosting Lewisian gneisses and metasedimentary rocks yield whole-rock values between −52 and −36 ‰.

4.6 δ^{34}S values

Three analyses of pyrites from the Scourie dikes returned δ^{34}S values between 1.2 and 1.8 ‰; these, along with their δ^{18}O values, are reported in Table S10. These results show that sulfur was likely sourced from the mantle-derived melts, not providing an additional insight into the interaction with meteoric water or seawater. Thus the δ^{34}S values are not regarded in subsequent discussion.

5.0 Discussion

5.1 Origin of δ^{18}O values in the Belomorian belt

The low δ^{18}O values in the Belomorian belt are concentrated around mafic intrusions dated at c. 2.4 Ga. The central parts of intrusions have mantle-like δ^{18}O values (c. 5.6 ‰) whereas low δ^{18}O values occur in host rocks adjacent to and along the contacts of the intrusions. We interpret this as due to hydrothermal alteration of the Archean protoliths induced by intrusion of the early Paleoproterozoic mafic magmas, with the high-Al rocks near the contacts related to chemical alteration of the protoliths. The O-isotope signatures were likely attained while the magma body was still hot enabling low δ^{18}O meteoric water to interact with the host rocks at high temperature when the fractionation between most minerals and water is minimal (about 1-3 ‰; Zheng, 1993). Such process is well known and has been documented elsewhere where intrusions interacted with low δ^{18}O meteoric waters at high temperatures (300 – 500 °C; e.g. Taylor et al., 1971). Later metamorphism is unlikely to have generated these O-isotope values because during solid-state recrystallization the δ^{18}O values of metamorphosed rocks are largely governed by that of the protoliths (Taylor, 1974; Valley, 1986; Hoefs, 2018 and references therein). This is further supported by the δ^{18}O values and ages of zircons from these rocks: the Archean or Paleoproterozoic cores have normal δ^{18}O values while metamorphic rims have low δ^{18}O values which formed at 1.89 Ga by crystallization from the low δ^{18}O hydrothermally altered protoliths (see data in Bindeman et al., 2014). Consequently, we interpret our low δ^{18}O and Δ^{17}O values as due to hydrothermal alteration occurring close to the time of emplacement of the mafic bodies.

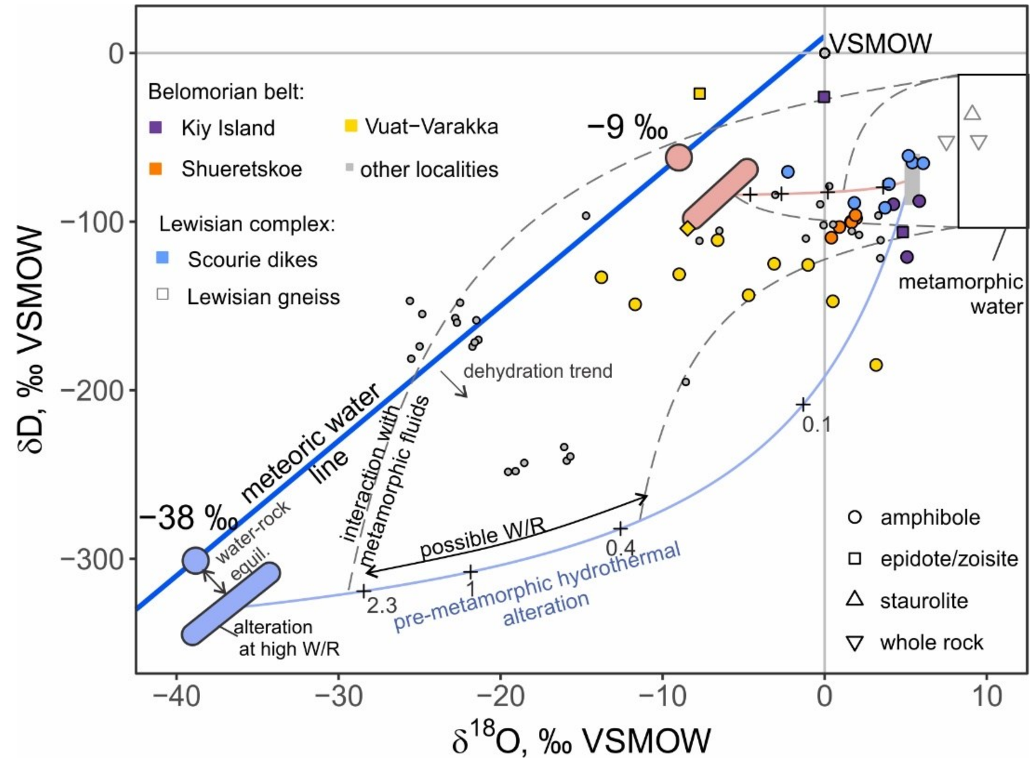

Figure 10. Hydrogen and O-isotope compositions of the Belomorian belt rocks and the Scourie dikes including the hosting Lewisian gneiss. The low $\delta^{18}O$ rocks from the Belomorian belt described here are color coded as shown in the legend. Grey-filled circles plotted after analyses published in Bindeman and Serebryakov (2011). See Figure S2 (see Appendix D) for the list of localities from previous studies shown here. In the Belomorian belt, the measured δD values represent a mixture of inputs from original isotopic composition of hydrothermally altered rocks (shown as solid colored curves with crosses at different W/R ratios) and interaction with metamorphic fluids (dashed grey curves). The initial pre-metamorphic range of possible values is shown with curved arrows at W/R ratios as indicated by the triple O-isotope approach, between about 2.3 and 0.4. The compositions of original hydrothermally altered rocks at infinitely high W/R ratios are shown with oval shapes. Equilibrium meteoric waters computed from the $\Delta^{17}O$ data are shown with red and blue circles. The contribution of dehydrating reactions is shown with the arrow and is likely small due to high-temperature fractionation between minerals and water. In the Scourie dikes, the extent of preservation of original δD values and metamorphic overprint is unresolved, however some amphiboles have δD values slightly lower than accepted δD range of mantle-derived rocks (Hoefs, 2018), and about 60 ‰ lower than the δD values of hosting Lewisian gneiss indicating possible presence of meteoric component in the dikes. For dike localities shown here see Figure S2.

The $\Delta^{17}O$ approach is used here to reconstruct the meteoric water involved in the ancient hydrothermal systems and to account for the unknown extent of isotopic exchange that modified pristine meteoric water (as described in Section 1.2). In the

Belomorian belt, the Vuat Varakka locality (and other ultra-low $\delta^{18}O$ occurrences such as Khitoostrov and Varatskoe; see Fig. 1) indicate involvement of meteoric water with $\delta^{18}O$ of about −38 ‰, which in the modern world corresponds to the $\delta^{18}O$ value of high-latitude glacial ice and snow (Fig. 9A). The triple O-isotope composition of rocks from Shueretskoe and Kiy Island indicates involvement of much heavier $\delta^{18}O$ value of meteoric water of around −9 ‰, which is characteristic of near-coastal regions in the modern world and generally, precipitation at low latitudes (Dansgaard, 1964; Bowen, 2010). Thus, the original meteoric water was, from place to place, variable in its $\delta^{18}O$ composition and this is recorded in the observed differences in the Belomorian belt rocks that span about 40 ‰ in $\delta^{18}O$. The triple O-isotope composition of these rocks allows to reconstruct the extent of isotopic exchange within the ancient hydrothermal systems: the W/R mass ratios varied from 0.1 to 2.3 (see Fig. 9). We should acknowledge that these are minimum estimates of W/R ratios since the rocks likely interacted with metamorphic fluids. Interaction with metamorphic fluids is registered in these rocks using H-isotope values (see Section 5.3); thus the O-isotope values could have been shifted only a few per mil (if at all) due to abundance of oxygen in rocks (Taylor, 1974). Bindeman et al. (2014) attributed ~+3 ‰ shifts measured *in situ* within single grains of corundums and zircons to interaction with metamorphic fluids in the Belomorian belt. Interaction with metamorphic fluids would shift the $\Delta^{17}O$, likely, towards the values of continental crust rocks (see Fig. 9). However, 3 ‰ shifts constitute only a small fraction of the total range of observed $\delta^{18}O$ values in the Belomorian belt localities spanning over about 40 ‰. We consider that the $\delta^{18}O$ values of the rocks within each locality dominantly reflect the effect of variable W/R ratios, while the values across the belt also reflect differences in compositions of local meteoric waters.

5.2 Origin of low $\delta^{18}O$ values in the Scourie dikes

The range of $\delta^{18}O$ values measured in Scourie dikes is consistent with the previous investigations (see Fig. 8; Cartwright and Valley, 1991; Cartwright and Valley, 1992; Davies et al., 2015). Magmatic origin of low $\delta^{18}O$ values in the Scourie dikes (Cartwright and Valley, 1991; Cartwright and Valley, 1992; Davies et al., 2015) was originally suggested based on preservation of small high-temperature, magmatic (600-800 °C) O-isotope fractionation recorded by mineral pair measurements from unsheared, coarse-grained parts of dikes and absence of low $\delta^{18}O$ values in the host rocks. In addition, our measurements of hosting Archean orthogneisses, mafic granulites, metasedimentary units of the Assynt terrain and younger rocks from the South Harris Igneous complex returned values above +5.4 ‰. Based on the new insights offered by the combined $\delta^{18}O$-$\Delta^{17}O$ measurements presented here, we attempt to explain the origin of isotopic signature of the lowest $\delta^{18}O$ Loch na h dike, and possibly the other Scourie dikes too. We should first note that the comparatively high $\delta^{18}O$ values measured in sheared zones (up to +6 ‰; Cartwright and Valley, 1991) and variable $\delta^{18}O$ values measured along strike likely represent complex post-emplacement interaction with crustal fluids during subsequent metamorphic events, e.g. Laxfordian event (see Fig. 8B). Conforming to this is the fact that we did not find any $\delta^{18}O$ values lower than those measured in low-Ca zircons that experienced least amount of radiation damage (Davies et al., 2015). Similar to interpretation of the O-isotope data measured in zircons, we consider the lowest $\delta^{18}O$ value measured within the same dike to be the most reflective of the original magmatic signal. This suggests that the $\delta^{18}O$ values of +5.0 - 5.4 ‰ measured by us and Davies et al. (2015) in the chilled margin of the lowest $\delta^{18}O$ Loch na h dike is due to subsequent interaction with fluids, which is also now supported by the petrographic evidence (Fig. 7). Below we outline possible mechanisms that could have generated the low $\delta^{18}O$ signature in the Scourie dikes rocks.

Original studies (Cartwright and Valley, 1991) identified dikes with values 3 ‰ lower than the $\delta^{18}O$ expected for mantle-derived magmas (c. 5.6 ‰), interpreting this as a result of melting of low $\delta^{18}O$ hydrothermally altered oceanic crust. However, the range now extends to negative values recorded in amphiboles, magnetites and in zircons of the Loch na h dike (Davies et al., 2015), corresponding to $\delta^{18}O$ value of equilibrium melt of about -2.5 ‰. Generation of such low $\delta^{18}O$ magmas is not compatible with melting of lower oceanic crust and requires an addition of hydrothermally altered component that experienced high-temperature isotope exchange with isotopically negative meteoric water in subaerial environment. The lowest value that can be achieved by altered oceanic crust is ~ +2 ‰; this constraint is derived from high temperature fractionation between pristine seawater ($\delta^{18}O = 0$ ‰) and secondary minerals at infinitely high W/R ratios. Such values are sparsely present in the oceanic crust. The overall range of seafloor hydrothermally altered rocks is between +2 and +5 ‰, with average values of about +3-4 ‰ (Alt and Teagle, 2000). Much lower $\delta^{18}O$ of Archean seawater and thus, possibly much lower $\delta^{18}O$ values of altered oceanic crust, presents a possible explanation for the low $\delta^{18}O$ values of the Scourie dikes, however all known examples of submarine altered basalts of Archean and early Paleoproterozoic age exhibit $\delta^{18}O$ values comparable to modern-day oceanic crust (e.g., Holmden and Muehlenbachs, 1993; Furnes et al., 2007; Hodel et al., 2018; Zakharov and Bindeman 2019).

We thus suggest that contamination of mantle-derived melts by low $\delta^{18}O$ hydrothermally altered rocks is a more probable explanation. Based on the new $\Delta^{17}O$ data and insights from the Belomorian belt rocks, we explore the possibility of reconstructing $\delta^{18}O$ value of the protoliths assuming that the isotopic signature was generated by mixing between isotopic composition of hydrothermally altered rocks and mantle-derived mafic magmas. If the uncontaminated magmas had $\delta^{18}O$ values of MORB, the values recorded in the Loch na h dike reflect contribution of very low $\delta^{18}O$ component which experienced alteration by meteoric water with $\delta^{18}O$ values in a broad range, between −45 and −25 ‰ (Fig. 9B). The relationship between $\delta^{18}O$ and $\Delta^{17}O$ in meteoric waters (Luz and Barkan, 2010) was likely similar to the modern (Bindeman and Lee, 2018), constraining the amount of hydrothermally altered rock incorporated into the mantle-derived melts to about 20-30 % (Fig. 9B). This number would be higher if the protoliths were altered at lower water-rock ratios and vice versa. This explanation is based on the lowest $\delta^{18}O$ Loch na h dike, assuming that it records the highest fraction or/and the lowest $\delta^{18}O$ value of assimilated component. It is possible that other dikes, with higher $\delta^{18}O$ values (+2 ‰) were produced by assimilation of smaller amounts of such low $\delta^{18}O$ component or by melting of the high-temperature altered oceanic crust, or both (Fig. 9). The limited range of $\delta^{18}O$ values in these dikes does not allow us to constrain the fraction of the $\delta^{18}O$ value of assimilated material.

We should note that this interpretation is independent of the exact mechanism by which the mantle-derived melts were able to incorporate low $\delta^{18}O$ rocks. Assimilation of solid rocks, partial melting and mixing, or even subduction of low $\delta^{18}O$ hydrothermally altered rocks in the melting region, all would lead to almost identical triple O-isotope signature of the resulted magma due to minimal isotopic fractionation at temperatures of magmatic solidus. Given that the estimated erosion level of the Assynt terrain corresponds to the lower crust levels (5-7 kbar; ~500 °C; O'Hara, 1961; Tarney, 1963), assimilation of low $\delta^{18}O$ hydrothermally altered rocks that originated in the near-surface environment presents a puzzling explanation. Moreover, no low $\delta^{18}O$ rocks were found in the area, including the numerous analysis published previously (Cartwright and Valley, 1992) and this study, where we searched for hydrothermally altered rocks within metasedimentary units near Stoer area all of which returned values +7 ‰ and higher (Table S5). Subduction of low $\delta^{18}O$ rocks into the melting region (i.e. contamination of the mantle source; Hughes et al., 2014) would be consistent with emplacement of dikes in the lower crust, however, low $\delta^{18}O$ hydrothermally altered rocks overall do not provide volumetrically significant reservoir of O-isotopes compared to the crustal and mantle reservoirs that participate in subduction and partial melting. Alternatively, we suggest that the low $\delta^{18}O$ signature of rather thick Scourie dikes, a least partly, might have originated during closely spaced syn-eruptive alteration and partial remelting of the mafic dikes. This would explain occurrence of somewhat diverse $\delta^{18}O$ values in zircons with homogenous U-Pb ages (Davies et al., 2015), variations in $\delta^{18}O$ values along strike measured within coarse-grained interiors and high MgO content of the dikes. Similar processes occur in modern LIPs and areas of extensive rifting, for example in the Columbia River Basalt province of North America or fissure basalts in Iceland, where heat derived from storage of large volumes of magmas promotes hydrothermal alteration, remelting and assimilation of low $\delta^{18}O$ crust (Bindeman et al., 2012; Colón et al., 2015).

5.3 Hydrogen isotopes

Because hydrogen is only a minor element weakly bonded in silicates, its isotope composition is often reset due to subsequent interaction with crustal fluids. Given that both the Belomorian rocks and Scourie dikes underwent variable extent of metamorphism, hydrogen isotopes likely experienced a wide variety of changes including interaction with metamorphic fluids and dehydrating reactions (Fig. 10). Consequently, we view the δD values as recording a mixed input from dehydration of the original protoliths and from the later reaction with metamorphic fluids. At the estimated temperatures of metamorphism in the Belomorian belt (600-700° C), fractionation between amphiboles and water is around 10 ‰ for δD (Suzuoki and Epstein, 1976), thus, amphiboles closely reflect the δD of metamorphic fluids. Previous dehydration reactions of preexisting minerals likely contributed to negative shifts of δD values. The lowest δD values were probably inherited from dehydration of those photoliths because secondary processes involving crustal fluids would only increase the δD values. This interpretation is supported by finding the correlation between the lowest δD values and the lowest δ^{18}O values (down to −235 ‰ δD and −27 ‰ in δ^{18}O reported by Bindeman et al., 2014). In this study, the Vuat Varakka locality contains δD values as low as −190 ‰ with δ^{18}O of −14 ‰, whereas the lowest δ^{18}O samples (−2 ‰) from the Shuereskoe and Kiy Island localities returned the lowest δD value of −100 ‰.

Compared to their Belomorian rocks, the low δ^{18}O Scourie dikes have higher δD values; these fall at the low end of the range for MORB, which is −90 to −60 ‰ (Fig. 10; Hoefs, 2018). Such values generally fit the proposed model above; the H-isotope composition indicates the dominant input from the mantle, allowing for a small addition of hydrothermally altered rocks. However, it is likely that dehydration during melting and post-emplacement alteration (as seen in thin sections) occurred, in combination obscuring the H-isotope signature of original melts. Clearly, the δD values of studied here rocks were significantly altered during subsequent interaction with crustal/metamorphic fluids. Hence, the triple O-isotope approach undertaken here provides a more robust record of interaction with ancient meteoric waters.

5.4 Implications for paleoclimate: paleolatitude and age constraints

This study relates two early Paleoproterozoic provinces that recorded interaction with very low δ^{18}O meteoric waters. Such record provides evidence for substantial portions of continental crust exposed above sea-level allowing for active hydrologic cycle to exist. The O-isotope ratios in precipitation vary largely as a function of mean annual surface temperature which in turn depends on the latitude position of the region (Dansgaard, 1964). For example, meteoric waters with δ^{18}O of −38 ± 3 ‰, as recorded in the Belomorian belt rocks, precipitate in cold, high-latitude regions such as Greenland and Antarctica, whereas precipitation of warm mid-latitude, near-costal climate zones have values of −9 ± 5 ‰; such are recorded at Shueretskoe and Kiy Island. To investigate the δ^{18}O of precipitation in the early Paleoproterozoic snowball Earth climate state with a narrow strip of ocean remaining unfrozen (Jormangand state; Abbot et al., 2011), Bindeman and Lee (2018) applied an isotope-enabled Global Circulation Model. Their results indicated following: (i) the relationship between mean annual temperature and δ^{18}O of precipitation is very similar to that in the modern-day climate, (ii) snowball-Earth-derived meteoric waters have sharp δ^{18}O gradients such that the δ^{18}O of precipitation at low- and mid-latitudes could vary between −60 and −10 ‰. Given that the rocks comprising the Belomorian belt were very likely located at low-latitudes at 2.44-2.41 Ga (Mertanen et al., 1999; Bindeman et al., 2010; Salminen et al., 2014), our δ^{18}O data are consistent with model predictions for steep δ^{18}O gradients in low latitudes. We acknowledge that the dearth of precise age constraints hinders our ability to provide precise temporal resolution for the hydrothermal alteration across the Belomorian belt but, given that analogous Neoproterozoic snowball Earth episodes lasted for tens of millions of years (e.g. Rooney et al., 2015), this shortcoming is not overly limiting. For the Scourie dikes, the reconstructed value of δ^{18}O of assimilated material is also indicative of meteoric waters in cold regions, which is similar to the triple O-isotopic composition of the low δ^{18}O rocks from the Belomorian belt. The close paleogeographic position of the two (Bleeker, 2003; Ernst and Bleeker, 2010) would be consistent with possible generation of low δ^{18}O rocks and their incorporation into mantle-derived melts during the rifting and intrusion of massive amount of mafic magmas in the early Paleoproterozoic during globally cold climate.

Given our results, we encourage further O-isotopic characterization of magmatic and hydrothermally altered rocks that span the time interval to potentially overlap with the known episodes of early Paleoproterozoic glaciations. Similar to modern Iceland, magmas stored in the shallow crust initiate abundant hydrothermal systems that should leave an O-isotope imprint of contemporaneous meteoric water in the host rocks, which then could be remelted or recycled to produce new low δ^{18}O magmas (Taylor, 1971; Hattori and Muehlenbachs, 1982; Wotzlaw et al., 2012). Further, we suggest O-isotopes of dikes as a predictive tool for cross-cratonic correlations based on coeval low δ^{18}O rocks associated with magmatism, i.e. similar to "bar coding" of mafic dike swarms (e.g. Bleeker and Ernst, 2006). The δ18O values of possible coeval analogues of Scourie dikes found in the fragments of North Atlantic craton (Fig. 11) could provide an effective tool to "bar code" connection between continental cratons in the early Paleoproterozoic. We thereby suggest sampling 2.44-2.38 Ga mafic dikes across Canada and Greenland using the coarse-grained interiors and their encasing host rocks, especially if mineralogical and textural relationships suggest contemporaneous hydrothermal alteration.

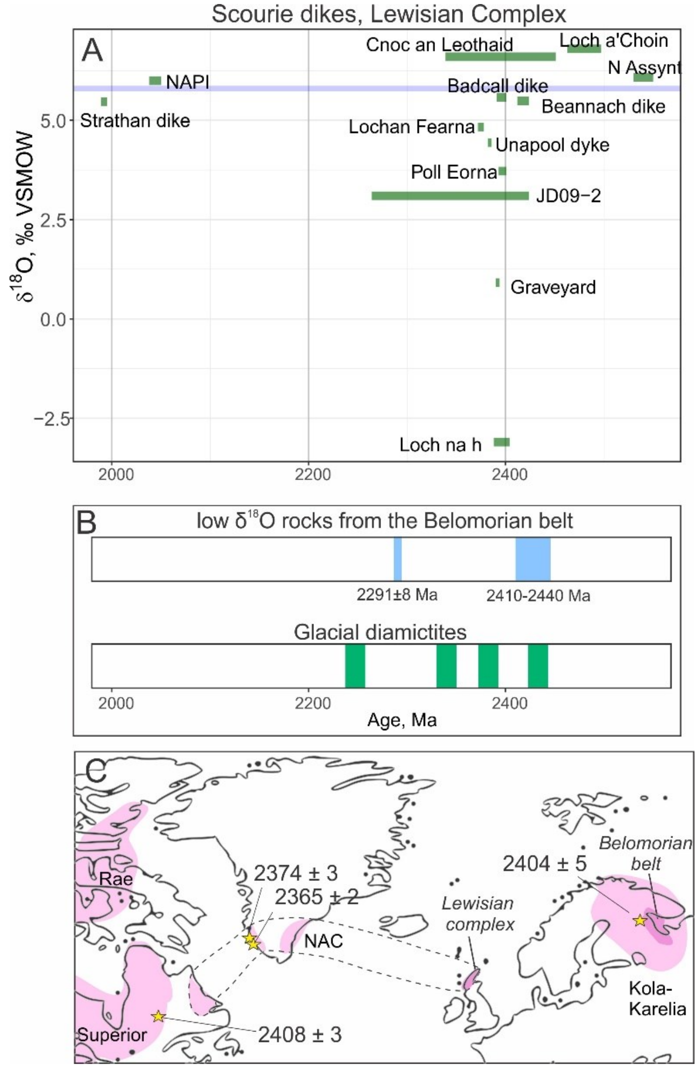

Figure 11. The ages of Scourie dikes (A), low $\delta^{18}O$ rocks from the Belomorian belt and Paleoproterozoic glacial diamictites (B). The map of the North Atlantic region (C) shows the areal extent of exposed Archean cratons (North Atlantic craton = NAC) and some previously dated dike swarms (Superior craton dates from Krogh, 1994; NAC dates from Nilsson et al., 2013; Karelia craton dates from Stepanova et al., 2017) that could be coeval with the low $\delta^{18}O$ Scourie dikes of the Lewisian complex. Measuring their $\delta^{18}O$ values could assist paleogeographic reconstructions of the early Paleoproterozoic. The bar width for Scourie dikes corresponds to the error in U-Pb age (Heaman and Tarney, 1989; Davies and Heaman, 2014).

6.0 Summary

Pervious work identified at least one episode of early Paleoproterozoic glaciation recorded in the low $\delta^{18}O$ rocks of the Belomorian belt (Bindeman et al., 2010; Bindeman and Serebryakov, 2011; Bindeman et al., 2014; Zakharov et al., 2017). It has been proposed, that these rocks recorded the environmental conditions at low latitudes, where meteoric waters had $\delta^{18}O$ of approximately -40 ‰, reflecting the global cooling of the planet. In this study we support this evidence with a new set of triple oxygen isotope measurements from the occurrence of very low $\delta^{18}O$ rocks at Vuat Varakka that reveal involvement of meteoric waters with $\delta^{18}O$ of −38 ‰. We also show that some localities (Kiy Island and Shueretskoe) in the southern Belomorian belt record meteoric waters with $\delta^{18}O$ value of around −9 ‰. These estimated values of meteoric waters are diverse and reflect temporal or/and geographic variations of the early Paleoproterozoic precipitation.

A possible connection between the low $\delta^{18}O$ Belomorian belt rocks and the Scourie dikes, Lewisian complex is investigated using the triple oxygen isotope approach. We found that the $\delta^{18}O$ values of Scourie dikes extend as low as -3 ‰ recorded by amphiboles as they are resistant to secondary alteration. This value is most consistent with involvement of very low $\delta^{18}O$ material in the genesis of Scourie dike magma. The exact mechanism of incorporation of such material is inconclusive; however, the reconstructed triple oxygen isotope composition of the assimilated material is strikingly similar to the isotopic signature of the Belomorian belt rocks. This serves as a potential evidence for connection between the Lewisian complex and the Baltic shield in the early Paleoproterozoic and presence of active hydrologic cycle that promoted generation of such low $\delta^{18}O$ material incorporated by igneous processes.

CHAPTER VII

CONCLUSION

In this dissertation, my investigations focus on involvement of ancient meteoric waters and ancient seawater in hydrothermal systems with important implications for paleoclimate, secular changes in isotope budget of hydrosphere and general geochemistry of water-rock exchange. Specifically, using triple oxygen isotopes in hydrothermally altered rocks, I provide new insights into the state of hydrologic cycle during the early Paleoproterozoic and substantiate the evidence by studies of water-rock interaction in modern-day hydrothermal systems, both from subaerial and submarine environments.

In Chapter II, modern-day geothermal areas of Iceland, such as Krafla and Reykjanes, are used to study the effects of water-rock interaction on the triple oxygen isotope compositions of minerals and fluids from hydrothermally altered crust. I find that the δD, $\delta^{18}O$ and $\Delta^{17}O$ of the well fluids are shifted due to interaction with rocks and near-surface boiling. These two processes have distinct trends of fractionation in the triple isotope space making it a promising tool for geothermal research. The estimated effective water-rock ratios recorded in the well fluid vary between 0.1 and 2. The isotopic composition of minerals provide estimates of temperature and triple oxygen isotope estimates of the fluids, which are similar to those measured directly in the wells. This study uses the well-controlled environments of drilled Icelandic geothermal areas to test the novel application of triple oxygen isotopes to modern allowing me to extend the approach to the studies of ancient hydrothermal systems.

Chapter III provides new constraints on the triple oxygen and hydrogen isotope composition of seawater in the early Paleoproterozoic. The 2.43-2.41 Ga hydrothermally altered rocks preserved within the Vetreny belt, Baltic Shield record high-temperature (300-360 °C) interaction between komatiitic basalts and contemporaneous seawater. Using quartz-epidote pairs and microthermometry measurements of fluid inclusions, the $\delta^{18}O$ and $\Delta^{17}O$ values of seawater-derived fluids are evaluated using temperature-dependent fractionation of oxygen isotopes. The Vetreny belt epidote has triple oxygen isotope composition very similar to the epidote extracted from modern oceanic crust. The estimated initial seawater values are $\delta^{18}O = -1.7 \pm 1.1$ ‰ and $\Delta^{17}O = 0.0 \pm 0.1$ ‰. The original δD values of high-temperature hydrothermal fluids are still preserved by some epidote samples, while other hydrous minerals likely lost their original isotope integrity. The δD of the early Paleoproterozoic seawater was likely within the realm of the Cenozoic values, varying between -20 and +20 ‰. The reconstructed seawater values indicate that the balance between circulation of seawater at mid-ocean ridges and continental weathering control the isotope composition of seawater over the long (on the order of10 Ma) timescales. These results are important for all subsequent chapters of this dissertation as they provide basis for studying the early Paleoproterozoic hydrological cycle. This chapter also presents triple oxygen isotope measurements of the modern seafloor rocks extracted by the Ocean Drilling Program ODP, site 504B in the Eastern Pacific Ocean.

In Chapter IV, I present preliminary results of studying the effect of low marine sulfate content in the Precambrian on seawater-basalt exchange reactions. This study relies on combined Δ^{17}O and ^{87}Sr/^{86}Sr shifts recorded in epidote from the Vetreny belt to determine the role of hydrothermal circulation on the isotope budget of strontium in seawater. New constraints are given for the ratio of seawater/mantle-derived Sr that make up Sr in hydrothermal fluids. High ^{87}Sr/^{86}Sr ratios measured in the Vetreny belt epidote support the previous oxygen isotope seawater estimates from Chapter III. The preliminary conclusion of this study is that the Archean and Proterozoic (before ~600 Ma) oceanic crust was experiencing exchange with hydrothermal fluids that had a high proportion of seawater-derived Sr as a result of extremely low sulfate in the Precambrian oceans. The low oxidative capacity of continental weathering cycle might play a fundamental role in modulating the ^{87}Sr/^{86}Sr values of the submarine fluids before about 0.6 Ga.

Chapter V provides an evidence for very low δ^{18}O precipitation at near-equatorial latitudes based on triple oxygen isotope investigation of 2.45-2.22 Ga hydrothermal systems from the Baltic Shield, Russia. This study illustrates that the very low δ^{18}O values (as low as -27 ‰) measured in the hydrothermally altered rocks from the Belomorian belt of the Baltic Shield likely formed during the cold climate of the early Paleoproterozoic, i.e. during the first series of snowball Earth glaciations. These results are important because they give quantitative estimates of climate conditions through the relationship between the $\delta^{18}O$ values of meteoric water and mean annual temperature. Temperatures of about -40 °C existed at low latitudes (near 30 °) in the early Paleoproterozoic as reconstructed by the triple oxygen isotope compositions of multiple hydrothermal systems of the Belomorian belt. These systems likely formed in subglacial environment and their ages were determined using high-precision U-Pb methods pinning the estimated low $\delta^{18}O$ values of precipitation to 2.44-2.41 Ga and to 2.29 Ga (precise age 2.291 ± 0.008 Ga).

Chapter VI examines multiple new occurrences of subglacial hydrothermal systems from the Belomorian belt, Baltic Shield. These occurrences are now traced along the distance of 500 km. The triple oxygen isotope approach constrains the $\delta^{18}O$ of precipitation to about -40 ‰, similar to the previous estimates from Chapter V. However, I discovered that several southern-most localities within the Belomorian belt might contain a record of meteoric waters with $\delta^{18}O$ around -10 ‰. These variations reflect either temporal or geographic differences between local precipitations on the Baltic Shield. In case of possible geographic variability of meteoric water values, they point at the presence of active hydrological cycle over the subaerial portions of continental crust in the early Paleoproterozoic. In the same chapter, I explore the potential link between these low $\delta^{18}O$ rocks of the Belomorian belt and the low $\delta^{18}O$ 2.41-2.37 Ga Scourie dikes of Lewisian complex, NW Scotland. The mechanism of incorporation of low $\delta^{18}O$ component in the Scourie dike magma is inconclusive and the exact origin of the material itself is uncertain as well. However, my triple oxygen isotope reconstructions suggest that the high-temperature interaction between low $\delta^{18}O$ meteoric waters ($\delta^{18}O = -35 \pm 10$ ‰) and crustal rocks must have happened to produce the isotope signature of Scourie dikes. The similarity between the Belomorian rocks and the material incorporated by the Scourie dikes allows for some speculations on the paleogeographic connection between the Baltic Shield and the Lewisian complex. The commonality of the isotopic signatures between the provinces also indicate the universal effect of globally cold climate and active hydrological cycle on the oxygen isotope budget of continental hydrothermal systems.

My work outlines the future direction for the research on water-rock interaction. The future work should address the dependency between physical parameters of the hydrothermal systems and the isotopic shifts of hydrothermal fluids. Particularly, how far and how long do fluids penetrate within the crust before they lose their original oxygen isotope integrity? This question is relevant because the ancient hydrothermal systems studied here are exposed at deep erosional levels and we are left with the result of long-lasting hydrothermal activity.

To continue the line of my investigations, the future research should aim to identify the low $\delta^{18}O$ signatures of the early Paleoproterozoic climate elsewhere outside of the Baltic Shield. Such findings, combined with precise geochronological dating, may offer a novel way to reconstruct the paleogeographic locations of ancient continental blocks. In the current state of reconstructions, the paleogeographic locations are somewhat tentative and are subjected to speculations. The $\delta^{18}O$ signatures of meteoric waters along a longitudinal traverse would be an important parameter in reconstructing both the climate patterns and paleogeographic locations in the early Earth's history. Additionally, the temporal evolution of oxygen isotope composition of the terrestrial hydrosphere is still under the long-lasting debate. New approaches, measurements and models are needed to reconstruct the $\delta^{18}O$ value of ancient seawater and to reconcile the existing paradox of low oxygen isotope values measured in the Precambrian marine sediments. I am hopeful that the future studies will make use of the triple oxygen isotope approach to disentangle the effect of diagenetic alteration, temperature-dependent fractionation and variability of the actual seawater values using ancient marine record.

APPENDIX A

CHAPTER II SUPPORTING INFORMATION

Table S1. Triple oxygen isotope raw values of samples and internal standards. Values are in ‰.

sample	material	locality	$\delta'^{17}O$, raw	±s.e.	$\delta'^{18}O$, raw	±s.e.	$\Delta'^{17}O$, raw	±s.e.	internal standard*	$\delta'^{17}O$ standard, raw	$\delta'^{18}O$ standard, raw	$\Delta'^{17}O$ standard, raw	adjustment $\delta'^{17}O$	adjustment $\delta'^{18}O$	$\delta'^{17}O$, VSMOW	$\delta'^{18}O$, VSMOW	$\Delta'^{17}O$, VSMOW
GER5	epidote	Geitafell	-2.737	0.010	-5.049	0.005	-0.059	0.011	SCO	2.698	5.325	-0.127	0.021	0.185	-2.758	-5.234	0.018
GER5	quartz	Geitafell	1.095	0.007	2.258	0.003	-0.103	0.007	SCO	2.698	5.325	-0.127	0.021	0.185	1.074	2.073	-0.026
GER1	garnet	Geitafell	-2.959	0.010	-5.542	0.004	-0.019	0.010	SCO	2.719	5.335	-0.111	0.042	0.195	-3.001	-5.737	0.043
GER5	garnet	Geitafell	-4.215	0.008	-7.841	0.007	-0.055	0.009	SCO	2.850	5.551	-0.095	0.173	0.411	-4.388	-8.253	-0.010
GTF25	epidote	Geitafell	-2.841	0.010	-5.322	0.004	-0.018	0.010	SCO	2.719	5.335	-0.111	0.042	0.195	-2.883	-5.517	0.044
GTF25	quartz	Geitafell	1.215	0.009	2.414	0.004	-0.065	0.009	SCO	2.719	5.335	-0.111	0.042	0.195	1.173	2.219	-0.004
GTF28	epidote	Geitafell	-3.371	0.009	-6.305	0.004	-0.027	0.009	SCO	2.719	5.335	-0.111	0.042	0.195	-3.413	-6.500	0.035
GER16	quartz	Geitafell	-0.753	0.008	-1.409	0.003	-0.006	0.008	SCO	3.132	6.015	-0.059	0.455	0.875	-1.208	-2.284	0.003
GER34	quartz	Geitafell	1.485	0.007	2.853	0.004	-0.028	0.007	SCO	3.132	6.015	-0.059	0.455	0.875	1.030	1.978	-0.019
GER16	quartz	Geitafell	-0.077	0.008	-0.151	0.004	0.003	0.008	SCO	3.147	6.001	-0.036	0.470	0.861	-0.547	-1.011	-0.010
GER34	quartz	Geitafell	1.255	0.007	2.312	0.003	0.028	0.007	SCO	3.147	6.001	-0.036	0.470	0.861	0.784	1.451	0.015
KO6 1730m	epidote	Krafla	-7.063	0.014	-13.287	0.006	-0.014	0.014	SCO	2.719	5.335	-0.111	0.042	0.195	-7.104	-13.482	0.048
KO6 1730m	quartz	Krafla	-1.304	0.012	-2.286	0.005	-0.091	0.012	SCO	3.044	5.883	-0.077	0.367	0.743	-1.671	-3.029	-0.064
KO6 1868m	epidote	Krafla	-7.176	0.009	-13.537	0.003	0.005	0.009	SCO	2.719	5.335	-0.111	0.042	0.195	-7.218	-13.732	0.067
KJ36 744m	quartz	Krafla	-1.495	0.012	-0.034	0.005	-0.033	0.012	SCO	2.948	5.736	-0.095	0.271	0.596	-1.766	-0.630	-1.432
KJ36 744m	quartz	Krafla	-0.886	0.008	-0.024	0.004	-0.024	0.008	SCO	2.948	5.736	-0.095	0.271	0.596	-1.157	-0.620	-0.828
KJ36 744m	quartz	Krafla	-1.314	0.009	-0.048	0.004	-0.048	0.009	SCO	2.948	5.736	-0.095	0.271	0.596	-1.585	-0.644	-1.243
IDDP-1 1220m	epidote	Krafla	-5.241	0.007	-9.901	0.003	0.012	0.008	SCO	3.132	6.015	-0.059	0.455	0.875	-5.696	-10.777	0.021
IDDP-1 1220m	quartz	Krafla	-1.552	0.008	-2.884	0.003	-0.022	0.007	SCO	3.132	6.015	-0.059	0.455	0.875	-2.007	-3.759	-0.013
K-26 1020m	quartz	Krafla	-3.399	0.007	-6.405	0.004	-0.001	0.007	SCO	3.132	6.015	-0.059	0.455	0.875	-3.854	-7.281	0.008

Table S1 continued

sample	material	locality	δ'^{17}O, raw	±s.e.	δ'^{18}O, raw	±s.e.	Δ'^{17}O, raw	±s.e.	internal standard*	δ'^{17}O standard, raw	δ'^{18}O standard, raw	Δ'^{17}O standard, raw	adjustment δ'^{17}O	adjustment δ'^{18}O	δ'^{17}O, VSMOW	δ'^{18}O, VSMOW	Δ'^{17}O, VSMOW
IDDP-1 1220m	quartz	Krafla	-2.228	0.008	-4.187	0.004	-0.006	0.008	SCO	3.147	6.001	-0.036	0.470	0.861	-2.698	-5.048	-0.020
KJ-21 550m	quartz	Krafla	-2.481	0.006	-4.730	0.004	0.028	0.007	SCO	3.147	6.001	-0.036	0.470	0.861	-2.951	-5.591	0.015
RN12 1070m	epidote	Reykjanes	0.868	0.006	1.675	0.002	-0.021	0.006	SCO	3.044	5.883	-0.077	0.367	0.743	0.501	0.932	0.006
RN12 1070m	epidote	Reykjanes	1.229	0.006	2.419	0.004	-0.054	0.007	SCO	3.044	5.883	-0.077	0.367	0.743	0.862	1.676	-0.027
RN12 1070m	quartz	Reykjanes	3.156	0.010	6.060	0.004	-0.059	0.010	SCO	2.909	5.618	-0.072	0.232	0.478	2.924	5.582	-0.037
RN12 1070m	quartz	Reykjanes	3.262	0.013	6.271	0.004	-0.065	0.013	SCO	2.909	5.618	-0.072	0.232	0.478	3.030	5.793	-0.043
RN17B 2900m	epidote	Reykjanes	0.287	0.006	0.755	0.003	-0.113	0.006	SCO	2.595	5.135	-0.129	-0.082	-0.005	0.369	0.760	-0.034
RN17B 2900m	epidote	Reykjanes	0.086	0.010	0.337	0.004	-0.093	0.010	SCO	2.595	5.135	-0.129	-0.082	-0.005	0.168	0.342	-0.014
RN17B 2805.5m	epidote	Reykjanes	0.806	0.007	1.581	0.003	-0.033	0.007	SCO	3.132	6.015	-0.059	0.455	0.875	0.351	0.706	-0.023
IDDP1	rhyolitic glass	Krafla	1.546	0.009	3.032	0.005	-0.062	0.010	SCO	2.857	5.459	-0.039	0.176	0.306	1.371	2.726	-0.076
IDDP1	rhyolitic glass	Krafla	1.938	0.004	3.771	0.007	-0.063	0.007	UOG	3.757	7.211	-0.068	0.352	0.691	1.586	3.080	-0.048
IDDP1	rhyolitic glass	Krafla	1.512	0.004	3.006	0.008	-0.083	0.009	UOG	3.545	6.802	-0.063	0.140	0.282	1.372	2.724	-0.073
KRF-14	rhyolitic glass	Krafla	1.566	0.003	3.094	0.007	-0.075	0.007	UOG	3.545	6.802	-0.063	0.140	0.282	1.426	2.813	-0.066

*SCO - San Carlos Olivine δ'^{17}O = 2.677 ‰ and δ'^{18}O = 5.140 ‰ (Pack et al., 2016); UOG – University of Oregon garnet δ'^{17}O = 3.391 ‰ and δ'^{18}O = 6.499 ‰.

Table S2. The oxygen isotope values of Geitafell samples determined by conventional method (conversion of O_2 to CO_2; see methods main text).

Sample	mineral	Latitude	Longitude	Distance from intrusive contact, meters.	$\delta^{18}O$, ‰
GTF2	epidote	64.43694	-15.3915	1040	-1.79
GTF11	epidote	64.42697	-15.3904	290	-2.23
GTF15	quartz	64.42857	-15.3884	493	-0.74
GTF15	epidote	64.42857	-15.3884	493	-4.57
GTF20	quartz	64.41063	-15.41	299	3.62
GTF31	epidote	64.35686	-15.3919	376	-4.50
GTF33	quartz	64.364	-15.4012	233	2.93
Geit-I-8	pyroxene	64.4226	-15.4411	0	4.69
Geit-I-8	magnetite	64.4226	-15.4411	0	2.06
GER3	quartz	64.4128	-15.3569	1763	5.19

APPENDIX B

CHAPTER III SUPPORTING INFORMATION

Text S1. Standartization, San Carlos olivine

San Carlos olivine (SCO) was used as a standard within each analytical session to monitor accuracy of the analyses. Individual measurements of SCO and dates of each session are listed in Table A1. The previously published analysis of SCO performed using fluorination of VSMOW yielded $\delta'^{18}O = 5.140$ and $\delta'^{17}O = 2.677$ (Pack et al., 2016) and is accepted here as a point of reference. The raw values of the unknowns are listed in Table S8. Each session was adjusted by the difference between analyzed SCO and composition given in Pack et al. (2016).

Table S1. Analysis of SCO from each analytical session used for monitoring the accuracy of analyses.

Date yyyy/mm/dd	$\delta^{17}O$	SE	$\delta^{18}O$	SE	$\delta'^{17}O$	$\delta'^{18}O$	$\Delta'^{17}O$	SE
2017/01/23	2.820	0.015	5.548	0.006	2.816	5.533	-0.120	0.015
2017/01/23	2.704	0.008	5.277	0.006	2.700	5.263	-0.091	0.008
2017/01/27	2.608	0.013	5.132	0.006	2.604	5.119	-0.111	0.014
2017/01/27	3.072	0.015	5.999	0.004	3.067	5.981	-0.106	0.015
2017/05/16	2.876	0.008	5.512	0.004	2.872	5.497	-0.044	0.008
2017/06/16	2.793	0.008	5.369	0.006	2.789	5.354	-0.052	0.009
2017/06/16	2.713	0.009	5.287	0.003	2.709	5.273	-0.088	0.009
2017/07/17	2.621	0.007	5.093	0.004	2.617	5.080	-0.078	0.008
2017/09/01	2.758	0.012	5.308	0.004	2.754	5.294	-0.055	0.013
2017/09/05	2.913	0.010	5.634	0.004	2.909	5.618	-0.071	0.010
2017/10/04	3.049	0.011	5.900	0.004	3.044	5.882	-0.076	0.011
average					2.807	5.445	-0.081	
σ					0.155	0.292	0.025	
SE					0.047	0.088	0.008	

Table S2. Mineralogical and chemical composition of hydrothermally altered rocks from the Vetreny Belt as determined by XRD and XRF.

Sample name	VB25	VB16	VB10A	GO13	GO24	My1a	SH11-16	8122-2
Rock type	Massive altered basalt	Pillow basalt rind	Interpillow fill	Massive altered basalt	Massive altered basalt	Altered basalts from hyaloclastite	Massive altered basalt	Altered basalts from hyaloclastite
Mineral								
Chlorite	10.7	25.5	-	8.6		8.8	14.7	7.9
Amphibole	71.2	53.1	-	71.1		67.2	63.9	72.7
Phlogopite	-	8.1	-	3.1		4.5	-	2.5
Plagioclase	3.3	5.7	-	4.2		5.1	2.7	7.6
Epidote	2.7	5.3	-	9.2		-	6.9	5.1
Quartz	4.4	2.3	94.6	3.8		5.5	6.3	4.2
Diopside	7.7	-	5.4	-		4.1	5.5	-
Prehnite	-	-	-	-		4.8	-	-
SiO_2, wt.%				47.17	45.87		45.78	45.76
TiO_2				0.90	0.99		0.74	0.91
Al_2O_3				10.11	11.11		7.14	12.07
$Fe_2O_3^{total}$				15.22	17.20		15.34	14.38
MnO				0.29	0.35		0.32	0.29
MgO				10.70	8.23		16.28	8.48
CaO				13.28	13.56		13.76	15.62
Na_2O				1.15	1.61		0.00	1.56
K_2O				0.63	0.63		0.08	0.39
P_2O_5				0.05	0.08		0.08	0.07
Rb, ppm				8	14		-	11
Sr				266	308		64	390
Ba				345	192		39	105
Zr				129	131		70	129
Y				51	48		25	44
Nb				10	7		-	7
Sc				34	27		35	32
V				285	307		280	285
Cr				1452	919		1968	1347
Ni				424	212		637	347
Cu				253	230		28	391
Zn				129	154		112	112
Ga				21	25		17	24

Table S3. Spot analyses of chlorites.

Sample-area	Mya1-6	Mya1-8	GO25-2
Analysis no.	168G	192G	73G
Na_2O	-	-	-
K_2O	0.04	0.03	0.01
Al_2O_3	20.11	20.87	21.87
MgO	18.68	19.31	15.58
FeO	18.23	18.38	22.42
CaO	0.03	0.05	0.17
MnO	0.20	0.19	0.17
TiO_2	0.04	0.04	0.02
SiO_2	27.24	25.78	28.24
Cl	-	0.01	-
Total	84.55	84.64	88.45

Table S4. Spot analyses of diopsides.

Sample-area	VB16-1	VB16-1	VB16-1	VB16-1	VB16-2	VB16-2	VB16-2
Analysis no.	237 G	239 G	243 G	245 G	248 G	249 G	252 G
Na_2O	0.06	0.07	0.07	0.08	0.13	0.13	0.08
K_2O	0.00	0.00	0.00	0.01	0.00	0.00	0.00
Al_2O_3	0.35	1.21	0.35	0.78	0.54	0.44	0.53
MgO	15.90	15.80	16.84	15.34	12.29	11.83	11.66
FeO	4.18	3.44	3.62	4.47	8.34	9.24	9.46
CaO	27.03	27.17	26.23	26.89	25.94	25.92	25.73
MnO	0.24	0.23	0.19	0.26	1.05	1.03	0.98
TiO_2	0.00	0.00	0.01	0.02	0.00	0.01	0.00
SiO_2	55.21	55.49	55.75	55.47	53.67	53.40	52.53
Cl	nd	nd	nd	nd	nd	nd	nd
Total	102.94	103.40	103.04	103.33	101.95	101.99	100.98

Table S5. Spot analyses of epidotes.

Sample-area	VB16-3	VB16-4	VB16-4	VB16-4	Mya1-3	Mya1-4	Mya1-6	Mya1-6	Mya1-7	Mya1-8	Mya1-10
Analysis no.	268 G	280 G	285 G	288 G	131 G	137 G	147 G	157 G	178 G	193 G	219 G
Rock type	Interpillow fill	Interpillow fill	Interpillow fill	Interpillow fill	altered basalt	altered basalt	altered basalt	altered basalt	altered basalt	altered basalt	altered basalt
Na_2O	0.00	0.00	0.00	0.00	0.00	0.00	0.00	0.00	0.00	0.01	0.00
K_2O	0.00	0.00	0.00	0.00	0.01	0.04	0.00	0.01	0.00	0.01	0.00
Al_2O_3	28.10	26.80	25.77	25.47	26.87	26.60	23.77	28.83	28.37	28.14	25.81
MgO	0.16	0.00	0.00	0.00	0.64	0.50	0.15	0.02	0.28	0.00	0.59
Fe_2O_3	6.56	8.54	9.49	9.50	6.86	8.07	8.55	5.93	5.96	7.10	9.46
CaO	24.91	24.92	24.93	24.71	24.01	23.44	22.95	24.77	24.40	24.93	24.77
MnO	0.12	0.06	0.06	0.10	0.22	0.21	0.11	0.23	0.21	0.26	0.09
TiO_2	0.03	0.02	0.01	0.01	0.39	0.08	0.50	0.08	0.10	0.01	0.13
SiO_2	38.64	38.59	38.01	38.20	39.93	39.16	44.72	39.01	39.64	39.63	39.26
Cl	nd	nd	nd	nd	nd	nd	nd	nd	nd	nd	nd
Total	97.85	98.03	97.29	97.02	98.25	97.28	99.88	98.26	98.35	99.37	99.16
Formula coefficients:											
Na	0.00	0.00	0.00	0.00	0.00	0.00	0.00	0.00	0.00	0.00	0.00
K	0.00	0.00	0.00	0.00	0.00	0.00	0.00	0.00	0.00	0.00	0.00
Al	2.67	2.55	2.48	2.46	2.53	2.54	2.18	2.72	2.67	2.63	2.43
Mg	0.02	0.00	0.00	0.00	0.08	0.06	0.02	0.00	0.03	0.00	0.07
Fe^{3+}	0.40	0.52	0.58	0.59	0.41	0.49	0.50	0.36	0.36	0.42	0.57
Ca	2.15	2.16	2.18	2.17	2.06	2.03	1.92	2.12	2.08	2.12	2.12
Mn	0.01	0.00	0.00	0.01	0.01	0.01	0.01	0.02	0.01	0.02	0.01
Ti	0.00	0.00	0.00	0.00	0.02	0.01	0.03	0.00	0.01	0.00	0.01
Si	3.11	3.12	3.11	3.13	3.19	3.17	3.49	3.12	3.16	3.14	3.14
$Fe^{3+}/(Al+Fe^{3+})$	0.13	0.17	0.19	0.19	0.14	0.16	0.19	0.12	0.12	0.14	0.19

Table S6. Spot analyses of amphiboles

Sample-area	VB16-4	VB16-4	VB16-4	VB16-4	Mya1-2	Mya1-4	Mya1-4	Mya1-4	Mya1-4	Mya1-5	Mya1-10	Mya1-10	GO25-1	GO25-1
Analysis no.	277 G	278 G	283 G	289 G	126 G	133 G	134 G	135 G	136 G	144 G	229 G	230 G	52 G	53 G
Rock type	Interpillow fill	Interpillow fill	Interpillow fill	Interpillow fill	altered basalt	Interpillow fill	Interpillow fill	Interpillow fill	Interpillow fill	altered basalt	altered basalt	massive	massive	massive
Na_2O	0.23	0.25	0.36	0.09	0.36	0.46	0.36	0.28	0.43	0.54	0.33	0.40	0.29	0.22
K_2O	0.07	0.20	0.30	0.04	0.08	0.14	0.19	0.09	0.40	0.17	0.31	0.14	0.06	0.03
Al_2O_3	2.67	3.25	3.93	1.47	3.52	5.85	4.69	3.17	4.90	6.14	4.82	4.79	2.95	2.16
MgO	15.45	14.98	13.73	15.92	16.66	16.56	16.77	17.27	15.99	14.81	15.21	16.27	17.67	17.68
FeO	12.23	12.50	11.85	11.92	10.05	10.74	10.34	9.83	10.18	10.37	9.79	10.36	12.73	16.48
CaO	13.44	13.43	12.69	13.63	12.59	11.70	11.91	12.48	12.67	13.51	11.47	12.67	8.92	5.84
MnO	0.23	0.25	0.23	0.26	0.22	0.27	0.26	0.25	0.27	0.26	0.24	0.27	0.37	0.56
TiO_2	0.00	0.00	0.03	0.02	0.06	0.10	0.11	0.07	0.18	2.52	0.39	0.23	0.09	0.10
SiO_2	54.55	53.30	54.79	54.66	54.26	52.02	53.03	54.48	52.85	50.98	55.58	53.54	54.59	55.37
Cl	0.03	0.14	0.21	0.02	0.00	0.00	0.00	0.00	0.00	0.00	0.01	0.00	0.00	0.00
Total	98.89	98.31	98.10	98.03	97.79	97.84	97.65	97.92	97.86	99.28	98.14	98.66	97.65	98.42
Na	0.06	0.07	0.10	0.02	0.10	0.13	0.10	0.08	0.12	0.15	0.09	0.11	0.08	0.06
K	0.01	0.04	0.05	0.01	0.01	0.02	0.03	0.02	0.07	0.03	0.06	0.02	0.01	0.00
Al	0.44	0.55	0.66	0.25	0.59	0.97	0.78	0.53	0.81	1.02	0.80	0.79	0.49	0.36
Mg	3.26	3.18	2.93	3.39	3.51	3.48	3.53	3.63	3.36	3.10	3.21	3.40	3.74	3.75
Fe	1.45	1.49	1.42	1.42	1.19	1.26	1.22	1.16	1.20	1.22	1.16	1.21	1.51	1.96
Ca	2.04	2.05	1.95	2.08	1.91	1.77	1.80	1.88	1.92	2.03	1.74	1.90	1.36	0.89
Mn	0.03	0.03	0.03	0.03	0.03	0.03	0.03	0.03	0.03	0.03	0.03	0.03	0.04	0.07
Ti	0.00	0.00	0.00	0.00	0.01	0.01	0.01	0.01	0.02	0.27	0.04	0.02	0.01	0.01
Si	7.71	7.59	7.85	7.80	7.67	7.33	7.49	7.68	7.46	7.16	7.87	7.50	7.75	7.89

Table S7. The δD, $\delta^{18}O$, H_2O wt. % and $\delta^{13}C$ measured of hydrothermally altered rocks from the Vetreny Belt

Sample	$\delta^{18}O$, ‰ VSMOW	δD, ‰ VSMOW	H_2O, wt. %	$\delta^{13}C$, ‰ VPDB
Myandukha locality				
Altered basalts (actinolite + chlorite + albite + epidote)				
8122-1b	1.03	-179	4.1	
8122-1a	2.20	-164	2.4	
My1-b	2.97	-192	2.2	
8122-2b	1.94	-155	2.4	
VB8A-1	3.48	-168	3.3	
VB8A-2	3.26	-168	3.4	
VB8A-3	3.21	-169	3.3	
VB-25	3.55	-139	4.0	
VB16-1	3.51	-181	5.1	
VB9-1	2.85	-181	3.1	
VB16-3	3.35	-179	2.5	
VB9-4	2.88	-186	4.8	
VB14-4	1.24	-160	1.8	
VB10B-1	2.99	-69	2.1	
VB10B-4	2.73	-101	2.9	
Epidotes				
VB24	3.11	-8	1.9	
VB24A	2.87			
VB14C	-0.34	-20	1.7	
VB8A	3.08	-32	2.0	
VB8B	2.97	-51	2.1	
Clear quartz from quartz veins				
VB12	5.66			
VB13	6.05			
VB14c	5.67			
VB17	8.26			
VB18	8.12			
VB24	9.27			
VB8A	8.56			
VB8B	7.83			
Quartz veins with other minerals and interpillow fills (quartz + epidote + chlorite + actinolite + diopside)				
8122-2a	5.53	-192	1.3	
My1-a	3.94	-179	2.2	
VB10A	6.57			
VB-10A	6.00			
VB10B	6.97			
VB10B-2	6.55	-99	0.3	
VB10B-3	6.84	-131	0.5	
VB11	4.68			

Table S7 Continued.

Mineral/Sample	$\delta^{18}O$, ‰ VSMOW	δD, ‰ VSMOW	H_2O, wt. %	$\delta^{13}C$, ‰ VPDB
VB11	2.70			
VB14	3.30			
VB14 (1)	2.83			
VB14-2	3.02	-116	1.1	
VB14-3	1.90	-150	1.8	
VB15	3.24			
VB16	7.45			
VB-16(1)	5.61			
VB16-2	7.08	-119	0.3	
VB16-4	4.67	-96	0.5	
VB16-5	3.64	-151	1.6	
VB19	8.67			
VB19 (1)	7.49			
VB20	8.07			
VB21	8.21			
VB22	6.67			
VB23	4.58			
VB-26	2.86			
VB26b	6.53			
VB26b	1.81	-112	0.6	
VB-27	2.48			
VB-28	3.21			
VB-28	3.13			
VB-9	6.39			
VB-9 (1)	6.37			
VB-9 (2)	5.40			
VB9-2	3.35	-128	1.4	
VB9-3	5.65	-119	0.7	
Calcite				
VPCarb_1	7.05			−2.31
VB8A	7.37			0.07
VB14C	4.08			−5.36
1321	7.32			−4.01
Golec locality				
Altered basalts (actinolite + chlorite + albite + epidote)				
GO-25	1.73	-203	1.2	
GO-13	2.22	-191	3.2	
GO-24	1.81	-210	1.7	
Clear quartz from quartz veins				
GO-11	6.15			
GO-2	4.40			
GO-21	4.15			
GO-22	5.13			

Table S7 Continued.

Mineral/Sample	$\delta^{18}O$, ‰ VSMOW	δD, ‰ VSMOW	H_2O, wt. %	$\delta^{13}C$, ‰ VPDB
GO-23	5.16			
GO-26	4.64			
GO-4	5.06			
GO-7	6.17			
Quartz veins with other minerals (quartz + epidote + chlorite)				
GO-10	5.52			
GO-12	6.02			
GO-17B	6.44			
Epidote				
Golec	-0.25	-119	2.1	
Golec (repeated)		-141	2.0	
GO-22	-0.97	-56	2.1	
GO-4	-0.06	-23	1.9	
Mafic layered intrusion Ruiga (hornblende + plagioclase + serpentine + chlorite)				
RU-7	1.76	-187	2.5	
RU-6	2.46	-161	2.0	
RU-1	3.68			
RU-2	1.63			
RU-9	1.76			
Shapochka locality				
Altered basalt (actinolite + chlorite + albite + epidote)				
SH11-16A	2.22	-188	3.6	
Quartz vein (quartz + albite + epidote)				
SH11-16b-1	5.43			

Table S8. Raw high-precision triple oxygen isotopic analysis of hydrothermally altered rocks and minerals from the Vetreny belt and ODP Hole 504B.

Date mm/dd/yyyy	Sample	material	δ^{17}O, ‰	SE	δ^{18}O ‰	SE	δ'^{18}O, ‰	δ'^{17}O, ‰	Δ'^{17}O, ‰	SE
ODP Hole 504B										
10/4/2017	70-48R 20-22	altered basalt	3.665	0.010	7.090	0.003	3.659	7.065	-0.090	0.010
09/5/2017	83-80R, 106-108	quartz	5.219	0.011	10.036	0.002	5.205	9.986	-0.092	0.011
09/5/2017	83-80R, 106-108	quartz	4.973	0.009	9.572	0.004	4.960	9.526	-0.093	0.009
10/4/2017	83-90R 71-72	altered basalt	1.897	0.011	3.824	0.004	1.895	3.816	-0.129	0.011
09/1/2017	83-90R, 148-149	epidote	1.859	0.013	3.620	0.003	1.857	3.614	-0.060	0.013
09/1/2017	83-90R, 148-149	quartz	4.555	0.008	8.762	0.004	4.545	8.724	-0.083	0.009
09/1/2017	83-90R, 148-149	quartz	4.384	0.007	8.388	0.004	4.374	8.353	-0.057	0.007
09/5/2017	83-90R, 71-72	epidote	1.485	0.009	2.888	0.004	1.484	2.884	-0.046	0.010
09/5/2017	83-90R, 71-72	epidote	1.451	0.009	2.833	0.003	1.450	2.829	-0.051	0.009
09/1/2017	83-90R, 71-72	quartz	4.805	0.008	9.327	0.003	4.793	9.283	-0.132	0.009
09/1/2017	83-90R, 71-72	quartz	4.407	0.013	8.476	0.004	4.398	8.440	-0.080	0.013
Vetreny belt										
01/27/2017	GO-22	epidote	-0.758	0.014	-1.292	0.005	-0.758	-1.292	-0.073	0.015
01/27/2017	GO-22	quartz	2.649	0.011	5.207	0.004	2.645	5.193	-0.110	0.011
01/27/2017	GO-25	altered basalt	0.859	0.014	1.819	0.004	0.858	1.817	-0.106	0.014
06/16/2017	GO4	epidote	-0.143	0.005	-0.147	0.003	-0.143	-0.147	-0.065	0.005
06/16/2017	GO4	quartz	2.581	0.008	5.025	0.002	2.577	5.013	-0.082	0.008
01/27/2017	VB-14C	quartz	2.546	0.010	5.042	0.003	2.542	5.029	-0.126	0.010
01/23/2017	VB-24	epidote	1.421	0.010	2.831	0.005	1.419	2.827	-0.080	0.010
01/23/2017	VB-24	quartz	4.414	0.011	8.586	0.005	4.404	8.549	-0.131	0.011
05/16/2017	VB-25	altered basalt	1.791	0.007	3.509	0.003	1.789	3.503	-0.069	0.007
01/27/2017	VB8A	epidote	1.298	0.012	2.559	0.008	1.297	2.556	-0.059	0.012
01/27/2017	VB8A	quartz	4.487	0.012	8.733	0.007	4.476	8.695	-0.136	0.013
05/16/2017	VB9	altered basalt	1.641	0.009	3.242	0.003	1.639	3.237	-0.078	0.009
07/17/2017	VB8A	epidote	1.473	0.011	2.930	0.004	1.472	2.925	-0.080	0.011
07/17/2017	VB8A	epidote	1.478	0.010	2.927	0.004	1.477	2.922	-0.073	0.010
07/17/2017	VB8A	quartz	4.436	0.009	8.636	0.005	4.426	8.599	-0.136	0.009
07/17/2017	VB8A	quartz	4.432	0.008	8.532	0.003	4.422	8.495	-0.084	0.008

APPENDIX C

CHAPTER V SUPPORTING INFORMATION

Text S1. Oxygen isotope analyses.

To extract O_2 from silicate minerals we used CO_2-laser fluorination line with pre-distilled BrF_5 as a reagent. The line includes face seal Ni gasket connection and a vacuum system with a diffusion pump and high-cathode gauge/getter that allows us to maintain vacuum in the 10^{-6}-10^{-7} torr range, three liquid nitrogen traps downstream the fluorination chamber and a boiling mercury diffusion pump to strip away any remaining F_2 gas left after disproportionation of BrF_5 upon laser fluorination. Previously, such a system allowed precise measurement of ^{17}O without NF contamination which interferes with mass 33 ($^{17}O^{18}O$ molecule). For this work, we built a distillation system with two 5Å molecular sieves which was used to purify O_2 from other gases. Each analysis was additionally monitored for NF (Pack et al., 2007); reported analyses have no evidence of substantial signal on mass/charge ratio of 52 which traces NF contamination. The mass spectrometer Finnigan MAT 253 was used in dual inlet mode (8 cycles, three times each sample) to precisely determine $\delta^{18}O$ and $\delta^{17}O$ values of analyzed minerals and whole rocks. Our reference gas was measured relative the air samples by Eugeni Barkan at the University of Jerusalem in order to analyze the unknowns and calibrate them relative to SMOW (Barkan and Luz, 2003). There is a systematic deviation of $\Delta^{17}O$ (about 40 ppm) in our materials (silicate standards, mantle minerals and samples from Khitoostrov) relative to the published data for the same materials (Pack and Herwartz, 2014). Most of the output was recalibrated relative to Gore Mt. Garnets silicate standards UWG-2 with $\delta^{18}O = 5.80‰$, $\Delta^{17}O = -0.102$ ‰ (Pack and Herwartz, 2014; Valley et al., 1995), and UOG with $\delta^{18}O = 6.52$ and $\Delta^{17}O = -0.102$ ‰. The choice of calibration does not affect the interpretation and can always be recalibrated using our initial data (Table S1).

Test S2. U-Pb geochronology by in situ method (SHRIMP-RG).

Dating the intrusion from the Khitoostrov locality with world's lowest $\delta^{18}O$ values and bulls eye alteration pattern was performed in two samples (X245 and CH341) using the Sensitive High Resolution Ion Microprobe with Reverse Geometry (SHRIMP-RG) at Stanford University. The initial isotopic ratio data are available (see Supplementary File).

Spot locations were guided by cathodoluminesce images performed prior to analysis. This helped us avoid metamorphic rims of 1.9 Gyr and rare inherited (> 2.4 Ga) zircons. Using resolution of about 20 µm, we analyzed zircons in rims and cores in order to find grains without metamorphic overgrowth. Calculated Pb/U ages for zircon are standardized relative to Temora-2 (416.8 Ma; Black et al., 2004), which were analyzed repeatedly throughout the duration of the analytical session. Data reduction for geochronology follows the methods described by Williams (1997) and Ireland and Williams (2003) using the MS Excel add-in programs Squid2.51 and Isoplot3.764 of Ludwig (2009; 2012). The measured $^{206}Pb/^{238}U$, $^{207}Pb/^{235}U$, and $^{207}Pb/^{206}Pb$ were corrected for common Pb using ^{204}Pb, based on a model Pb composition from Stacey and Kramers (1975). The calculated $^{207}Pb/^{206}Pb$ ages of zircons determined by SHRIMP-RG range from ~1.8 Ga to ~2.3 Ga, which we interpret to reflect several stages of various degrees of Pb-loss that occurred after the emplacement of the intrusion. Eight zircon analyses with the age older than 2.3 Ga are interpreted to be Archean xenocrysts and were omitted from the interpretation of age of the intrusion.

Text S3. U-Pb geochronology using CA-ID-TIMS.

To better resolve the age of the intrusion and avoid analyzing zircons that experienced Pb-loss, grains with primary igneous intrusion ages of around 2400 Myr were selected for whole grain U-Pb and Pb-Pb analyses by Chemical Abrasion Isotope Dilution Thermal Ionization Mass Spectrometer (CA-ID-TIMS) performed at the University of Geneva. Zircons were extracted from the epoxy grain mount and were annealed at 1000°C for 48 h in quartz crucibles in muffle furnace. In order to minimize the effects of secondary lead loss each individual zircon grain was placed into pre-cleaned Savillex capsule and chemically abraded in HF + trace HNO_3 at 180°C for up to 14h in Parr bombs (Mattinson et al., 2005). Most of the grains were completely dissolved after 4h, for the remaining grains stepwise chemical abrasion was performed on every 2 to 4 hours. The grain fragments resulting from the intensive chemical abrasion disintegration of a single zircon crystal were treated separately. This approach allows spatial resolution in the analysed zircon grains. The full information about the following dissolution using EARTHTIME ^{202}Pb-^{205}Pb-^{235}U-^{238}U tracer (Condon et al., 2015), chemistry and technical details on instrument calibration, mass fractionation and blank control can be found elsewhere (Zeh et al., 2015). All common Pb in the zircon analyses was attributed to the procedural blank with the following lead isotopic composition: $^{206}Pb/^{204}Pb$ = 17.10±1.2, $^{207}Pb/^{204}Pb$ = 15.07±0.7, $^{208}Pb/^{204}Pb$ = 36.17±0.7 (1σ, %). The accuracy of the measured data was assessed by repeated analysis of the 2Ga synthetic solution (Condon et al., 2008). The 2Ga synthetic solution measured with EARTHTIME ^{202}Pb-^{205}Pb-^{235}U-^{238}U tracer yielded mean $^{207}Pb/^{206}Pb$ = 1999.92±0.18/0.37/6.0 Ma (MSWD=0.86, n=25). All data are reported in the Supplemental File with internal errors only, including counting statistics, uncertainties in correcting for mass discrimination, and the uncertainty in the common (blank) Pb composition.

Total of 12 CA-ID-TIMS measurements yield discordant and concordant zircons (see Fig. 3B). The initial isotopic ratio data are available (Supplemental File). One concordant age at 2291±8 Myr is interpreted to be the age on intrusion. This date is consistent with what is observed in SHRIMP-RG data (Fig. 3A). A concordant zircon with Pb-Pb age of 1873±2 Myr is interpreted to define the age of metamorphic event. Other zircons are discordant and were affected by recent Pb-loss.

Table S1. The δ^{18}O, δ^{17}O and Δ^{17}O values of Paleoproterozoic hydrothermally altered rocks.

Locality/sample	mineral	Calibrated to air O_2						Calibrated to silicate standard UOG (δ18O = 6.52 ‰; Δ17O = -102 ‰)		
		δ^{18}O	SE	δ^{17}O	SE	Δ^{17}O	SE	δ^{18}O	δ^{17}O	Δ^{17}O
					Varatskoe					
V41	garnet	-20.14	0.004	-10.77	0.010	-0.086	0.010	-19.85	-10.64	-0.107
V100	pyroxene	5.82	0.003	2.96	0.008	-0.129	0.009	6.01	3.09	-0.098
V40	garnet	-20.31	0.004	-10.89	0.008	-0.112	0.009	-20.12	-10.75	-0.081
					Kiy island					
Ki-9	garnet	-1.70	0.004	-0.99	0.008	-0.086	0.009	-1.50	-0.85	-0.055
Ki-9-1	garnet	-0.59	0.004	-0.37	0.011	-0.063	0.012	-0.39	-0.24	-0.032
Height 128										
KV-10	garnet	-10.00	0.004	-5.46	0.005	-0.156	0.007	-9.80	-5.32	-0.125
KV-10	amphibole	-8.74	0.004	-4.74	0.013	-0.103	0.013	-8.55	-4.61	-0.072
					Khitoostrov					
X411	garnet	9.85	0.004	5.02	0.009	-0.204	0.010	8.053	4.15	-0.126
X425	garnet	-26.07	0.003	-14.00	0.010	-0.165	0.010	-27.870	-14.87	-0.086
X417	garnet	-7.91	0.005	-4.35	0.011	-0.155	0.012	-9.707	-5.23	-0.077
X417-1	garnet	-7.73	0.004	-4.28	0.008	-0.182	0.009	-9.530	-5.16	-0.104
X425-1	garnet	-23.27	0.004	-12.52	0.005	-0.172	0.006	-25.071	-13.39	-0.094
K-4	garnet	-16.87	0.005	-9.11	0.007	-0.161	0.008	-18.663	-9.98	-0.083
K-1	garnet	-22.04	0.006	-11.84	0.008	-0.144	0.010	-23.838	-12.71	-0.066

The value of Δ^{17}O is calculated based on the equation $\Delta^{17}O = \delta^{17}O - 0.5305 \cdot \delta^{18}O$; SE – standard error

APPENDIX D

CHAPTER VI SUPPORTING INFORMATION

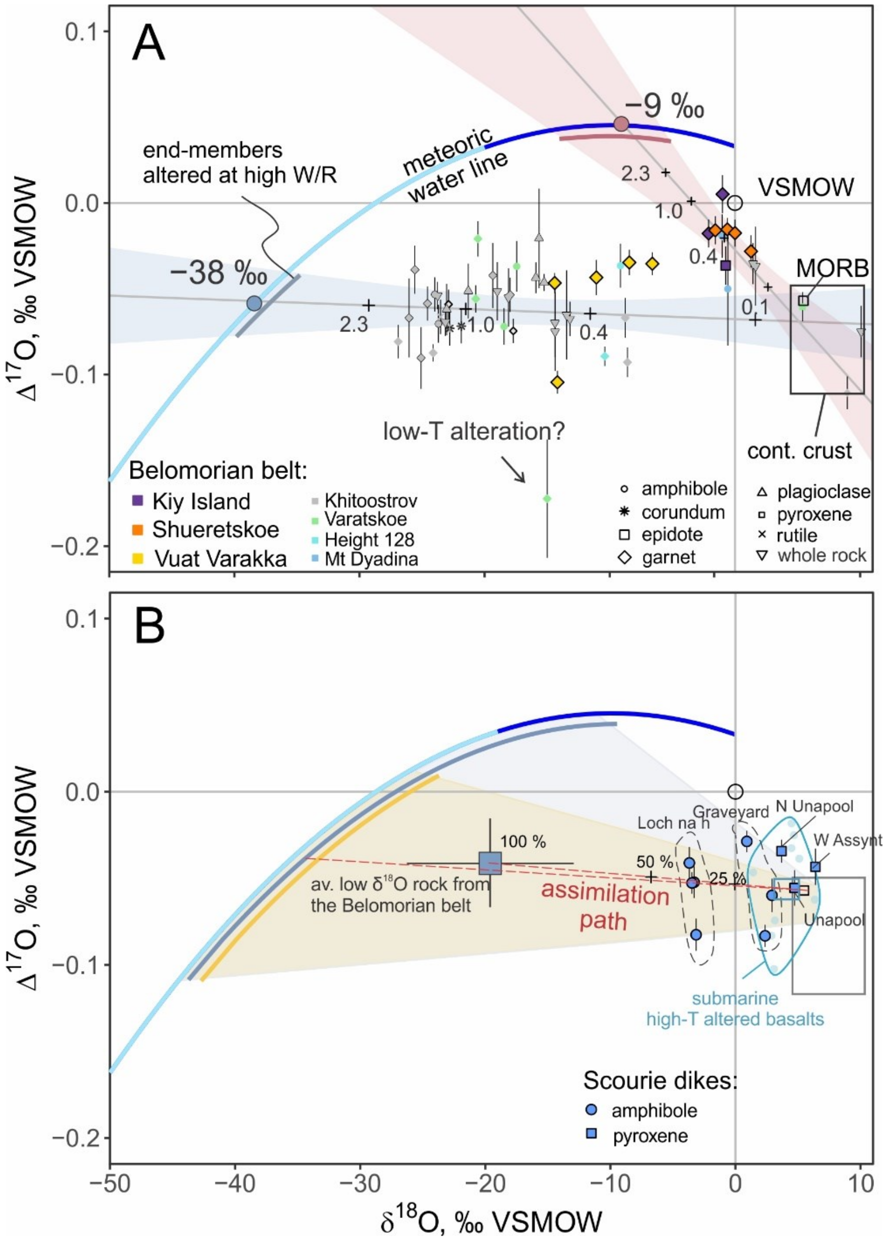

Figure S1. A - Modified Figure 9A from the main text showing color-coding for the Belomorian belt localities from previous publications (Bindeman and Serebryakov, 2011; Bindeman 2014; see main text for references). B – Modified Figure 9B showing Scourie dike localities as annotated.

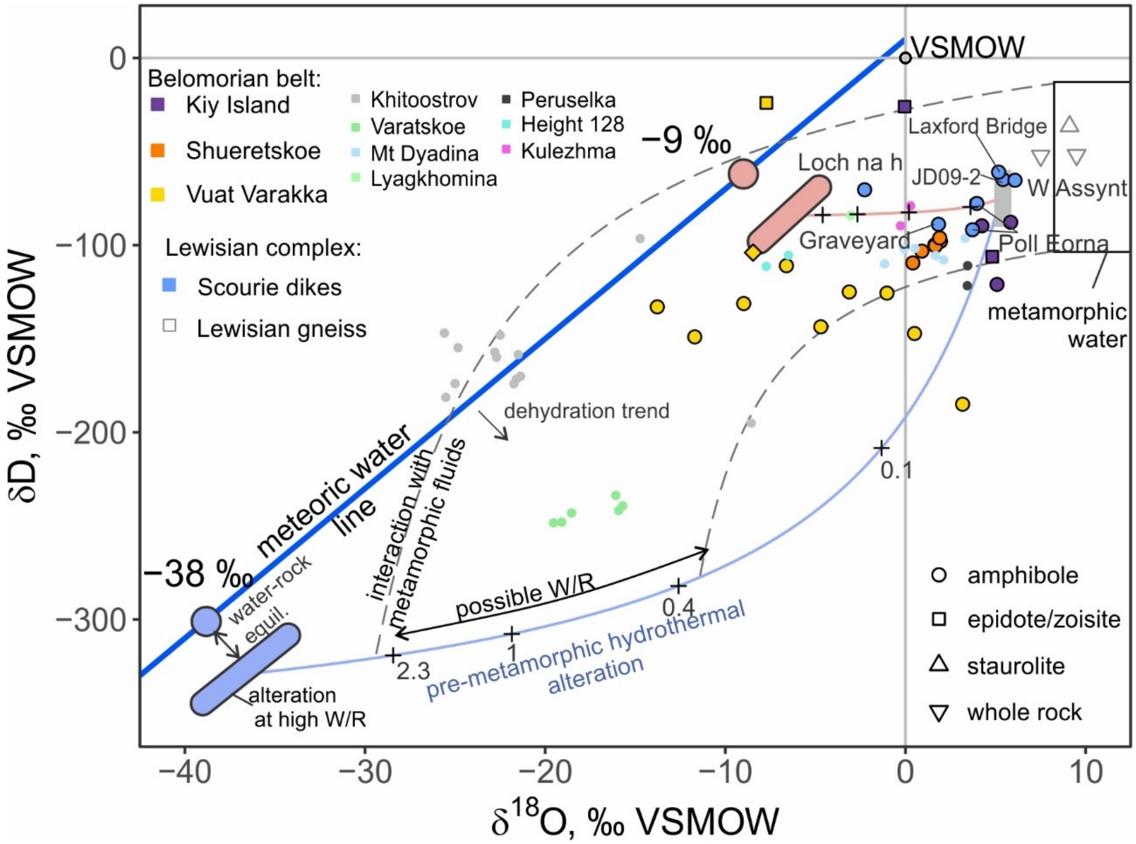

Figure S2. Modified Figure 10 from the main text showing different color-coding for the Belomorian belt localities from previous publications (A) and Scourie dike localities as annotated (B)

Table S1. The $\delta^{18}O$ values (in ‰ VSMOW) of the Belomorian belt samples as determined by conventional oxygen isotope analysis

Latitude	Longitude	Sample	Mineral analyzed	$\delta^{18}O$	Locality
66.34133	33.04286	CH341	garnet	5.45	Khitoostrov
66.33117	33.10228	X-638	garnet	4.97	Khitoostrov
66.33114	33.06933	X-639	kyanite	3.19	Khitoostrov
66.33114	33.06933	X-639A	garnet	4.26	Khitoostrov
66.33114	33.06933	X-639b	garnet	4.72	Khitoostrov
66.33061	33.05944	X-640	garnet	4.60	Khitoostrov
66.31506	33.04278	X-644	garnet	5.17	Khitoostrov
66.31506	33.03853	X-646	quartz	9.56	Khitoostrov
66.32356	33.03325	X-647	garnet	0.50	Khitoostrov
66.33000	33.03386	X-648	quartz	9.45	Khitoostrov
64.00279	37.86967	Ki-01	pyroxene	4.59	Kiy Island
64.00447	37.87078	Ki-02	amphibole	4.46	Kiy Island
64.00569	37.86825	Ki-03	pyroxene	5.09	Kiy Island
64.00569	37.86825	Ki-03	amphibole	4.86	Kiy Island
64.00892	37.86527	Ki-04	kyanite	5.43	Kiy Island

Table S1 Continued.

Latitude	Longitude	Sample	Mineral analyzed	$\delta^{18}O$	Locality
64.00874	37.86459	Ki-05	garnet	3.86	Kiy Island
64.00880	37.86443	Ki-06	zoisite	4.82	Kiy Island
64.00880	37.86443	Ki-06	amphibole	4.54	Kiy Island
64.01086	37.86443	Ki-07	quartz	7.91	Kiy Island
64.00272	37.87959	Ki-08	corundum	4.21	Kiy Island
64.00319	37.88748	Ki-09	garnet	-0.51	Kiy Island
64.00319	37.88748	Ki-09	epidote	-0.05	Kiy Island
64.00319	37.88748	Ki-09	garnet	-2.10	Kiy Island
64.00319	37.88748	Ki-09	garnet	-0.99	Kiy Island
64.00319	37.88748	Ki-09	epidote	-0.74	Kiy Island
64.00638	37.87421	Ki-10	quartz	7.99	Kiy Island
64.00829	37.86718	Ki-11	amphibole	5.08	Kiy Island
64.00829	37.86718	Ki-11A	pyroxene	4.76	Kiy Island
64.00881	37.86443	Ki-12	kyanite	5.76	Kiy Island
64.00891	37.86527	Ki-13	garnet	3.80	Kiy Island
64.00892	37.86527	Ki-14	corundum	6.58	Kiy Island

Table S1 Continued.

Latitude	Longitude	Sample	Mineral analyzed	$\delta^{18}O$	Locality
64.00892	37.86527	Ki-14	zoisite	5.67	Kiy Island
64.00850	37.86629	Ki-15	amphibole	4.55	Kiy Island
64.00365	37.87555	Ki-16	corundum	4.42	Kiy Island
64.00256	37.88021	Ki-18	amphibole	5.16	Kiy Island
63.99713	37.88796	Ki-19	garnet	4.74	Kiy Island
64.74748	34.78872	SH-01	garnet	1.00	Shueretskoe
64.74748	34.78872	SH-01A	quartz	4.14	Shueretskoe
64.74743	34.78883	SH-01A	quartz	3.90	Shueretskoe
64.74748	34.78872	SH-02	garnet	1.23	Shueretskoe
64.74748	34.78872	SH-02A	kyanite	2.64	Shueretskoe
64.74748	34.78872	SH-03	garnet	1.82	Shueretskoe
64.74748	34.78872	SH-03	amphibole	1.63	Shueretskoe
64.74748	34.78872	SH-04	garnet	2.01	Shueretskoe
64.74748	34.78872	SH-05	garnet	2.00	Shueretskoe
64.74748	34.78872	SH-05A	quartz	4.34	Shueretskoe
64.74748	34.78872	SH-05A	garnet	1.51	Shueretskoe

Table S1 Continued.

Latitude	Longitude	Sample	Mineral analyzed	$\delta^{18}O$	Locality
64.74748	34.78872	SH-06	quartz	4.83	Shueretskoe
64.74748	34.78872	SH-06A	quartz	4.36	Shueretskoe
64.74748	34.78872	SH-06B	quartz	4.41	Shueretskoe
64.74748	34.78872	SH-07	garnet	1.94	Shueretskoe
64.74748	34.78872	SH-07	quartz	5.37	Shueretskoe
64.74748	34.78872	SH-08	garnet	1.64	Shueretskoe
64.74748	34.78872	SH-08	amphibole	1.94	Shueretskoe
64.74748	34.78872	SH-08	amphibole	1.64	Shueretskoe
64.74748	34.78872	SH-09	garnet	2.39	Shueretskoe
64.74748	34.78872	SH-09	quartz	4.18	Shueretskoe
64.74748	34.78872	SH-10	garnet	0.98	Shueretskoe
64.74748	34.78872	SH-10	quartz	4.35	Shueretskoe
64.74748	34.78872	SH-10	amphibole	1.93	Shueretskoe
64.74743	34.78883	SH-11	quartz	3.90	Shueretskoe
64.74743	34.78883	SH-11A	garnet	1.08	Shueretskoe

Table S1 Continued.

Latitude	Longitude	Sample	Mineral analyzed	$\delta^{18}O$	Locality
64.74743	34.78883	SH-11A	garnet	0.80	Shueretskoe
64.74743	34.78883	SH-11B	garnet	0.61	Shueretskoe
64.74743	34.78883	SH-11B	garnet	0.53	Shueretskoe
64.74743	34.78883	SH-12	garnet	1.37	Shueretskoe
64.74741	34.78887	SH-13	garnet	1.17	Shueretskoe
64.74739	34.78896	SH-14	garnet	1.46	Shueretskoe
64.74757	34.78899	SH-15	amphibole	1.90	Shueretskoe
64.74749	34.78894	SH-15	garnet	1.44	Shueretskoe
64.74747	34.78903	SH-15A	quartz	5.24	Shueretskoe
64.74747	34.78903	SH-16	garnet	1.54	Shueretskoe
64.74757	34.78899	SH-17	kyanite	1.99	Shueretskoe
64.74747	34.78903	SH-17	garnet	1.87	Shueretskoe
64.74749	34.78894	SH-18	kyanite	1.42	Shueretskoe
64.74741	34.78887	SH-18	garnet	1.17	Shueretskoe
64.74739	34.78909	SH-19	quartz	3.68	Shueretskoe

Table S1 Continued.

Latitude	Longitude	Sample	Mineral analyzed	$\delta^{18}O$	Locality
64.74749	34.78894	SH-19	garnet	0.88	Shueretskoe
64.74757	34.78899	SH-20	garnet	1.84	Shueretskoe
64.74757	34.78899	SH-20	amphibole	1.66	Shueretskoe
64.74739	34.78909	SH-21	garnet	1.36	Shueretskoe
64.74773	34.79369	SH-25	garnet	3.02	Shueretskoe
64.72090	34.73504	TE-01	garnet	1.22	Shueretskoe
64.72168	34.73503	TE-02	garnet	1.28	Shueretskoe
64.72149	34.73540	TE-04	amphibole	0.91	Shueretskoe
64.72104	34.73683	TE-09	garnet	0.01	Shueretskoe
64.72188	34.73625	TE-10	garnet	-0.72	Shueretskoe
64.72188	34.73625	TE-10	garnet	-1.57	Shueretskoe
64.72167	34.73644	TE-11	garnet	-0.06	Shueretskoe
64.72167	34.73644	TE-11	garnet	-0.61	Shueretskoe
64.72224	34.73678	TE-12	amphibole	0.41	Shueretskoe
66.22189	33.11369	V14-02	garnet	5.52	Varatskoe
66.22189	33.11369	V14-03	garnet	7.68	Varatskoe

Table S1 Continued.

Latitude	Longitude	Sample	Mineral analyzed	$\delta^{18}O$	Locality
66.21486	33.10811	V14-04	garnet	6.78	Varatskoe
66.21000	33.10047	V14-07	garnet	5.84	Varatskoe
66.20461	33.09900	V14-10	garnet	7.46	Varatskoe
66.20483	33.10017	V14-11	garnet	6.77	Varatskoe
66.35644	33.13389	NK14-17-1	garnet	8.44	Vuat Varakka
66.35644	33.13389	NK14-17-2	garnet	8.27	Vuat Varakka
66.35661	33.13278	NK14-18-3	garnet	4.94	Vuat Varakka
66.35661	33.13258	NK14-18-5	garnet	4.80	Vuat Varakka
66.35642	33.13283	NK14-19-3	garnet	3.93	Vuat Varakka
66.35642	33.13283	NK14-19-4	amphibole	5.20	Vuat Varakka
66.35642	33.13283	NK14-19-5	garnet	5.15	Vuat Varakka
66.35642	33.13283	NK14-19-7	garnet	4.04	Vuat Varakka
66.35650	33.13283	NK14-19-8	amphibole	5.67	Vuat Varakka
66.35067	33.16238	NK15-032	garnet	1.64	Vuat Varakka
66.35074	33.16281	NK15-032A	garnet	4.88	Vuat Varakka

Table S1 Continued.

Latitude	Longitude	Sample	Mineral analyzed	$\delta^{18}O$	Locality
66.35138	33.16334	NK15-033	garnet	-5.04	Vuat Varakka
66.35138	33.16334	NK15-033	garnet	-4.44	Vuat Varakka
66.35138	33.16334	NK15-033-2	garnet	-3.89	Vuat Varakka
66.35138	33.16334	NK15-033-4A	garnet	-4.71	Vuat Varakka
66.34966	33.16096	NK15-034	garnet	4.45	Vuat Varakka
66.34966	33.16096	NK15-034-1	garnet	8.06	Vuat Varakka
66.34966	33.16096	NK15-034-4	whole rock	4.82	Vuat Varakka
66.34826	33.16234	NK15-035-1	garnet	4.69	Vuat Varakka
66.34826	33.16234	NK15-035-8	garnet	3.98	Vuat Varakka
66.34816	33.16269	NK15-036	garnet	4.09	Vuat Varakka
66.35130	33.15918	NK15-038	garnet	4.96	Vuat Varakka
66.35130	33.15918	NK15-038-2	garnet	5.74	Vuat Varakka
66.35026	33.16248	NK15-039-1	garnet	4.45	Vuat Varakka
66.34978	33.16284	NK15-040-1	garnet	4.28	Vuat Varakka
66.34969	33.16380	NK15-041	garnet	4.55	Vuat Varakka

Table S1 Continued.

Latitude	Longitude	Sample	Mineral analyzed	$\delta^{18}O$	Locality
66.34969	33.16380	NK15-041-1	garnet	3.48	Vuat Varakka
66.34965	33.17014	NK15-042	garnet	-3.31	Vuat Varakka
66.34965	33.17014	NK15-042-1	garnet	-4.05	Vuat Varakka
66.34965	33.17014	NK15-042-1	garnet	-3.88	Vuat Varakka
66.34966	33.17171	NK15-043	garnet	5.49	Vuat Varakka
66.34829	33.16833	NK15-044-1	epidote	-4.33	Vuat Varakka
66.34806	33.16664	NK15-045	garnet	3.63	Vuat Varakka
66.32784	33.01345	NK15-051	garnet	6.90	Vuat Varakka
66.32355	33.03328	NK15-052-1	garnet	0.49	Vuat Varakka
66.32276	33.03312	NK15-053-1	garnet	6.61	Vuat Varakka
66.32054	33.03385	NK15-054	garnet	6.66	Vuat Varakka
66.31910	33.03443	NK15-055	garnet	6.68	Vuat Varakka
66.31852	33.03864	NK15-056A	garnet	6.60	Vuat Varakka
66.31824	33.04103	NK15-057	garnet	5.38	Vuat Varakka
66.31804	33.04147	NK15-057A-2	whole rock	6.77	Vuat Varakka

Table S1 Continued.

Latitude	Longitude	Sample	Mineral analyzed	$\delta^{18}O$	Locality
66.32433	33.03346	NK15-058	garnet	5.08	Vuat Varakka
66.32703	33.03294	NK15-059	garnet	5.07	Vuat Varakka
66.32724	33.07833	NK15-061	garnet	7.57	Vuat Varakka
66.35810	32.97707	NK15-063	garnet	6.87	Vuat Varakka
66.36330	32.96730	NK15-064	garnet	7.50	Vuat Varakka
66.36915	32.96007	NK15-065	garnet	7.32	Vuat Varakka
66.34246	33.04052	NK15-073	garnet	1.55	Vuat Varakka
66.35115	33.15506	NK15-077	garnet	6.99	Vuat Varakka
66.34985	33.15633	NK15-078A	garnet	7.35	Vuat Varakka
66.35053	33.15299	NK15-079	garnet	7.51	Vuat Varakka
66.36522	33.20023	NK15-080	garnet	3.69	Vuat Varakka
66.36522	33.20023	NK15-080-3	garnet	4.73	Vuat Varakka
66.36522	33.20023	NK15-080-4	garnet	4.00	Vuat Varakka
66.35200	33.17578	NK15-087	garnet	8.37	Vuat Varakka
66.34932	33.17589	NK15-089	garnet	5.58	Vuat Varakka

Table S1 Continued.

Latitude	Longitude	Sample	Mineral analyzed	δ^{18}O	Locality
66.34599	33.16759	NK15-090	garnet	3.94	Vuat Varakka
66.34659	33.16162	NK15-093	garnet	-4.62	Vuat Varakka
66.34659	33.16162	NK15-093-5	garnet	-5.58	Vuat Varakka
66.34659	33.16162	NK15-093-7	epidote/zoisite	-7.72	Vuat Varakka
66.34659	33.16162	NK15-093-8	garnet	8.75	Vuat Varakka
66.35246	33.14386	NK15-095-1	garnet	8.74	Vuat Varakka
66.34732	33.16163	NK15-101	garnet	-4.20	Vuat Varakka
66.34732	33.16163	NK15-101-1	garnet	-3.00	Vuat Varakka
66.30397	32.77917	NK15-108	garnet	7.70	Vuat Varakka
66.34662	33.16175	NK16-039	garnet	7.99	Vuat Varakka
66.34850	33.14919	NK16-043	garnet	6.68	Vuat Varakka
66.34571	33.15678	NK16-046	garnet	7.86	Vuat Varakka
66.34583	33.16243	NK16-047	garnet	8.47	Vuat Varakka
66.34621	33.16255	NK16-048	garnet	8.68	Vuat Varakka
66.34621	33.16255	NK16-048-1	garnet	3.05	Vuat Varakka

Table S1 Continued.

Latitude	Longitude	Sample	Mineral analyzed	$\delta^{18}O$	Locality
66.34621	33.16255	NK16-048-2	garnet	5.66	Vuat Varakka
66.34456	33.16017	NK16-051	garnet	4.91	Vuat Varakka
66.34548	33.16208	NK16-052	garnet	3.72	Vuat Varakka
66.34895	33.15605	NK16-053	garnet	7.53	Vuat Varakka
66.34718	33.15891	NK16-054	garnet	5.37	Vuat Varakka
66.34583	33.16166	NK16-055	garnet	-3.82	Vuat Varakka
66.34728	33.16195	NK16-055-3	garnet	-3.99	Vuat Varakka
66.34583	33.16166	NK16-055-5	garnet	-6.46	Vuat Varakka
66.34583	33.16166	NK16-055-6	garnet	-6.11	Vuat Varakka
66.34829	33.15311	NK16-057	garnet	7.70	Vuat Varakka
66.34571	33.16142	NK16-058-21	garnet	-9.16	Vuat Varakka
66.34571	33.16142	NK16-058-39	garnet	-9.18	Vuat Varakka
66.34571	33.16142	NK16-058-40	garnet	-5.36	Vuat Varakka
66.34571	33.16142	NK16-058-8	garnet	-6.11	Vuat Varakka
66.34569	33.15992	NK16-060	garnet	4.16	Vuat Varakka

Table S1 Continued.

Latitude	Longitude	Sample	Mineral analyzed	$\delta^{18}O$	Locality
66.34405	33.16072	NK16-062	garnet	9.21	Vuat Varakka
66.34615	33.16146	NK16-063	garnet	-10.54	Vuat Varakka
66.34615	33.16146	NK16-063-1	garnet	-10.27	Vuat Varakka
66.34615	33.16146	NK16-063-5	garnet	-10.75	Vuat Varakka
66.34662	33.16103	NK16-064	garnet	-5.79	Vuat Varakka
66.34662	33.16103	NK16-064-2	garnet	-8.72	Vuat Varakka
66.34662	33.16103	NK16-064-3	garnet	-8.53	Vuat Varakka
66.35115	33.19247	NK16-065	garnet	8.06	Vuat Varakka
66.35133	33.19687	NK16-067	garnet	8.15	Vuat Varakka
66.34628	33.16154	NK16-069	garnet	-10.46	Vuat Varakka
66.35142	33.15116	NK16-40	garnet	7.96	Vuat Varakka
66.34868	33.15507	NK16-44	garnet	7.97	Vuat Varakka
66.34813	33.15718	NK16-45	garnet	7.96	Vuat Varakka
66.34455	33.15888	NK16-50	garnet	5.36	Vuat Varakka
66.34571	33.16142	NK16-58-33	garnet	-9.13	Vuat Varakka

Table S1 Continued.

Latitude	Longitude	Sample	Mineral analyzed	$\delta^{18}O$	Locality
66.34662	33.16103	NK16-64-4	garnet	-9.16	Vuat Varakka
66.35778	33.13078	S-01	garnet	9.21	Vuat Varakka
66.35811	33.13214	S-02	garnet	8.13	Vuat Varakka
66.35811	33.13214	S-03	garnet	6.25	Vuat Varakka
66.35819	33.13267	S-06	garnet	7.09	Vuat Varakka
66.35819	33.13267	S-07	garnet	7.76	Vuat Varakka
66.35842	33.13314	S-08	garnet	7.46	Vuat Varakka
66.35958	33.13422	S-10	garnet	5.89	Vuat Varakka
66.35958	33.13422	S-11	garnet	6.99	Vuat Varakka
66.35725	33.13247	S-12	garnet	5.90	Vuat Varakka
66.35608	33.13311	S-14	garnet	-0.42	Vuat Varakka
66.35608	33.13312	S-15	garnet	-10.09	Vuat Varakka
66.35608	33.13312	S-16	garnet	-9.17	Vuat Varakka
66.35597	33.13330	S-17	garnet	-12.49	Vuat Varakka
66.35597	33.13330	S-18	amphibole	-11.88	Vuat Varakka

Table S1 Continued.

Latitude	Longitude	Sample	Mineral analyzed	$\delta^{18}O$	Locality
66.35597	33.13330	S-18A	garnet	-13.62	Vuat Varakka
66.35597	33.13330	S-18A	amphibole	-8.98	Vuat Varakka
66.35591	33.13342	S-19	quartz	-1.47	Vuat Varakka
66.35592	33.13342	S-19A	garnet	-1.64	Vuat Varakka
66.35592	33.13342	S-19B	garnet	-5.02	Vuat Varakka
66.35592	33.13342	S-19C	garnet	6.83	Vuat Varakka
66.35575	33.13333	S-20	garnet	-13.29	Vuat Varakka
66.35575	33.13333	S-20A	quartz	-0.58	Vuat Varakka
66.35575	33.13333	S-21	amphibole	4.43	Vuat Varakka
66.35575	33.13333	S-22	garnet	7.40	Vuat Varakka
66.35558	33.13356	S-28A	garnet	-11.74	Vuat Varakka
66.35556	33.13367	S-32	garnet	5.61	Vuat Varakka
66.35558	33.13356	S-33	garnet	7.10	Vuat Varakka
66.35539	33.13386	S-35	garnet	-10.53	Vuat Varakka
66.35539	33.13386	S-37	garnet	-10.44	Vuat Varakka

Table S1 Continued.

Latitude	Longitude	Sample	Mineral analyzed	$\delta^{18}O$	Locality
66.35525	33.13408	S-38A	garnet	-8.74	Vuat Varakka
66.35525	33.13408	S-38B	garnet	7.36	Vuat Varakka
66.35422	33.18631	S-40	garnet	4.68	Vuat Varakka
66.34258	33.17167	S-44	garnet	6.02	Vuat Varakka
66.34408	33.16128	S-46	garnet	9.20	Vuat Varakka
66.34236	33.15353	S-47	garnet	5.70	Vuat Varakka
66.35475	33.13525	S-49A	garnet	-6.94	Vuat Varakka
66.35739	33.12728	S-50	garnet	8.57	Vuat Varakka
66.35511	33.12464	S-51	garnet	7.75	Vuat Varakka
66.35306	33.12761	S-52	garnet	8.25	Vuat Varakka
66.35318	33.13062	S-53	garnet	7.61	Vuat Varakka
66.35194	33.13067	S-54	garnet	7.82	Vuat Varakka
66.35353	33.11700	S-56	garnet	8.11	Vuat Varakka
66.35189	33.10747	S-57	garnet	8.09	Vuat Varakka
66.35469	33.08233	S-58	garnet	8.41	Vuat Varakka

Table S1 Continued.

Latitude	Longitude	Sample	Mineral analyzed	$\delta^{18}O$	Locality
66.35328	33.16106	S-59	garnet	5.01	Vuat Varakka
66.35233	33.16044	S-60	garnet	5.50	Vuat Varakka
66.34864	33.16313	S-61	pyroxene	5.24	Vuat Varakka
66.34864	33.16313	S-61A	pyroxene	4.83	Vuat Varakka
66.34864	33.16313	S-61B	garnet	4.74	Vuat Varakka
66.34828	33.16503	S-62	garnet	3.00	Vuat Varakka
66.34828	33.16503	S-62A	amphibole	4.01	Vuat Varakka
66.34786	33.16614	S-63	garnet	5.14	Vuat Varakka
66.34844	33.16586	S-64	garnet	7.33	Vuat Varakka
66.34844	33.16587	S-64A	garnet	4.36	Vuat Varakka
66.34811	33.16672	S-65	garnet	-1.03	Vuat Varakka
66.34783	33.16742	S-66	garnet	4.95	Vuat Varakka
66.34797	33.16294	S-67	garnet	6.96	Vuat Varakka
66.34797	33.16294	S-67A	garnet	4.85	Vuat Varakka
66.34833	33.16211	S-68	garnet	6.11	Vuat Varakka

Table S1 Continued.

Latitude	Longitude	Sample	Mineral analyzed	$\delta^{18}O$	Locality
66.34833	33.16211	S-68A	garnet	4.76	Vuat Varakka
66.35279	33.15761	S-69	garnet	7.95	Vuat Varakka
66.35544	33.13364	S-70	garnet	5.54	Vuat Varakka
66.35544	33.13364	S-71	garnet	-11.58	Vuat Varakka
66.35558	33.13356	S-72	garnet	-12.84	Vuat Varakka
66.35486	33.13861	S-73	garnet	8.37	Vuat Varakka
66.35526	33.13365	S-74	garnet	8.21	Vuat Varakka
66.35543	33.13496	S-75	garnet	7.32	Vuat Varakka
66.34527	33.15856	S-88	pyroxene	5.29	Vuat Varakka
66.34527	33.15856	S-88A	garnet	6.97	Vuat Varakka
66.34847	33.14693	S-89	garnet	7.72	Vuat Varakka
66.35269	33.14272	S-91	garnet	8.26	Vuat Varakka

Table S2. The $\delta^{18}O$ values of coexisting minerals extracted from the Belomorian belt samples reported in ‰ (VSMOW) with corresponding equilibrium temperature estimates. Abbreviations are as follows: gt – garnet, amph – amphibole, qtz – quartz, ky – kyanite, px – pyroxene, zo – zoisite, ep – epidote, crn – corundum.

Sample	Locality	gt	amph	qtz	ky	px	zo	ep	crn	gt-mineral	calc. equil. T, °C*	calc. equil. T, °C**
SH-03	Shueretskoe	1.82	1.63							0.2	174	
SH-08	Shueretskoe	1.64	1.94							-0.3	NA	
SH-15	Shueretskoe	1.44	1.9							-0.5	NA	
SH-20	Shueretskoe	1.84	1.66							0.2	174	
S-18A	Vuat Varakka	-13.62	-8.98							-4.6	NA	
SH-05A	Shueretskoe	1.51		4.34						-2.8		801
SH-07	Shueretskoe	1.94		5.37						-3.4		691
SH-09	Shueretskoe	2.39		4.18						-1.8		1064
SH-10	Shueretskoe	0.98	1.93	4.35						1.0/-3.4	NA	691
SH-19	Shueretskoe	0.88		3.68						-2.8		691
SH-17	Shueretskoe	1.87			1.99					-2.8		
SH-18	Shueretskoe	1.17			1.42					-0.1		
Ki-09	Kiy Island	-0.51						-0.05		-0.5		
										amph-mineral		
Ki-03	Kiy Island		4.86			5.09				-0.3		
Ki-06	Kiy Island		4.54				4.82			-0.3		
										zo-crn		
Ki-14	Kiy Island						5.67		6.58	-0.9		

* - equilibrium temperature computed from fractionation between almandine and diopside (close proxy to amphibole). Due to small fractionation (close to 0 ‰ at 600 °C; Valley, 2003), small analytical uncertainties result in large uncertainties of estimated equilibrium temperatures producing NAs and unrealistic estimates.

** - equilibrium temperature calculated from fractionation between garnet (almandine) and quartz (Zheng, 1993)

Table S3. The $\delta^{18}O$ values (in ‰ VSMOW) of the Scourie dikes as determined by conventional oxygen isotope analysis (see methods)

Latitude	Longitude	Sample	Dike name	Description	Mineral analyzed	$\delta^{18}O$
58.17140	-5.305971	SCD44D	Achmelvich bay	Interior (coarse-grained)	amphibole	4.82
58.35272	-5.166977	SCD2	Graveyard	Interior	amphibole	2.63
58.34645	-5.155866	SCD39	Graveyard	Interior	amphibole	2.32
58.34325	-5.149407	SCD41	Graveyard	Interior	amphibole	1.83
58.33681	-5.134849	SCD42	Graveyard	Interior	amphibole	4.18
58.35274	-5.166821	SCD5	Graveyard	Host rock (at contact)	quartz	9.28
58.36433	-5.087432	SCD14A	JD09-2	Interior	amphibole	5.41
58.39012	-5.024905	SCD13	Laxford bridge	Amphibolite (meta-Scourie)	amphibole	5.17
58.18458	-5.111461	SCD35	Loch na h	Interior	amphibole	-2.27
58.18458	-5.111461	SCD35	Loch na h	Interior	plagioclase	2.92
58.18458	-5.111461	SCD35	Loch na h	Interior	plagioclase	2.84
58.18458	-5.111461	SCD35	Loch na h	Interior	magnetite	-3.27
58.18437	-5.111744	SCD36A	Loch na h	Chilled margin (inner contact)	whole rock	5.04
58.18437	-5.111744	SCD36B	Loch na h	Host rock	whole rock	7.51

Table S3 Continued.

Latitude	Longitude	Sample	Dike name	Description	Mineral analyzed	$\delta^{18}O$
58.18462	-5.111603	SCD45	Loch na h	Interior (coarse-grained)	amphibole	-2.22
58.18462	-5.111603	SCD45	Loch na h	Interior (coarse-grained)	plagioclase	1.69
58.18462	-5.111603	SCD45	Loch na h	Interior (coarse-grained)	magnetite	-4.47
58.18462	-5.111603	SCD45	Loch na h	Interior (coarse-grained)	magnetite	-4.78
58.18683	-5.120700	SCDTPA	Loch na h	Interior (coarse-grained)	amphibole	-2.37
58.18683	-5.120700	SCDTPA	Loch na h	Interior (coarse-grained)	amphibole	-2.41
58.18683	-5.120700	SCDTPA	Loch na h	Interior (coarse-grained)	plagioclase	3.23
58.18533	-5.114617	SCDTPB	Loch na h	Interior (coarse-grained)	amphibole	-2.40
58.18533	-5.114617	SCDTPB	Loch na h	Interior (coarse-grained)	plagioclase	-0.36
58.22749	-5.300747	SCD26B	N Clashnessie	Interior	whole rock	2.73
58.23343	-5.247036	SCD27	N of Loch Poll	Interior	whole rock	3.80
58.26355	-5.040705	SCD37A	N Unapool	Interior	amphibole	3.63
58.26355	-5.040705	SCD37B	N Unapool	Chilled margin (northern inner contact)	whole rock	5.07
58.26246	-5.035890	SCD38	N Unapool	Interior	amphibole	3.49
58.24113	-5.193850	SCD29A	Nedd dyke	Interior	whole rock	5.48

Table S3 Continued.

Latitude	Longitude	Sample	Dike name	Description	Mineral analyzed	$\delta^{18}O$
58.24076	-5.195653	SCD30A	Nedd dyke fork	Interior	amphibole	3.96
58.35899	-5.161833	SCD12	Poll Eorna	Interior	amphibole	4.88
58.34854	-5.132669	SCD40A	Poll Eorna	Interior	amphibole	3.96
58.35982	-5.164986	SCD8	Poll Eorna	Interior	amphibole	3.72
58.35990	-5.164841	SCD9A	Poll Eorna	Chilled margin	whole rock	4.91
58.24162	-5.008136	SCD32	S Unapool	Interior	amphibole	3.80
58.24991	-5.009302	SCD34	Unapool	Interior	pyroxene	4.44
58.24991	-5.009302	SCD34	Unapool	Interior	pyroxene	4.72
58.18951	-5.317980	SCD16	unnamed1	Interior (5m inward from contact); foliated	amphibole	5.57
58.19720	-5.300990	SDC22A	unnamed2	Interior	amphibole	3.04
58.19720	-5.300990	SDC22B	unnamed2	Chilled margin (inner contact)	amphibole	6.71
58.19694	-5.301483	SCD23	unnamed3	Interior	amphibole	8.43
58.18855	-5.106696	SCD46A	W Assynt	Interior (coarse-grained)	pyroxene	6.08

Table S4. The $\delta^{18}O$ values of coexisting minerals (in ‰ VSMOW) extracted from the Loch na h dike with corresponding equilibrium temperature estimates. Fractionations are listed twice where duplicates are available. Abbreviations are as follows: amph – amphibole, plgs – plagioclase, mt – magnetite

Sample	Locality	amph	plgs	mt	plgs - amph	calc. equil. T, °C*	amph-mt	calc. equil. T, °C**
SCD35	Loch na h	-2.27	2.92	-3.27	5.2	244	1.0	1608
			2.84		5.1	249		
SCD45		-2.22	1.69	-4.47	3.9	324	2.3	967
				-4.78			2.6	894
SCDTPA		-2.37	3.23		6.2	200		
		-2.41			5.6	225		
SCDTPB		-2.40	-0.36		2.0	560		

*-equilibrium temperature calculated from fractionation between plagioclase (An40) and diopside (Chiba et al., 1989)

**-equilibrium temperature calculated from fractionation between diopside and magnetite (Chiba et al., 1989)

Table S5. The $\delta^{18}O$ values of Archean gneisses from Lewisan complexs (samples SDC-) and Paleoproterozoic South Harris Igneous Complex rocks (samples T-). Values reported in ‰ VSMOW.

Latitude	Longitude	Sample	Description	Mineral analyzed	$\delta^{18}O$
58.35443	-5.155087	SCD7	Mafic granulite	garnet	5.85
58.19175	-5.303868	SCD17	Aluminous schist with staurolite, kyanite from Stoer area	staurolite	9.11
58.19212	-5.303722	SCD18	Mafic granulite	amphibole	8.57
58.19764	-5.301242	SCD20	Garnet-biotite schist from Stoer area	garnet	8.25
58.19699	-5.301493	SDC21	Brecciated amphibolite/could be dike	amphibole (frag)	8.35
58.19699	-5.301493	SDC21	Brecciated amphibolite/could be dike	amphibole (cement)	7.68
58.19675	-5.301881	SCD24	Garnet-biotite schist from Stoer area	garnet	8.98
58.19671	-5.301751	SCD25	Aluminous schist with staurolite from Stoer area	corundum	7.16
58.19671	-5.301751	SCD25	Aluminous schist with staurolite, kyanite from Stoer area	staurolite	8.03
58.19671	-5.301751	SCD25	Aluminous schist with staurolite, kyanite from Stoer area	staurolite	8.10

Table S5 Continued.

Latitude	Longitude	Sample	Description	Mineral analyzed	$\delta^{18}O$
58.24310	-5.213611	SCD28A	Mafic granulite	pyroxene	6.60
58.24310	-5.213611	SCD28B	Quartz vein	quartz	7.46
57.76630	-6.975200	T170	Meta-anorthosite from Roneval Complex, South Harris	garnet	5.40
57.77650	-6.980200	T51	Metagrabbro from Roneval Complex, South Harris	garnet	5.45
57.76010	-6.985200	T44	Garnet-kyanite-biotite schist hosting Roneval Complex, South Harris	garnet	9.19

Table S6. Triple oxygen isotope composition of samples from the Belomorian belt as determined by high-precision analysis (see methods). All values are reported in per mil. Uncorrected data is reported as raw values (δ^{18}Oraw) and as raw linearized values (δ'^{18}Oraw*). Corrected values are denoted as ‘VSMOW adjusted’.

Sample	Date analyzed	Mineral analyzed	Locality	δ^{17}O, raw	±s.e.	δ^{18}O, raw	±s.e	δ'^{17}O, raw	δ'^{18}O, raw	Δ'^{17}O, raw	±s.e.	δ^{17}O, VSMOW adjusted	δ^{18}O, VSMOW adjusted	Δ^{17}O, VSMOW adjusted
NK16-055-5	11/10/2017	garnet	Vuat Varakka	-3.303	0.007	-6.120	0.003	-3.309	-6.139	-0.052	0.007	-3.537	-6.601	-0.035
NK16-058-032	11/10/2017	garnet	Vuat Varakka	-4.278	0.007	-7.959	0.004	-4.287	-7.991	-0.048	0.007	-4.512	-8.440	-0.035
NK16-063	11/10/2017	garnet	Vuat Varakka	-5.686	0.010	-10.598	0.003	-5.702	-10.654	-0.050	0.010	-5.920	-11.077	-0.043
S72	12/3/2017	garnet	Vuat Varakka	-7.495	0.007	-13.877	0.002	-7.523	-13.975	-0.109	0.007	-7.630	-14.186	-0.105
S72	12/1/2017	garnet	Vuat Varakka	-7.730	0.006	-14.399	0.003	-7.760	-14.504	-0.066	0.006	-7.686	-14.401	-0.047
TE10	12/3/2017	garnet	Shueretskoe	-0.711	0.008	-1.254	0.002	-0.711	-1.255	-0.045	0.008	-0.847	-1.567	-0.016
TE11	12/3/2017	garnet	Shueretskoe	-0.201	0.006	-0.294	0.004	-0.201	-0.294	-0.045	0.007	-0.337	-0.607	-0.015
TE2	12/3/2017	garnet	Shueretskoe	0.788	0.009	1.595	0.003	0.788	1.594	-0.057	0.009	0.652	1.282	-0.028
TE9	12/3/2017	garnet	Shueretskoe	0.122	0.008	0.319	0.003	0.122	0.319	-0.047	0.008	-0.015	0.006	-0.018

* - δ'^{x}O notation is defined as $1000 \cdot \ln((\delta^{X}O/1000)+1)$, where X is 17 or 18 after Miller (2002; see references in main text). The values were adjusted to reference material San Carlos olivine (SCO): $\delta'^{17}O = 2.677$, $\delta'^{18}O = 5.140$, $\Delta'^{17}O = -0.049$ (Pack et al., 2016). The difference between measured reference materials and the SCO was applied to the linearized values of unknowns within the same analytical session (see Date analyzed).

Table S7. Triple oxygen isotope composition of samples from the Scourie dikes as determined by high-precision analysis (see methods). All values are reported in per mil. Uncorrected data is reported as raw values (δ^{18}Oraw) and as raw linearized values (δ'^{18}Oraw*). Corrected values are denoted as 'VSMOW adjusted'.

Sample	**Date analyzed**	**Mineral analyzed**	**Locality**	**δ^{17}O, raw**	±s.e.	**δ^{18}O, raw**	±s.e.	**δ'^{17}O, raw**	**δ'^{18}O, raw**	**Δ'^{17}O, raw**	±s.e.	**δ^{17}O, VSMOW adjusted**	**δ^{18}O, VSMOW adjusted**	**Δ^{17}O, VSMOW adjusted**
SCD2	5/16/2017	amphibole	Graveyard	1.228	0.006	2.550	0.004	1.227	2.547	-0.124	0.006	1.171	2.366	-0.084
SCD35	5/16/2017	amphibole	Loch na h	-1.697	0.009	-2.964	0.003	-1.698	-2.969	-0.123	0.009	-1.754	-3.148	-0.084
SCD34	12/1/2017	pyroxene	Unapool	2.399	0.010	4.717	0.004	2.396	4.706	-0.100	0.010	2.443	4.716	-0.058
SCD38	12/1/2017	pyroxene	N Unapool	1.875	0.006	3.687	0.003	1.873	3.680	-0.079	0.007	1.919	3.685	-0.036
SCD41	12/1/2017	amphibole	Graveyard	0.409	0.006	0.910	0.003	0.409	0.910	-0.074	0.006	0.453	0.909	-0.029
SCD46A	12/1/2017	pyroxene	W Assynt	3.297	0.010	6.392	0.003	3.292	6.372	-0.088	0.011	3.342	6.391	-0.049
SCD2	7/10/2018	amphibole	Graveyard	1.699	0.009	3.364	0.004	1.698	3.359	-0.084	0.010	1.487	2.919	-0.061
SCDTPA	7/10/2018	amphibole	Loch na h	-1.595	0.009	-2.861	0.003	-1.596	-2.865	-0.076	0.009	-1.806	-3.304	-0.054
SCDTPB	7/11/2018	amphibole	Loch na h	-1.700	0.009	-3.054	0.004	-1.702	-3.059	-0.079	0.009	-1.998	-3.685	-0.043
SCDTPB	7/11/2018	amphibole	Loch na h	-1.602	0.006	-2.847	0.004	-1.603	-2.851	-0.090	0.006	-1.899	-3.478	-0.054

*- See the footnote of Table S6 for the linearized notations

Table S8. Triple oxygen isotope composition of reference materials SCO (San Carlos olivine) and UOG (University of Oregon garnet)*

Reference material	Date analyzed	δ^{17}O	±s.e.	δ^{18}O	±s.e.	δ'^{17}O	δ'^{18}O	Δ'^{17}O	±s.e.	δ'^{17}Ooffset	δ'^{18}Ooffset
UOG 1.670	5/16/2017	3.454	0.007	6.706	0.004	3.448	6.683	-0.098	0.008	0.057	0.184
SCO 1.40	12/1/2017	2.637	0.011	5.154	0.005	2.633	5.141	-0.094	0.011	-0.044	0.001
SCO 1.125	12/3/2017	2.781	0.008	5.434	0.003	2.777	5.419	-0.097	0.008	0.100	0.279
SCO 1.190	11/10/2017	2.917	0.011	5.640	0.004	2.912	5.624	-0.071	0.011	0.235	0.485
SCO 1.40	12/1/2017	2.637	0.011	5.154	0.005	2.633	5.141	-0.094	0.011	-0.044	0.001
SCO 1.026	7/10/2018	2.893	0.008	5.600	0.005	2.889	5.584	-0.073	0.009	0.212	0.444
SCO 0.903	7/11/2018	3.016	0.011	5.867	0.004	3.011	5.850	-0.092	0.011	0.334	0.711
SCO 0.957	7/11/2018	2.944	0.010	5.711	0.004	2.939	5.695	-0.082	0.010	0.262	0.555

*-UOG accepted value is δ'^{17}O = 3.391, δ'^{18}O = 6.499; SCO δ'^{17}O = 2.677, δ'^{18}O = 5.140

Table S9. The $\delta^{18}O$, δD (‰ VSMOW) and H_2O wt. % values of the Belomorian belt rocks, Scourie dikes and Lewisian gneisses.

Sample	Mineral analyzed	$\delta^{18}O$	δD	H_2O, wt. %	Province	Locality
Ki-06	zoisite	4.82	-106.2	2.0	Belomorian belt	Kiy Island
Ki-09	epidote	-0.05	-26.0	1.9	Belomorian belt	Kiy Island
Ki-11	amphibole	5.08	-121.4	2.1	Belomorian belt	Kiy Island
Ki-15	amphibole	4.56	-121.1	2.1	Belomorian belt	Kiy Island
Kii-1	amphibole	4.24	-89.7	3.6	Belomorian belt	Kiy Island
KO-25	amphibole	5.84	-87.8	2.1	Belomorian belt	Kiy Island
SH-03	amphibole	1.63	-99.9	2.2	Belomorian belt	Shueretskoe
SH-05	biotite	NA	-105.4	1.9	Belomorian belt	Shueretskoe
SH-08	amphibole	1.94	-98.0	2.0	Belomorian belt	Shueretskoe
SH-15	amphibole	1.90	-96.2	1.8	Belomorian belt	Shueretskoe
SH-20	amphibole	1.66	-100.4	2.9	Belomorian belt	Shueretskoe
TE-04	amphibole	0.91	-103.2	1.8	Belomorian belt	Shueretskoe
TE-12	amphibole	0.41	-109.5	1.4	Belomorian belt	Shueretskoe
NK15-093-7	amphibole	-7.72	-24.0	1.9	Belomorian belt	Vuat-Varkka
NK15-101	amphibole	-3.12	-125.0	1.9	Belomorian belt	Vuat-Varkka

Table S9 Continued.

Sample	Mineral analyzed	$\delta^{18}O$	δD	H_2O, wt. %	Province	Locality
NK16-55-5	amphibole	-6.61	-111.0	2.4	Belomorian belt	Vuat-Varkka
NK16-58-32	biotite	-8.46	-104.0	3.5	Belomorian belt	Vuat-Varkka
S-18	amphibole	-8.98	-131.2	2.0	Belomorian belt	Vuat-Varkka
S-19A	amphibole	-4.70	-143.7	1.8	Belomorian belt	Vuat-Varkka
S-28A	amphibole	-11.70	-149.0	2.8	Belomorian belt	Vuat-Varkka
S-62	amphibole	3.17	-185.0	1.8	Belomorian belt	Vuat-Varkka
S-65	amphibole	-1.03	-125.6	2.2	Belomorian belt	Vuat-Varkka
S-72	amphibole	-13.78	-133.0	2.0	Belomorian belt	Vuat-Varkka
X647	amphibole	0.50	-147.2	1.9	Belomorian belt	Vuat-Varkka
SCD17	staurolite	9.11	-36.5	4.5	Lewisian complex	Aluminous metasediment
SCD41	amphibole	1.83	-88.9	1.6	Lewisian complex	Graveyard
SCD14A	amphibole	5.41	-64.9	1.8	Lewisian complex	JD09-2
SCD13	amphibole	5.17	-61.0	1.6	Lewisian complex	Laxford bridge (meta-Scourie)
SCD36B	whole rock	7.51	-52.3	1.1	Lewisian complex	Lewisian gneiss
SCD5	whole rock	9.50	-51.9	1.8	Lewisian complex	Lewisian gneiss

Table S9 Continued.

Sample	Mineral analyzed	$\delta^{18}O$	δD	H_2O, wt. %	Province	Locality
SCD35	amphibole	-2.27	-70.4	1.5	Lewisian complex	Loch na h
SCD40A	amphibole	3.96	-77.7	1.1	Lewisian complex	Poll Eorna
SCD8	amphibole	3.72	-91.8	0.7	Lewisian complex	Poll Eorna
SCD46A	amphibole	6.08	-65.4	0.9	Lewisian complex	W Assynt

Table S10. Sulfur isotope analyses of sulfides extracted from Scourie dikes reported in ‰ VCDT (Vienna-Canyon Diablo Troilite)

Sample	Dike	$\delta^{34}S$
SCD-39	Graveyard	1.2
SCD-46A	W Assynt	1.8
SCD-41	Graveyard	1.1

REFERENCES CITED

Chapter II

Alt, J. C., & Teagle, D. A. H. (2000). Hydrothermal alteration and fluid fluxes in ophiolites and oceanic crust. *Special Paper 349: Ophiolites and Oceanic Crust: New Insights from Field Studies and the Ocean Drilling Program*, *394*, 273–282. https://doi.org/10.1130/0-8137-2349-3.273

Ármannsson, H., Fridriksson, T., Gudfinnsson, G. H., Ólafsson, M., Óskarsson, F., & Thorbjörnsson, D. (2014). IDDP-The chemistry of the IDDP-01 well fluids in relation to the geochemistry of the Krafla geothermal system. *Geothermics*, *49*, 66–75. https://doi.org/10.1016/j.geothermics.2013.08.005

Arnórsson, S. (1978). Major Element Chemistry of the Geothermal Sea-Water at Reykjanes and Svartsengi, Iceland. *Mineralogical Magazine*, *42*(322), 209–220. https://doi.org/10.1180/minmag.1978.042.322.07

Bao, H., Cao, X., & Hayles, J. A. (2016). Triple Oxygen Isotopes : Fundamental Relationships and Applications. *Annual Review of Earth and Planetary Sciences*, *44*, 463–492. https://doi.org/10.1146/annurev-earth-060115-012340

Barkan, E., & Luz, B. (2005). High precision measurements of $^{17}O/^{16}O$ and $^{18}O/^{16}O$ ratios in H_2O. *Rapid Communications in Mass Spectrometry*, *19*(24), 3737–3742. https://doi.org/10.1002/rcm.2250

Bindeman, I. N., Serebryakov, N. S., Schmitt, A. K., Vazquez, J. A., Guan, Y., Azimov, P. Y., … Dobrzhinetskaya, L. (2014). Field and microanalytical isotopic investigation of ultradepleted in 18o paleoproterozoic "slushball earth" rocks from Karelia, Russia. *Geosphere*, *10*(2), 308–339. https://doi.org/10.1130/GES00952.1

Bindeman, I. N., Zakharov, D. O., Palandri, J., Greber, N. D., Dauphas, N., Retallack, G. J., … Bekker, A. (2018). Rapid emergence of subaerial landmasses and onset of a modern hydrologic cycle 2.5 billion years ago. *Nature*, *557*(7706), 545–548. https://doi.org/10.1038/s41586-018-0131-1

Bird, D. K., & Spieler, A. R. (2004). Epidote in Geothermal Systems. *Reviews in Mineralogy and Geochemistry*, *56*(1), 235–300. https://doi.org/10.2138/gsrmg.56.1.235

Cao, X., & Liu, Y. (2011). Equilibrium mass-dependent fractionation relationships for triple oxygen isotopes. *Geochimica et Cosmochimica Acta*, *75*(23), 7435–7445. https://doi.org/10.1016/j.gca.2011.09.048

Craig, H. (1961). Isotopic variations in meteoric waters. *Science*, *133*(3465), 1702–1703.

Criss, R. E., & Taylor Jr, H. P. (1986). Meteoric-hydrothermal systems. *Reviews in Mineralogy*, *16*, 373–424.

Dansgaard, W. (1964). Stable isotopes in precipitation. *Tellus*, *16*(4), 436–468. https://doi.org/10.3402/tellusa.v16i4.8993

Darling, W. G., & Ármannsson, H. (1989). Stable isotopic aspects of fluid flow in the Krafla, N??mafjall and Theistareykir geothermal systems of northeast Iceland. *Chemical Geology*, *76*(3–4), 197–213. https://doi.org/10.1016/0009-2541(89)90090-9

Dilles, J. H., Solomon, G. C., Taylor, H. P., & Einaudi, M. T. (1992). Oxygen and hydrogen isotope characteristics of hydrothermal alteration at the Ann-Mason porphyry copper deposit, Yerington, Nevada. *Economic Geology*, *87*(1), 44–63.

Dixon, J. E., Bindeman, I. N., Kingsley, R. H., Simons, K. K., Le Roux, P. J., Hajewski, T. R., … Walowski, K. J. (2017). Light stable isotopic compositions of enriched mantle sources: Resolving the dehydration paradox. *Geochemistry, Geophysics, Geosystems*, *18*(11), 3801–3839.

Eiler, J. M. (2001). Oxygen isotope variations of basaltic lavas and upper mantle rocks. *Reviews in Mineralogy and Geochemistry*, *43*(1), 319–364.

Elders, W. A., Friðleifsson, G. Ó., Zierenberg, R. A., Pope, E. C., Mortensen, A. K., Guðmundsson, Á., … Bird, D. K. (2011). Origin of a rhyolite that intruded a geothermal well while drilling at the Krafla volcano, Iceland. *Geology*, *39*(3), 231–234.

Fortier, S. M., & Giletti, B. J. (1989). An empirical model for predicting diffusion coefficients in silicate minerals. *Science*, *245*(4925), 1481–1484.

Fridleifsson, G. O. (1983). Geology and the alteration history of the Geitafell central volcano, southeast Iceland.

Giggenbach, W. F. (1992). Isotopic shifts in waters from geothermal and volcanic systems along convergent plate boundaries and their origin. *Earth and Planetary Science Letters*, *113*, 495–510. https://doi.org/10.1080/00185868.1978.9948092

Graham, C. M. (1981). Experimental hydrogen isotope studies III: Diffusion of hydrogen in hydrous minerals, and stable isotope exchange in metamorphic rocks. *Contributions to Mineralogy and Petrology*, *76*(2), 216–228.

Gregory, R. T., & Taylor, H. P. (1981). An oxygen isotope profile in a section of Cretaceous oceanic crust, Samail Ophiolite, Oman: Evidence for $\delta^{18}O$ buffering of the oceans by deep (>5 km) seawater-hydrothermal circulation at mid-ocean ridges. *Journal of Geophysical Research: Solid Earth*, *86*(B4), 2737–2755. https://doi.org/10.1029/JB086iB04p02737

Hattori, K., & Muehlenbachs, K. (1982). Oxygen isotope ratios of the Icelandic crust. *Journal of Geophysical Research: Solid Earth*, *87*(B8), 6559–6565.

Hayba, D. O., & Ingebritsen, S. E. (1997). Multiphase groundwater flow near cooling plutons. *Journal of Geophysical Research B: Solid Earth*, *102*(6), 12235–12252. https://doi.org/10.1029/97JB00552

Hayles, J., Gao, C., Cao, X., Liu, Y., & Bao, H. (2018). Theoretical calibration of the triple oxygen isotope thermometer. *Geochimica et Cosmochimica Acta*, *235*, 237–245. https://doi.org/10.1016/j.gca.2018.05.032

Herwartz, D., Pack, A., Krylov, D., Xiao, Y., Muehlenbachs, K., Sengupta, S., & Di Rocco, T. (2015). Revealing the climate of snowball Earth from $\Delta^{17}O$ systematics of hydrothermal rocks. *Proceedings of the National Academy of Sciences*, *112*(17), 5337–5341. https://doi.org/10.1073/pnas.1422887112

Kyser, T. K., & Kerrich, R. (1991). Retrograde exchange of hydrogen isotopes between hydrous minerals and water at low temperatures. *Geochemical Society, Special Publication*, *3*(3), 409–422.

Kyser, T. K., & O'Neil, J. R. (1984). Hydrogen isotope systematics of submarine basalts. *Geochimica et Cosmochimica Acta*, *48*(10), 2123–2133.

Liotta, D., Brogi, A., Ruggieri, G., Rimondi, V., Zucchi, M., Helgadóttir, H. M., … Friðleifsson, G. Ó. (2018). Fracture analysis, hydrothermal mineralization and fluid pathways in the Neogene Geitafell central volcano: insights for the Krafla active geothermal system, Iceland. *Journal of Volcanology and Geothermal Research*, (in press). https://doi.org/10.1016/j.jvolgeores.2018.11.023

Luz, B., & Barkan, E. (2010). Variations of $^{17}O/^{16}O$ and $^{18}O/^{16}O$ in meteoric waters. *Geochimica et Cosmochimica Acta*, *74*(22), 6276–6286. https://doi.org/10.1016/j.gca.2010.08.016

Manning, C. E., & Ingebritsen, S. E. (1999). Permeability of the continental crust: Implications of geothermal data and metamorphic systems. *Reviews of Geophysics*, *37*(1), 127–150.

Matsuhisa, Y., Goldsmith, J. R., & Clayton, R. N. (1978). Mechanisms of hydrothermal crystallization of quartz at 250 °C and 15 kbar. *Geochimica et Cosmochimica Acta*, *42*(2), 173–182. https://doi.org/10.1016/0016-7037(78)90130-8

Matthews, A. (1994). Oxygen isotope geothermometers for metamorphic rocks. *Journal of Metamorphic Geology*, *12*(3), 211–219.

Miller, M. F. (2002). Isotopic fractionation and the quantification of 17O anomalies in the oxygen three-isotope system: an appraisal and geochemical significance. *Geochimica et Cosmochimica Acta*, *66*(11), 1881–1889.

Muehlenbachs, K., & Clayton, R. N. (1976). Oxygen isotope composition of the oceanic crust and its bearing on seawater. *Journal of Geophysical Research*, *81*(23), 4365. https://doi.org/10.1029/JB081i023p04365

Norton, D. L. (1984). Theory of hydrothermal systems. *Annual Review of Earth and Planetary Sciences*, *12*(1), 155–177.

Ohmoto, H., & Rye, R. O. (1974). Hydrogen and oxygen isotopic compositions of fluid inclusions in the Kuroko Deposits, Japan. *Economic Geology*, *69*(6), 947–953. https://doi.org/10.2113/gsecongeo.69.6.947

Ólafsson, J., & Riley, J. P. (1978). Geochemical studies on the thermal brine from Reykjanes (Iceland). *Chemical Geology*, *21*(3–4), 219–237. https://doi.org/10.1016/0009-2541(78)90046-3

Pack, A., & Herwartz, D. (2014). The triple oxygen isotope composition of the Earth mantle and understanding δO17 variations in terrestrial rocks and minerals. *Earth and Planetary Science Letters*, *390*, 138–145. https://doi.org/10.1016/j.epsl.2014.01.017

Pack, A., Tanaka, R., Hering, M., Sengupta, S., Peters, S., & Nakamura, E. (2016). The oxygen isotope composition of San Carlos olivine on the VSMOW2-SLAP2 scale. *Rapid Communications in Mass Spectrometry*, *30*, 1495–1504. https://doi.org/10.1002/rcm.7582

Pope, E. C., Bird, D. K., Arnórsson, S., & Giroud, N. (2016). Hydrogeology of the Krafla geothermal system, northeast Iceland. *Geofluids*, *16*(1), 175–197. https://doi.org/10.1111/gfl.12142

Pope, E. C., Bird, D. K., & Arnórsson, S. (2014). Stable isotopes of hydrothermal minerals as tracers for geothermal fluids in Iceland. *Geothermics*, *49*, 99–110. https://doi.org/10.1016/j.geothermics.2013.05.005

Pope, E. C., Bird, D. K., Arnórsson, S., Fridriksson, T., Elders, W. A., & Fridleifsson, G. Ó. (2009). Isotopic constraints on ice age fluids in active geothermal systems: Reykjanes, Iceland. *Geochimica et Cosmochimica Acta*, *73*(15), 4468–4488. https://doi.org/10.1016/j.gca.2009.03.033

Pope, E. C. (2011). *Hydrogen and oxygen isotope fractionation in hydrous minerals as indicators of fluid source in modern and fossil metasomatic environments*. Stanford University.

Sharp, Z. D., Gibbons, J. A., Maltsev, O., Atudorei, V., Pack, A., Sengupta, S., … Knauth, L. P. (2016). A calibration of the triple oxygen isotope fractionation in the SiO2-H2O system and applications to natural samples. *Geochimica et Cosmochimica Acta*, *186*, 105–119. https://doi.org/10.1016/j.gca.2016.04.047

Sharp, Z. D., Wostbrock, J. A. G., & Pack, A. (2018). Mass-dependent triple oxygen isotope variations in terrestrial materials. *Geochemical Perspectives Letters*, *7*, 27–31. https://doi.org/10.7185/geochemlet.1815

Sveinbjörnsdóttir, Á. (1991). Composition of geothermal minerals from saline and dilute fluids - Krafla and Reykjanes, Iceland. *Lithos*, *27*(4), 301–315. https://doi.org/10.1016/0024-4937(91)90005-6

Sveinbjornsdottir, A. E., Coleman, M. L., & Yardley, B. W. D. (1986). Origin and history of hydrothermal fluids of the Reykjanes and Krafla geothermal fields, Iceland. *Contributions to Mineralogy and Petrology*, *94*(1), 99–109.

Tanaka, R., & Nakamura, E. (2013). Determination of 17O-excess of terrestrial silicate/oxide minerals with respect to Vienna Standard Mean Ocean Water (VSMOW). *Rapid Communications in Mass Spectrometry*, *27*(2), 385–397. https://doi.org/10.1002/rcm.6453

Taylor, H P. (1974). The application of oxygen and hydrogen isotope studies to problems of hydrothermal alteration and ore deposition. *Economic Geology*, *69*(6), 843–883.

Taylor, H P, & Forester, R. W. (1979). An oxygen and hydrogen isotope study of the Skaergaard Instrusion and its country rocks: A description of a 55-M.Y. old fossil hydorthermal system. *J. Petrol.*, *20*(3), 355–419.

Taylor, Hugh P. (1977). Water/rock interactions and the origin of H_2O in granitic batholiths: Thirtieth William Smith lecture. *Journal of the Geological Society*, *133*(6), 509–558.

Thorlacius, J. M. (1991). Petrological studies of the Geitafell central volcano, SE Iceland.

Troyer, R., Reed, M. H., Elders, W. A., & Fridleifsson, G. O. (2007). Iceland Deep Drilling Project (IDDP):(IV) Fluid Inclusion Microthermometry of the Geitafell Hydrothermal System-a Possible Analog of the Active Krafla System. In *AGU Fall Meeting Abstracts*.

Truesdell, A. H., & Hulston, J. R. (1980). Isotopic evidence on environments of geothermal systems. In *Handbook of environmental isotope geochemistry. Vol. 1*.

Urey, H. C. (1947). The thermodynamic properties of isotopic substances. *Journal of the Chemical Society (Resumed)*, 562–581.

Valley, J. W., Bindeman, I. N., & Peck, W. H. (2003). Empirical calibration of oxygen isotope fractionation in zircon. *Geochimica et Cosmochimica Acta*, *67*(17), 3257–3266.

Wostbrock, J. A. G., Sharp, Z. D., Sanchez-Yanez, C., Reich, M., van den Heuvel, D. B., & Benning, L. G. (2018). Calibration and application of silica-water triple oxygen isotope thermometry to geothermal systems in Iceland and Chile. *Geochimica et Cosmochimica Acta*, *234*, 84–97. https://doi.org/10.1016/j.gca.2018.05.007

Wotzlaw, J. F., Bindeman, I. N., Schaltegger, U., Brooks, C. K., & Naslund, H. R. (2012). High-resolution insights into episodes of crystallization, hydrothermal alteration and remelting in the Skaergaard intrusive complex. *Earth and Planetary Science Letters*, *355–356*, 199–212. https://doi.org/10.1016/j.epsl.2012.08.043

Zakharov, D. O., & Bindeman, I. N. (2019). Triple oxygen and hydrogen isotopic study of hydrothermally altered rocks from the 2.43–2.41 Ga Vetreny belt, Russia: An insight into the early Paleoproterozoic seawater. *Geochimica et Cosmochimica Acta*, *248*, 185–209. https://doi.org/10.1016/j.gca.2019.01.014

Zakharov, D. O., Bindeman, I. N., Slabunov, A. I., Ovtcharova, M., Coble, M. A., Serebryakov, N. S., & Schaltegger, U. (2017). Dating the Paleoproterozoic snowball Earth glaciations using contemporaneous subglacial hydrothermal systems. *Geology*, *45*(7), 667–670. https://doi.org/10.1130/G38759.1

Zheng, Y. F. (1993). Calculation of oxygen isotope fractionation in hydroxyl-bearing silicates. *Earth and Planetary Science Letters*, *120*(3–4), 247–263. https://doi.org/10.1016/0012-821X(93)90243-3

Chapter III

Alexander R. J., Harper G. D. and Bowman J. R. (1993) Oceanic Faulting and Fault-Controlled Subseafloor Hydrothermal Alteration in the Sheeted Dike Complex of the Josephine Ophiolite. *J. Geophys. Res. Earth* **98**, 9731–9759.

Alt J. C. and Bach W. (2006) Oxygen isotope composition of a section of lower oceanic crust, ODP Hole 735B. *Geochemistry, Geophys. Geosystems* **7**, 1–18.

Alt J. C., Laverne C., Vanko D. a, Tartarotti P., Teagle D. a H., Bach W., Zuleger E., Ezringer J., Honnorez J., Pezard P. a, Becker K., Salisbury M. H. and Wilkens R. H. (1996) Hydrothermal alteration of a section of upper oceanic crust in the easter equatorial Pacific: A synthesis of results from Site 504 (DSDP Legs 69, 70, and 83, and ODP Legs 111, 137, 140, and 148). *Proc. Ocean Drill. Program, Sci. Results* **148**, 417–434.

Alt J. C., Muehlenbachs K. and Honnorez J. (1986) An oxygen isotopic profile through the upper kilometer of the oceanic crust, DSDP Hole 504B. *Earth Planet. Sci. Lett.* **80**, 217–229.

Alt J. C., Zuleger E. and Erzinger J. (1995) Mineralogy and stable isotopic compositions of the hydrothermally altered lower sheeted dike complex, hole 504B, leg 140. *Proc. Ocean Drill. Progr. Sci. Results* **137**, 155–166.

Astafieva M. M., Rozanov A. Y., Sharkov E. V, Chistyakov A. V, Bogina M. M. and Hoover R. B. (2009) Volcanic glasses as habitat for microfossils: evidence from the early Paleoproterozoic pillow lavas of Karelia and their modern analogues in the Mid-Atlantic Ridge. *Instruments Methods Astrobiol. Planet. Mission. XII, SPIE Proc.* **7441**, 1-12.

Avice G., Marty B., Burgess R., Hofmann A., Philippot P., Zahnle K. and Zakharov D. (2018) Evolution of atmospheric xenon and other noble gases inferred from Archean to Paleoproterozoic rocks. *Geochim. Cosmochim. Acta* **232**, 82–100.

Bao H., Cao X. and Hayles J. A. (2016) Triple Oxygen Isotopes : Fundamental Relationships and Applications. *Annu. Rev. Earth Planet. Sci.* **44**, 463–492.

Bekker A., Holland H. D., Wang P.-L. L., Rumble D., Stein H. J., Hannah J. L., Coetzee L. L. and Beukes N. J. (2004) Dating the rise of atmospheric oxygen. *Nature* **427**, 117–120.

Bindeman I. N., Bekker A. and Zakharov D. O. (2016) Oxygen isotope perspective on crustal evolution on early Earth: A record of Precambrian shales with emphasis on Paleoproterozoic glaciations and Great Oxygenation Event. *Earth Planet. Sci. Lett.* **437**, 101–113. Available at: http://dx.doi.org/10.1016/j.epsl.2015.12.029.

Bindeman I. N. and Lee J. E. (2017) The possibility of obtaining ultra-low-δ18O signature of precipitation near equatorial latitudes during the Snowball Earth glaciation episodes. *Precambrian Res.*

Bindeman I. N., Serebryakov N. S., Schmitt A. K., Vazquez J. A., Guan Y., Azimov P. Y., Astafiev B. Y., Palandri J. and Dobrzhinetskaya L. (2014) Field and microanalytical isotopic investigation of ultradepleted in ^{18}O Paleoproterozoic "slushball earth" rocks from Karelia, Russia. *Geosphere* **10**, 308–339.

Bindeman I.N., Zakharov D.O., Palandri J., Greber N.D., Retallack G.J., Hofmann A., Dauphas N., Lackey J.S. and Bekker, A. (2018) Rapid growth of subaerial crust and the onset of a modern hydrologic cycle at the Archean-Proterozoic transition. *Nature*, **557**, 545-557.

Bird D. K. and Spieler A. R. (2004) Epidote in Geothermal Systems. *Rev. Mineral. Geochemistry* **56**, 235-300.

Bischoff J. L., Rosenbauer R. J. and Pitzer K. S. (1986) The system NaCl-H_2O: Relations of vapor-liquid near the critical temperature of water and of vapor-liquid-halite from 300° to 500°C. *Geochim. Cosmochim. Acta* **50**, 1437–1444.

Bowen, G. J. (2010). Waterisotopes.org. Gridded maps of the isotopic composition of meteoric precipitation.

Bushmin, S. A., & Glebovitsky, V. A. (2008). Scheme of mineral facies of metamorphic rocks. *Geol. of Ore Dep.* ***50***, 659.

Cao X. and Liu Y. (2011) Equilibrium mass-dependent fractionation relationships for triple oxygen isotopes. *Geochim. Cosmochim. Acta* **75**, 7435–7445.

Chacko T., Riciputi R., Cole R. and Horita, J. T. (1999) A new technique for determining equilibrium hydrogen isotope fractionation factors using the ion microprobe: application to the epidote-water system. *Geochim. Cosmochim. Acta* **63**–**1**, 1–10.

Cummins, R. C., Finnegan, S., Fike, D. A., Eiler, J. M., & Fischer, W. W. (2014). Carbonate clumped isotope constraints on Silurian ocean temperature and seawater δ18O. *Geochim. Cosmochim. Acta* **140**, 241-258.

Dodson M. H. (1973) Closure temperature in cooling geochronological and petrological systems. *Contrib. to Mineral. Petrol.* **40**, 259–274.

Depaolo D. J. (2006) Isotopic effects in fracture-dominated reactive fluid – rock systems. *Geochim. Cosmochim. Acta* **70**, 1077–1096.

Eiler J. M. (2011) Paleoclimate reconstruction using carbonate clumped isotope thermometry. *Quat. Sci. Rev.* **30**, 3575–3588.

Fonneland-Jorgensen H., Furnes H., Muehlenbachs K. and Dilek Y. (2005) Hydrothermal alteration and tectonic evolution of an intermediate- to fast-spreading back-arc oceanic crust: Late Ordovician Solund-Stavfjord ophiolite, western Norway. *Isl. Arc* **14**, 517–541.

Foustoukos D. I. and Seyfried W. E. (2007) Fluid Phase Separation Processes in Submarine Hydrothermal Systems. *Rev. Mineral. Geochemistry* **65**, 213–239.

Furnes H., de Wit M., Staudigel H., Rosing M. and Muehlenbachs K. (2007) A vestige of Earth's oldest ophiolite. *Science* **315**, 1704–1707.

Graham C. M. and Sheppard S. M. F. (1980) Experimental hydrogen isotope studies, II. Fractionations in the systems epidote-NaCl-H2O, epidote-CaCl2-H2O and epidote-seawater, and the hydrogen isotope composition of natural epidotes. *Earth Planet. Sci. Lett.* **49**, 237–251.

Grassineau N. V., Mattey D. P. and Lowry D. (2001) Sulfur isotope analysis of sulfide and sulfate minerals by continuous flow-isotope ratio mass spectrometry. *Anal. Chem.* **73**, 220–225.

Gregory R. T. and Taylor H. P. (1981) An oxygen isotope profile in a section of Cretaceous oceanic crust, Samail Ophiolite, Oman: Evidence for δ18O buffering of the oceans by deep (>5 km) seawater-hydrothermal circulation at mid-ocean ridges. *J. Geophys. Res. Solid Earth* **86**, 2737–2755.

Gumsley A. P., Chamberlain K. R., Bleeker W., Söderlund U., de Kock M. O., Larsson E. R. and Bekker A. (2017) Timing and tempo of the Great Oxidation Event. *Proc. Natl. Acad. Sci.* **114**, 201608824.

Gutzmer J., Banks D. A., Lüders V., Hoefs J., Beukes N. J. and von Bezing K. L. (2003) Ancient sub-seafloor alteration of basaltic andesites of the Ongeluk Formation, South Africa: Implications for the chemistry of Paleoproterozoic seawater. *Chem. Geol.* **201**, 37–53.

Gutzmer J., Pack A., Lüders V., Wilkinson J., Beukes N. and Niekerk H. (2001) Formation of jasper and andradite during low-temperature hydrothermal seafloor metamorphism, Ongeluk Formation, South Africa. *Contrib. to Mineral. Petrol.* **142**, 27–42.

Harper G. D., Bowman J. and Kuhns R. (1988) A field, chemical, and stable isotope study of subseafloor metamorphism of the Josephine ophilote, California-Oregon. *J. Geophys. Res.* **93**, 4625–4656.

Hayles, J., Gao, C., Cao, X., Liu, Y., & Bao, H. (2018). Theoretical calibration of the triple oxygen isotope thermometer. *Geochimica et Cosmochimica Acta*, *235*, 237–245. https://doi.org/10.1016/j.gca.2018.05.032

Heaton T. H. E. and Sheppard S. M. F. (1977) Hydrogen and oxygen isotope evidence for sea-water-hydrothermal alteration and ore deposition, Troodos complex, Cyprus. *Geol. Soc. London, Spec. Publ.* **7**, 42–57.

Herwartz D., Pack A., Krylov D., Xiao Y., Muehlenbachs K., Sengupta S. and Di Rocco T. (2015) Revealing the climate of snowball Earth from Δ17O systematics of hydrothermal rocks. *Proc. Natl. Acad. Sci.* **112**, 5337–5341.

Horita J. and Wesolowski D. J. (1994) Liquid-vapor fractionation of oxygen and hydrogen isotopes of water from the freezing to the critical temperature. *Geochim. Cosmochim. Acta* **58**, 3425–3437.

Hey M. H. (1954) A New Review of the Chlorites. *Mineral. Mag.* **30**, 277–292.

Hodel F., Macouin M., Trindade R. I. F., Triantafyllou A., Ganne J., Chavagnac V., Berger J., Rospabé M., Destrigneville C., Carlut J., Ennih N. and Agrinier P. (2018) Fossil black smoker yields oxygen isotopic composition of Neoproterozoic seawater. *Nat. Commun.*

Hoefs, J. (2015), *Stable isotope geochemistry*, 7th Edition, Springer, Berlin, 389 pp.

Holland, H.D. (1984). *The chemical evolution of the atmosphere and oceans.* Princeton University Press. 598 pp.

Holmden C. and Muehlenbachs K. (1993) The 18O/16O Ratio of 2-Billion-Year-Old Seawater Inferred from Ancient Oceanic Crust. *Science* **259**, 1733–1736.

Hren M. T., Tice M. M. and Chamberlain C. P. (2009) Oxygen and hydrogen isotope evidence for a temperate climate 3.42 billion years ago. *Nature* **462**, 205–208.

Imbrie, J., J. D. Hays, D. G. Martinson, A. McIntyre, A. C. Mix, J. J. Morley, N. G. Pisias, W. L. Prell, and N. J. Shackleton (1984) The orbital theory of Pleistocene climate: Support from a revised chronology, of the marine $\delta^{18}O$ record, in *Milankovitch and Climate, Part 1*, ed. Berger, 269–305, Springer, New York.

Jaffrés J. B. D., Shields G. A. and Wallmann K. (2007) The oxygen isotope evolution of seawater: A critical review of a long-standing controversy and an improved geological water cycle model for the past 3.4 billion years. *Earth-Science Rev.* **83**, 83–122.

Kasting J. F., Howard M. T., Wallmann K., Veizer J., Shields G. and Jaffrés J. (2006) Paleoclimates, ocean depth, and the oxygen isotopic composition of seawater. *Earth Planet. Sci. Lett.* **252**, 82–93.

Kawahata H., Kusakabe M. and Kikuchi Y. (1987) Strontium, oxygen, and hydrogen isotope geochemistry of hydrothermally altered and weathered rocks in DSDP Hole 504B, Costa Rica Rift. *Earth Planet. Sci. Lett.* **85**, 343–355.

Kempton P. D., Hawkesworth C. J. and Fowler M. (1991) Geochemistry and isotopic composition of gabbros from layer 3 of the Indian ocean crust, hole 735B. *Proc. Ocean Drill. Program, Sci. Results* **118**, 127–143.

Knauth L. P. and Lowe D. R. (1978) Oxygen isotope geochemistry of cherts from the Onverwacht Group (3.4 billion years), Transvaal, South Africa, with implications for secular variations in the isotopic composition of cherts. *Earth Planet. Sci. Lett.* **41**, 209–222.

Knauth L. P. and Lowe D. R. (2003) High Archean climatic temperature inferred from oxygen isotope geochemistry of cherts in the 3.5 Ga Swaziland Supergroup, South Africa. *Bull. Geol. Soc. Am.* **115**, 566–580.

Korenaga J., Planavsky N. J. and Evans D. A. D. (2017) Global water cycle and the coevolution of the Earth's interior and surface environment. *Philos. Trans. R. Soc. A Math. Eng. Sci.* **375**, 20150393.

Kulikov V. S., Bychkova Y. V., Kulikova V. V., Kostitsyn Y. A., Pokrovsky O. S. and Vasilev M. V. (2008) The Ruiga intrusion: A typical example of a shallow-facies Paleoproterozoic peridotite-gabbro-komatiite-basaltic association of the Vetreny Belt, Southeastern Fennoscandia. *Petrology* **16**, 531–551.

Kulikov V. S., Bychkova Y. V., Kulikova V. and Ernst R. (2010) The Vetreny Poyas (Windy Belt) subprovince of southeastern Fennoscandia: An essential component of the ca. 2.5-2.4 Ga Sumian large igneous provinces. *Precambrian Res.* **183**, 589–601.

Kurokawa H., Foriel J., Laneuville M., Houser C. and Usui T. (2018) Subduction and atmospheric escape of Earth's seawater constrained by hydrogen isotopes. *Earth Planet. Sci. Lett.*

Kyser T. K. and Kerrich R. (1991) Retrograde exchange of hydrogen isotopes between hydrous minerals and water at low temperatures. *Geochemical Soc. Spec. Publ.* **3**, 409–422.

Laverne C., Vanko D. A, Tartarotti P. and Alt J. C. (1995) Chemistry and geothermometry of secondary minerals from the deep sheeted dike complex, Hole 504B. *Proc. Ocean Drill. Program, Sci. Results* **137/140**, 167–189.

Leake B., Woolley A., Arps C. E. S., Birch W. D., Gilbert M. G., Grice J. D., Hawthorne F. C. and others (1997) Nomenclature of Amphiboles: Report of the Subcommittee on Amphiboles of the International Mineralogical Association Commission on New Minerals and Mineral Names. *Can. Mineral.* **82**, 1019–1037.

Lécuyer C., Gillet P. and Robert F. (1998) The hydrogen isotope composition of seawater and the global water cycle. *Chem. Geol.* **145**, 249–261.

Lécuyer C., Gruau G., Fruh-Green G. L. and Picard C. (1996) Hydrogen isotope composition of Early Proterozoic seawater. *Geology* **24**, 291–294.

Luz B. and Barkan E. (2010) Variations of $^{17}O/^{16}O$ and $^{18}O/^{16}O$ in meteoric waters. *Geochim. Cosmochim. Acta* **74**, 6276–6286.

Lyons T. W., Reinhard C. T. and Planavsky N. J. (2014) The rise of oxygen in Earth's early ocean and atmosphere. *Nature* **506**, 307–15.

Marin-Carbonne J., Chaussidon M. and Robert F. (2012) Micrometer-scale chemical and isotopic criteria (O and Si) on the origin and history of Precambrian cherts: Implications for paleo-temperature reconstructions. *Geochim. Cosmochim. Acta* **92**, 129–147.

Martin E., Bindeman I., Balan E., Palandri J., Seligman A. and Villemant B. (2017) Hydrogen isotope determination by TC/EA technique in application to volcanic glass as a window into secondary hydration. *J. Volcanol. Geotherm. Res.* **348**, 49–61.

Matsuhisa Y., Goldsmith J. R. and Clayton R. N. (1978) Mechanisms of hydrothermal crystallization of quartz at 250°C and 15 kbar. *Geochim. Cosmochim. Acta* **42**, 173–182.

Matthews A. (1994) Oxygen isotope geothermometers for metamorphic rocks. *J. Metamorph. Geol.* **12**, 211–219.

Matthews, A., Goldsmith, J. R., & Clayton, R. N. (1983). Oxygen isotope fractionations involving pyroxenes: the calibration of mineral-pair geothermometers. *Geochim. Cosmochim. Acta* **47**, 631-644.

Melezhik V. A., Prave A. R., Fallick A. E., Hanski E. J., Lepland A., Kump L. R. and Strauss H. (2013) Reading the archive of earth's oxygenation: Volume 3: Global Events and the Fennoscandian Arctic Russia - Drilling Early Earth Project. *Front. Earth Sci.* **8**.

Mezhelovskaya S. V., Korsakov A. K., Mezhelovskii A. D. and Bibikova E. V. (2016) Age Range of Formation of Sedimentary Volcanogenic Complex of the Vetreny Belt (the Southeast of the Baltic Shield). *Stratigr. Geol. Correl.* **24**, 105–117.

Miller M. F. (2002) Isotopic fractionation and the quantification of Δ^{17}O anomalies in the oxygen three-isotope system: An appraisal and geochemical significance. *Geochim. Cosmochim. Acta* **66**, 1881–1889.

Muehlenbachs K. (1998) The oxygen isotopic composition of the oceans, sediments and the seafloor. *Chem Geol* **145**, 263–273.

Muehlenbachs K. and Clayton R. N. (1976) Oxygen isotope composition of the oceanic crust and its bearing on seawater. *J. Geophys. Res.* **81**, 4365.

Nehlig P. (1991) Salinity of oceanic hydrothermal fluids: a fluid inclusion study. *Earth Planet. Sci. Lett.* **102**, 310–325.

Ojakangas R. W., Marmo J. S. and Heiskanen K. I. (2001) Basin evolution of the Paleoproterozoic Karelian Supergroup of the Fennoscandian (Baltic) shield. *Sediment. Geol.* **141–142**, 255–285.

Pack A. and Herwartz D. (2014) The triple oxygen isotope composition of the Earth mantle and understanding Δ^{17}O variations in terrestrial rocks and minerals. *Earth Planet. Sci. Lett.* **390**, 138–145.

Pack A., Tanaka R., Hering M., Sengupta S., Peters S. and Nakamura E. (2016) The oxygen isotope composition of San Carlos olivine on the VSMOW2-SLAP2 scale. *Rapid Commun. Mass Spectrom.* **30**, 1495–1504.

Perry Jr, E. C. (1967). The oxygen isotope chemistry of ancient cherts. *Earth Planet. Sci. Lett. 3*, 62-66.

Pope E. C., Bird D. K. and Rosing M. T. (2012) Isotope composition and volume of Earth's early oceans. *Proc. Natl. Acad. Sci.* **109**, 4371–4376.

Pope E. C., Bird D. K. and Arnórsson S. (2014) Stable isotopes of hydrothermal minerals as tracers for geothermal fluids in Iceland. *Geothermics* **49**, 99–110.

Prokoph A., Shields G. A. and Veizer J. (2008) Compilation and time-series analysis of a marine carbonate δ^{18}O, δ^{13}C, ^{87}Sr/^{86}Sr and δ^{34}S database through Earth history. *Earth-Science Rev.* **87**, 113–133.

Puchtel I. S., Haase K. M., Hofmann A. W., Chauvel C., Kulikov V. S., Garbe-Schönberg C. D. and Nemchin A. A. (1997) Petrology and geochemistry of crustally contaminated komatiitic basalts from the Vetreny Belt, southeastern Baltic Shield: Evidence for an early Proterozoic mantle plume beneath rifted Archean continental lithosphere. *Geochim. Cosmochim. Acta* **61**, 1205–1222.

Puchtel I. S., Hofmann A. W., Mezger K., Shchipansky A. A., Kulikov V. S. and Kulikova V. V. (1996) Petrology of a 2.41 Ga remarkably fresh komatiitic basalt lava lake in Lion Hills, central Vetreny Belt, Baltic Shield. *Contrib. to Mineral. Petrol.* **124**, 273–290.

Puchtel I. S., Touboul M., Blichert-Toft J., Walker R. J., Brandon A. D., Nicklas R. W., Kulikov V. S. and Samsonov A. V (2016) Lithophile and siderophile element systematics of Earth ' s mantle at the Archean – Proterozoic boundary: Evidence from 2.4 Ga komatiites. *Geochim. Cosmochim. Acta* **180**, 227–255.

Robert F. and Chaussidon M. (2006) A palaeotemperature curve for the Precambrian oceans based on silicon isotopes in cherts. *Nature* **443**, 969–972.

Salminen J., Halls H. C., Mertanen S., Pesonen L. J., Vuollo J. and Söderlund U. (2014) Paleomagnetic and geochronological studies on Paleoproterozoic diabase dykes of Karelia, East Finland-Key for testing the Superia supercraton. *Precambrian Res.* **244**, 87–99.

Schiffman P. and Smith B. M. (1988) Petrology and Oxygen Isotope Geochemistry of a Fossil Seawater Hydrothermal System Within the Solea Graben, Northern Troodos Ophiolite, Cyprus. *J. Geophys. Res.* **93**, 4612–4624.

Schrag, D. P., Hampt, G., and Murray, D. W. (1996). Pore Fluid Constraints on the Temperature and Oxygen Isotopic Composition of the Glacial Ocean. *Science*, **272**, 1930–1932.

Seal R. R. (2006) Sulfur Isotope Geochemistry of Sulfide Minerals. *Rev. Mineral. Geochemistry* **61**, 633–677.

Sengupta S. and Pack A. (2018) Triple oxygen isotope mass balance for the Earth's oceans with application to Archean cherts. *Chem. Geol.* **495**, 18–26.

Shackleton N. J. and Kennett J. P. (1975) Paleotemperature History of the Cenozoic and the Initiation of Antarctic Glaciation: Oxygen and Carbon Isotope Analyses in DSDP Sites 277, 279 and 281. In *Initial Reports of the Deep Sea Drilling Project, 29*.

Shanks W. C. (2001) Stable isotopes in seafloor hydrothermal systems. *Rev. Mineral. Geochemistry* **43**, 469–526.

Sharkov E. V, Trubkin N. V, Krassivskaya I. S., Bogatikov O. A., Mokhov A. V, Chistyakov A. V and Evseeva K. A. (2004) Structural and Compositional Characteristics of the Oldest Volcanic Glass in the Early Paleoproterozoic Boninite-Like Lavas of Southern Karelia. *Petrology* **12**, 264–280.

Sharp Z. D. and Kirschner D. L. (1994) Quartz-calcite oxygen isotope thermometry: A calibration based on natural isotopic variations. *Geochim. Cosmochim. Acta* **58**, 4491–4501.

Sharp Z. D., Gibbons J. A., Maltsev O., Atudorei V., Pack A., Sengupta S., Shock E. L. and Knauth L. P. (2016) A calibration of the triple oxygen isotope fractionation in the SiO2-H2O system and applications to natural samples. *Geochim. Cosmochim. Acta* **186**, 105–119. Available at: http://dx.doi.org/10.1016/j.gca.2016.04.047.

Shields G. and Veizer J. (2002) The Precambrian marine carbonate isotope database: version 1.1. *Geochemistry Geophys. Geosystems* **3**, 1–12.

Shmulovich K. I., Landwehr D., Simon K. and Heinrich W. (1999) Stable isotope fractionation between liquid and vapour in water–salt systems up to 600°C. *Chem. Geol.* **157**, 343–354.

Stakes D. S. and O'Neil J. R. (1982) Mineralogy and stable isotope geochemistry of hydrothermally altered oceanic rocks. *Earth Planet. Sci. Lett.* **57**, 285–304.

Strand K. O. and Laajoki K. (1993) Palaeoproterozoic glaciomarine sedimentation in an extensional tectonic setting: the Honkala Formation, Finland. *Precambrian Res.* **64**, 253–271.

Taylor, H. P. (1977) Water/rock interactions and the origin of H_2O in granitic batholiths: Thirtieth William Smith lecture. *Journal of the Geological Society* **133**, 509-558.

Taylor, S. R., & McLennan, S. M. (1985) *The continental crust: Its evolution and composition*. Blackwell, Oxford.

Turchyn A. V., Alt J. C., Brown S. T., DePaolo D. J., Coggon R. M., Chi G., Bédard J. H. and Skulski T. (2013) Reconstructing the oxygen isotope composition of late Cambrian and Cretaceous hydrothermal vent fluid. *Geochim. Cosmochim. Acta* **123**, 440–458.

Vanko D. A., Laverne C., Tartarotti P. and Alt J. C. (1996) Chemistry and origin of secondary minerals from the deep sheeted dikes cored during Leg 148 (Hole 504B). *Proc. Ocean Drill. Program, Sci. Results* **148**, 71–86.

Veizer J., Ala D., Azmy K., Bruckschen P., Buhl D., Bruhn F., Carden G. a. F., Diener A., Ebneth S., Godderis Y., Jasper T., Korte C., Pawellek F., Podlaha O. G. and Strauss H. (1999) ^{87}Sr/^{86} Sr, δ^{13}C and δ^{18}O evolution of Phanerozoic seawater. *Chem. Geol.* **161**, 59–88.

Veizer J. and Prokoph A. (2015) Temperatures and oxygen isotopic composition of Phanerozoic oceans. *Earth-Science Rev.* **146**, 92–104.

Wallmann K. (2001) The geological water cycle and the evolution of marine δ^{18}O values. *Geochim. Cosmochim. Acta* **65**, 2469–2485.

Wallmann K. (2004) Impact of atmospheric CO2 and galactic cosmic radiation on Phanerozoic climate change and the marine δ18O record. *Geochemistry, Geophys. Geosystems* **5**.

Wark, D. A., & Watson, E. B. (2006). TitaniQ: a titanium-in-quartz geothermometer. *Contributions to Mineralogy and Petrology*, *152*(6), 743-754.

Wenner D. B. and Taylor H. P. (1974) D/H and O^{18}/O^{16} studies of serpentinization of ultramaflc rocks. *Geochim. Cosmochim. Acta* **38**, 1255–1286.

Wostbrock J. A. G., Sharp Z. D., Sanchez-Yanez C., Reich M., van den Heuvel D. B. and Benning L. G. (2018) Calibration and application of silica-water triple oxygen isotope thermometry to geothermal systems in Iceland and Chile. *Geochim. Cosmochim. Acta* **234**, 84–97. Available at: https://doi.org/10.1016/j.gca.2018.05.007.

Zahnle K. J., Catling D. C. and Claire M. W. (2013) The rise of oxygen and the hydrogen hourglass. *Chem. Geol.* **362**, 26–34.

Zakharov D. O., Bindeman I. N., Slabunov A. I., Ovtcharova M., Coble M. A., Serebryakov N. S. and Schaltegger U. (2017) Dating the Paleoproterozoic snowball Earth glaciations using contemporaneous subglacial hydrothermal systems. *Geology* **45**, 5–8.

Zheng Y. F. (1993) Calculation of oxygen isotope fractionation in hydroxyl-bearing silicates. *Earth Planet. Sci. Lett.* **120**, 247–263.

Chapter IV

Alt, J C, Laverne, C., Vanko, D. a, Tartarotti, P., Teagle, D. a H., Bach, W., … Wilkens, R. H. (1996). Hydrothermal alteration of a section of upper oceanic crust in the easter equatorial Pacific: A synthesis of results from Site 504 (DSDP Legs 69, 70, and 83, and ODP Legs 111, 137, 140, and 148). *Proceedings of the Ocean Drilling Program, Scientific Results*, *148*, 417–434.

Alt, Jeffrey C., & Teagle, D. A. H. (2000). Hydrothermal alteration and fluid fluxes in ophiolites and oceanic crust. *Special Paper 349: Ophiolites and Oceanic Crust: New Insights from Field Studies and the Ocean Drilling Program*, *394*, 273–282. https://doi.org/10.1130/0-8137-2349-3.273

Alt, Jeffrey C, Davidson, G. J., Teagle, D. A. H., & Karson, J. A. (2003). Isotopic composition of gypsum in the Macquarie Island ophiolite: Implications for the sulfur cycle and the subsurface biosphere in oceanic crust. *Geology*, *31*(6), 549–552.

Antonelli, M. A., Pester, N. J., Brown, S. T., & DePaolo, D. J. (2017). Effect of paleoseawater composition on hydrothermal exchange in midocean ridges. *Proceedings of the National Academy of Sciences*, *114*(47), 12413–12418. https://doi.org/10.1073/pnas.1709145114

Bach, W., & Humphris, S. E. (1999). Relationship between the Sr and O isotope compositions of hydrothermal fluids and the spreading and magma-supply rates at oceanic spreading centers. *Geology*, *27*(12), 1067–1070.

Baumgartner, L. P., & Valley, J. W. (2001). Stable isotope transport and contact metamorphic fluid flow. *Reviews in Mineralogy and Geochemistry*, *43*(1), 415–467.

Berner, E. K., & Berner, R. A. (1996). Marginal marine environments: estuaries. *The Global Environment: Water, Air and Geochemical Cycles. Prentice-Hall, Upper Saddle River, NJ*, 284–311.

Berner, R. A. (2004). A model for calcium, magnesium and sulfate in seawater over Phanerozoic time. *American Journal of Science*, *304*(5), 438–453.

Bowman, J. R., Willett, S. D., & Cook, S. J. (1994). Oxygen isotopic transport and exchange during fluid flow: one-dimensional models and applications. *American Journal of Science*, *294*, 1–55.

Brown, S. T., Kennedy, B. M., DePaolo, D. J., Hurwitz, S., & Evans, W. C. (2013). Ca, Sr, O and D isotope approach to defining the chemical evolution of hydrothermal fluids: Example from Long Valley, CA, USA. *Geochimica et Cosmochimica Acta*, *122*, 209–225. https://doi.org/10.1016/j.gca.2013.08.011

DePaolo, D. J. (2006). Isotopic effects in fracture-dominated reactive fluid-rock systems. *Geochimica et Cosmochimica Acta*, *70*(5), 1077–1096. https://doi.org/10.1016/j.gca.2005.11.022

Elderfield, H., & Greaves, M. J. (1981). Strontium isotope geochemistry of Icelandic geothermal systems and implications for sea water chemistry. *Geochimica et Cosmochimica Acta*, *45*(11), 2201–2212.

Greber, N. D., Dauphas, N., Bekker, A., Ptáček, M. P., Bindeman, I. N., & Hofmann, A. (2017). Titanium isotopic evidence for felsic crust and plate tectonics 3.5 billion years ago. *Science*, *357*(6357), 1271–1274.

Habicht, K. S., Gade, M., Thamdrup, B., Berg, P., & Canfield, D. E. (2002). Calibration of sulfate levels in the Archean ocean. *Science*, *298*(5602), 2372–2374.

Halverson, G. P., Dudás, F. Ö., Maloof, A. C., & Bowring, S. A. (2007). Evolution of the ^{87}Sr/^{86}Sr composition of Neoproterozoic seawater. *Palaeogeography, Palaeoclimatology, Palaeoecology*, *256*(3–4), 103–129.

Halverson, G. P., & Hurtgen, M. T. (2007). Ediacaran growth of the marine sulfate reservoir. *Earth and Planetary Science Letters*, *263*(1–2), 32–44.

Harris, M., Coggon, R. M., Smith-duque, C. E., Cooper, M. J., Milton, J. A., & Teagle, D. A. H. (2015). Channelling of hydrothermal fluids during the accretion and evolution of the upper oceanic crust : Sr isotope evidence from ODP Hole 1256D. *Earth and Planetary Science Letters*, *416*, 56–66. https://doi.org/10.1016/j.epsl.2015.01.042

Hayba, D. O., & Ingebritsen, S. E. (1997). Multiphase groundwater flow near cooling plutons. *Journal of Geophysical Research B: Solid Earth*, *102*(6), 12235–12252. https://doi.org/10.1029/97JB00552

Horita, J., Zimmermann, H., & Holland, H. D. (2002). Chemical evolution of seawater during the Phanerozoic: Implications from the record of marine evaporites. *Geochimica et Cosmochimica Acta*, *66*(21), 3733–3756.

Ichikuni, M., & Musha, S. (1978). Partition of strontium between gypsum and solution. *Chemical Geology*, *21*(3–4), 359–363.

Kadko, D., Gronvold, K., & Butterfield, D. (2007). Application of radium isotopes to determine crustal residence times of hydrothermal fluids from two sites on the Reykjanes Peninsula , Iceland, *71*, 6019–6029. https://doi.org/10.1016/j.gca.2007.09.018

Kadko, D., & Moore, W. (1988). Radiochemical constraints on the crustal residence time of submarine hydrothermal fluids: Endeavour Ridge. *Geochimica et Cosmochimica Acta*, *52*(3), 659–668.

Kah, L. C., Lyons, T. W., & Frank, T. D. (2004). Low marine sulphate and protracted oxygenation of the Proterozoic biosphere. *Nature*, *431*(7010), 834.

Lassey, K. R., & Blattner, P. (1988). Kinetically controlled oxygen isotope exchange between fluid and rock in one-dimensional advective flow. *Geochimica et Cosmochimica Acta*, *52*(8), 2169–2175. https://doi.org/10.1016/0016-7037(88)90197-4

Laurent, O., Martin, H., Moyen, J.-F., & Doucelance, R. (2014). The diversity and evolution of late-Archean granitoids: Evidence for the onset of "modern-style" plate tectonics between 3.0 and 2.5 Ga. *Lithos*, *205*, 208–235.

Lyons, T. W., Reinhard, C. T., & Planavsky, N. J. (2014). The rise of oxygen in Earth's early ocean and atmosphere. *Nature*, *506*(7488), 307.

Marks, N., Zierenberg, R. A., & Schiffman, P. (2015). Strontium and oxygen isotopic pro fi les through 3 km of hydrothermally altered oceanic crust in the Reykjanes Geothermal System , Iceland. *Chemical Geology*, *412*, 34–47. https://doi.org/10.1016/j.chemgeo.2015.07.006

Matthews, A. (1994). Oxygen isotope geothermometers for metamorphic rocks. *Journal of Metamorphic Geology*, *12*(3), 211–219.

Millot, R., Asmundsson, R., Négrel, P., Sanjuan, B., & Bullen, T. D. (2009). Multi-isotopic (H, O, C, S, Li, B, Si, Sr, Nd) approach for geothermal fluid characterization in Iceland. *Geochimica et Cosmochimica Acta Supplement*, *73*, A883.

Mills, R. A., Teagle, D. A. H., & Tivey, M. K. (1998). 10 . FLUID MIXING AND ANHYDRITE PRECIPITATION WITHIN THE TAG MOUND 1, *158*, 119–127.

Norton, D. (1978). Sourcelines, sourceregions, and pathlines for fluids in hydrothermal systems related to cooling plutons. *Economic Geology*, *73*(1), 21–28.

Pack, A., Tanaka, R., Hering, M., Sengupta, S., Peters, S., & Nakamura, E. (2016). The oxygen isotope composition of San Carlos olivine on the VSMOW2-SLAP2 scale. *Rapid Communications in Mass Spectrometry*, *30*, 1495–1504. https://doi.org/10.1002/rcm.7582

Reed, M. H., Spycher, N. F., & Palandri, J. (2010). Users Guide for CHIM-XPT. *University of Oregon, Eugene*.

Shanks III, W. C. (2001). Stable isotopes in seafloor hydrothermal systems: vent fluids, hydrothermal deposits, hydrothermal alteration, and microbial processes. *Reviews in Mineralogy and Geochemistry*, *43*(1), 469–525.

Shields, G., & Veizer, J. (2002). The Precambrian marine carbonate isotope database: version 1.1. *Geochemistry Geophysics Geosystems*, *3*(6), 1–12. https://doi.org/10.1029/2001GC000266

Stolper, D. A., & Keller, C. B. (2018). A record of deep-ocean dissolved O2 from the oxidation state of iron in submarine basalts. *Nature*, *553*(7688), 323–327. https://doi.org/10.1038/nature25009

Tanaka, R., & Nakamura, E. (2013). Determination of ^{17}O-excess of terrestrial silicate/oxide minerals with respect to Vienna Standard Mean Ocean Water (VSMOW). *Rapid Communications in Mass Spectrometry*, *27*(2), 385–397. https://doi.org/10.1002/rcm.6453

Tang, M., Chen, K., & Rudnick, R. L. (2016). Archean upper crust transition from mafic to felsic marks the onset of plate tectonics, *351*(6271), 115–118. https://doi.org/10.1126/science.aad5513

Turchyn, A. V., Alt, J. C., Brown, S. T., DePaolo, D. J., Coggon, R. M., Chi, G., … Skulski, T. (2013). Reconstructing the oxygen isotope composition of late Cambrian and Cretaceous hydrothermal vent fluid. *Geochimica et Cosmochimica Acta*, *123*, 440–458. https://doi.org/10.1016/j.gca.2013.08.015

Wood, J. R., & Hewett, T. A. (1982). Fluid convection and mass transfer in porous sandstones—A theoretical model. *Geochimica et Cosmochimica Acta*, *46*(10), 1707–1713.

Yeung, L. Y., Hayles, J. A., Hu, H., Ash, J. L., & Sun, T. (2018). Scale distortion from pressure baselines as a source of inaccuracy in triple-isotope measurements. *Rapid Communications in Mass Spectrometry*, *32*(20), 1811–1821.

Zakharov, D. O., & Bindeman, I. N. (2019). Triple oxygen and hydrogen isotopic study of hydrothermally altered rocks from the 2.43–2.41 Ga Vetreny belt, Russia: An insight into the early Paleoproterozoic seawater. *Geochimica et Cosmochimica Acta*, *248*, 185–209. https://doi.org/10.1016/j.gca.2019.01.014

Zheng, Y. F. (1993). Calculation of oxygen isotope fractionation in hydroxyl-bearing silicates. *Earth and Planetary Science Letters*, *120*(3–4), 247–263. https://doi.org/10.1016/0012-821X(93)90243-3

Chapter V

Amelin, Y.V., Heaman, L.M., and Semenov, V.S., 1995, U-Pb geochronology of layered mafic intrusions in the eastern Baltic Shield: Implications for the timing and duration of Paleoproterozoic continental rifting: Precambrian Research, v. 75, p. 31–46, doi:10.1016/0301-9268(95)00015-W.

Barkan, E., and Luz, B., 2003, High-precision measurements of 17O/16O and 18O/16O of O2 and O2/Ar ratio in air: Rapid Commun Mass Spectrom, v. 17, no. 24, p. 2809–2814, doi: 10.1002/rcm.1267.

Bekker, A., 2014, Huronian glaciation, in Gargaud, M., et al., eds., Encyclopedia of Astrobiology: Berlin, Heidelberg, Springer-Verlag, p. 1–8, doi:10.1007/978-3-642-27833-4_742-4.

Bekker, A., Holland, H.D., Wang, P.-L.L., Rumble, D., Stein, H.J., Hannah, J.L., Coetzee, L.L., and Beukes, N.J., 2004, Dating the rise of atmospheric oxygen: Nature, v. 427, p. 117–120, doi:10.1038/nature02260.

Bibikova, E.V., Bogdanova, S.V., Glebovitsky, V.A., Claesson, S., and Skiold, T., 2004, Evolution of the Belomorian Belt: NORDSIM U-Pb zircon dating of the Chupa paragneisses, magmatism, and metamorphic stages: Petrology, v. 12, p. 195–210.

Bindeman, I.N., and Serebryakov, N.S., 2011, Geology, Petrology and O and H isotope geochemistry of remarkably 18O-depleted Paleoproterozoic rocks of the Belomorian Belt, Karelia, Russia, attributed to global glaciation 2.4Ga: Earth and Planetary Science Letters, v. 306, p. 163–174, doi:10.1016/j.epsl.2011.03.031.

Bindeman, I.N., Schmitt, A.K., and Evans, D.A.D., 2010, Limits of hydrosphere-lithosphere interaction: Origin of the lowest-known 18O silicate rock on Earth in the Paleoproterozoic Karelian rift: Geology, v. 38, p. 631–634, doi:10.1130/G30968.1.

Bindeman, I.N., Serebryakov, N.S., Schmitt, A.K., Vazquez, J.A., Guan, Y., Azimov, P.Y., Astafiev, B.Y., Palandri, J., and Dobrzhinetskaya, L., 2014, Field and microanalytical isotopic investigation of ultradepleted in 18O paleoproterozoic “slushball earth” rocks from Karelia, Russia: Geosphere, v. 10, p. 308–339, doi:10.1130/GES00952.1.

Black, L.P., Kamo, S.L., Allen, C.M., Davis, D.W., Aleinikoff, J.N., Valley, J.W., Mundil, R., Campbell, I.H., Korsch, R.J., Williams, I.S., and Foudoulis, C., 2004, Improved 206Pb/238U microprobe geochronology by the monitoring of a trace-element-related matrix effect; SHRIMP, ID-TIMS, ELA-ICP-MS and oxygen isotope documentation for a series of zircon standards: Chemical Geology, v. 205, no. 1–2, p. 115–140, doi: 10.1016/j.chemgeo.2004.01.003.

Bleeker, W., and Ernst, R., 2006, Short-lived mantle generated magmatic events and their dyke swarms: The key unlocking Earth’s paleogeographic record back to 2.6 Ga, in Hanski, E., et al., eds., Dyke Swarms–Time Markers of Crustal Evolution: London, Taylor & Francis Group, p. 3–26, doi:10.1201/NOE0415398992.ch1.

Brasier, A.T., Martin, A.P., Melezhik, V.A., Prave, A.R., Condon, D.J., and Fallick, A.E., 2013, Earth’s earliest global glaciation? Carbonate geochemistry and geochronology of the Polisarka Sedimentary Formation, Kola Peninsula, Russia: Precambrian Research, v. 235, p. 278–294, doi:10.1016/j.precamres.2013.06.007.

Condon, D., 2015, The Bushveld Complex was emplaced and cooled in less than one million years - results of zirconology, and geotectonic implications: Earth and Planetary Science Letters, v. 418, p. 103–114, doi: 10.1016/j.epsl.2015.02.035.

Condon, D., Mclean, N., Schoene, B., Bowring, S., Parrish, R., Stephen, N., 2008, Synthetic U-Pb ‘standard’ solutions for ID-TIMS geochronology: Geochimica et Cosmochimica Acta, v. 72 (12A), A175-A175, doi: 10.1016/j.gca.2008.05.006.

Condon, D.J., Schoene, B., McLean, N.M., Bowring, S.A., and Parrish, R.R., 2015, Metrology and traceability of U-Pb isotope dilution geochronology (EARTHTIME Tracer Calibration Part I): Geochimica et Cosmochimica Acta, v. 164, p. 464–480, doi: 10.1016/j.gca.2015.05.026.

Dansgaard, W., 1964, Stable isotopes in precipitation: Tellus, v. 16, p. 436–468, doi:10.3402/tellusa.v16i4.8993.

Evans, D.A.D., Beukes, N.J., and Kirschvink, J.L., 1997, Low-latitude glaciation in the Palaeoproterozoic era: Nature, v. 386, p. 262–266, doi:10.1038/386262a0.

Gärtner, C., Bahlburg, H., Melezhik, V.A., and Berndt, J., 2014, Dating Palaeoproterozoic glacial deposits of the Fennoscandian Shield using detrital zircons from the Kola Peninsula, Russia: Precambrian Research, v. 246, p. 281–295, doi:10.1016/j.precamres.2014.03.014.

Herwartz, D., Pack, A., Krylov, D., Xiao, Y., Muehlenbachs, K., Sengupta, S., and Di Rocco, T., 2015, Revealing the climate of snowball Earth from □17O systematics of hydrothermal rocks: Proceedings of the National Academy of Sciences of the United States of America, v. 112, p. 5337–5341, doi:10.1073/pnas.1422887112.

Hoffman, P.F., 2013, The Great Oxidation and a Siderian snowball Earth: MIF-S based correlation of Paleoproterozoic glacial epochs: Chemical Geology, v. 362, p. 143–156, doi:10.1016/j.chemgeo.2013.04.018.

Ireland, T.R., and Williams, I.S., 2003, considerations in zircon geochronology by SIMS, in Hanchar, J.M. and Hoskin, W.O., eds., Reviews in Mineralogy and Geochemistry, Mineralogical Society of America, Volume 53, p. 215-241.

Kirschvink, J.L., Gaidos, E.J., Bertani, L.E., Beukes, N.J., Gutzmer, J., Maepa, L.N., and Steinberger, R.E., 2000, Paleoproterozoic snowball earth: Extreme climatic and geochemical global change and its biological consequences: Proceedings of the National Academy of Sciences of the United States of America, v. 97, p. 1400–1405, doi:10.1073/pnas.97.4.1400.

Kulikov, V.S., Bychkova, Y.V., Kulikova, V., and Ernst, R., 2010, The Vetreny Poyas (Windy Belt) subprovince of southeastern Fennoscandia: An essential component of the ca. 2.5–2.4Ga Sumian large igneous provinces: Precambrian Research, v. 183, p. 589–601, doi:10.1016/j.precamres.2010.07.011.

Lobach-Zhuchenko, S.B., Arestova, N.A., Chekulaev, V.P., Levsky, L.K., Bogomolov, E.S., and Krylov, I.N., 1998, Geochemistry and petrology of 2.40–2.45 Ga magmatic rocks in the north-western Belomorian Belt, Fennoscandian Shield, Russia: Precambrian Research, v. 92, p. 223–250, doi:10.1016/S0301-9268(98)00076-X.

Ludwig, K.R., 2009, Squid 2: A user's manual, Berkeley Geochronology Center Special Publication, no. 5, p. 110.

Ludwig, K.R., 2012, Isoplot 3.75: A geochronological toolkit for Excel: Berkeley Geochronology Center Special Publication, no. 5, p. 75.

Luz, B., and Barkan, E., 2010, Variations of 17O/16O and 18O/16O in meteoric waters: Geochimica et Cosmochimica Acta, v. 74, p. 6276–6286, doi:10.1016/j.gca.2010.08.016.

Mattinson, J.M., 2005, Zircon U-Pb chemical abrasion ("CA-TIMS") method: Combined annealing and multi-step partial dissolution analysis for improved precision and accuracy of zircon ages: Chemical Geology, v. 220, no. 1-2, p. 47–66, doi: 10.1016/j.chemgeo.2005.03.011.

Mertanen, S., Vuollo, J.I., Huhma, H., Arestova, N.A., and Kovalenko, A., 2006, Early Paleoproterozoic–Archean dykes and gneisses in Russian Karelia of the Fennoscandian Shield—New paleomagnetic, isotope age and geochemical investigations: Precambrian Research, v. 144, p. 239–260, doi:10.1016/j.precamres.2005.11.005.

Muehlenbachs, K., 1998, The oxygen isotopic compostion of the oceans, sediments and the seafloor: Chemical Geology, v. 145, p. 263–273.

Pack, A., and Herwartz, D., 2014, The triple oxygen isotope composition of the Earth mantle and understanding $\Delta^{17}O$ variations in terrestrial rocks and minerals: Earth and Planetary Science Letters, v. 390, p. 138–145, doi:10.1016/j.epsl.2014.01.017.

Pack, A., and Herwartz, D., 2014, The triple oxygen isotope composition of the Earth mantle and understanding δO17 variations in terrestrial rocks and minerals: Earth and Planetary Science Letters, v. 390, p. 138–145, doi: 10.1016/j.epsl.2014.01.017.

Pack, A., Toulouse, C., and Przybilla, R., 2007, Determination of oxygen triple isotope ratios of silicates without cryogenic separation of NF3 - Technique with application to analyses of technical O2 gas and meteorite classification: Rapid Communications in Mass Spectrometry, v. 21, no. 22, p. 3721–3728, doi: 10.1002/rcm.3269.

Pesonen, L.J., Elming, S.-A., Mertanen, S., Pisarevsky, S., D'Agrella-Filho, M., Meert, J., Schmidt, P., Abrahamsen, N., and Bylund, G., 2003, Paleomagnetic configuration of supercontinents during the Proterozoic: Tectonophysics, v. 375, p. 289–324, doi:10.1016/S0040-1951(03)00343-3.

Rasmussen, B., Bekker, A., and Fletcher, I.R., 2013, Correlation of Paleoproterozoic glaciations based on U-Pb zircon ages for tuff beds in the Transvaal and Huronian Supergroups: Earth and Planetary Science Letters, v. 382, p. 173–180, doi:10.1016/j.epsl.2013.08.037.

Salminen, J., Halls, H.C., Mertanen, S., Pesonen, L.J., Vuollo, J., and Söderlund, U., 2014, Paleomagnetic and geochronological studies on Paleoproterozoic diabase dykes of Karelia, East Finland-Key for testing the Superia supercraton: Precambrian Research, v. 244, p. 87–99, doi:10.1016/j.precamres.2013.07.011.

Slabunov, A.I., Kulikova, V.V., Stepanov, V.S., Kulikov, V.S., Matukov, D.I., and Kevlich, V.I., 2006, U-Pb geochronology of zircons from Kiyostrovskogo layered massif, Belomorian mobile belt and correlation of Paleoproterozoic magmatism of south-eastern Fennoscandian shield, in Proceedings, Isotopnoe datirovanie processov rudoobrazovaniya, magmatisma, osadkonakopleniya i metamorfisma, Moscow 2006, p. 281–286.

Slabunov, A.I., Volodichev, O.I., Skublov, S.G., and Berezin, A.V., 2011, Main stages of the formation of paleoproterozoic eclogitized gabbro-norite: Evidence from U–Pb (SHRIMP) dating of zircons and study of their genesis: Doklady Earth Sciences, v. 437, p. 396–400, doi:10.1134/S1028334X11030202.

Stacey, J.S., and Kramers, J.D., 1975, Approximation of terrestrial lead isotope evolution by a two-stage model: Earth and Planetary Science Letters, v. 26, no. 2, p. 207–221, doi: 10.1016/0012-821X(75)90088-6.

Stepanova, A.V., Salnikova, E.B., Samsonov, A.V., Egorova, S.V., Larionova, Y.O., and Stepanov, V.S., 2015, The 2.31 Ga mafic dykes in the karelian craton, eastern fennoscandian shield: U-Pb age, source characteristics and implications for continental break-up processes: Precambrian Research, v. 259, p. 43–57, doi:10.1016/j.precamres.2014.10.002.

Trendall, A.F., Compston, W., Williams, I.S., Armstrong, R.A., Arndt, N.T., McNaughton, N.J., Nelson, D.R., Barley, M.E., Beukes, N.J., De Laeter, J.R., Retief, E.A., and Thorne, A.M., 1990, Precise zircon U-Pb chronological comparison of the volcano-sedimentary sequences of the Kaapvaal and Pilbara Cratons between about 3.1 and 2.4 Ga, in Proceedings, Third International Archean Symposium, Perth, p. 81–83.

Valley, J.W., Kitchen, N., Kohn, M.J., Niendorf, C.R., and Spicuzza, M.J., 1995, UWG-2, a garnet standard for oxygen isotope ratios: Strategies for high precision and accuracy with laser heating: Geochimica et Cosmochimica Acta, v. 59, no. 24, p. 5223–5231, doi: 10.1016/0016-7037(95)00386-X.

Williams, I.S., 1997, U-Th-Pb geochronology by ion microprobe: not just ages but histories: Society Economic Geologists Reviews in Economic Geology, v. 7, p. 1-35.

Zeh, A., Ovtcharova, M., Wilson, A.H., and Schaltegger, U., 2015, The Bushveld Complex was emplaced and cooled in less than one million years - results of zirconology, and geotectonic implications: Earth and Planetary Science Letters, v. 418, p. 103–114, doi: 10.1016/j.epsl.2015.02.035.

Chapter VI

Abbot D. S., Voigt A. and Koll D. (2011) The Jormungand global climate state and implications for Neoproterozoic glaciations. *J. Geophys. Res. Atmos.* **116**.

Alt J. C. and Teagle D. A. H. (2000) Hydrothermal alteration and fluid fluxes in ophiolites and oceanic crust. *Geol. Soc. Am. Spec. Pap.* **349**, 273–282.

Antropov, P. Ya and Kratz, K.O (1960) *Geology of USSR, Volume 37: Karelian ASSR.*

Balagansky V. V., Timmerman M. J., Kozlova N. Y. and Kislitsyn R. V. (2001) A 2.44 Ga syn-tectonic mafic dyke swarm in the Kolvitsa Belt, Kola Peninsula, Russia: Implications for early Palaeoproterozoic tectonics in the north-eastern Fennoscandian shield. *Precambrian Res.* **105**, 269–287.

Beach A. (1973) The mineralogy of high temperature shear zones at Scourie, N.W. Scotland. *J. Petrol.* **14**, 231–248.

Bibikova E. V, Bogdanova S. V, Glebovitsky V. A., Claesson S. and Skiold T. (2004) Evolution of the Belomorian Belt: NORDSIM U-Pb zircon dating of the Chupa paragneisses, magmatism, and metamorphic stages. *Petrology* **12**, 195–210.

Bindeman I. N. and Lee J. E. (2018) The possibility of obtaining ultra-low-δ^{18}O signature of precipitation near equatorial latitudes during the Snowball Earth glaciation episodes. *Precambrian Res.* **319**, 211-219.

Bindeman I. N. and Serebryakov N. S. (2011) Geology, Petrology and O and H isotope geochemistry of remarkably 18O-depleted Paleoproterozoic rocks of the Belomorian Belt, Karelia, Russia, attributed to global glaciation 2.4Ga. *Earth Planet. Sci. Lett.* **306**, 163–174.

Bindeman I. N., Schmitt a. K. and Evans D. a. D. (2010) Limits of hydrosphere-lithosphere interaction: Origin of the lowest-known δ^{18}O silicate rock on Earth in the Paleoproterozoic Karelian rift. *Geology* **38**, 631–634.

Bindeman I. N., Serebryakov N. S., Schmitt A. K., Vazquez J. A., Guan Y., Azimov P. Y., Astafiev B. Y., Palandri J. and Dobrzhinetskaya L. (2014) Field and microanalytical isotopic investigation of ultradepleted in ^{18}O paleoproterozoic "slushball earth" rocks from Karelia, Russia. *Geosphere* **10**, 308–339.

Bleeker W. (2003) The late Archean record: A puzzle in ca. 35 pieces. *Lithos* **71**, 99–134.

Bleeker W. and Ernst R. (2006) Short-lived mantle generated magmatic events and their dyke swarms: The key unlocking Earth's paleogeographic record back to 2.6 Ga. *Time Markers Crustal Evol.*, 1–24.

Bowen, G. J. (2010). Waterisotopes.org. Gridded maps of the isotopic composition of meteoric precipitation.

Bridgwater D., Mengel F., Fryer B., Wagner P. and Hansen S. C. (1995) Early Proterozoic mafic dykes in the North Atlantic and Baltic cratons: field setting and chemistry of distinctive dyke swarms. *Geol. Soc. London, Spec. Publ.* **95**, 193–210.

Cartwright I. and Valley J. W. (1991) Low-^{18}O Scourie dike magmas from the Lewisian complex, northwestern Scotland. *Geology* **19**, 578–581.

Cartwright I. and Valley J. W. (1992) Oxygen-isotope geochemistry of the Scourian complex, northwest Scotland. *J. Geol. Soc. London.* **149**, 115–125.

Chiba H., Chacko T., Clayton R. N. and Goldsmith J. R. (1989) Oxygen isotope fractionations involving diopside, forsterite, magnetite, and calcite: Application to geothermometry. *Geochim. Cosmochim. Acta* **53**, 2985–2995.

Colón, D. P., Bindeman, I. N., Stern, R. A., & Fisher, C. M. (2015). Isotopically diverse rhyolites coeval with the Columbia River Flood Basalts: evidence for mantle plume interaction with the continental crust. *Terra Nova*, **27**, 270-276.

Cliff, R. A., Gray, C. M., & Huhma, H. (1983). A Sm-Nd isotopic study of the South Harris Igneous Complex, the Outer Hebrides. *Contrib. Mineral. Petrol.* **82**, 91–98.

Dansgaard, W., 1964, Stable isotopes in precipitation, *Tellus*, **16**, 436–468.

Davies J. H. F. L. and Heaman L. M. (2014) New U-Pb baddeleyite and zircon ages for the Scourie dyke swarm: A long-lived large igneous province with implications for the Paleoproterozoic evolution of NW Scotland. *Precambrian Res.* **249**, 180–198.

Davies J. H. F. L., Stern R. A., Heaman L. M., Rojas X. and Walton E. L. (2015) Resolving oxygen isotopic disturbance in zircon: A case study from the low δ^{18}O Scourie dikes, NW Scotland. *Am. Mineral.* **100**, 1952–1966.

Ernst R. and Bleeker W. (2010) Large igneous provinces (LIPs), giant dyke swarms, and mantle plumes: significance for breakup events within Canada and adjacent regions from 2.5 Ga to the Present. *Can. J. Earth Sci.* **47**, 695–739.

Evans D. A., Beukes N. J. and Kirschvink J. L. (1997) Low-latitude glaciation in the Palaeoproterozoic era. *Nature* **386**, 262–266.

Farver, J. R., and Giletti, B. J. (1985). Oxygen diffusion in amphiboles. *Geochim. Cosmochim. Acta* **49**, 1403-1411.

Furnes H., de Wit M., Staudigel H., Rosing M. and Muehlenbachs K. (2007) A vestige of Earth's oldest ophiolite. *Science* **315**, 1704–1707.

Glebovitsky and Bushmin (1983) *Post-migmatite metasomatism*. Nauka, Leningrad.

Grassineau N. V., Mattey D. P. and Lowry D. (2001) Sulfur isotope analysis of sulfide and sulfate minerals by continuous flow-isotope ratio mass spectrometry. *Anal. Chem.* **73**, 220–225.

Gumsley A. P., Chamberlain K. R., Bleeker W., Söderlund U., de Kock M. O., Larsson E. R. and Bekker A. (2017) Timing and tempo of the Great Oxidation Event. *Proc. Natl. Acad. Sci.* **114**, 201608824.

Hattori K. and Muehlenbachs K. (1982) Oxygen Isotope Ratios of the Icelandic Crust. *J. Geophys. Res.* **87**, 6559–6565.

Heaman L. M. (1997) Global mafic volcanism at 2.45 Ga: remnants of an ancient large igneous province? *Geology* **25**, 299–302.

Heaman L. M. and Tarney J. (1989) U–Pb baddeleyite ages for the Scourie dyke swarm, Scotland: evidence for two distinct intrusion events. *Nature* **340**, 705–708.

Herwartz D., Pack A., Krylov D., Xiao Y., Muehlenbachs K., Sengupta S. and Di Rocco T. (2015) Revealing the climate of snowball Earth from Δ^{17}O systematics of hydrothermal rocks. *Proc. Natl. Acad. Sci.* **112**, 5337–5341.

Hodel F., Macouin M., Trindade R. I. F., Triantafyllou A., Ganne J., Chavagnac V., Berger J., Rospabé M., Destrigneville C., Carlut J., Ennih N. and Agrinier P. (2018) Fossil black smoker yields oxygen isotopic composition of Neoproterozoic seawater. *Nat. Commun.* **9***,* 1453.

Hoefs J. (2018) *Stable Isotope Geochemistry*, p. 285. Springer.

Hoffman P. F. (2013) The Great Oxidation and a Siderian snowball Earth: MIF-S based correlation of Paleoproterozoic glacial epochs. *Chem. Geol.* **362**, 143–156.

Holmden C. and Muehlenbachs K. (1993) The 18O/16O Ratio of 2-Billion-Year-Old Seawater Inferred from Ancient Oceanic Crust. *Science* **259**, 1733–1736.

Hughes H. S. R., McDonald I., Goodenough K. M., Ciborowski T. J. R., Kerr A. C., Davies J. H. F. L. and Selby D. (2014) Enriched lithospheric mantle keel below the Scottish margin of the North Atlantic Craton: Evidence from the Palaeoproterozoic Scourie Dyke Swarm and mantle xenoliths. *Precambrian Res.* **250**, 97–126.

Kohn M. J. and Valley J. W. (1998) Obtaining equilibrium oxygen isotope fractionations from rocks : theory and examples. *Contrib. Mineral. Petrol.* **132**, 209–224.

Krogh, T. E. (1994). Precise U-Pb ages for Grenvillian and pre-Grenvillian thrusting of Proterozoic and Archean metamorphic assemblages in the Grenville Front tectonic zone, Canada. *Tectonics*, **13**, 963-982.

Kulikov V. S and, Kulikova V. V. (1990) Geology of Kiy Island archipelago, White Sea. Petrozavodsk, Karelian Research Centre, 3–5.

Kulikov V. S., Bychkova Y. V., Kulikova V. V. and Ernst R. (2010) The Vetreny Poyas (Windy Belt) subprovince of southeastern Fennoscandia: An essential component of the ca. 2.5-2.4 Ga Sumian large igneous provinces. *Precambrian Res.* **183**, 589–601.

Lobach-Zhuchenko S. B., Arestova N. A., Chekulaev V. P., Levsky L. K., Bogomolov E. S. and Krylov I. N. (1998) Geochemistry and petrology of 2.40-2.45 Ga magmatic rocks in the north-western Belomorian Belt, Fennoscandian Shield, Russia. *Precambrian Res.* **92**, 223–250.

Luz B. and Barkan E. (2010) Variations of $^{17}O/^{16}O$ and $^{18}O/^{16}O$ in meteoric waters. *Geochim. Cosmochim. Acta* **74**, 6276–6286.

Martin E., Bindeman I., Balan E., Palandri J., Seligman A. and Villemant B. (2017) Hydrogen isotope determination by TC/EA technique in application to volcanic glass as a window into secondary hydration. *J. Volcanol. Geotherm. Res.* **348**, 49–61.

Melezhik V. A. and Hanski E. J. (2013) *Reading the Archive of Earth's Oxygenation*. **1**, 111-178

Mertanen S., Halls H. C., Vuollo J. I., Pesonen L. J. and Stepanov V. S. (1999) Paleomagnetism of 2.44 Ga mafic dykes in Russian Karelia, eastern Fennoscandian shield - implications for continental reconstructions. *Precambrian Res.* **98**, 197–221.

Miller M. F. (2002) Isotopic fractionation and the quantification of 17O anomalies in the oxygen three-isotope system: An appraisal and geochemical significance. *Geochim. Cosmochim. Acta* **66**, 1881–1889.

Nilsson M. K. M., Söderlund U., Ernst R. E., Hamilton M. A., Scherstén A. and Armitage P. E. B. (2010) Precise U-Pb baddeleyite ages of mafic dykes and intrusions in southern West Greenland and implications for a possible reconstruction with the Superior craton. *Precambrian Res.* **183**, 399–415.

Nilsson M. K. M., Klausen M. B., Söderlund U. and Ernst R. E. (2013) Precise U-Pb ages and geochemistry of Palaeoproterozoic mafic dykes from southern West Greenland: Linking the North Atlantic and the Dharwar cratons. *Lithos* **174**, 255–270. Available at: http://dx.doi.org/10.1016/j.lithos.2012.07.021.

O'Hara M.J. (1961) Petrology of the Scourie Dyke, Sutherland. *Min. Mag.* **32**, 848-865

Pack A. and Herwartz D. (2014) The triple oxygen isotope composition of the Earth mantle and understanding $\Delta^{17}O$ variations in terrestrial rocks and minerals. *Earth Planet. Sci. Lett.* **390**, 138–145.

Pack A., Tanaka R., Hering M., Sengupta S., Peters S. and Nakamura E. (2016) The oxygen isotope composition of San Carlos olivine on the VSMOW2-SLAP2 scale. *Rapid Commun. Mass Spectrom.* **30**, 1495–1504.

Park R. G. (1995) Palaeoproterozoic Laurentia-Baltica relationships: a view from the Lewisian. *Geol. Soc. London, Spec. Publ.* **95**, 211–224.

Rooney, A. D., Strauss, J. V., Brandon, A. D., & Macdonald, F. A. (2015). A Cryogenian chronology: Two long-lasting synchronous Neoproterozoic glaciations. *Geology*, **43**, 459-462.

Salminen J., Halls H. C., Mertanen S., Pesonen L. J., Vuollo J. and Söderlund U. (2014) Paleomagnetic and geochronological studies on Paleoproterozoic diabase dykes of Karelia, East Finland-Key for testing the Superia supercraton. *Precambrian Res.* **244**, 87–99.

Sengupta S. and Pack A. (2018) Triple oxygen isotope mass balance for the Earth's oceans with application to Archean cherts. *Chem. Geol.* **495**, 18–26.

Sharp Z. D., Gibbons J. A., Maltsev O., Atudorei V., Pack A., Sengupta S., Shock E. L. and Knauth L. P. (2016) A calibration of the triple oxygen isotope fractionation in the SiO_2-H_2O system and applications to natural samples. *Geochim. Cosmochim. Acta* **186**, 105–119.

Sharp Z. D., Wostbrock J. A. G. and Pack A. (2018) Mass-dependent triple oxygen isotope variations in terrestrial materials. *Geochemical Perspect. Lett.* **7**, 27–31.

Skiöld T., Bogdanova S., Gorbatschev R. and Bibikova E. (2001) Timing of late Palaeoproterozoic metamorphism in the northern Belomorian Belt, White Sea region: Conclusions from U-Pb isotopic data and P-T evidence. *Bull. Geol. Soc. Finl.* **73**, 59–73.

Slabunov A.I., Kulikova V.V., Stepanov V.S., Kulikov V.S., Matukov D.I., and Kevlich V.I. (2006) U-Pb geochronology of zircons from Kiyostrovskogo layered massif, Belomorian mobile belt and correlation of Paleoproterozoic magmatism of south-eastern Fennoscandian shield, *in* Proceedings, Isotopnoe datirovanie processov rudoobrazovaniya, magmatisma, osadkonakopleniya i metamorfisma, Moscow 2006, p. 281-286.

Stepanova A. and Stepanov V. (2010) Paleoproterozoic mafic dyke swarms of the Belomorian Province, eastern Fennoscandian Shield. *Precambrian Res.* **183**, 602–616.

Stepanova A. V., Salnikova E. B., Samsonov A. V., Larionova Y. O., Egorova S. V. and Savatenkov V. M. (2017) The 2405 Ma doleritic dykes in the Karelian Craton: A fragment of a Paleoproterozoic large igneous province. *Dokl. Earth Sci.* **472**, 72–77.

Suzuoki T. and Epstein S. (1976) Hydrogen isotope fractionation between OH-bearing minerals and water. *Geochim. Cosmochim. Acta* **40**, 1229–1240.

Tarney J. and Weaver B. L. (1987) Geochemistry of the Scourian complex : petrogenesis and tectonic models. In *Park, R.G. and Tarney, J. (eds.), Evolution of the Lewisian and Comparable Precambrian High Grade Terrains, Geol. Soc. Spec. Pub.* pp. 45–56.

Tarney J. and Weaver B. L. (1987) Mineralogy, petrology and geochemistry of the Scourie dykes : petrogenesis and crystallization processes in dykes intruded at depth. In *Park, R.G. and Tarney, J. (eds.), Evolution of the Lewisian and Comparable Precambrian High Grade Terrains, Geol. Soc. Spec. Pub.* pp. 217–233.

Tarney, J. (1963) Assynt Dykes and their metamorphism. *Nature* **199**, 672–674.

Taylor H. P. (1977) Water/rock interactions and the origin of in granitic batholiths. *Geol. Soc. Spec. Publ. London* **133**, 509–558.

Taylor Jr. H. P. (1971) Oxygen Isotope Evidence for Large-Scale Interaction between Meteoric Ground Waters and Tertiary Granodiorite Intrusions, Western Cascade Range, Oregon. *J. Geophys. Res.* **76**, 7855–7874.

Taylor H. P. (1974) The Application of Oxygen and Hydrogen Isotope Studies to Problems of Hydrothermal Alteration and Ore Deposition. *Econ. Geol.* **69**, 843–883.

Valley, J.W. (1986) Stable isotope geochemistry of metamorphic rocks. In *Valley, J.W., Taylor H.P. and O'Neil J.R. (eds) Stable isotopes in high temperature geological processes. Reviews in Mineralogy* **16**, 445-489.

Weaver, B.L. and Tarney, J., (1981). The Scourie Dyke Suite: petrogenesis and geochemical nature of the Proterozoic sub-continental mantle. Contrib. Mineral. Petrol. 78, 175–188.

Wheeler J., Park R. G., Rollinson H. R. and Beach A. (2010) The Lewisian Complex: insights into deep crustal evolution. *Geol. Soc. London, Spec. Publ.* **335**, 51–79.

Whitehouse M. J., Bridgwater D. and Park R. G. (1997) Detrital zircon ages from the Loch Maree Group, Lewisian complex, NW Scotland: confirmation of a Palaeoproterozoic Laurentia-Fennoscandia connection. *Terra Nov.* **9**, 260–263.

Wotzlaw, J. F., Bindeman, I. N., Schaltegger, U., Brooks, C. K., & Naslund, H. R. (2012). High-resolution insights into episodes of crystallization, hydrothermal alteration and remelting in the Skaergaard intrusive complex. *Earth and Planetary Science Letters*, **355**, 199-212.

Zakharov D. O., Bindeman I. N., Slabunov A. I., Ovtcharova M., Coble M. A., Serebryakov N. S. and Schaltegger U. (2017) Dating the Paleoproterozoic snowball Earth glaciations using contemporaneous subglacial hydrothermal systems. *Geology* **45**, 5–8.

Zakharov D. O. and Bindeman I. N. (2019) Triple oxygen and hydrogen isotopic study of hydrothermally altered rocks from the 2.43 – 2.41 Ga Vetreny belt, Russia : An insight into the early Paleoproterozoic seawater. *Geochim. Cosmochim. Acta* **248**, 185–209. Available at: https://doi.org/10.1016/j.gca.2019.01.014.

Zheng Y.-F. (1993) Calculation of oxygen isotope fractionation in anhydrous silicate minerals. *Geochim. Cosmochim. Acta* **57**, 1079–1091.